ISBN 978-82-471-1697-5 (printed ver.)
ISBN 978-82-471-1698-2 (electronic ver.)
ISSN 1503-8181

Doctoral theses at NTNU, 2009:153

Tone M. Vestbøstad

A Numerical Study of Wave-in-Deck Impact using a Two-dimensional Constrained Interpolation Profile Method

Doctoral Thesis
Tone M. Vestbøstad

NTNU
Norwegian University of
Science and Technology

Doctoral theses at NTNU, 2009:153

NTNU

NTNU
Norwegian University of
Science and Technology

Thesis for the degree of
philosophiae doctor
Faculty of Engineering Science and Technology
Department of Marine Technology

NTNU
Norwegian University of
Science and Technology

Tone M. Vestbøstad

A Numerical Study of Wave-in-Deck Impact using a Two-dimensional Constrained Interpolation Profile Method

Thesis for the degree of philosophiae doctor

Trondheim, August 2009

Norwegian University of
Science and Technology
Faculty of Engineering Science and Technology
Department of Marine Technology

NTNU
Norwegian University of
Science and Technology

NTNU
Norwegian University of Science and Technology

Thesis for the degree of philosophiae doctor

Faculty of Engineering Science and Technology
Department of Marine Technology

ISBN 978-82-471-1697-5 (printed ver.)
ISBN 978-82-471-1698-2 (electronic ver.)
ISSN 1503-8181

Doctoral Theses at NTNU, 2009:153

Printed by Tapir Uttrykk

A Numerical Study of Wave-in-Deck Impact using a Two-dimensional Constrained Interpolation Profile Method

by

Tone M. Vestbøstad

SUBMITTED IN PARTIAL FULFILLMENT
OF THE REQUIREMENTS FOR THE DEGREE OF
DOCTOR PHILOSOPHIAE

NTNU
Innovation and Creativity

Norway

2009

Abstract

A Constrained Interpolation Profile method following Hu and Kashiwagi (2004) is developed for wave impact applications. Two-dimensional, unsteady, viscous and incompressible flow is assumed. The numerical model is a finite difference high-order up-wind scheme for solving the Navier–Stokes equations. A domain-embedding, staggered Cartesian grid is used for the spatial discretization. The water and air phases are modeled as one fluid. The material properties vary across the domain, and the free surface is modeled as a layer rather than a sharp interface. Different surface capturing schemes based on density functions are tested.

Benchmark tests focusing on marine applications are used to develop the code and demonstrate the capabilities and limitations of the method. A numerical wave tank is developed and validated using both higher order wave theory and experimental results from physical wave tanks. Progressive, regular waves are simulated. Wave impact simulations are performed for a simplified, fixed deck structure. Horizontal and vertical global forces are computed. Different combinations of wave height, wave period and airgap are used in the simulations. The impact process is studied. Parameter studies for wave crest variation and airgap changes are performed. Results are compared with existing experimental results. The global loading process for multiple impacts on the deck box is discussed using both numerical and experimental results.

Acknowledgments

This work has been carried out under the supervision of Professor Odd M. Faltinsen at the Centre for Ships and Offshore Structures, Norwegian University of Science and Technology. His contributions and continuous guidance is highly acknowledged.

The work is supported by my employer, StatoilHydro and has been carried out as a part-time activity. Dr. Sverre Haver at the Department of Marine Structures and Risers has supervised this study. I am very grateful for his tireless support, encouragement and guidance, and for being my mentor for more than ten years. Also, many of my other colleagues at StatoilHydro supported me. Geir Løland, Trond Stokka Meling and Narve Oma deserve thanks for ensuring continuous funding. Special thanks to Professor Ove Tobias Gudmestad for both scientific and administrative support, and to Tor Inge Fossan and Torbjørg Opedal for letting me carry out this work at very busy times for our department at StatoilHydro.

Dr. Changhong Hu at the Research Institute of Applied Mechanics, Kyushu University, is acknowledged for his help and many useful suggestions on the development of the CIP code.

At the Department of Marine Hydrodynamics and CeSOS at NTNU, I enjoyed the encouraging and positive environment made by my fellow students. My gratitude goes to David Kristiansen and Trygve Kristiansen, for valuable scientific discussions, for help on practical, numerical and theoretical matters, and for large amounts of coffee. Thank you most of all for making this outsider always feel welcome and included.

Dr. Rolf J. Baarholm is highly acknowledged for providing his experimental data from 1998, and for letting me participate in the experiments performed by MARINTEK in 2008. Thanks for many fruitful discussions and for sharing your formidable knowledge on the topic of wave-in-deck impacts with me.

I am grateful also to the staff at the Department of Mechanical and Structural Engineering and Materials Science at the University of Stavanger, who let me stay as their guest for two years while working on this PhD. Special thanks to Professor Jasna B. Jakobsen and Dr. Katrine van Raaij for enjoyable social and scientific discussions. I'll miss the numerous latte's at Bok-kafeen together with you.

The following persons are acknowledged for proof-reading: David Kristiansen and Sverre Haver for proof-reading the entire thesis, and Jasna B. Jakobsen, Katrine van Raaij and Rolf Baarholm for proof-reading parts of the thesis.

My love and my gratitude go to my husband, Gunnar. Your everlasting support and optimistic view of life has made all the difference. Thank you also for being a wonderful father for our three children, and for coping with an absent wife during my frequent stays in Trondheim and long hours at the office. Finally, thanks to my three children; Ingunn, Eivind and Lena, for keeping the importance of my study in the right perspective.

Contents

Nomenclature

General rules:

- Only the most used symbols are listed in the follwing section.
- The meaning of a symbol is given at least when introduced in the thesis.
- In some cases, the same symbol is used to denote different quantities.

Subscripts:

0	initial value or eigenvalue
i	spatial direction ($i = 1, 2$ denotes horizontal and vertical direction, respectively)
k, l	grid indices in horizontal and vertical direction

Superscripts:

$*$	intermediate or artificial value
n	time step

Symbols:

A_{33}	added mass coefficient in heave
B	deck box breadth
B_{33}	potential damping coefficient in heave
C_{33}	stiffness coefficient in heave
C_S	slamming coefficient
E_k	kinetic energy
E_p	potential energy
F_b	buoyancy force
F_i	force or approximation function
G_i	derivative of the approximation function

H	wave height
H_b	deck box height
L	deck box length or wave tank length
N_x	number of cells in horizontal direction
N_y	number of cells in vertical direction
R	cylinder radius
S_0	wavemaker stroke
S_b	body boundary
S_w	tank walls
S_{ij}	viscous stress tensor
T	wave period
T_0	eigenperiod
U_0	outer velocity
U_i	body velocity
V	impact velocity
V_1	water volume
a	tank breadth
c	Courant number
d	water depth
f_b	body force
f_N	Nyquist frequency
f_c	cut-off frequency
f_d	damping force
g	acceleration of gravity
g_k	flux at cell no. k
h	water depth
h_{WT}	height of wave tank
k	wave number
n_i	normal vector in the ith direction
p	pressure
p_D	hydrodynamic pressure
r_c	cylinder radius
t	time
u	horizontal velocity
u_b	boundary cell velocity

u_{bl}	boundary layer velocity
u_i	fluid velocity
v	vertical velocity
x_i	spatial coordinate
y	vertical coordinate
Δt	time step size
Δx	horizontal grid size
Δy	vertical grid size
Ω	computational domain
Φ	velocity potential
Ψ	transformation function
β	THINC surface steepness parameter
δ	boundary layer thickness
δ_{ij}	Kronecker delta
δy_L	surface layer thickness
ε	error
η_2	sway motion
η_3	heave motion
η_A	motion amplitude
η_D	airgap
λ	wave length
μ	viscosity coefficient
μ_{cr}	critical damping
μ_{p}	artificial damping
ν	kinematic viscosity coefficient
ρ	mass density
ϕ_1	water density function
ϕ_2	air density function
ϕ_3	body density function
ϕ_m	density function
ω	circular wave frequency
ζ	free surface
ζ_A	wave amplitude
ζ_C	wave crest height

List of Abbreviations

1D	One-dimensional
2D	Two-dimensional
3D	Three-dimensional
BEM	Boundary Element Method
CCUP	CIP Combined and Unified Procedure
CeSOS	Centre for Ships and Offshore Structures
CFD	Computational Fluid Dynamics
CFL	Courant-Friedrichs-Lewy
CIP	Constrained Interpolation Profile
CSL	Conservative Semi-Lagrangian
DD	Domain Decomposition
FDM	Finite Difference Method
FEM	Finite Element Method
FVM	Finite Volume Method
LS	Level Set
MAC	Marker and Cell
MMS	US Minerals Management Service
NCS	Norwegian Continental Shelf
NTNU	Norwegian University of Science and Technology
NWT	Numerical Wave Tank
PSA	Petroleum Safety Authority
SPH	Smoothed Particle Hydrodynamics
THINC	Tangent of Hyperbola for Interface Capturing
TLP	Tension Leg Platform
VoF	Volume of Fluid

Chapter 1

Introduction

1.1 Motivation

When designing offshore platforms, an air gap, i.e. a positive distance between the design waves and the platform deck, is provided. During the lifetime of an offshore platform, the actual airgap may change. Improved methodology and increased amount of measured data may lead to increased design wave estimates. For fixed platforms, subsidence of the seabed may lead to decreased deck height. For floating structures, reanalysis using improved methods may reveal less air gap than assumed in the original design. Also, platforms are subjected to modifications during its lifetime, introducing changes to layout and topside weight. This may also have adverse effects on the air gap for important equipment, structural parts or for the entire structure.

When the air gap is decreased, the chance of waves hitting the platform deck is increased. For such an event, the global loads on the platform may exceed the original design loads. The Facilities Regulations of the Petroleum Safety Authority (PSA) states that accidental and environmental loads with an annual probability greater than 10^{-4} shall not cause the loss of a main safety function (PSA, 2001). In this context, the main safety function includes the main load carrying capacity, safe areas such as the living quarters and evacuation routes including life boats.

To be able to assess the safety of a platform with insufficient air gap and consider the possibility of re-qualification, accurate predictions of loads from wave-in-deck events are necessary. Such an event is complex to analyze. It involves extreme sea states, where the kinematics of the waves are uncertain. The geometry of the platform substructure may change the incoming wave, rendering the inflow even more complicated and violent. The impact event itself will also depend on the platform geometry and motion. Large local forces may occur, which may damage

important safety functions such as the life boats. For massive wave in deck impacts, the primary interest in a re-qualification process is however the global loads on the platform. In the industry, the use of model tests is still the preferred method for predicting such loads. The interest for development and use of more sophisticated numerical tools such as Navier-Stokes solvers is however increasing for these type of problems. Numerical computations are less costly than model tests. Also, such methods can provide far more information than model tests, since details of the flow and forces on the structure can be output at any position, and it is easy to change case parameters. However, the industry still consider the Navier-Stokes solvers to be too inaccurate to base the complete assessment on such computations. Also, a realistic 3-D analysis is still computationally costly and time consuming. In present projects, it is common to use a combination of experiments and numerical computations. This practice often gives a better understanding of the phenomenon than either of the two provides separately. It is important to remember that both experiments and numerical computations have error sources and represent a simplified model of the reality.

1.2 Background

Why is wave impact in platform decks of special interest now? On the Norwegian Continental Shelf, many platforms are ageing, i.e. they are close to exceeding their design service life. Some have already gone through re-qualification processes in order to prolong their service lives. Figure 1.1 shows the installation year of offshore platforms in the Norwegian sector from 1972 to 2000 (Ersdal, 2008). Recent numbers from the PSA shows that 72 out of 88 platforms are more than 10 years old. 47 platforms are 20 years old or more. Most platforms are designed for a service life of 20-25 years.

In the same period of time, the design waves have generally increased both in the North Sea and in the Norwegian sea (Haver 2008, priv. comm.). Figures 1.2 and 1.3 shows the design crest height with an annual exceedance of 10^{-2} and 10^{-4} for different areas of the Norwegian Continental Shelf recommended by Statoil in the years 1985-2008. There has been an increase in the recommended crest heights. This effect is partly due to an increased amount of measured data at the cites of the offshore platforms. The main reason is however that the estimation methods have changed. Oceanographers have obtained a better understanding of the wave climate and improved the methodology for predicting extreme wave heights during the last two decades. The surface waves are more non-Gaussian than assumed previously.

Different methods are indicated in Fig. 1.2 and 1.3. The values denoted (DW) are computed by using the measured data to estimate the significant wave height

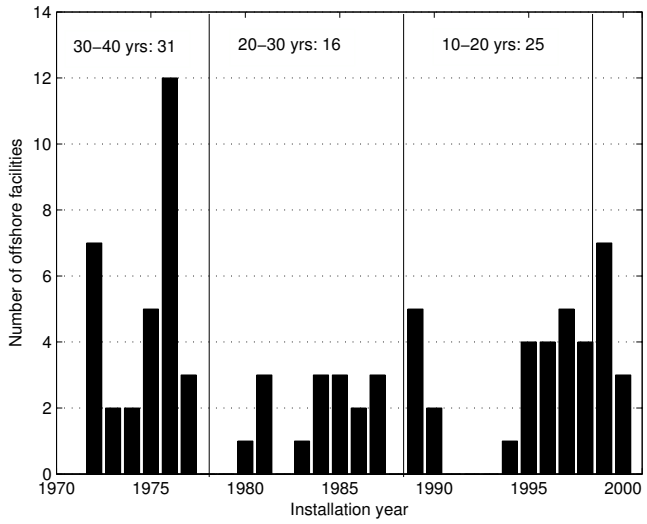

Figure 1.1: Installation year for existing offshore production facilities on the Norwegian Continental Shelf (Ersdal, 2008).

and maximum wave height with an annual exceedance of 10^{-2} or 10^{-4}. The wave crest height is then decided using 5th order Stokes theory for a given design wave height and period. The values denoted (DC) are methods where the wave crest is estimated directly. After 2000, this is done by performing a long term analysis of the measured data and including a short term distribution that includes non-Gaussian sea. As a result, there is a distinct increase in recommended values around year 2000. The trend is especially evident for the 10^{-4} annual exceedance, which is of most interest in connection with wave-in-deck events. The 10^{-4} values are of course more sensitive to changes in the data than the 10^{-2} values.

The combination of ageing platforms and generally increased extreme wave estimates makes the wave-in-deck scenario a very relevant issue on the Norwegian Continental Shelf.

When the waves exceed the air gap of a platform and hit the topside, the loads on the platform are, as mentioned in Sec. 1.1, greatly increased compared to design values. This may have catastrophic consequences for the structure. Examples of events where wave impacts in deck most likely lead to total loss of an offshore platform, were painfully abundant during the hurricanes Katrina and Rita in the Gulf of Mexico in 2005. According to US Minerals Management Service (MMS), 115 permanent installations were destroyed and 53 were severely damaged (Smith,

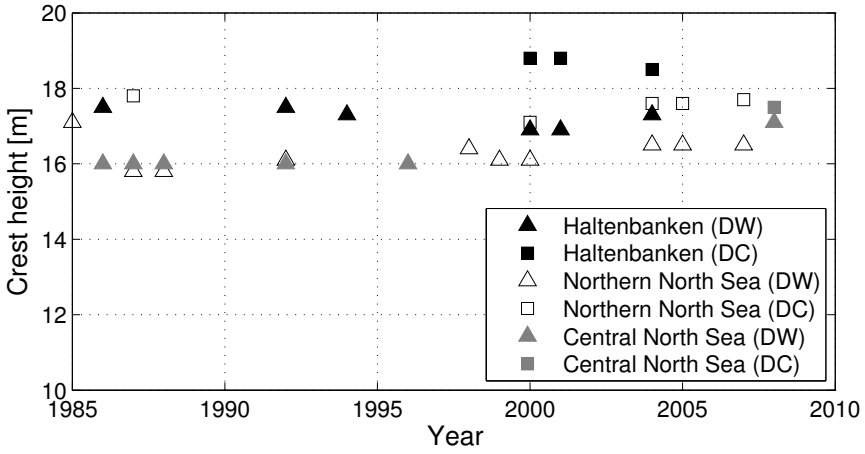

Figure 1.2: Statoil recommended 10^{-2} annual probability crest height from 1985 to 2008 for three different areas of the Norwegian Continental Shelf. Values denoted (DW -Design Wave) indicate that wave crest is estimated using 5th order Stokes theory given extreme wave height. Values denoted (DC -Design Crest) are obtained by estimating the crest directly.

2006). Many of these installations were more than 20 years old. But also fairly new platforms suffered severe damage, such as the Mars TLP (installed in 1996). The Typhoon TLP (installed in 2001) suffered a total loss, as it capsized during the hurricane Rita, see Fig. 1.4. Fortunately, no lives were lost offshore due to the hurricanes Katrina and Rita, since the installations in the Gulf of Mexico are evacuated prior to hurricanes. This practice can justify a lower safety level than is practiced for example on the Norwegian Continental Shelf, where installations are normally not evacuated during severe storms. However, after Katrina and Rita, the engineering standards and regulations are being revised for the Gulf of Mexico.

An example of decreased air gap due to updated wave climate on the Norwegian Continental Shelf is the Heidrun TLP. The estimated wave crest with 10^{-4} annual probability of exceedance increased from 21 m to 24 m. Extensive model tests were performed as part of the effort to re-qualify the platform for further service. Figure 1.5 shows a snapshot from the model test. The challenge for this platform was the ringing loads that occur in the tethers when waves impact the columns or deck beams.

Updated extreme wave estimates is one of the major reasons for increased risk of waves in deck, subsidence of the sea bed is the other. In the Norwegian sector, the subsidence of the Ekofisk field is the most famous and severe case. The

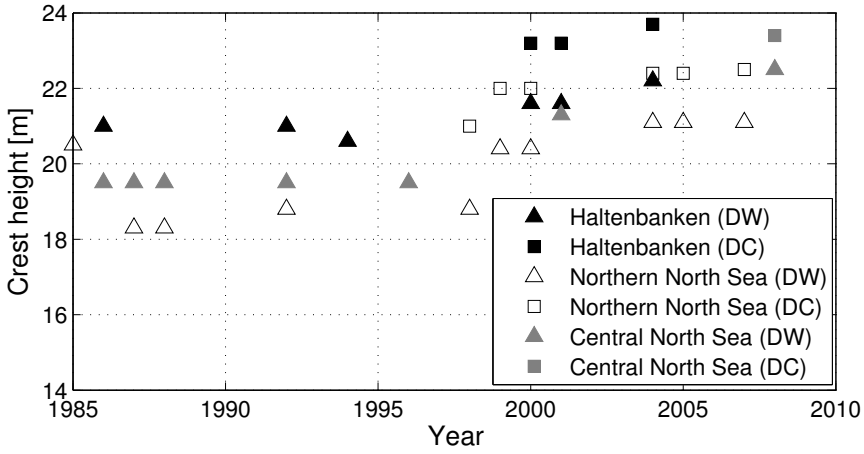

Figure 1.3: Statoil recommended 10^{-4} annual probability crest height from 1985 to 2008 for three different areas of the Norwegian Continental Shelf. Values denoted (DW -Design Wave) indicate that wave crest is estimated using 5th order Stokes theory given extreme wave height. Values denoted (DC -Design Crest) are obtained by estimating the crest directly.

(a) Before Hurricane Rita (b) After Hurricane Rita

Figure 1.4: The Typhoon Tension Leg Platform before and after Hurricane Rita (Photos available at www.rigzone.com).

subsidence was first discovered in 1984. In 2004, the sea bed had subsided 8.5 m (Mathiesen, 2004). The process is continuing with approximately 10 cm per year.

Figure 1.5: Snapshot from a model test for the re-qualification of the Heidrun TLP. Photo: Marintek

The subsidence launched many investigations into wave impact in platform decks, see Sec. 1.3. Platforms were jacked up or replaced. A cylindrical concrete wall was installed to protect the Ekofisk center, see Fig. 1.6. A more recent example of subsidence is the Late Life project at Statfjord A, were it was assumed that continued production would lead to subsidence of 0.5–1.5 m. The design wave crest with annual probability of 10^{-4} will in the worst case exceed the airgap, (Stansberg et al., 2004). Model tests were performed as part of the re-qualification of the platform.

1.3 Previous and ongoing work

Wave impact is a topic in many marine applications, and has been of interest in offshore engineering as long as the industry has existed. In the early years, it was however impacts on horizontal structural parts in the splash zone that was the major concern (see e.g. Dalton and Nash, 1976; Kaplan and Siblert, 1976; Faltinsen et al., 1977). The subsidence of the Ekofisk field launched many investigations into wave impact in platform decks during the 80's and early 90's. Using the theory developed in Kaplan and Siblert (1976), computations of wave impact forces on flat plates in platform decks were performed and compared with full-scale measure-

(a) During installation (b) Installation completed

Figure 1.6: The installation of the Ekofisk tank in 1989. (Photos available at www.norskolje.museum.no)

ments and experiments in Kaplan (1992); Kaplan et al. (1995).

One of the first analyses of wave impacts on platform decks using an advanced numerical model was presented in Baarholm (2001). In this work, a theoretical approach based on Wagner's method was compared with a 2–D fully nonlinear Boundary Element Method (BEM). The computations were validated against model tests. The nonlinear BEM predicted the force history quite accurately. However, the BEM is generally not stable for violent flows. It breaks down when the curvature of the free surface becomes too large unless special precautions are taken. The model test was used to verify that the correct physics were captured by the method. The BEM code was thus able to run until the final stages of the first impact. Only vertical forces were computed by the model and measured in the experiments.

The global structural response of a jacket platform exposed to wave-in-deck loading was examined in van Raaij (2005). A simplified wave load model was used, and a comprehensive review of simplified industry methods for computing the wave loads was given.

A recent research project that lead to a commercial 3–D CFD code for marine hydrodynamics applications was the Joint Industry Project (JIP) called ComFlow (see Kleefsman et al., 2005; Buchner and Bunnik, 2007; Veldman, 2006). The ComFlow code is based on the Finite Volume Method, using a Volume of Fluid surface capturing scheme (see Sec. 1.4).

Another, ongoing research project is called the Wave Impact JIP and is lead by Marintek, Trondheim. In this JIP, an engineering tool based on Wagner's method is

developed (see Baarholm, 2005; Stansberg et al., 2005). This tool provides an estimate of the vertical force history using input from diffraction-radiation frequency domain computations (such as WAMIT) together with Wagner's theory and a time domain computation of the added mass of the wetted deck. The resulting forces compare quite well with model test results, but is limited to vertical forces.

A statistical approach to the wave-in-deck problem is addressed by Kota and Moan (2008). Here, the wave loads are computed using a von Kármán's approach. Irregular waves were used.

1.4 Numerical methods for marine hydrodynamics

The methods where the Navier-Stokes equations are attempted solved directly are often referred to as Computational Fluid Dynamics (CFD) methods, as opposed to e.g. BEM codes, where the LaPlace equation is solved. In the last decade, computer power has enabled more computationally costly methods such as CFD codes to become popular. Many codes include turbulence modeling, but for marine wave-structure interaction problems, the pressure term often dominate the forces. Viscosity plays a role in violent flow, but boundary layer flow is less important. Separation occurs at sharp corners. Turbulence modeling is therefore not discussed here.

Compared to BEM codes, most Navier–Stokes solvers have the benefit of being robust and stable in violent flow conditions. This is due to the explicit, upwind schemes they often rely on when solving the governing equations. This is however done at a cost, and many such schemes are ridden by loss of accuracy due to numerical diffusion (Löhner et al., 2005). Conservation of mass is often a challenge as well. They are also numerically more costly than BEM codes. The different CFD codes have different strategies for solving these challenges.

The most fundamental consideration is how to treat a fluid in a discretized fashion. The most common approach is to divide the computational domain into small cells. The grid can be regular or irregular, follow the internal geometry of structures and surfaces (boundary-fitted grids), or be independent of the structure geometry and interfaces (domain embedding grids). The discretization methods using a grid are usually divided into three main types:

- Finite Difference Methods (FDM)
- Finite Volume Methods (FVM)
- Finite Element Methods (FEM)

Comprehensive descriptions of the three methods can be found in many textbooks and lecture notes (see e.g. Hirsch, 1988; Ferziger and Perić, 2002; Herfjord, 1995a). Dividing the computational domain into a grid is however not the only way of discretizing the field equations. So-called gridless methods also exist, where particle methods such as the Smoothed Particle Hydrodynamics (SPH) method is the most common example. Other methods that often are classified as gridless are Spectral methods (Canuto et al., 2006) and Lattice Boltzmann methods (Succi, 2001).

The equations in the Navier-Stokes methods are solved in spatial coordinates as the fluid flow evolves in time. Just as the space coordinates, time must be discretized. Since there is no backward influence, the time evolution is computed using some time stepping procedure. First order and higher order methods exist. The methods can be explicit or implicit (Ferziger and Perić, 2002).

The treatment of the air-water interface and body (if present) is dependent on the choice of discretization method, but numerous approaches are often available for each flow solver. The interface methods can be divided into interface tracking methods and interface capturing methods. The interface tracking methods follow the free surface in time. The free surface is thus treated as a sharp interface. For grid methods, this approach is used together with boundary fitted grids, where the grid follows the interface. Regridding is thus an important trait of the interface tracking method. Particle methods are implicitly also surface tracking methods, since all fluid particles are followed in time. For the surface capturing methods, the interface is independent of the grid. Thus, the interface must be reconstructed for each time step using indirect methods. Such methods do not define a sharp interface. Many different surface capturing methods are in use. Examples are:

- Volume of Fluid (VoF), (see e.g. Kleefsman et al., 2005; Hirt and Nichols, 1981)
- Level Set (LS), (see e.g. Osher and Fedkiw, 2002; Enright et al., 2002)
- Color Functions (such as the CIP surface capturing methods, see Sec. 3.5)

For boundary-fitted grids, the body is naturally tracked. For domain embedding or gridless methods, the body can be modeled as an interface, i.e. the surface capturing methods mentioned above can be used. Other approaches use ghost cells or overlapping grids. For particle methods, special body particles may be used (Faltinsen and Timokha, 2009, Ch. 10).

Various CFD methods are in use both within the industry and the research community. The diffraction-radiation panel programs such as WAMIT based on linear or second order potential theory (i.e. BEM methods) have been industry

practice for more than 30 years. Commercial Navier-Stokes solvers are also in use, although not on a regular basis for wave-structure interaction problems. These are mostly based on FDM or FVM using VoF surface capturing, such as the general Fluent and Flow3D, and the more specialized Comflow (see Sec. 1.3).

In the research community, a wide variety of methods are used and developed. The present PhD work is done in association with the Centre for Ships and Offshore Structures (CeSOS). It is therefore natural to refer specifically to the methods in use at the Centre. At CeSOS, research has been performed using or developing both grid methods and gridless methods. BEM and hybrid methods are also used. A review of some relevant research projects and the CFD methods used at CeSOS are given below.

Sloshing in LNG tanks was studied by Pàkozdi (2008) using the SPH method. A new numerical program was developed for the analysis of two-dimensional unsteady, incompressible, inviscid and single-phase flows. Improvement of the classical SPH of Monaghan (1992) for different parts of the method was achieved. Different time integration methods, a new density definition scheme and Moving Least Square SPH were implemented in the numerical code. The most appropriate configuration for the sloshing simulations was chosen. A parallel code was implemented. Dedicated sloshing experiments were performed to compare with the SPH simulations. A good review of the SPH method and its applications including a comparison with the CIP method is given in Monaghan et al. (2003).

The first PhD study at CeSOS using the CIP method, was performed by Zhu (2006). The applications were water entry and exit of circular cylinders and water entry loads on ship sections. An example of a 3D simulation of green water on a ship deck was also performed. Wave impact on fish farming structures is another ongoing PhD project using the CIP method (Kristiansen and Faltinsen, 2008). A more detailed review of the development and applications of the CIP method is given in Sec. 2.2.

A Domain-Decomposition (DD) method using BEM together with a Navier-Stokes solver is developed through a long-term cooperation between CeSOS and INSEAN in Italy. The idea with the Domain Decomposition method is to benefit from the accuracy and cost-efficiency of the BEM, combined with the robustness of a Navier-Stokes solver, in this case a FDM code combined with a Level Set surface capturing method. The BEM and Navier-Stokes solver are used in different parts of the computational domain. The Navier-Stokes solver is used when violent nonlinear flow occurs. The method has been used on water shipping and impact on deck structures for ships in harsh weather conditions (Colicchio et al., 2006). The challenge for DD methods is the transition zone where two fundamentally different numerical models are to be coupled.

Fully nonlinear BEM is used in many applications, among others the water

shipping problem mentioned above (Greco, 2001). Recently, impact on planing vessels was studied by Sun and Faltinsen (2006) using nonlinear BEM. A structural analysis was included in the model, and hydroelasticity was considered for shell structures.

A Navier-Stokes method aiming to treat sharp corners and thin plates accurately was developed by Berthelsen and Faltinsen (2008). An immersed boundary method for the incompressible Navier-Stokes equations in irregular domains is developed using a local ghost cell approach. The ghost cell value is determined locally for each irregular grid cell. The time stepping is done explicitly using a second order Runge-Kutta method. The spatial derivatives are approximated by finite difference methods on a staggered, Cartesian grid. The WENO scheme is used to treat the convective terms, while all other terms are discretized with central schemes. The method is tested and validated for objects with sharp corners, such as a facing square and a chamfered plate.

1.5 The present project

As discussed in Sec. 1.4, the research at CeSOS has a strong focus on the development of Navier-Stokes solvers. The Constrained Interpolation Profile (CIP) method has recently been introduced to the CeSOS community through projects by visiting scholar Dr. Changhong Hu and PhD student Xinying Zhu (see also Sec. 2.2). The CIP method seems promising in many aspects: relatively simple code for the flow solver, accurate computation of the advection terms, relatively good conservation properties. A sample code for a simple 2-D dam-breaking case was received from Dr. Changhong Hu. The main work of this PhD project has thus been to develop a 2-D CIP code for wave impact applications.

1.5.1 Scope of work and limitations

As mentioned in Sec. 1.1, a wave-in-deck impact event is hydrodynamically very complex. Figure 1.7 shows some of the aspects that must be accounted for. A complete analysis would require a 3-D model and the possibility to use irregular waves. Long-term simulations would be needed to obtain data for a stochastic analysis. Since the CIP code is to be developed and validated for this application, such a goal is unrealistic. Also, the simulations are limited by CPU cost. The goal of the present work is to use the method to compute wave-in-deck loads on a simplified 2D structure. The global loading process on the structure is considered. A deterministic approach is taken. Regular, steady state waves are modeled using a numerical wave tank. Waves and airgaps are prescribed such that impacts of

different magnitude occur. Multiple impacts are studied, and the effect of previous impacts on the inflow condition and global loads are included. It is assumed that the waves are not distorted by the structure prior to the first impact, i.e. it is assumed that diffraction from the platform substructure is negligible. This assumption is commonly used for jacket-type structures. Only fixed platforms are considered. The fluid is assumed to be incompressible and viscous. No turbulence model is used. Figure 1.8 illustrates the simplified wave-in-deck impact considered in this work.

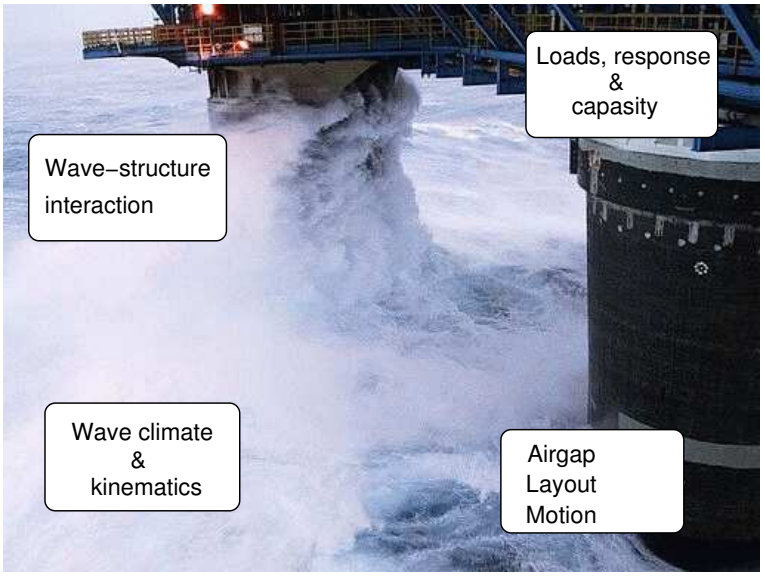

Figure 1.7: Aspects of a real-life wave-in-deck event. (Photo:StatoilHydro)

Validation and verification is an important part of the development work. Different benchmark tests are performed in order to build up different parts of the code and present the capacities and limitations of the numerical model.

The wave impact simulations are compared with experimental results. It was however a deliberate choice not to perform dedicated experiments, but base both validation of the code and comparison with wave-in-deck simulations on previous experimental results. The idea was that there is a large amount of existing experimental data that is not fully analyzed, both commercial and academic experiments. Also, the same experimental data can be used for validating different numerical methods. However, care must be taken when using previous experiments. Error sources and set-up details of the experiments must be studied. The wave impact experiments used in this work are of good quality. The first experiments were how-

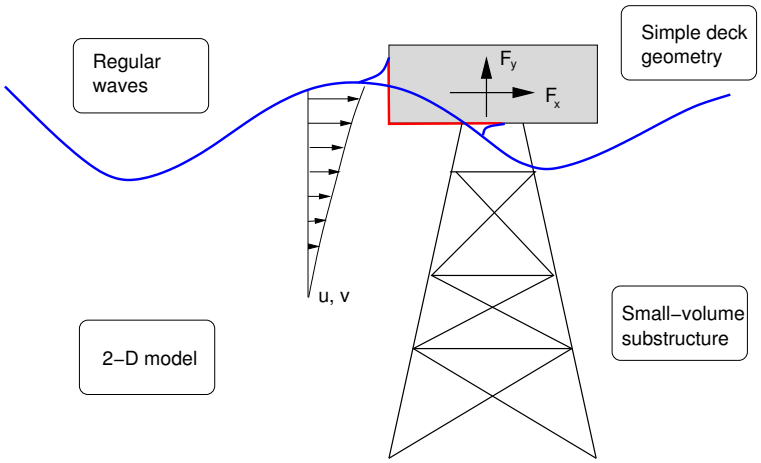

Figure 1.8: Simplified wave-in-deck event.

ever performed nine years ago, giving some restrictions on the number of measuring devises, use of camera and sampling frequency of the force history. The other set of experiments were performed in 2008. The data from this experiment are obtained using up-to-date equipment.

1.5.2 Major contributions

Constrained Interpolation Profile Method A CIP code following Hu and Kashiwagi (2004) is developed for a wave-in-deck impact application. Several benchmark tests focusing on marine hydrodynamics applications are performed to present the capability and limitations of the numerical method. Mass and energy conservation are shown to be satisfactory for the intended applications.

Surface capturing method Several surface capturing methods are tested. The original CIP method and the linear transformation enhancement method show undesired increase in the surface layer thickness for long simulations, i.e. 5-10 wave periods. The tangent transformation surface enhancement method is easy to implement and robust during simulations. The surface layer shows however some growth using this method for long simulations. The THINC surface capturing method is more complicated to implement and is computationally more costly during simulations than the other methods. Using this method, the surface layer stays within 1 or 2 cells even for long simulations. The use of the THINC method may however lead to numerical problems

during simulations. Undisturbed waves were simulated obtaining excellent agreement with theoretical wave kinematics using the THINC method. Successful wave impact simulations were however not obtained due to numerical instabilities. The tangent transformation enhancement algorithm is therefore used for the wave impact simulations.

Numerical wave tank It is demonstrated that a numerical wave tank can be modeled using the CIP method. The wavemaker model seems to correspond well with a physical piston wavemaker. Progressive, regular waves are successfully simulated. Both the wave elevation and the wave velocity profiles are in good agreement with fifth order Stokes wave theory. The wave elevation compares well with experimental results.

Wave-in-deck impact Multiple wave-in-deck impacts are simulated in the numerical wave tank. Vertical and horizontal global forces on a fixed deck box are computed. Cases with different wave conditions and airgaps are simulated. The impact process is studied. Parameter studies on the sensitivity to wave crest height and airgap height is presented. The effect of disturbance of the incoming waves due to previous impacts is demonstrated. The computed results are compared with experimental results from two different model tests.

1.5.3 Outline of the thesis

The thesis is split into four parts: Introducion, Theory, Verification and Applications:

Introduction The motivation for the work and a review of previous and ongoing work are given in Ch. 1.

Theory A review of the development and application of the CIP method for solving the Navier-Stokes equations is given in Ch. 2. The description of the CIP method for the advection equation is presented. Some examples of solving the advection equation using the CIP method are also included. The governing equations and the complete numerical model is presented in Ch. 3. The preferred methods for the flow solver, grid and time marching scheme are presented and discussed. A first evaluation of the different surface capturing schemes is given.

Verification The benchmark tests used to develop the code are presented in Ch. 4. Water flow in a closed tank, added mass and damping forces on a cylinder and water entry are cases used.

Application The development and application of the numerical wave tank is given in Ch. 5. The generated waves are compared with wave theory and with experiments. Finally, the wave impact simulations are presented and compared with experimental results in Ch. 6.

A summary and suggestions for further work are given in Ch. 7. Parts of the work presented in this thesis have been published in Vestbøstad and Faltinsen (2007a,b); Vestbøstad et al. (2008).

Chapter 2

The Constrained Interpolation Profile (CIP) method

2.1 Introduction

In this chapter, a short presentation of the Constrained Interpolation Profile (CIP) method is given with emphasis on the advection computation. First, a review of the development of the CIP method is given. Then, one-dimensional and two-dimensional advection computations using the CIP method is presented. A description of the complete numerical model is given in Ch. 3.

2.2 Review of the CIP method

The CIP method was introduced some 20 years ago, under the name "Cubic Interpolated Pseudo-Particle Method" (Takewaki et al., 1985). Originally, it was proposed as a method for solving simple hyperbolic-type equations. Later, the method was developed for solving the Navier-Stokes equations for compressible and incompressible multiphase flows. Elastic-plastic effects and surface tension have also been included (Yabe et al., 2000). Research using the CIP method within different fields of fluid dynamics has lead to different variants of the method, both for the flow solver, the surface capturing method and the discretization method. The treatment of body boundary conditions may also differ. A review of some different variants and their applications in the field of marine hydrodynamics is given below.

A flow solver called the CIP Combined and Unified Procedure (CCUP) was introduced for marine hydrodynamic applications in Hu and Kashiwagi (2003), and is also described in Zhu (2006). This flow solver is used in the present work.

Examples of applications of the CCUP method are water entry and exit of a circular cylinder, water entry loads on ship sections and green water on deck of a ship (Faltinsen et al., 2005). For e.g. sloshing problems, the mass conservation properties of the method is very important. An exactly conservative CIP flow solver with features similar to Finite-Volume methods has been developed. The method is called the CIP–Conservative Semi-Lagrangian (CSL) methods (Tanaka et al., 2000; Yabe et al., 2001; Xiao and Yabe, 2001). Both a second order (CSL2) and fourth order (CSL4) variant exist. These methods are far more complicated to implement than the CCUP method. Simulations of violent sloshing was performed using a CIP-CSL flow solver (Hu and Kashiwagi, 2007).

Several surface capturing methods have been combined with the flow solvers mentioned above. Most of them are based on density functions (see Sec. 3.5). In the simplest surface capturing method, the density function is advected with the flow using the CIP method (Zhu et al., 2005). For long simulations, the free surface layer thickness may however increase due to numerical diffusion. This may lead to loss of accuracy in the simulations. Surface enhancement algorithms is therefore often used (Hu and Kashiwagi, 2004). The density function is then transformed before advection is performed. The transformation function is constructed such that the discontinuity across the free surface is more well-behaved.

A version of the CSL method, CSL3, has also been used as surface capturing method (see Kishev et al., 2005, 2006). Simulations of sloshing in a 2-D square tank was performed. The CCUP method including compressibility was used for the flow solver.

Another surface capturing method is presented in Mutsuda and Faltinsen (2007), where massless Lagrangian particles are put into the Eulerian grid and advected with the flow, thus combining a particle surface capturing method with a CIP flow solver. 2–D simulations of dam breaking, wave breaking in shallow water, water entry and sloshing is performed.

Yet another surface capturing method, initially developed for VoF methods, is the Tangent of Hyperbola for Interface Capturing (THINC) scheme (Xiao et al., 2005; Yokoi, 2007). This method was used together with the CCUP flow solver for 3-D simulations of the interaction between ship motion and green water shipping, and 2-D and 3-D simulations of water entry of a circular cylinder. Simulations of violent sloshing using a CIP-CSL2 flow solver together with the THINC scheme was published in the same article (Hu and Kashiwagi, 2007).

The CIP simulations referred to above are all performed on a staggered Cartesian grid (see Sec. 3.3). In fluid-structure interaction simulations, complicated structure geometries are a challenge for Cartesian grids. CIP simulations has therefore been performed using so-called Soroban grids. This is an unstructured grid system consisting of straight lines and grid points moving along those lines, as in

an abacus (*soroban* is the Japanese word for abacus). Simulations are performed on cases like flow past a cylinder, a wave-making wedge and wave induced motions of a container ship (Yabe et al., 2007; Takizawa et al., 2007).

It is fair to say that the CIP method (and CFD methods in general) is still under development in the field of marine hydrodynamics. It is not easy to draw any conclusions on which CIP variant that has the best performance based on the simulations discussed above. Most likely, some variants may be well-suited for some applications, and other variants for other applications, dependent on where the challenges are. Figure 2.1 shows an overview over flow solvers, surface capturing methods and discretization methods in use within the CIP method. Bold letters in white boxes indicate the methods used in the present work. The choice of methods are discussed in Ch. 3.

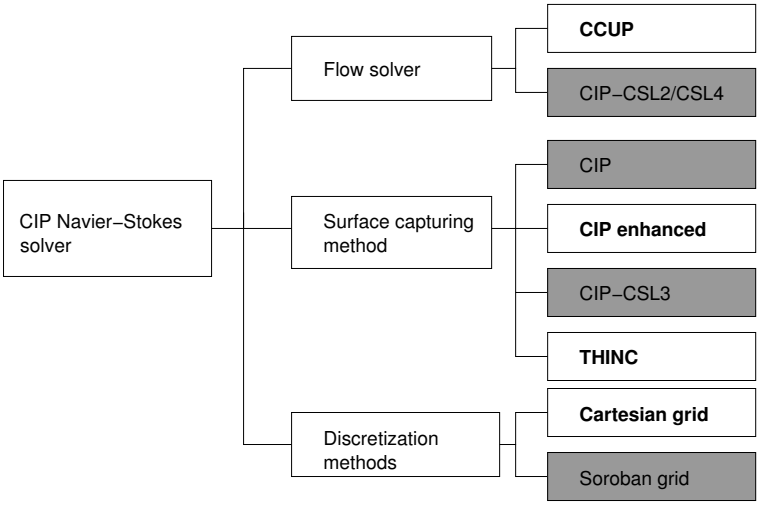

Figure 2.1: Overview of flow solvers, surface capturing methods and discretization methods in use within the CIP method. White boxes with bold letters indicate the methods used in the present work.

2.3 One-dimensional CIP

For the present application, an important term in the Navier-Stokes equations is the advection term. In a numerical scheme such as the fractional step method, it is important that the advection terms are solved with acceptable accuracy (Yabe et al., 2000).

When solving the advection equation, the CIP scheme uses both the function

and its spatial derivatives. The spatial derivatives of the advected function is thus treated as independent variables and has to be solved for. This gives a higher-order method using information from only one computational cell. Benefits of using values from only one cell is that the scheme is compact, constructing interpolation functions of high accuracy with fewer computational stencils. The need for special treatment of the boundary cells is reduced and lower order approximations of derivatives at the boundaries are avoided (Yabe et al., 2000) . To explain the method, a simple one–dimensional advection equation is considered. The linear advection equation in one dimension is given as:

$$\frac{\partial f}{\partial t} + u\frac{\partial f}{\partial x} = 0 \tag{2.1}$$

where $f(x,t)$ is the advected function and the advection velocity $u(x,t)$ is a function of time t and space x. By spatially differentiating Eq. 2.1, another equation is obtained:

$$\frac{\partial g}{\partial t} + u\frac{\partial g}{\partial x} = -g\frac{\partial u}{\partial x} \tag{2.2}$$

where $g = \frac{\partial f}{\partial x}$.

Assume that the advection velocity u is constant and positive. The profile of f inside the upwind element $x_{k-1} < x < x_k$ for the present time step n can then be approximated by a third-order polynomial F_k^n, see Eq. 2.3.

$$F_k^n(x) = a_k\left(x - x_k\right)^3 + b_k\left(x - x_k\right)^2 + c_k\left(x - x_k\right) + d_k \tag{2.3}$$

The four unknown coefficients in Eq. 2.3 can be determined using the the known values of f^n and g^n at the end points x_{k-1} and x_k, where $\Delta x_k = x_k - x_{k-1}$:

$$\begin{aligned} a_k &= \frac{g_k^n + g_{k-1}^n}{\Delta x_k^2} - \frac{2\left(f_k^n - f_{k-1}^n\right)}{\Delta x_k^3} \\ b_k &= \frac{2g_k^n + g_{k-1}^n}{\Delta x_k} - \frac{3\left(f_k^n - f_{k-1}^n\right)}{\Delta x_k^2} \\ c_k &= g_k^n \\ d_k &= f_k^n \end{aligned} \tag{2.4}$$

The profile at the next time step is then estimated by shifting the profile with $-u\Delta t$, where Δt is the size of the next time step. Thus, f_k^{n+1} and g_k^{n+1} can be found as:

$$f_k^{n+1} \approx F_k^n\left(x_k - u\Delta t\right) = -a_k\left(u\Delta t\right)^3 + b_k\left(u\Delta t\right)^2 - c_k\left(u\Delta t\right) + d_k \tag{2.5}$$

$$g_k^{n+1} \approx \frac{dF_k^n\left(x_k - u\Delta t\right)}{dx} = 3a_k\left(u\Delta t\right)^2 - 2b_k\left(u\Delta t\right) + c_k \tag{2.6}$$

In Fig. 2.2, the procedure described above is illustrated. An example function f is prescribed on a grid with cell size $\Delta x = 0.01$ and advected with a constant velocity $u = 1$. A time step $\Delta t = 0.006$ is used. The approximation function F is computed using Eqs. 2.3 and 2.4. Both the exact and approximate solution is shown for the next time step. The black and blue dots denote the cell values for the discretized solution. Note that since f is a step function, errors occur at the discontinuity. This will be further discussed below and in Sec. 3.5.

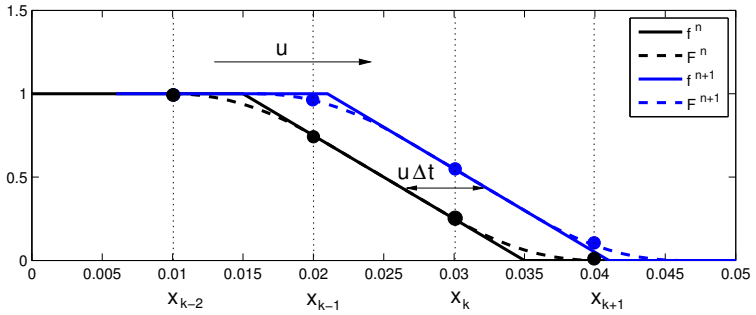

Figure 2.2: Illustration of advection using the CIP method. The function f and the approximation function F is advected one time step Δt.

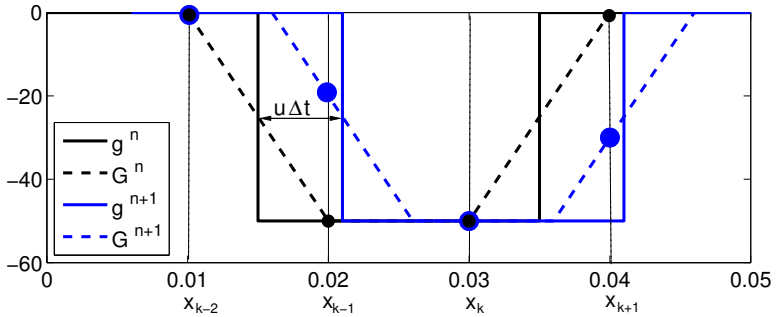

Figure 2.3: Illustration of advection using the CIP method. The derivative function g and its approximation function G is advected one time step Δt.

The procedure above is described for one dimension and using a cubic polynomial. Polynomials of other orders can be used. It should be noted that in the

method description above, the advection velocity u is assumed positive and constant in time and space. For the general case, the right-hand side of Eq. 2.2 is non-zero. The derivative g must then be corrected using e.g. a central difference scheme as given in Eq. 2.7. $\tilde{g}_i^{n+1}$ is found from Eq. 2.6.

$$g_k^{n+1} = \tilde{g}_k^{n+1} + \tilde{g}_k^{n+1} \Delta t \frac{u_{k+1} - u_{k-1}}{\Delta x_k + \Delta x_{k-1}} \tag{2.7}$$

2.4 Stability criterion

The stability criterion for the advection equation is discussed in textbooks like Ferziger and Perić (2002) and Strikwerda (2004). By setting up the algebraic equation for the discretization for f^{n+1} and performing an eigenvalue analysis of the coefficient matrix, the stability criteria can be obtained from the requirement that all eigenvalues must be less than unity for the error $\varepsilon = ||f^n - f^{n-1}|| = \sqrt{\sum_i (f_i^n - f_i^{n-1})^2}$ to decrease with n. This is called the von Neumann method stability analysis when the boundary conditions are ignored. The method is described in detail for different finite difference schemes in Strikwerda (2004). Since the CIP method uses a polynomial fitting method, but with the spatial derivatives as an independant variable, the von Neumann analysis is difficult to use directly. A modified von Neumann analysis was performed for the linear advection equation by Utsumi et al. (1997). It was shown that the scheme is stable if the following condition is satisfied:

$$c = \frac{u \Delta t}{\Delta x} \leq 1.0 \tag{2.8}$$

where c is the Courant number. $c < 1$ is called the Courant-Friedrichs-Lewy (CFL) Condition. If a diffusion term is included in the advection equation, it becomes:

$$\frac{\partial f}{\partial t} + u \frac{\partial f}{\partial x} = \frac{\mu}{\rho} \frac{\partial^2 f}{\partial^2 x} \tag{2.9}$$

This equation is in the literature often used as a model equation for the Navier-Stokes equations, and is thus appropriate in this context. When the diffusion term is included (see Eq. 2.9), stability analysis of upwind schemes (such as the CIP method) gives the following condition (Ferziger and Perić, 2002):

$$\Delta t < \frac{1}{\frac{2\mu \Delta t}{\rho \Delta x^2} + \frac{u}{\Delta x}} \tag{2.10}$$

Using $c = u\Delta t / \Delta x$ and $d = \mu \Delta t / \rho \Delta x^2$, Eq. 2.10 can be rewritten as:

$$1 < \frac{1}{2d + c} \tag{2.11}$$

However, for the applications in this thesis, $c \gg d$, and Eq. 2.11 reduces to the CFL-condition given in Eq. 2.8. The CFL condition can be used to decide the size of the time step to ensure a stable solution. An adaptive time stepping procedure is used in the numerical model, see Sec. 3.4.3.

2.5 Linear advection- 1-D CIP versus an analytical solution

In this section, the linear advection equation is used to study the performance of the CIP method. This is also a first verification of the advection part of the numerical model. The initial condition is chosen so that the function is smooth, and thus an analytical solution exists also for the spatial derivative of the advected function. This makes it possible to verify the solution of spatial derivative of the equation also.

The linear advection equation in one dimension is given in Eq. 2.1. The initial condition is $f(x, 0) = f_0(x)$. An analytical solution using transformation of variables is described in Strikwerda (2004). The variables are changed to τ and ξ, where $\tau = t$, such that $\tilde{f}(\xi, \tau) = f(x, t)$. The advection equation can thus be rewritten in transformed coordinates:

$$\begin{aligned} \frac{\partial \tilde{f}}{\partial \tau} &= \frac{\partial t}{\partial \tau}\frac{\partial f}{\partial t} + \frac{\partial x}{\partial \tau}\frac{\partial f}{\partial x} \\ &= \frac{\partial f}{\partial t} + \frac{\partial x}{\partial \tau}\frac{\partial f}{\partial x} \\ &= \frac{\partial f}{\partial t} + u\frac{\partial f}{\partial x} \\ &= 0 \end{aligned} \tag{2.12}$$

Thus, we get a system of ordinary differential equations:

$$\frac{dx}{d\tau} = u(x, \tau), \quad x(0) = \xi \tag{2.13}$$

$$\frac{d\tilde{f}}{d\tau} = 0, \quad \tilde{f}(\xi, 0) = f_0(\xi) \tag{2.14}$$

Two examples are used to test the performance of the CIP scheme. For both examples, the initial value of the function f is chosen to be:

$$f_0(x) = \begin{cases} \sin^2(\pi x) & \text{for } 0 < x < 1 \\ 0.0 & \text{otherwise} \end{cases} \tag{2.15}$$

In the first example, let the advection velocity be constant, say $u = 1.0$. The solution of the system given in Eq. 2.13 is then:

$$\xi = x - ut \tag{2.16}$$

$$\tag{2.17}$$

$$f(x - ut, t) = \begin{cases} \sin^2(\pi(x - ut)) & \text{for } ut < x < 1 + ut \\ 0.0 & \text{otherwise} \end{cases} \tag{2.18}$$

The spatial derivative of the advection equation also have an analytic solution given the initial condition above. The solution of $g(x,t) = \frac{\partial f}{\partial x}$ can be solved separately using the method by Strikwerda (2004) as described above, or by differentiating the solution of f:

$$g(x - ut, t) = \begin{cases} 2\pi \sin(\pi(x - ut)) \cos(\pi(x - ut)) & \text{for } ut < x < 1 + ut \\ 0.0 & \text{otherwise} \end{cases} \tag{2.19}$$

In the second example, let the advection velocity vary spatially, $u(x,t) = x$. The initial condition is the same as in the example above. The solution of the system given in Eq. 2.13 is then:

$$\xi = xe^{-t} \tag{2.20}$$

$$\tag{2.21}$$

$$f\left(xe^{-t}, t\right) = \begin{cases} \sin^2\left(\pi x e^{-t}\right) & \text{for } 0 < x < e^t \\ 0.0 & \text{otherwise} \end{cases} \tag{2.22}$$

The solution for the spatial derivative is:

$$g\left(xe^{-t}, t\right) = \begin{cases} 2\pi e^{-t} \sin\left(\pi x e^{-t}\right) \cos\left(\pi x e^{-t}\right) & \text{for } 0 < x < e^t \\ 0.0 & \text{otherwise} \end{cases} \tag{2.23}$$

An analytic expression for both f and g is now obtained for the two examples. A simple program is made computing solutions using the 1-D CIP method for the to cases. The computed results for f and g can then be compared with the analytical solutions above. The computational domain is $x = [0.0, 5.0]$. The convergence of the method is studied as the domain is divided into $N = 25$, 50, 100, and 200 regular cells. For both examples, the Courant number is kept constant for the different grids. The time step is thus varied for the different grids. For the first example, where $u = 1$, the Courant number is set to $c = 0.1$. For the second example, where $u = x$, the maximum velocity is $u_{\max} = x_{\max} = 5.0$. The maximum velocity is used when computing c, so $c = u_{\max}\Delta t/\Delta x$. The Courant number for the second example is set to $c = 0.5$. In this way, the cell sizes and time step sizes are the same for the two examples.

Figures 2.4(a) and 2.5(a) show the analytical and the numerical solution of Eq. 2.1 with the initial conditions given in Eq. 2.15, and with an advection velocity $u = 1$ and $u = x$, repectively. The number of cells are $N = 100$. For the second example, the function is advected until the beginning of the bell shape has reached $x = 4.0$ which corresponds to 277 time steps. Figures 2.4(b) and 2.4(b) show the advection of the corresponding spatial derivatives g, plotted together with G_x of the CIP method. We see that for both the function and its derivative, the CIP method performs well. This should not be surprising, since the function is smooth and the cell size relatively small. For real flow problems, areas with steep gradients and near-step functions occur. Especially for the treatment of the free surface, the method for solving the advection equations must be able to deal with advecting a sharp function. The performance of the CIP method in such cases are discussed in Sec. 3.5.

The error between the exact solutions f_{EX} and the numerical solutions f_{CIP} at a time step n can be quantified using the 2-norm $\|\cdot\|$ of the solution vectors (Strikwerda, 2004):

$$\begin{aligned} \|E_N\|_2^f &= \|f_{\mathrm{EX}}^n - f_{\mathrm{CIP}}^n\|_{\Delta x} \\ &= \left(\Delta x \sum_{k=1}^{N} |f_{k\mathrm{EX}}^n - f_{k\mathrm{CIP}}^n|^2\right)^{1/2} \end{aligned} \tag{2.24}$$

where $\|E_N\|_2$ is the 2-norm when using N cells. The exact solution f_{EX}^n at the time step n is evaluated at the grid nodes k. Since the spatial derivative g is analytical, the same error norm can be used to compare g_{EX} and g_{CIP}. The order of accuracy of the solution γ such that $\|E_N\| \sim \mathcal{O}(\Delta x^\gamma)$ is equal to the order of accuracy of the scheme for smooth initial data (Strikwerda, 2004). The order of accuracy of the solution can be approximated by Eq. 2.25 (Berthelsen and Faltinsen, 2008):

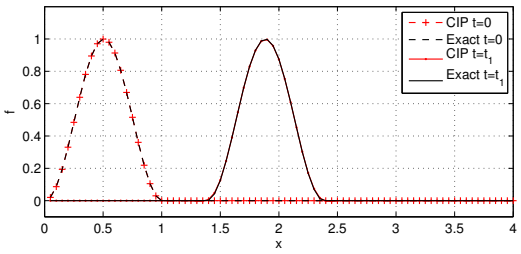

(a) Solution of f

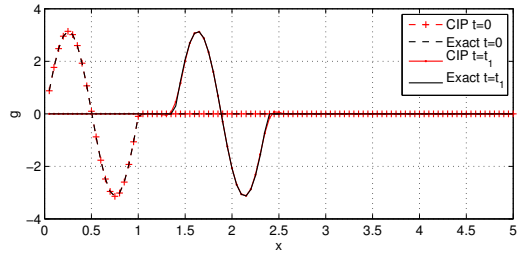

(b) Solution of g

Figure 2.4: Advection of f and g for an example with $u = 1$; comparison of CIP and analytical solution at t=0 and after 277 time steps ($\Delta x = 0.05$).

$$\gamma = \frac{\log(\|E_{N/2}\|/\|E_N\|)}{\log(2)} \tag{2.25}$$

where N denotes the number of cells. The simple test cases presented above can thus be used to check of the order of accuracy of the CIP scheme. Table 2.1 shows the error for the 4 grid variants for example 1 and 2. As expected, the error is decreased for decreasing cell size. The order of accuracy tends to 2 for the constant velocity, but is only of order 1 when the velocity varies with x. This is probably due to the explicit Euler scheme for the time stepping. A further discussion on the order of the complete numerical model is given in Sec. 3.4.1.

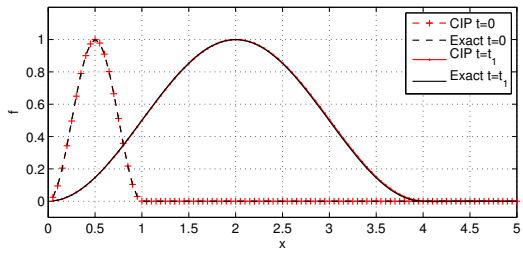

(a) Solution of f

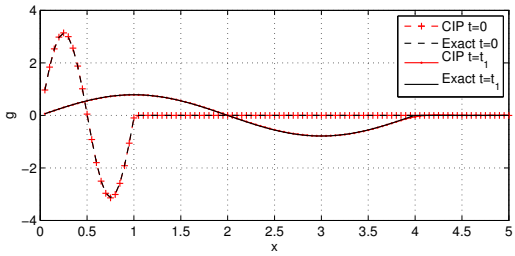

(b) Solution of g

Figure 2.5: Advection of f and g for an example with $u = x$; comparison of CIP and analytical solution at t=0 and after 277 time steps ($\Delta x = 0.05$).

Table 2.1: Error for different constant grid configurations for example no. 1, with $u = 1$ vs. $u = x$. $\|E_N\|_2^f$ and $\|E_N\|_2^g$ denotes the 2-norm (see Eq. 2.25) for f and g, respectively. γ^f is the order of accuracy of the solution.

$u = 1$

Case no.	Grid size	Δx	Δt	$\|E_N\|_2^f$	$\|E_N\|_2^g$	γ^f
1	25	2.0e-1	2.0e-2	6.24e-2	6.52e-1	
2	50	1.0e-1	1.0e-2	1.38e-2	1.84e-1	2.18
3	100	5.0e-2	5.0e-3	3.04e-3	6.45e-2	2.17
4	200	2.5e-2	2.5e-3	7.45e-4	2.79e-2	2.03

$u = x$

Case no.	Grid size	Δx	Δt	$\|E_N\|_2^f$	$\|E_N\|_2^g$	γ^f
1	25	2.0e-1	2.0e-2	5.09e-2	1.14e-2	
2	50	1.0e-1	1.0e-2	1.98e-2	4.56e-2	2.20
3	100	5.0e-2	5.0e-3	9.06e-3	2.10e-2	1.13
4	200	2.5e-2	2.5e-3	4.40e-3	9.70e-2	1.04

2.6 Two-dimensional CIP method

The two dimensional advection equation is:

$$\frac{\partial f}{\partial t} + u\frac{\partial f}{\partial x} + v\frac{\partial f}{\partial y} = 0 \tag{2.26}$$

where u and v are the advection velocities in x- and y-direction, respectively. In two dimensions, some more choices on how to perform the advection using CIP are available, although the principles are the same as in one dimension. Using a cubic polynomial function, it is easy to expand the one-dimensional method directly. This is referred to as A-type CIP. An alternative method is to use directional splitting, solving the advection equation first in one direction, then in the other. The solution from the first direction is then used as an intermediate estimate when solving the second direction. This is referred to as M-type CIP. The advantage of the M-type is that the method is easy to expand to three dimensions and any estimation function can be used. There is however some loss of accuracy. In the present method, the A-type is used as presented below. The M-type is however used in connection with the THINC surface capturing scheme, see Sec. 3.5.3.

The estimate for the next time step, f^{n+1} is given as:

$$f^{n+1}(\mathbf{x}) = F^n(\mathbf{x} - \mathbf{u}\Delta t) \tag{2.27}$$

where $\mathbf{x} = (x, y)$, and the superscript n denotes the present time step. For a given grid point (k, l), the upwind cell is found, defined by four corners, (k, l), (kw, l), (k, lw) and (kw, lw). The upwind indices kw and lw is found by evaluating the direction of the fluid velocity at the grid point (k, l):

$$kw = k - \text{sign}(u_{k,l}) \qquad lw = l - \text{sign}(v_{k,l}) \tag{2.28}$$

The advected variable f is approximated by a 2–D cubic polynomial F^n:

$$\begin{aligned} F^n(\eta_1, \eta_2) \quad = \quad & C_{30}\eta_1^3 + C_{21}\eta_1^2\eta_2 + C_{12}\eta_1\eta_2^2 + C_{03}\eta_2^3 + C_{20}\eta_1^2 \\ & + C_{11}\eta_1\eta_2 + C_{02}\eta_2^2 + C_{10}\eta_1 + C_{01}\eta_2 + C_{00} \end{aligned} \tag{2.29}$$

where

$$\eta_1 = x - x_k \quad \eta_2 = y - y_l \tag{2.30}$$

The 10 unknown coefficients in Eq. 2.29 are found using the known values of the variable and spatial derivatives of the variable at the four grid points, in the same

way as shown in Eq. 2.4. For a 2–D case this actually gives 12 known values, so it is not necessary to use all of them. In the present code, the spatial derivatives for the point farthest away (i.e. the upwind point), are not used in the computations, see Fig. 2.6. The coefficients of Eq. 2.29 is defined in Eq. A.1 in App. A.2.

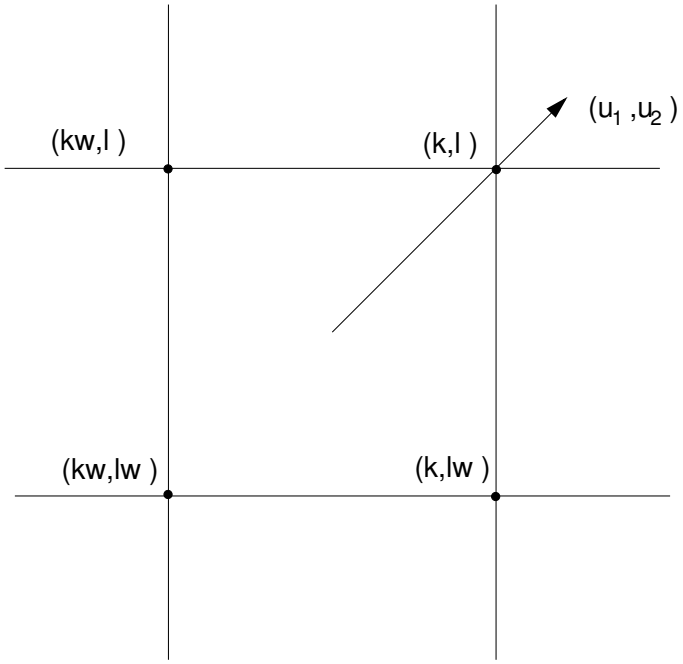

Figure 2.6: Illustration of the upwind cell. The indices (k, l) denotes the node in question. Given the velocity vector u_1, u_2, the upwind cell is determined by Eq. 2.28. The upwind indices are denoted by kw and lw.

Values for the next time step must also be found for the spatial derivatives in x– and y–direction, i.e. $g_x = \frac{\partial f}{\partial x}$ and $g_y = \frac{\partial f}{\partial y}$. The estimates for g_x and g_y are:

$$\begin{aligned} G_x^n(\eta_1, \eta_2) &= \frac{\partial F}{\partial x} \qquad (2.31) \\ &= 3C_{30}\eta_1^2 + 2C_{21}\eta_1\eta_2 + C_{12}\eta_2^2 + 2C_{20}\eta_1 + C_{11}\eta_2 + C_{10} \\ G_y^n(\eta_1, \eta_2) &= \frac{\partial F}{\partial y} \qquad (2.32) \\ &= C_{21}\eta_1^2 + 2C_{12}\eta_1\eta_2 + 3C_{03}\eta_2^2 + C_{11}\eta_1 + 2C_{02}\eta_2 + C_{01} \end{aligned}$$

The estimated profiles in the cell are then propagated with the velocity vector $\mathbf{u}^n = (u_{k,l}^n, v_{k,l}^n)$:

$$f^{n+1}(\mathbf{x}) = F^n\left(\mathbf{x} - \mathbf{u}^n \Delta t\right) \tag{2.33}$$

$$g_x^{n+1}(\mathbf{x}) = G_x^n\left(\mathbf{x} - \mathbf{u}^n \Delta t\right) \tag{2.34}$$

$$g_y^{n+1}(\mathbf{x}) = G_y^n\left(\mathbf{x} - \mathbf{u}^n \Delta t\right) \tag{2.35}$$

where the vector $\mathbf{x} = (x, y)$. It should be noted that for the spatial derivative of the variable, there are residual terms coming from the derivation of the advection equation, see Eq. 2.2. The derivatives g_x and g_y must therefore be corrected for this source term. In the present code, this is done with a central difference scheme, see App. A.2.

Chapter 3

The Numerical model

3.1 Introduction

The present numerical model is a finite difference high-order up-wind scheme for solving the Navier–Stokes equations. The name of the method refers to the scheme used to solve the advection part of the Navier–Stokes equations, as discussed in Ch. 2.

A domain-embedding, staggered Cartesian grid is used for the spatial discretization. The water and air phases are modeled as one fluid. The material properties vary across the domain. The free surface is thus not the boundary of the computational domain, but merely the interface between the two phases. This prevents difficulties with the definition of the free surface and the treatment of the free surface boundary conditions. However, it imposes new challenges as the free surface is modeled as a layer rather than a sharp interface. The gradients of material properties are steep across the surface layer.

The flow solver is the main solution algorithm where the velocity and pressure fields are solved. The surface capturing method keeps track of the position of the interfaces and thus the values for the material properties at any position of the computational domain. As discussed in Ch. 2, different combinations of flow solvers and surface capturing methods can be used. They are however closely interlinked as the local values of the material properties affect the flow field and vice versa.

In this chapter, the complete numerical model is presented and discussed. First, the governing equations are presented together with the basic limitations and assumptions. Then the choice of grid, flow solver and surface capturing method is presented and discussed. Boundary conditions and initial conditions are also described.

3.2 The governing equations

Only two-dimensional applications will be considered in this work. Viscous, incompressible flow is assumed. The governing equations are thus:

$$\frac{\partial u_i}{\partial t} + u_j \frac{\partial u_i}{\partial x_j} = -\frac{1}{\rho}\frac{\partial p}{\partial x_i} + \frac{1}{\rho}\frac{\partial}{\partial x_j} S_{ij} + \frac{1}{\rho} F_i^b \tag{3.1}$$

Cartesian indexing is used, where x_i and u_i is the spatial coordinate and velocity, respectively. The two spatial directions are denoted by $i = 1, 2$. The mass density is denoted ρ, the pressure p, and F_i^b is body force, i.e. the gravity force in the present applications. The viscous stress tensor S_{ij} is given as:

$$S_{ij} = \mu \left(\frac{\partial u_i}{\partial x_j} + \frac{\partial u_j}{\partial x_i} \right) \tag{3.2}$$

where μ is the dynamic viscosity coefficient. The continuity equation for incompressible flow is:

$$\frac{\partial u_i}{\partial x_i} = 0 \tag{3.3}$$

In addition to the field equations, boundary conditions on the body S_b and along the wave tank walls S_w must be defined. In the present work, no-slip conditions are normally specified at wave tank walls and body boundaries:

$$u_i = 0 \quad x_i \in S_w \tag{3.4}$$

$$u_i = U_i \quad x_i \in S_b \tag{3.5}$$

where U_i is the velocity of the body. The boundary conditions are discussed in more detail in Sec. 3.6. Since the fully non-linear Navier-Stokes equations are solved, the flow is not confined to be irrotational. Surface tension forces are neglected.

The air flow is included in the computations. The compressibility is however neglected, which obviously is more appropriate for the water than for the air. The air flow is not considered important for the simulation results unless the flow includes air entrapment. The geometry of the incident wave may cause air entrapment for the present application, e.g. if near breaking waves impact the deck box. In such cases, including compressibility must be considered. For the wave conditions simulated in the present work, air entrapment did not occur.

The CIP method can be used for both compressible and incompressible fluid, but including compressibility is numerically costly. The speed of sound in air and

water becomes a variable in the governing equations, and this increases the need for both spatial and temporal refinement. The changes in the code for including compressibility is trivial, but the performance of the simulations is not. The method including compressibility is described in Zhu (2006).

3.3 The discretization of the computational domain

The computational domain is discretized using a Cartesian grid. The grid is domain-embedding, i.e. the grid lines do not necessarily follow the boundaries of the water, body and air. The grid is time-independent, which is one of the major benefits of using such a grid. No re-meshing is necessary during simulation. The grid is staggered, meaning that the variables are not evaluated at the same positions on the grid. The velocities are evaluated on the cell faces, while the pressure and material properties are evaluated in the middle of the cell, see Fig. 3.1. The use of staggered grid is common in many finite difference methods. According to Ferziger and Perić (2002), the use of staggered grid helps avoid convergence problems and oscillations in pressure and velocity fields. The drawback of such a grid is that it is logically more demanding to use compared to collocated grids. For complicated geometries, the use of a staggered grid becomes difficult. Soroban grids has been used together with the CIP method for complex geometries, see Sec. 2.2. In the present work, the geometry is simplified and a staggered Cartesian grid is well-suited.

In the present code, the possibility to use variable cell size in the grid is implemented. Both linear and cosine stretching is available. Care must however be taken to ensure correct spatial differentiation and interpolation of the variables on the grid.

Variable grids are desirable because this may increase accuracy and reduce computational cost by refining the grid in areas of the computational domain where there is large solution activity (steep gradients, large curvature, etc.), and use larger cells in smoother areas of the domain. Using a variable grid is however not always straightforward, and does not always give the desired effects. This topic was discussed in Veldman and Rinzema (1992), where it was shown that for unlucky combinations of discretization method and nonuniform grids, the opposite effect can occur; refining the grid in an area may be more costly but give less accurate results than using a uniform grid with the coarsest cell size. It was also shown that the local truncation error was not necessarily a good indicator for the global discretization error.

It is important to avoid abrupt changes in the grid size. On the other hand, constant variation or stretching of the grid reduces the accuracy. This effect is actually used as a wave damping device in the horizontal direction for the numerical wave

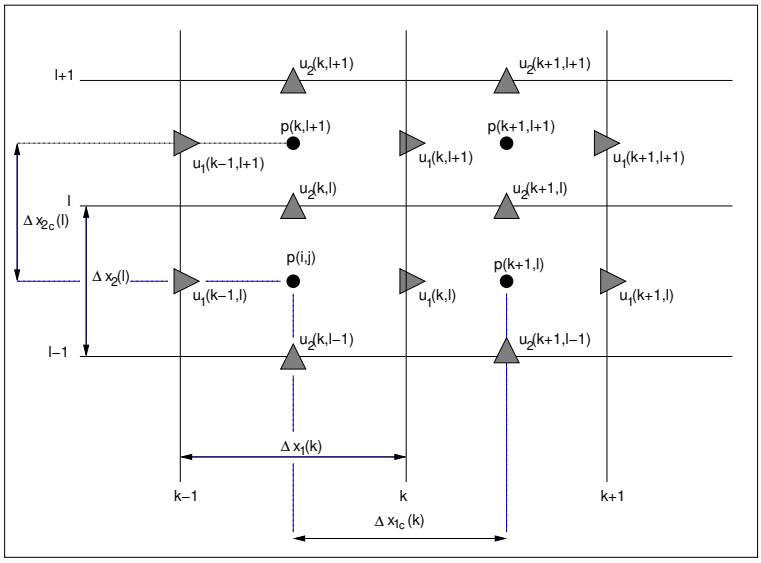

Figure 3.1: A section of the staggered Cartesian grid used in the present code. The indices in the horizontal and vertical directions are denoted k and l, respectively. The cell size is denoted Δx_i and the distance between cell mid-points is Δx_{Ci}. The velocities u_i are evaluated at the cell faces, while the pressure p is evaluated at the cell mid-point, together with material properties and density functions (not shown in figure).

tank, as described in Sec. 5.2.2. Performing grid dependency tests is one method for securing that the grid refinement has the desired effects.

3.4 The flow solver

As discussed in Ch. 2, there are several possible flow solvers within the CIP method. The method used in the present code, called the Combined and Unified Procedure (CCUP), is presented below. Another type of flow solvers mentioned in Sec. 2.2 are called the Conservative Semi-Lagrangian (CSL) methods. These solvers are more complicated to implement, but are said to have better conservation properties. The main application in the present work is a numerical wave tank. The requirement for mass conservation is thus not as important as for example for simulation of sloshing in a tank, where the eigenfrequency of the tank is strongly dependent on the water level in the tank. The mass conservation for the present code is however satisfactory (see Sec. 4.4 for a further discussion).

3.4.1 The fractional step method

The governing equations are marched forward in time using a fractional step method. This method was first suggested by Chorin (1968), and enables an explicit solution procedure including an implicit pressure term. The method can be combined with any method of spatial discretization and is suitable for unsteady flows (Ferziger and Perić, 2002). There is a need to ensure mass conservation at each time step, in contrast to steady flows where pressure-correction methods may be more suitable. If the time step is large, the fractional step method produces an error due to the operator splitting. The reduction of the time step is according to Ferziger and Perić (2002) the most appropriate means of improving accuracy.

There are many versions of the fractional step method. Both coupled and uncoupled methods exist. In the coupled methods, an approximate pressure is used in the first step estimating the intermediate velocities. Higher-order accuracy for the pressure computation may then be achieved. Coupled methods may however yield an incorrect pressure field. A discussion of different coupled schemes for Finite Element Methods is given in Tønnesen (1999). In the present method, an uncoupled method is used, i.e. the pressure is totally decoupled from the intermediate velocity. Uncoupled methods are restricted to first order temporal accuracy. Small time steps are therefore necessary for this method, as mentioned above. A second-order update of the pressure using an incremental pressure projection method proposed by Brown et al. (2001) is also tested, see App. B.3. In the present work, the incremental pressure projection method does not give any significant increase in accuracy for the test case, and gives a less efficient and less stable code.

The equation for the intermediate velocity $\mathbf{u}^*$ contains an advection term and a diffusion term in addition to the gravity force, see Eq. 3.1. The intermediate velocity can be computed by evaluating the advection–diffusion equation in its entirety, or by segregating the terms and using the time integration scheme most suitable for each term. In Meling (1998), both approaches were considered. It was found that segregation formulations may be beneficial because the advection term must be accurately computed to obtain stability of the scheme, while the diffusion term is of less importance.

In the present method, the terms are split and solved separately. This opens up for using the CIP method for the advection term, whilst the diffusion term is stepped forward using a forward Euler method. The fractional step method used for the present numerical scheme is described in more detail in the following.

Step 1: The advection equation

In the first step, the advection part of the Navier-Stokes equations is solved. This gives the first intermediate values for the fluid velocities, u_i^*, see Eq. 3.6.

$$\frac{u_i^* - u_i^n}{\Delta t} + u_j^n \frac{\partial u_i^n}{\partial x_j} = 0 \tag{3.6}$$

The two-dimensional CIP procedure described in Sec.2.6 is used to compute u_i^*.

Step 2: The diffusion equation

In the next step, all terms not related to pressure is included in the calculation. The intermediate velocity field from Step 1 is used as input. A simple forward Euler method is used for the time integration. New intermediate values for the fluid velocities, u_i^{**} are then obtained by:

$$\frac{u_i^{**} - u_i^*}{\Delta t} = \frac{1}{\rho} \frac{\partial}{\partial x_j} S_{ij} + f_i^b \tag{3.7}$$

where f_i^b denotes the acceleration of gravity for $i = 2$. The viscous stress tensor S_{ij} is defined by Eq. 3.2. Note that the non-conservative form of the diffusion terms are used. This is important especially when including compressibility, and enables a favorable treatment of multi-phase flow. A detailed discussion on this is given in Yabe et al. (2000).

Equation 3.7 is actually a simplified version of what is done in the numerical code. The double derivatives on the right hand side of Eq. 3.1 are in principle computed using a simple central difference scheme, but due to the staggered and variable grid, the values of μ and ρ must be treated with some care. The discretized equations used in the present code is given in App. A.3.

Step 3: The pressure Poisson equation

The pressure–velocity coupling of the next step is recast as a Poisson equation, solving the pressure for the next time step. The coupling between pressure and velocity is:

$$\frac{u_i^{n+1} - u_i^{**}}{\Delta t} = -\frac{1}{\rho} \frac{\partial p^{n+1}}{\partial x_i} \tag{3.8}$$

Taking the divergence of Eq. 3.8 and requiring that $\partial u_i^{n+1} / \partial x_i = 0$ because of continuity, the Poisson equation for the pressure is obtained, see Eq. 3.9. Note

that it is not assumed that the intermediate velocities u_i^{**} meets the continuity requirement. The divergence of the product of ρ and $\partial p^{n+1}/\partial x_i$ is used. According to Yabe et al. (2000), this gives a smoother function across the free surface. The details of how the computation of the left-hand term is implemented is given in App. A.3.2.

$$\frac{\partial}{\partial x_i}\left(\frac{1}{\rho}\frac{\partial p^{n+1}}{\partial x_i}\right) = \frac{1}{\Delta t}\frac{\partial u_i^{**}}{\partial x_i} \tag{3.9}$$

In finite difference form, the Poisson equation represents a sparse linear system for p^{n+1}. Solving this algebraic system is the numerically most costly part of the algorithm. In the present code, a method called Successive Over-Relaxations (SOR) is mostly used (Bruaset, 1995). This is a well-known and relatively simple method. It may, according to Hu (2005), be one of the most efficient stationary methods. Efficiency is important for the solution of this equation system, and improvements in this part of the code thus have a great pay-off in terms of simulation time and/or grid refinement. A preconditioned non-stationary iterative method called the Bi-Conjugate Gradient Stabilized (Bi–CGSTAB) method is therefore also implemented. The Bi–CGStab algorithm is described in many textbooks, e.g. Ferziger and Perić (2002). The particular version of the Bi–CGStab method used in the present code is described in Sleijpen and Fokkema (1993). The behavior of the two methods are discussed in App. B.2.

Step 4: Updating the velocity field

When the pressure for the next time step is found, Eq. 3.8 is used to update the fluid velocities. The time integration scheme of the flow solver for one time step is thus completed, and the primitive variables for the next time step, u_i^{n+1} and p^{n+1} is estimated. It should be noted that in order to keep track of the material properties and the interfaces, a surface capturing scheme is also included in the computations performed at each time step. The surface capturing methods used in the present code is presented in Sec. 3.5. An overview of the complete numerical procedure is given in Sec. 3.8.

3.4.2 Non-advection computation for the spatial derivatives

In the CIP method for the advection terms, the spatial derivatives of the velocity field are introduced as independent variables, see Sec. 2.3. In principle, this means that not only the Navier-Stokes equations, but also the spatial derivatives of the Navier-Stokes equations is to be solved. In practice, the diffusion term must be computed for the spatial derivatives of the velocity field. This computation can be

simplified by using the intermediate velocities u_i^* and u_i^{**} to compute $\partial u_i^{n+1}/\partial x_i$. The details are given in App. A.3.4. The final expression becomes:

$$\frac{\partial u_i^{n+1}}{\partial x_i} = \frac{\partial u_i^*}{\partial x_i} + \frac{1}{2\Delta x_i}\left(u_i^{**} - u_i^*\right) \tag{3.10}$$

In time, the independent computation of the spatial derivatives become inaccurate. Thus, it is necessary to update the derivatives by computing them directly from the velocities, i.e. by numerical differentiation. For the present code, this recomputation of the spatial derivatives is performed at every 30th time step, see also App. B.3.

3.4.3 Adaptive time stepping algorithm

The fractional step method described above is performed for each time step. As explained in Sec. 2.4, the stability of the scheme is governed by the CFL-condition $c < 1$. In the numerical code, adaptive time stepping is normally used. The time step is then automatically adjusted using the CFL-condition as a criterion. Adjusting the time step during simulation gives more efficient computations and a more robust code.

If the CFL-number is outside specified limits, the time step size is adjusted. The CFL-number is computed for the horizontal velocity u_1 and the vertical velocity u_2 as given in Eq. 3.11.

$$c = \frac{u_i^{\max}}{\Delta x_i^{\max}}\Delta t \tag{3.11}$$

where $u_i^{\max}$ is the maximum velocity in the computational domain, and $\Delta x_i^{\max}$ is the corresponding cell size where the maximum velocity occurred. Δt is the time step size. If $c^{\lim^-} > c > c^{\lim^+}$, a new time step is computed as:

$$\Delta t = \frac{c^{\lim^+}\Delta x_i^{\max}}{u_i^{\max}} \tag{3.12}$$

where $c^{\lim^+}$ and $c^{\lim^-}$ is the maximum and minimum limit of the CFL-number, respectively. In the simulations, these limit are usually set to 0.5 and 0.005. The CFL-number in the direction with the greatest velocities is chosen when evaluating the time step size.

3.5 The surface capturing scheme

Using the flow solver described above, the solution of the Navier–Stokes equations for the entire domain is marched forward in time. However, the position of the free surface and bodies (if any) in the fluid, and the value of the material properties such as density ρ and viscosity μ are also needed. Parallel with computing the fluid velocities and pressure, the position of the free surface and associated variables are therefore captured.

As mentioned above, several surface capturing methods can be used together with the flow solver described above. For the wave impact simulations, it is assumed a priori that it is important to keep the surface sharp in order to generate waves and simulate repeated impacts accurately. Therefore, different surface capturing methods are tested. Discussions on the performance of the methods are given in Ch. 4-6. In the following, the three surface capturing methods tested in this thesis are described:

- CIP
- CIP with sharpness enhancement
- THINC (Tangent of Hyperbola for Interface Capturing)

Common for all three methods is the use of density functions, $\phi_{\mathrm{m}}, \mathrm{m} = 1, 2, 3$. The indices denote water, air and body, respectively. The functions attain values in the range $[0.0, 1.0]$, and the sum of the density functions must be equal to unity in each cell. When e.g. the water density function $\phi_1 = 1.0$ for a grid cell, the others must equal zero and the cell is totally submerged in water. When two or more of the density functions have a nonzero value in a cell, the cell is at the free surface or body boundary, see Fig. 3.2. The free surface is defined at $\phi_1 = 0.5$.

For all three methods, the water density function is advected with the flow. Assuming rigid body motion, the body motion is either prescribed or governed by equations of motion. Thus, the body density function ϕ_3 can be computed by direct methods. The area covered by the body A_b is computed for each cell, and the body density function is then easily computed as $\phi_3 = A_b/(\Delta x_1 \Delta x_2)$. The density function for air, ϕ_2, is then derived from the other two:

$$\sum_{\mathrm{m}=1}^{3} \phi_{\mathrm{m}} = 1 \quad \text{i.e.} \quad \phi_2 = 1 - \phi_1 - \phi_3 \tag{3.13}$$

The phase dependent variables in each cell, i.e. the mass density ρ and the viscosity coefficient μ, can now be determined for each cell using the density functions:

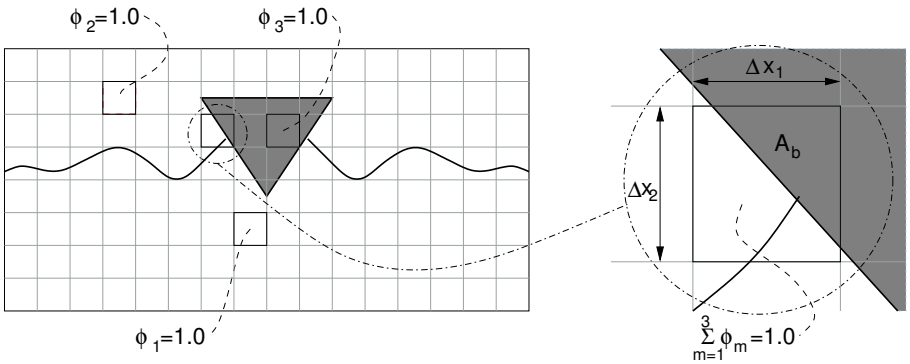

Figure 3.2: The use of the density functions to capture the interfaces within the computational domain. ϕ_1 denotes water density function, ϕ_2 denotes air and ϕ_3 denotes the body density function. The body density function is found by computing the area A_b in each cell covered by the body and divide by the total cell area, $\Delta x \Delta y$.

$$\rho = \rho_1\phi_1 + \rho_3\phi_3 + \rho_2\left(1 - \phi_1 - \phi_3\right) \tag{3.14}$$

$$\mu = \mu_1\phi_1 + \mu_3\phi_3 + \mu_2\left(1 - \phi_1 - \phi_3\right) \tag{3.15}$$

Here, the indices of ρ_1, ρ_2 and ρ_3 denotes the value of the mass density for water, air and body, respectively. μ_1, μ_2 and μ_3 denotes the viscosity coefficient for water, air and body.

3.5.1 CIP surface capturing scheme

This is the simplest surface capturing scheme, where the water density function is advected with the flow directly.

$$\frac{\partial \phi_1}{\partial t} + u_i \frac{\partial \phi_1}{\partial x_i} = 0 \tag{3.16}$$

The CIP method described in Sec. 2.6 can thus be used to solve for ϕ_1.

3.5.2 Sharpness enhancing algorithms

Initially, the water density function has a step function shape at the free surface. As demonstrated in Sec. 2.3, such a function is subjected to numerical diffusion even when using a higher order scheme such as the CIP procedure. The numerical

diffusion generally leads to a thickening of the surface layer as the time integration propagates, and the accuracy of the simulation will be reduced accordingly. Function transformation methods which makes the function smoother over the interface during advection is useful to reduce this effect. Using the CIP method, the transformed function $\Psi(\phi_1)$ rather than the density function itself is advected. Two such transformation functions are tested in the present work. One is a tangent function, taken from Yabe et al. (2001):

$$\Psi(\phi_1) = \tan[(1-\gamma)\pi(\phi_1 - 0.5)] \tag{3.17}$$

where γ is a small constant. According to Hu (2005), a sharp interface can be obtained using $\gamma = 0.02$. This algorithm is however somewhat costly numerically, because of the tangent function. Hu (2005) therefore suggests a linear transformation:

$$\Psi(\phi_1) = 0.5 + \alpha(\phi_1 - 0.5) \tag{3.18}$$

where $\alpha > 1$ is the sharpness enhancing factor. Hu (2005) recommends $\alpha = 1.2$.

For the water entry and exit problems studied in Zhu et al. (2005), no sharpening of the surface was used, but the duration of the simulations were not long. In the present work, both transformations are tested, see Ch. 4.

3.5.3 The THINC Interface capturing scheme

The Tangent of Hyperbola for Interface Capturing (THINC) scheme was first introduced by Xiao et al. (2005) for a VoF method. It has recently also been used together with the CIP method (see Hu and Kashiwagi, 2007). The scheme uses a piecewise continuous hyperbolic tangent function to approximate the density function inside the cells. This function is more suitable for approximating the step function behavior of the density function than the original interface capturing method for the CIP scheme, where a third order polynomial is used.

Overview of the method in 1-D

The density function for water ϕ_1, is advected with the flow.

$$\frac{\partial \phi_1}{\partial t} + u\frac{\partial \phi_1}{\partial x} = 0 \tag{3.19}$$

For the THINC scheme, Eq. 3.19 is written in the conservative form:

$$\frac{\partial \phi_1}{\partial t} + \frac{\partial(u\phi_1)}{\partial x} = \phi_1\frac{\partial u}{\partial x} \tag{3.20}$$

Integrating Eq. 3.20 over one time step $[t, t+\Delta t]$ and one cell $[x_{k-1}, x_k]$ gives:

$$\bar{\phi_1}_k^{\,n+1} = \bar{\phi_1}_k^{\,n} - \frac{1}{\Delta x_k}(g_k - g_{k-1}) + \bar{\phi_1}_k^{\,n}\frac{u_k - u_{k-1}}{\Delta x_k}\Delta t \tag{3.21}$$

where k denotes the cell index. The cell-averaged density function $\bar{\phi_1}_k^{\,n}$ is defined as:

$$\bar{\phi_1}_k^{\,n} = \frac{1}{\Delta x_k}\int_{x_{k-1}}^{x_k} \phi_1 dx \tag{3.22}$$

The flux g_k at the cell boundary is defined as:

$$g_k = \int_t^{t+\Delta t} (u\phi_1)_k dx \tag{3.23}$$

The profile inside the cell can be approximated by a piecewise modified hyperbolic tangent function $F_k(x)$:

$$F_k(x) = \frac{\alpha_k}{2}\left\{1 + \gamma_k \tanh\left[\beta\left(\frac{x - x_{k-1}}{\Delta x_k} - \delta_k\right)\right]\right\} \tag{3.24}$$

where α_k, β, γ_k and δ_k are coefficients to be decided. The coefficient β regulates the steepness of the surface layer. According to Yokoi (2007), $\beta = 3.5$ corresponds to a smoothing distance of one cell. The computation of the other coefficients in Eq. 3.24 and the details of the numerical procedure are described in App. A.4.

Figure 3.3 shows a square wave advected with a constant velocity of $u = 0.1$ m/s for 180 time steps. The grid size is $\Delta x = 0.05$ m and the CFL number is $c = 0.1$. Comparing the original CIP method with the THINC method, it is seen that the oscillations at the discontinuities of the wave is eliminated. The scheme reduces oscillations and keeps the surface very sharp.

For the original CIP scheme, expanding to multi-dimensions is quite straightforward by using a multidimensional polynomial. For the THINC scheme, it is more convenient to use directional splitting. This method is described in the next section.

3.5.4 Two-dimensional THINC

The directional splitting method is known from the original CIP method (see e.g. Zhu, 2006). In this type of method, the advection equation is solved for one direction at a time. For the original CIP method, it is straightforward to expand the computation of the third order polynomial to two dimensions. As described earlier, the direct method called A-type CIP, has therefore been used. For more complicated approximation functions and for expansion to three dimensions, it may be

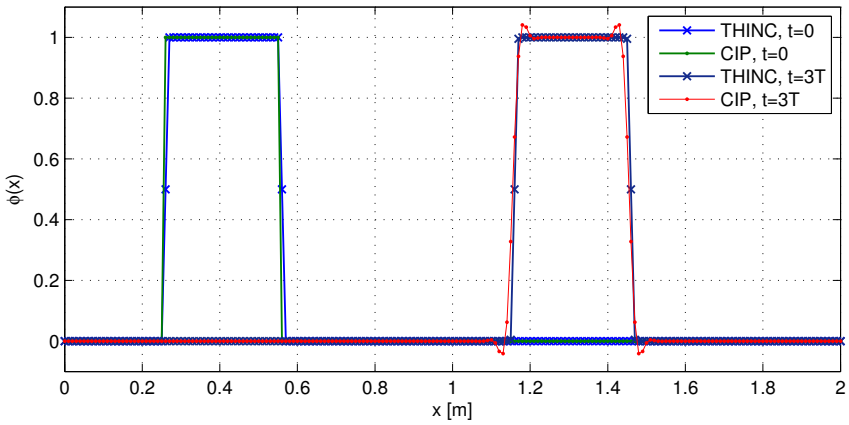

Figure 3.3: Advection of a square wave using CIP and THINC.

more efficient to use directional splitting. Directional splitting is used to expand the THINC procedure to 2-D. The directional splitting method presented here, is developed using the procedures described in Nakamura et al. (2001) and Yokoi (2007). The solution is performed by a reciprocal use of the 1-D solution described above. In two dimensions, the conservative advection equation (Eq. 3.20) becomes:

$$\frac{\partial \phi_1}{\partial t} + \frac{\partial \left(u_i \phi_1\right)}{\partial x_i} = \phi_1 \frac{\partial u_i}{\partial x_i} \tag{3.25}$$

where $i = 1, 2$ denotes the two spatial directions. The cell indices are denoted (k, l). Integrating over space and time to obtain the evolution of the cell-averaged density function $\bar{\phi}_1$, the directional splitting is used:

$$\bar{\phi}_1^* = \bar{\phi}_1^n - \frac{G^n_{1,k,l} - G^n_{1,k-1,l}}{\Delta x_{1k}} + \bar{\phi}_1^n \frac{u^n_{1,k,l} - u^n_{1,k-1,l}}{\Delta x_{1k}} \Delta t \tag{3.26}$$

$$\bar{\phi}_1^{n+1} = \bar{\phi}_1^* - \frac{G^*_{2,k,l} - G^*_{2,k,l-1}}{\Delta x_{2l}} + \bar{\phi}_1^n \frac{u^n_{1,k,l} - u^n_{1,k,l-1}}{\Delta x_{2l}} \Delta t \tag{3.27}$$

where, G_1 and G_2 are the fluxes in x_1- and x_2-direction, respectively. The flux in each direction η is computed using the 1-D THINC procedure:

$$G_{\eta,\mathrm{m}} = -\int_{\eta_\mathrm{m}}^{\eta_\mathrm{m} - \sigma_\mathrm{m} \Delta t} F_\mathrm{ms}(\eta) d\eta \tag{3.28}$$

$$F_{\mathrm{ms}}(\eta) = \frac{\alpha_{\mathrm{ms}}}{2}\left\{1 + \gamma_{\mathrm{ms}} \tanh\left[\beta\left(\frac{\eta - \eta_{\mathrm{ms}-1}}{\Delta\eta_{\mathrm{ms}}} - \delta_{\mathrm{ms}}\right)\right]\right\} \tag{3.29}$$

$$\mathrm{ms} = \begin{cases} \mathrm{m} & \text{for } \sigma_{\mathrm{m}} >= 0 \\ \mathrm{m}+1 & \text{otherwise} \end{cases} \tag{3.30}$$

Here, $\sigma = u_1$ for $\eta = x_1$ and $\sigma = u_2$ for $\eta = x_2$. The coefficients α, β, γ and δ are computed as described in Sec. A.4. Note that the flux in x_2–direction G_2^* is computed using the intermediate averaged density function $\bar{\phi}_1^*$.

3.5.5 Two-dimensional test cases

An advection test case of a square is performed, similar to that of Xiao et al. (2005). A 1.0×1.0 computational domain is divided into 64×64 cells. A 0.125×0.125 square is initially placed in the center of the domain, and advected using 3 different velocity fields. The advection computation is run for 160 steps with a maximum CFL number of 0.15. The results from using the THINC procedure is compared with results using the original CIP method and CIP with tangent transformation. Figures 3.4 and 3.5 show results for the velocity fields $(u_1, u_2) = (0.5, -1.0)$ and $(u_1, u_2) = (1.0, 1.0)$, respectively. Figure 3.4(a) and 3.5(a) show the square at the initial condition, the remaining figures shows the square after 160 time steps using (b) the THINC scheme, (c) the CIP scheme and (d) the tangent transformation. The contour lines for $\phi_1 = 0.05, 0.5$ and 0.95 are shown in the plots. Although the tangent transformation gives better results than the original CIP method, it cannot compete with the THINC method in terms of retaining the shape of the square.

The coefficient β controls the steepness of F_i, i.e. the thickness of the surface. All the references use $\beta = 3.5$, which is said to correspond with smoothing over one cell, see Sec. 3.5.3. In the examples above, $\beta = 3.5$ is used. To assess the effect of changing β, a parameter study is performed. The coefficient is varied from $\beta = 2.0{-}5.0$ in steps of 0.5. Figure 3.6 shows the advected square for velocity field no. 2, $(u_1, u_2) = (1.0, 1.0)$ using 3.6(a) $\beta = 2.0$, and 3.6(b) $\beta = 5.0$. Compared to Fig. 3.5(b), we see that the surface layer thickness increases with decreasing β and decrease with increasing β as expected. The shape of the square is however still preserved better than when using the tangent transformation, for all β. It is not necessarily beneficial to restrict the surface layer thickness too much. This may lead to numerical problems for the total numerical model. The performance of the THINC scheme used together with the CCUP flow solver is further discussed in Secs. 5.4.3 and 6.3.2.

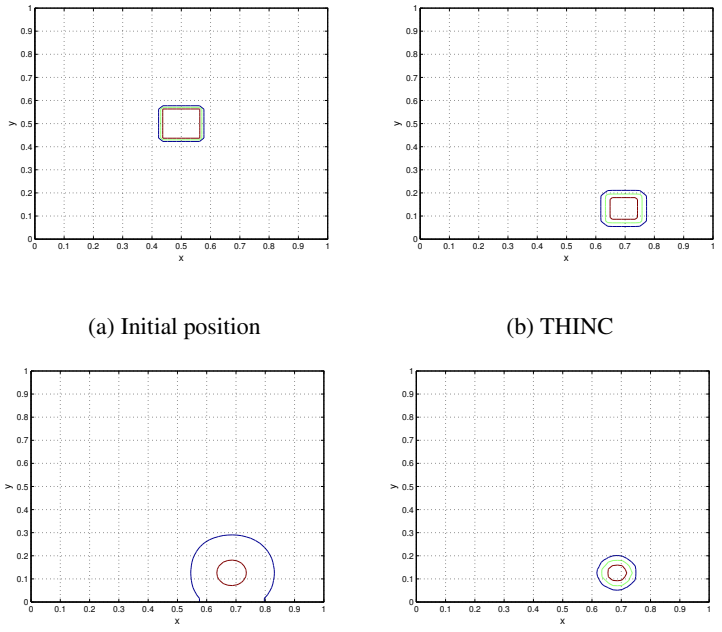

(a) Initial position

(b) THINC

(c) CIP

(d) Tangent transformation

Figure 3.4: Translation of a 2–D square initially centered in the computational domain, using different advection methods. The velocity field is $(u_1, u_2) = (0.5, -1.0)$. The contour lines for $\phi_1 = 0.05, 0.5$ and 0.95 are shown in the plots.

3.6 Boundary conditions

For all the applications of the present numerical model, the computational domain is set up as a rectangular water tank. To define the walls, roof and bottom of the tank, one layer of boundary cells are used, see Fig. 3.7.

A slip or a no-slip condition can be set along the walls, top and bottom of the tank. For the slip condition, the normal velocity is set to zero at the wall, while the tangent velocity is set equal to the value at the neighboring cell inside the tank. For a no-slip condition, the normal velocity is set to zero as before, while the tangent velocity is set equal to the value at the neighboring computational cell, but with opposite sign. Due to the staggered grid, this gives zero tangent velocity at the wall, assuming a cubic polynomial interpolation function. The difference between the two boundary conditions is illustrated in Fig. 3.8. The pressure of the boundary cells are set equal to the pressure in the neighboring computational cell. At the

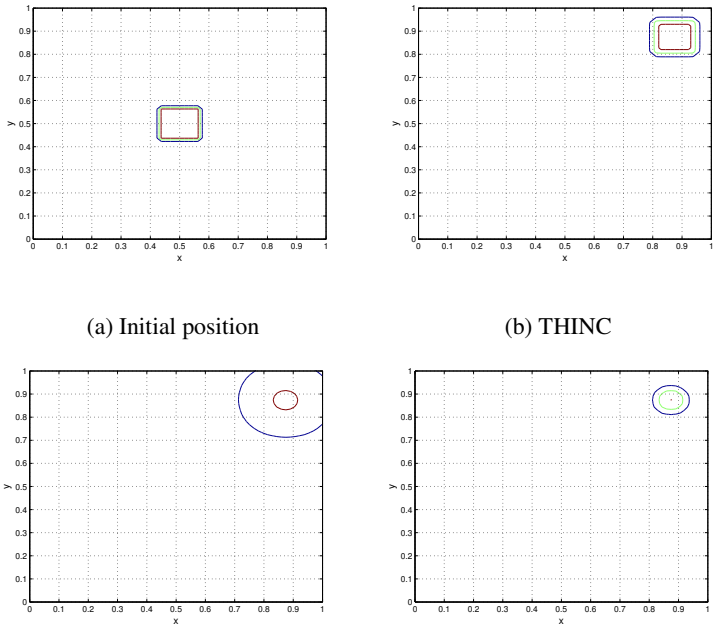

(a) Initial position

(b) THINC

(c) CIP

(d) Tangent transformation

Figure 3.5: Translation of a 2–D square initially centered in the computational domain, using different advection methods. The velocity field is $(u_1, u_2) = (1.0, 1.0)$. The contour lines for $\phi_1 = 0.05, 0.5$ and 0.95 are shown in the plots.

tank roof, the pressure is set to atmospheric pressure.

The body boundary condition is set using the body density function ϕ_3. For the applications in this thesis, the body is rigid and the body motion is prescribed. The velocity field in the computational domain can then be adjusted using:

$$u_i = U_i\phi_3 + u_i(1.0 - \phi_3) \tag{3.31}$$

where U_i is the velocity of the body, and u_i is the fluid velocity. For arbitrary geometries, the formulation in Eq. 3.31 gives an uncertainty or smoothing of one cell size for the body boundary condition. Small cell sizes may thus be necessary at the body. Figure 3.9 illustrates the difference in the velocity field between the body boundary and no-slip condition.

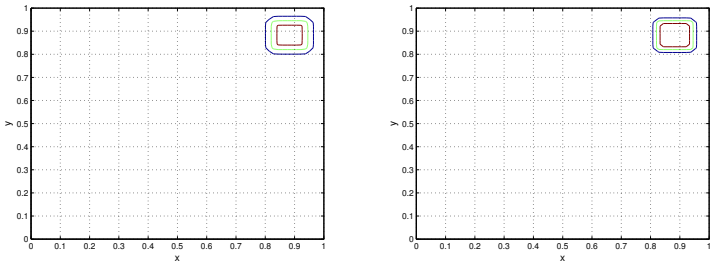

(a) $\beta = 2.0$ (b) $\beta = 5.0$

Figure 3.6: Translation of a 2–D square initially centered in the computational domain, using THINC with different smoothing parameter β. The velocity field is $(u_1, u_2) = (1.0, 1.0)$.

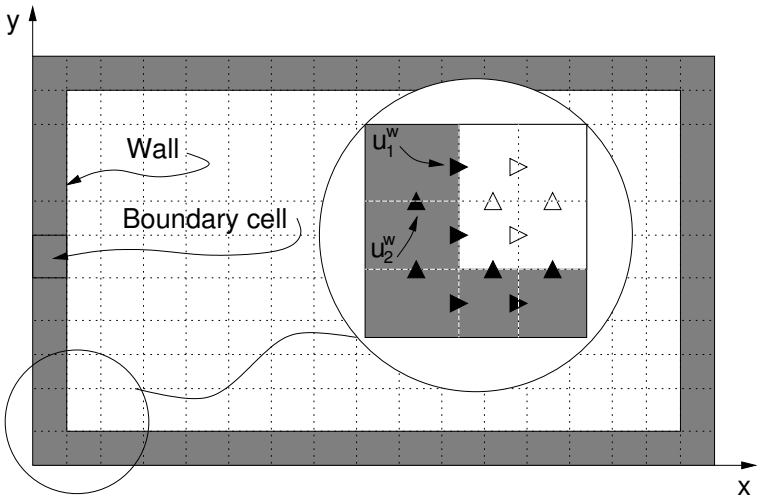

Figure 3.7: The computational domain, including one layer of boundary cells. The boundary conditions at the walls are imposed by setting the velocities u_1^w and u_2^w at the walls. The boundary and computational cells at the corner is enlarged to show the evaluation positions of the boundary velocities.

3.7 Force computation

The hydrodynamic force F_i on a rigid body is computed by integrating the pressure and skin friction along the body surface.

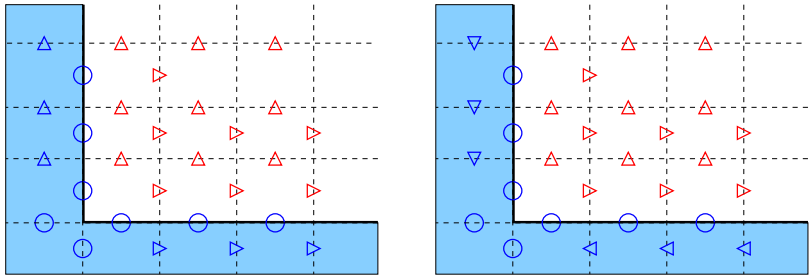

(a) Slip condition (b) No-slip condition

Figure 3.8: Illustration of boundary condition at tank wall and bottom. Circles denotes zero velocity. Blue color denotes boundary velocities, red color denotes computational cell velocities.

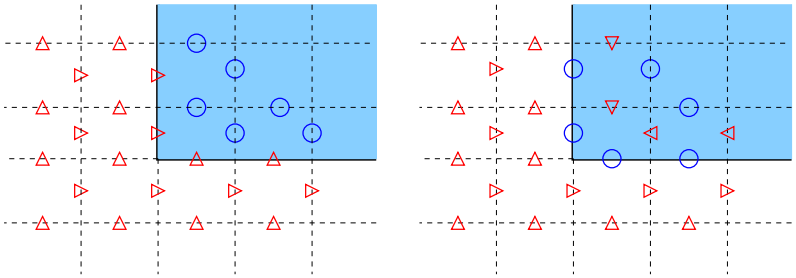

(a) Body density function (b) No-slip condition

Figure 3.9: Schematic comparison of the body boundary condition using ϕ_3 and no-slip condition for the corner of a body. Blue circles denotes velocity set to zero, red triangles denotes non-zero velocities.

$$F_i = \int_{S_b} (-p\delta_{ij})\, n_j dS_b + \int_{S_b} S_{ij} n_j dS \tag{3.32}$$

Here, S_b is the 2-D body surface, n_j is the j-th component of the outward unit normal vector. δ_{ij} is the Kronecker delta, and $S_{ij} = \mu(\partial u_i/\partial x_j + \partial u_j/\partial x_i)$. If pressure forces dominate and the friction force can be neglected, the force computation can be simplified. Assuming S_b is a closed surface, and that the artificial pressure inside the body is continuous, Gauss' theorem can be used. The first term

of Eq. 3.32 can be rewritten as:

$$F_i = -\iint_\Omega \frac{\partial p}{\partial x_i}\phi_3 d\Omega \tag{3.33}$$

Here, Ω denotes the computational domain. Since the position of the body is known in the cases below, the integration over the complete domain is not necessary, as only the cells with $\phi_3 > 0.0$ contribute to the force. Both force computation methods are implemented in the code, for verification purposes.

3.8 Overview of the numerical procedure

All the parts of the numerical method are described above. In this section, an overview over how the different parts are interconnected is given. At the time instance t^n, the pressure p^n, velocity field u_i^n, density functions ϕ_{m}^n, mass density ρ^n and viscous coefficient μ^n are known. The spatial derivatives of the velocity field $\partial u_i^n/\partial x_i$ and the velocity of the body U_i^n are also known. To compute values for all these variables for the next time step $t^{n+1} = t^n + \Delta t$, the following procedure is followed:

Advection step The velocity field and water density function are advected giving u_i^*, $\partial u_i^*/\partial x_i$, ϕ_1^{n+1} and $\partial\phi_1^{n+1}/\partial x_i$. The boundary values for u_i and ϕ_1 are updated.

Body update The position and motion of the body is updated giving ϕ_3^{n+1} and U^{n+1}, respectively. The water density function ϕ_1^{n+1} is adjusted due to ϕ_3^{n+1}. The air density function ϕ_2^{n+1} is found for the next time step using Eq. 3.13. The mass density ρ^{n+1} and viscous coefficient μ^{n+1} is found using Eqs. 3.14 and 3.15, respectively. The body boundary condition is then enforced using Eq. 3.31.

Diffusion step The diffusion step for the derivatives of the velocities is computed using Eq. 3.10, giving $\partial u_i^{n+1}/\partial x_i$. The diffusion step for the velocities is then computed using Eq. 3.7, giving u_i^{**}. The boundary conditions for the velocity field at the walls and body are updated again.

Poisson step The pressure Poisson equation is solved, giving p^{n+1}. The boundary conditions for the pressure is also updated.

Velocity update Finally, u_i^{n+1} is obtained using Eq. 3.8. The boundary conditions for the velocity field is updated once more.

All variables are now computed for the next time step. The time step size is then checked using the procedure described in Sec. 3.4.3. The numerical procedure described above isillustrated in Fig. 3.10.

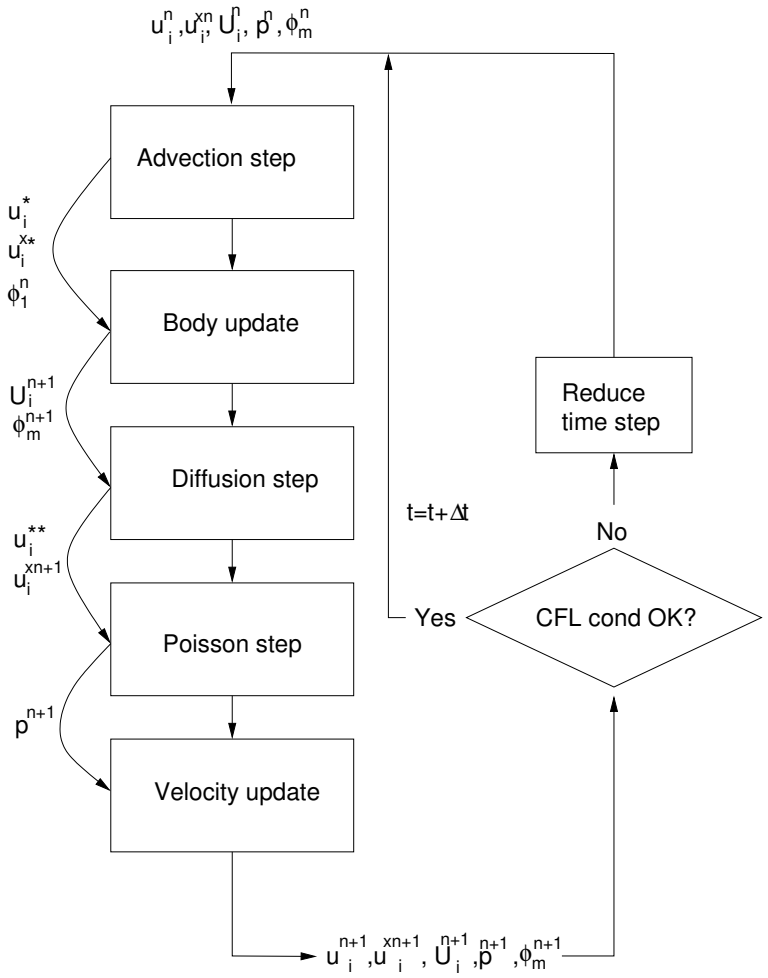

Figure 3.10: Flow diagram of the numerical procedure for one time step showing which variables are updated for each step. u_i denotes the velocity field, U_i denotes the body velocity, p denotes the pressure and ϕ_m denotes the density functions for water, air and body. Superscript n denotes the present time step, superscript x denotes spatial derivative and $*$ or $**$ denotes intermediate values.

Chapter 4

Benchmark tests

4.1 Introduction

In this chapter, benchmark tests used to develop the CIP code are presented. The goal of the development is to obtain a code that can simulate wave impact on a structure, i.e. violent, non-linear flow. But the code must also handle simpler cases for us to gain confidence in the more complicated simulations. The chosen benchmark tests provide such cases, and demonstrate the capabilities and limitations of the code. The CIP method is used also in other fields of fluid dynamics, and many generic test cases can be found in the literature, (see e.g. Yabe et al., 2000). The benchmark tests used in this work are chosen to be related to marine hydrodynamics.

The benchmark tests are also an important part of the verification and validation of the present CIP code. The notions of verification and validation should be clarified. The ITTC committee (ITTC, 1990, 2002) adopts the following definition:

Verification of a computer program means to check that the program is actually a correct representation of the mathematical model that form the basis for it.

Validation is the demonstration that the verified computer program is an adequate representation of the physical reality.

A short way of expressing this definition is given in Roache (1998): Verification is a question of solving the equations right, while validation is a question of solving the right equations. Note that in Roache (1998), verification is defined as comparisons with closed form mathematical solutions and validation as comparison with experiments, while benchmark tests are defined as code-to-code comparisons. Following this definition, some of the cases presented below are verification, some are benchmark tests and one is validation.

The verification of the CIP method for solving the Navier-Stokes equation is partly documented in previous work, see Sec. 2.2. Basic verification work for the present code is also performed, e.g as presented in Secs. 2.5 and 3.5.5. In this chapter, further verification is provided by comparing results with analytic solutions, and results from other numerical methods. Computation of impact forces caused by water entry are compared with another CIP code and then partly validated by comparison with experimental results.

4.2 Overview of benchmark tests

The benchmark tests used in the present work are described below.

Lid driven flow This case is commonly used to check the main parts of the flow solver and the viscous behavior of the flow (Ferziger and Perić, 2002). The computational domain is a rectangular tank completely filled with liquid. The roof of the tank is given a constant horizontal velocity. In time, steady-state vortices form in the liquid. The number and position of the vortices depend on the Reynolds number of the flow. There is no free surface and the geometry is simple. This is convenient for checking the performance of e.g. different iterative solvers. Detailed results for comparison are provided in Ghia et al. (1982). A useful discussion is also found in Herfjord (1995b). The present work on this test is described in App. B.2.

Standing waves in a rectangular tank In this test, a free surface is introduced. An initial velocity field is set up in the tank, causing standing waves. Grid dependency is checked. Conservation of mass and energy is monitored. The behavior at the boundary layer is studied. Linear potential theory and boundary layer theory are used for comparison.

Sway excitation of a rectangular tank Violent sloshing in e.g. ship tanks is a research field in its own right. In the present work, moderate free surface motion in a tank is considered. The computational domain is the same as in the previous test. External forcing is now used, modeling a tank subjected to sway motion. Convergence in time and space and surface sharpness enhancement algorithms are tested. The conservation of mass is monitored, together with surface layer growth. Linear potential theory as presented in Faltinsen (1978) is used for comparison in the present work, but also higher order potential theory, experiments and other CFD results exist (see e.g. Rognebakke, 2002).

Added mass and damping of a circular cylinder In this test, a body with prescribed motion is introduced, and thus the body and the force computations are implemented in the code. The computed hydrodynamic forces are compared with BEM computations by Baarholm (2001). Zhu (2006) computed the added mass and damping for a nearly rectangular ship section using the CIP method, but concluded that vortex shedding disturbed the results compared to linear potential flow.

Water entry of a circular cylinder A circular cylinder is forced through the water surface with constant speed. Water impact forces are computed. Comparisons are performed with previous CIP simulations (Zhu, 2006) and experimental results (Miao, 1989).

4.3 Standing waves in a rectangular tank

4.3.1 Case set-up

A fixed tank with half-breadth a and water depth h is considered, see Fig. 4.1. The water in the tank is given an initial velocity corresponding to the first natural anti-symmetric eigenmode given by linear potential theory. Solving the boundary value problem using linear potential theory, the velocity potential $\Phi_{\mathrm{n}}(x, y, t)$ is given as (Faltinsen and Timokha, 2009):

$$\Phi_{\mathrm{n}}(x, y, t) = \frac{g\zeta_A}{\omega_{\mathrm{n}}} \frac{\cosh\left[k_{\mathrm{n}}\left(y+h\right)\right]}{\cosh\left(k_{\mathrm{n}}h\right)} \sin(k_{\mathrm{n}}x)\cos(\omega_{\mathrm{n}}t) \quad , k_{\mathrm{n}} = \frac{2\mathrm{n}+1}{2a}\pi \tag{4.1}$$

where $\mathrm{n} = 0, 1, 2\ldots$ denotes the eigenmodes. ζ_A is the wave amplitude, k_{n} is the wave number and g is the acceleration of gravity. The wave frequency ω_{n} is found from the dispersion relation as a function of k_{n} and h, see Eq. 4.2.

$$\omega_{\mathrm{n}} = \sqrt{g k_{\mathrm{n}} \tanh(k_{\mathrm{n}}h)} \tag{4.2}$$

The velocity field (u, v) is given as:

$$u(x, y, t) = \frac{\partial \Phi_{\mathrm{n}}}{\partial x} = \omega_{\mathrm{n}}\zeta_A \frac{\cosh\left[k_{\mathrm{n}}\left(y+h\right)\right]}{\sinh\left(k_{\mathrm{n}}h\right)} \cos(k_{\mathrm{n}}x)\cos(\omega_{\mathrm{n}}t) \tag{4.3}$$

$$v(x, y, t) = \frac{\partial \Phi_{\mathrm{n}}}{\partial y} = \omega_{\mathrm{n}}\zeta_A \frac{\sinh\left[k_{\mathrm{n}}\left(y+h\right)\right]}{\sinh\left(k_{\mathrm{n}}h\right)} \sin(k_{\mathrm{n}}x)\cos(\omega_{\mathrm{n}}t) \tag{4.4}$$

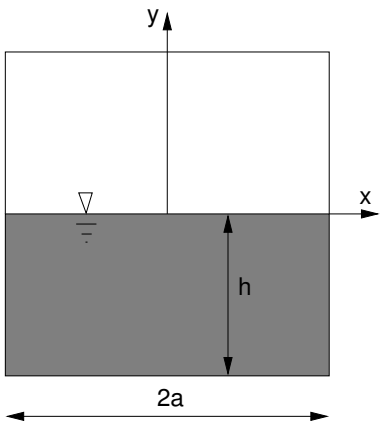

Figure 4.1: Rectangular tank with half–breadth a and water depth h. The horizontal axis lies at the mean free surface, and the vertical axis lies at the center of the tank.

The free surface elevation ζ is found from the linear free surface boundary condition:

$$\zeta(x,t) = -\frac{1}{g}\frac{\partial \Phi_{\mathrm{n}}}{\partial t}\bigg|_{y=0} = \zeta_A \sin(k_{\mathrm{n}} x)\sin(\omega_{\mathrm{n}} t) \tag{4.5}$$

The dynamic pressure p_D is:

$$p_D(x,y,t) = -\rho\frac{\partial \Phi_{\mathrm{n}}}{\partial t} = \rho g \zeta_A \frac{\cosh\left[k_{\mathrm{n}}\left(y+h\right)\right]}{\cosh\left(k_{\mathrm{n}} h\right)}\sin(k_{\mathrm{n}} x)\sin(\omega_{\mathrm{n}} t) \tag{4.6}$$

Details of the tank and the case set-up are given in Tab. 4.1. For the first eigenmode, $\mathrm{n} = 0$, the wavenumber is $k_0 = \pi/2a$, and the natural period becomes T_0 =1.182 s. Initially ($t = 0$ s), the dynamic pressure is zero for the entire domain, and the free surface is zero for all x. Thus, only the velocity field has non-zero values (see Eqs. 4.3–4.6). This makes the initial condition easy to implement in the numerical model. After the initial velocity field is given, no excitation is input to the tank, and free oscillations of standing waves are thus simulated. This case is suited for examining the energy conservation properties of the numerical method.

4.3.2 Energy conservation

The potential and kinetic energy are computed using Eqs. 4.7 and 4.8.

$$E_p = \frac{\rho g}{2}\int_{-a}^{a} \zeta^2 dx \tag{4.7}$$

Table 4.1: Wave tank dimensions, wave amplitude and first natural period.

Half-breadth	a	0.500	m
Water depth	h	0.500	m
Amplitude	ζ_A	0.025	m
Natural period	T_0	1.182	s

$$E_k = \frac{\rho}{2} \int_{-a}^{a} \int_{-h}^{\zeta} \left(u^2 + v^2\right) dxdy \tag{4.8}$$

The energy computed for the CIP simulations can be compared with the energy according to linear potential theory, which can easily be derived by substituting Eqs. 4.3–4.5 into Eqs. 4.7 and 4.8. For potential theory, the total energy $E_0 = E_k + E_p$ is constant in time, since no damping is included:

$$E_0 = \frac{1}{2}\rho g \zeta_A^2 a \tag{4.9}$$

In reality damping is present, mainly caused by viscous dissipation along the walls. In time, the damping will cause decay of the free surface amplitude. The damping in the numerical model can be compared with theoretical viscous dissipation for a flat plate, applied on the walls and bottom of the tank (see e.g. Schlichting and Gersten, 2000; Faltinsen and Timokha, 2009). Laminar flow is assumed. The viscous dissipation occurs at a much slower time scale than T_0. The time averaged rate of the viscous dissipation over one period and per unit length of the plate can be approximated as:

$$\overline{\frac{dE}{dt}} = -\frac{\mu}{2}\sqrt{\frac{\omega_0}{2\nu}} U_0^2 \tag{4.10}$$

where U_0 is the outer flow velocity and $\nu = \mu/\rho$ is the kinematic viscosity coefficient. Inserting $x = 0$ and $y = 0$ into Eqs. 4.3 and 4.4, gives the outer velocity along the vertical walls ($U_{0\mathrm{w}}$) and at the bottom ($U_{0\mathrm{b}}$), respectively:

$$U_{0\mathrm{w}}^2 = \omega_0^2 \zeta_A^2 \frac{\sinh^2 k_0 (y+h)}{\sinh^2 k_0 h} \tag{4.11}$$

$$U_{0\mathrm{b}}^2 = \omega_0^2 \zeta_A^2 \frac{\cos^2 k_0 x}{\sinh^2 k_0 h} \tag{4.12}$$

The viscous dissipation over one period at the walls and bottom then becomes:

$$\overline{\frac{dE}{dt}}_{\mathrm{w}} = -\frac{\mu}{2}\sqrt{\frac{\omega_0}{2\nu}}\omega_0^2\zeta_A^2\frac{1}{\sinh^2 k_0 h}\int_{-h}^{0}\sinh^2 k_0\,(y+h)\,dy \tag{4.13}$$

$$\overline{\frac{dE}{dt}}_{\mathrm{b}} = -\frac{\mu}{2}\sqrt{\frac{\omega_0}{2\nu}}\omega_0^2\zeta_A^2\frac{1}{\sinh^2 k_0 h}\int_{-a}^{a}\cos^2 k_0 x dx \tag{4.14}$$

For a 2-D case, the total viscous dissipation can be assumed to be the sum of these two contributions (note that there are two walls and one bottom):

$$\overline{\frac{dE}{dt}} = 2\overline{\frac{dE}{dt}}_{\mathrm{w}} + \overline{\frac{dE}{dt}}_{\mathrm{b}} = -2\frac{\alpha}{T}E \tag{4.15}$$

where:

$$\alpha = \pi\sqrt{\frac{\nu}{2\omega_{\mathrm{n}}a^2}}\left[1 + \frac{2k_{\mathrm{n}}(a-h)}{\sinh 2k_{\mathrm{n}}h}\right] \tag{4.16}$$

Integration of Eq. 4.15 gives:

$$\frac{E}{E_0} = \exp\left(-2\alpha\frac{t}{T}\right) \tag{4.17}$$

where E_0 is given by Eq. 4.9.

4.3.3 Grid dependency test

To get an idea of the conservation properties of the numerical model, a grid dependency study is performed. Since the amplitude is small, the cell size must be small in the free surface zone. To ensure accurate boundary conditions at the walls, the grid is also refined along the walls and tank bottom. Three grids are tested, with a vertical cell size in the free surface zone corresponding to $\zeta_A/\Delta y = 12.5, 25$ and 50. Table 4.2 shows the specifics of the grids.

Table 4.2: Grid specifics for the grid dependency tests

Grid	No. of cells	Min. cell size	Max. cell size
Base case	376×344	0.001	0.005
Coarse grid	272×266	0.002	0.005
Fine grid	716×716	0.0005	0.002

For the base case grid, a grid cell size of 0.001 m is used along the tank walls and bottom. In the free surface zone, the grid size is 0.001 m in the y–direction.

Elsewhere, the grid size is 0.005 m. The grid is changed gradually from one cell size to the other in transition zones of about 10 cells. Cosine stretching is used. Figure 4.2 shows the refinement zones in dark gray and transition zones in light gray.

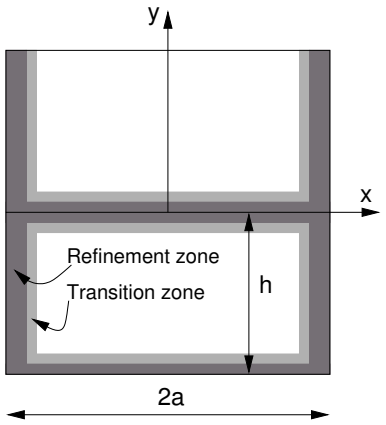

Figure 4.2: Grid refinement zones in the tank. Dark gray color denotes small cell sizes (grid refinement zone), light gray color denotes the transition zone where grid stretching is performed, and white color denotes normal cell size, see also Tab. 4.2.

The free surface at $x = -0.9a$ is shown in Fig. 4.3 for the three grids. There is little difference between the grids when considering the free surface elevation. The simulation using the fine grid is very slow, so only 5 wave periods (6.5 s) are simulated. The mass conservation property of the code is studied by monitoring the water volume, computed using Eq. 4.18

$$V_1 = \sum_{k=1}^{N_x} \sum_{l=1}^{N_y} \phi_1(k,l) \Delta x_k \Delta y_l \tag{4.18}$$

where V_1 is the water volume, $\phi_1(k,l)$ is the water density function for cell (k,l), N_x and N_y is the number of grid cells in the x– and y–direction, respectively. Figure 4.4 shows the change of volume in % of the original volume. It seems that the simulation using the coarse grid becomes unstable after about 11 periods. Apart from that, the change in volume is very small. The base case grid was run to about 20 periods, and the maximum volume change was 0.07%.

The total energy ratio E/E_0 is shown for the three grids in Fig. 4.5 together with the theoretical value given by Eq. 4.17. Note that the computed total energy for the coarse grid gives an early indication that this simulation may not be stable. For the other two grids, the total energy loss increases with time compared to the

theoretical value. This is assumed to have two causes. 1) There is more physical damping present than the viscous dissipation of Eq. 4.15. There will be energy loss due to the flow at the tank corners. In addition, there is some physical dissipation at the free surface. 2) The energy (and mass) is not perfectly conserved by the numerical model. The numerical dissipation is expected to decrease with grid refinement. This seems to be the case in Fig. 4.5.

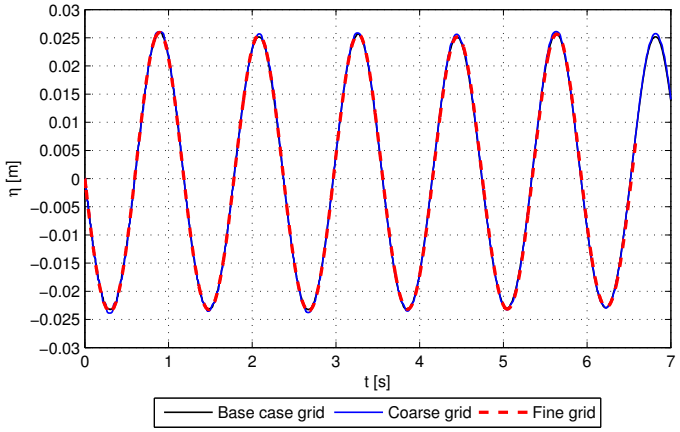

Figure 4.3: Grid dependency test: Free surface elevation ($\phi_1 = 0.5$) at $x = -0.9a$ for three different grids, see Tab. 4.2 for grid details.

For the two finest grids, there is an instant drop in total energy at $t = 0$ s. The reason for this is probably that the initial velocity field is computed from linear theory, giving slip conditions at the walls and tank bottom. The vertical velocity v is thus non-zero along the walls, and the horizontal velocity u is non-zero along the bottom of the tank (see Eqs. 4.11 and 4.12). In the CIP code, a no-slip condition is specified, requiring these velocities to be zero at the walls. During the first time steps, a boundary layer is thus formed. The gradients at the walls and bottom are steep, and the corresponding diffusion leads to the initial energy loss observed in Fig. 4.5. After that, the energy decreases more steadily for both grids.

The theoretical boundary layer velocity for an infinite flat plate can be computed as:

$$u_{\mathrm{bl}} = U_0 \left[\cos \omega_0 t - \exp\left(-y\sqrt{\frac{\omega_0}{2\nu}} \right) \cos\left(\omega_0 t - y\sqrt{\frac{\omega_0}{2\nu}} \right) \right] \tag{4.19}$$

where u_{bl} is the boundary layer velocity and U_0 is the outer velocity given by potential flow. The boundary layer thickness δ is computed as the distance from

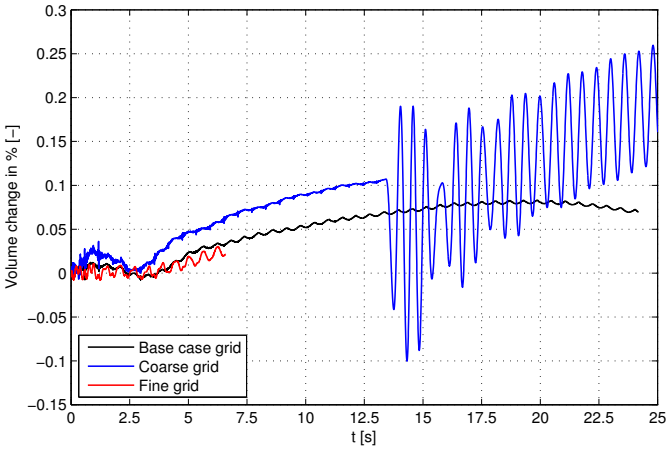

Figure 4.4: Grid dependency test: Water volume change for different grids, see Tab. 4.2 for grid details.

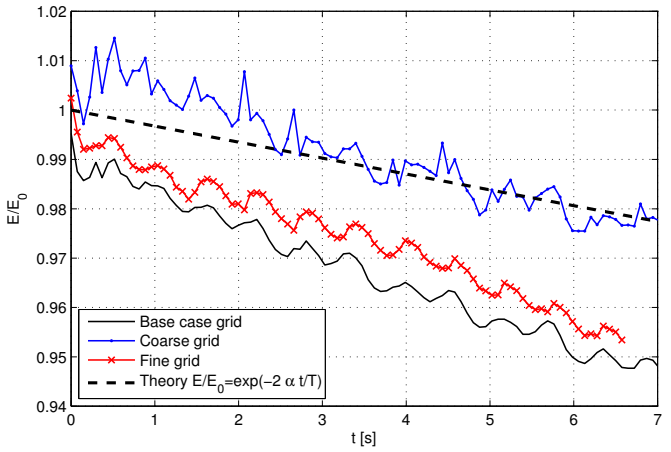

Figure 4.5: Grid dependency test: Total energy ratio E/E_0 for three different grids, see Tab. 4.2 for grid details.

the wall where $u_{\mathrm{bl}} = 0.99U_0$, giving $\delta = 0.009$ m. The base case grid has thus 9 cells in the boundary layer and the fine grid has 18 cells. Both grids should have sufficient refinement to capture the boundary layer flow. Fig. 4.6 shows the horizontal velocity close to the tank bottom. Theoretical boundary layer flow for an infinite plate is compared with the CIP computations after one wave period at $x = -a/2$. The initial velocity at $t = 0$ is also shown. The theoretical boundary

layer for an infinite plate is thicker than the CIP boundary layer for the tank. The CIP boundary layer was checked for $t = 4T_0$ also, and does not grow in time.

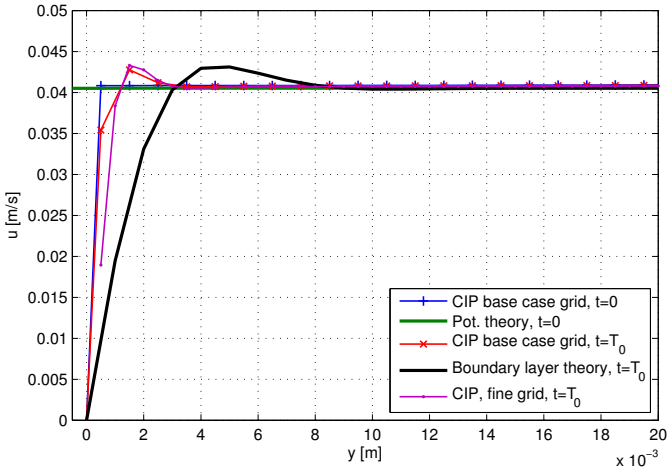

Figure 4.6: Comparison of simulated versus theoretical boundary layer at the tank bottom for the two finest grids, see Tab. 4.2 for grid details.

The standing wave case is in the present work also used for more basic verification work including a parameter study on different run-time variables. Results from this study is included in App. B.3

4.4 Sway excitation in a rectangular tank

4.4.1 Case set-up

The computational domain is the same as for the previous test, but instead of starting with an initial velocity field, the fluid is initially at rest. Sway motion η_2 is instead imposed on the tank:

$$\eta_2 = \eta_A \sin \omega t \tag{4.20}$$

where η_A is the sway amplitude and ω is the excitation frequency. The swaying motion is implemented by prescribing a horizontal velocity $u = \omega \eta_A \cos(\omega t)$ in the boundary cells. The natural frequencies are found using Eq. 4.2. The first eigenmode $\mathrm{n} = 0$ gives $k = \pi$ m^{-1}, corresponding to a natural period $T_0 = 1.182$ s. The second eigenmode gives $T_1 = 0.650$ s. In the present benchmark test, violent free surface behavior is avoided. The excitation periods are therefore kept

away from the eigenperiods and their multiples. Details of the tank and the case set-up is given in Tab. 4.3.

Table 4.3: Swaying tank case set-up

Half-breadth	a	0.500	m
Water depth	h	0.500	m
Sway amplitude	η_A	0.025	m
Oscillation periods	T	0.800	s
		2.400	s
Natural periods	T_0	1.182	s
	T_1	0.650	s
	T_2	0.506	s

4.4.2 Spatial and temporal grid dependency and mass conservation

The base case grid in Tab. 4.2 is used also for this case. The spatial grid dependency is discussed in Sec. 4.3.

Temporal grid dependency is checked by running simulations with both constant time steps of different lengths and with adaptive time stepping, see Sec. 3.4.3. The adaptive time stepping scheme gives more efficient simulations and less chance of breakdown during simulations, thus it is preferable to constant time steps. The simulations give identical results for adaptive time steps and constant time steps for $\Delta t = T/2000 - T/4000$. For longer time steps, the solver did not converge. This is due to that a relatively fine grid is used in the simulations.

The conservation of mass during the simulations are checked by computing the water volume at each time step using Eq. 4.18. Since the sway motion is modeled by imposing a velocity at the boarder cells, it is expected that the volume change is somewhat more than for the previous case. A net influx or outflow of water can occur for nonlinear free-surface behavior. The maximum volume change after six wave periods is 1.5%. For sloshing problems, the mass conservation is important because change of water volume will change the natural frequencies. Figure 4.7 shows the change in first and second natural period as a function of volume change. The volume change in the test case is acceptable, leading to a change in T_0 of 0.3%. Greater volume changes were however observed for simulations with excitation frequency close to the natural frequencies. As the wave elevation increases and becomes more violent, the imposed velocity at the boundary cells causes a net in- or outflow of water, as can be expected. The numerical dissipation at the free surface also increases. This is a known challenge for many numerical models in sloshing applications. The CIP-CSL methods (see Sec. 2.2) were developed to

improve the conservation properties of the flow solver. It is not as important for the wave tank application in the present work, and will not be pursued further here.

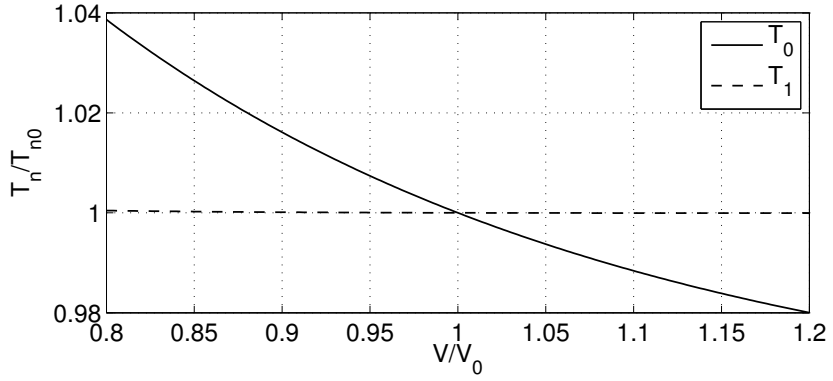

Figure 4.7: Change in the natural period of the tank as a function of volume change. V_0 and T_{n0} denotes the initial volume and natural period, V and T_n the actual volume and resulting natural period.

4.4.3 Effect of sharpness enhancement

As discussed in Sec. 3.5, the water density function ϕ_1 may be subjected to numerical diffusion for long simulations. This can be observed as a growth in the free surface layer that initially started with a width of one cell. The surface layer thickness δy_L is defined as the distance where $0.05 < \phi_1 < 0.95$. In the present case, the tangent and linear sharpness enhancement algorithms described in Sec. 3.5.2 are tested. Simulations are performed with both transformations. When comparing the free surface defined as $\phi_1 = 0.5$, the difference between the two methods is small, see Fig. 4.8. However, when comparing the surface layer thickness, it is clear that the tangent enhancement keeps the surface sharper than the linear enhancement. Figure 4.9 shows the surface layer thickness across the tank for time instances $t/T = 1 - 5$. The linear enhancement does not prevent surface layer growth efficiently. After $5T$, the surface layer has grown to more than $5\eta_A$. For the tangent sharpness enhancement method, the growth is significantly smaller. After $5T$, the surface layer is about $0.5\eta_A$.

Figure 4.10 shows snapshots of the free surface in the tank at $t = 1.5\ T$ using linear and tangent transformation of the density function. These simulations are performed for $T = 1.3$ s, which corresponds to $2T_1$. A more violent flow can therefore be expected. A small wave breaking event can be observed at the right hand wall. The dark red color denotes $\phi_1 = 1.0$, while the dark blue denotes

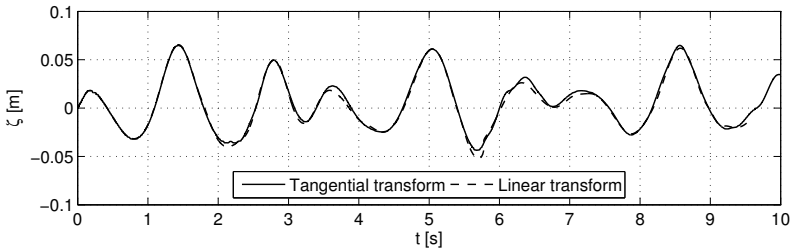

Figure 4.8: Effect of surface capturing method: Free surface elevation for $T = 1.8$ s using linear and tangent sharpness enhancement.

$\phi_1 = 0.0$. The lighter red color denotes $\phi_1 = 0.9 - 0.99$. In this case, the surface layer growth is already obvious for the linear enhancement, while it is significantly less for the tangent enhancement.

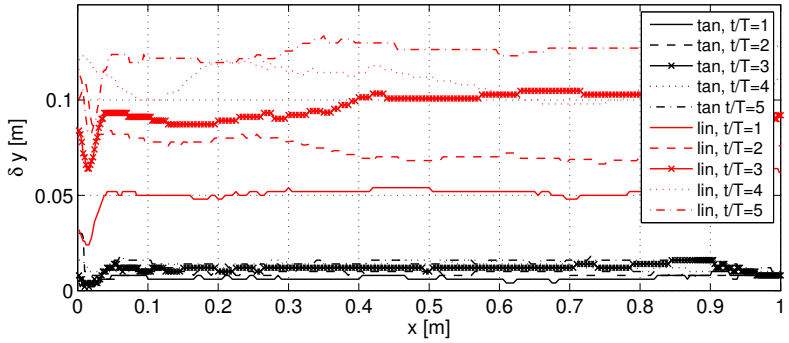

Figure 4.9: Effect of surface capturing method: Surface layer thickness δy (defined as $0.05 < \phi_1 < 0.95$) for $T = 1.8$ s using linear and tangent sharpness enhancement.

The linear transformation is computationally faster than the tangent transformation. The difference in the free surface elevation is not large, although the surface layer thickness is different. If the free surface elevation is the goal of the simulation, linear enhancement may suffice in many cases. On the other hand, if the velocity field or forces are important, a significant surface layer thickness will lead to inaccuracies.

The tangent transformation sometimes leads to a stepwise free surface at the beginning of the simulation (see e.g. Fig B.12), but is far more effective in preventing surface layer growth. The tangent transformation is thus chosen as the main surface capturing method for the further work. The method is compared with the THINC method for the numerical wave tank applications, see Ch. 5.

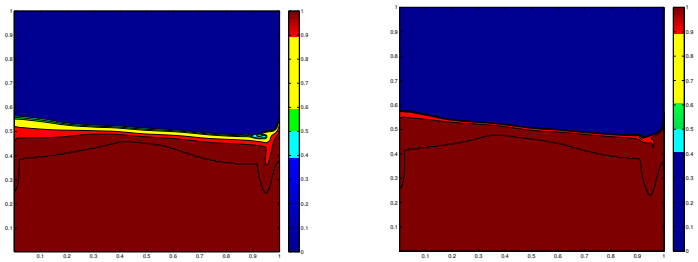

(a) Linear transformation (b) Tangent transformation

Figure 4.10: Effect of surface capturing method: Snapshot of the water density function ϕ_1 after $t = 1.5T$ for $T = 1.3$ s.

4.4.4 Comparison with linear potential theory

For the present case, a linear potential theory solution with artificial damping is presented in Faltinsen (1978) and Solaas (1995). Solving the Laplace equation with linear boundary conditions for the sway excitation described above, the velocity potential $\Phi(x, y, t)$ can be written as:

$$\begin{aligned}\Phi(x,y,t) \quad = \quad & \sum_{n=0}^{\infty} \sin\left(k_{\mathrm{n}} x\right) \left\{ A_c \frac{2}{a} \left(\frac{1}{k_{\mathrm{n}}}\right)^2 (-1)^n \cos\omega t \right. \\ & + \cosh\left(k_{\mathrm{n}}\left(y+h\right)\right) \left[e^{\frac{\mu_p}{2} t} \left(A_{\mathrm{n}} \cos\alpha_{\mathrm{n}} t + B_{\mathrm{n}} \sin\alpha_{\mathrm{n}} t\right) \right. \\ & \left. \left. + C_{\mathrm{n}} \cos\omega t + D_{\mathrm{n}} \sin\omega t \right] \right\}\end{aligned} \tag{4.21}$$

where $A_c = \eta_A \omega$ and $\alpha_{\mathrm{n}} = \sqrt{\omega_{\mathrm{n}}^2 - \mu_p/4}$. The dispersion relation is given by Eq. 4.2 and the wave number k_{n} is defined in Eq. 4.1. The artificial damping μ_p is included in the potential theory to take into account the dissipation at the boundary layer along the tank walls, as discussed in Sec. 4.3. The damping is expressed as a percentage of the critical damping, μ_{cr}, see Eq. 4.22. In Faltinsen (1978), 5% of critical damping was used in the computations.

$$\mu_{\mathrm{cr}} = 2\sqrt{g \frac{\pi}{2a} \tanh\left(\frac{\pi}{2a} h\right)} \tag{4.22}$$

If there is no excitation, and the damping is set to zero, Eq. 4.21 reduces to the

velocity potential of the eigenmodes, see Eq. 4.1. The coefficients A_{n}, B_{n}, C_{n} and D_{n} are given in Eqs. 4.23–4.26.

$$A_{\mathrm{n}} = -C_{\mathrm{n}} \tag{4.23}$$

$$B_{\mathrm{n}} = -\frac{1}{\alpha_{\mathrm{n}}}\left(K_{\mathrm{n}} + \frac{\mu_p}{2}C_{\mathrm{n}} + \omega D_{\mathrm{n}}\right) \tag{4.24}$$

$$C_{\mathrm{n}} = -\frac{K_{\mathrm{n}}\mu_p\left(\omega_{\mathrm{n}}^2 - \omega^2\right) + \mu_p\omega^2 K_{\mathrm{n}}}{\left(\omega_{\mathrm{n}}^2 - \omega^2\right)^2 + \mu_p^2\omega^2} \tag{4.25}$$

$$D_{\mathrm{n}} = \frac{K_{\mathrm{n}}\omega\left(\omega_{\mathrm{n}}^2 - \omega^2\right) - \mu_p^2\omega K_{\mathrm{n}}}{\left(\omega_{\mathrm{n}}^2 - \omega^2\right)^2 + \mu_p^2\omega^2} \tag{4.26}$$

Here, K_{n} is given as:

$$K_{\mathrm{n}} = \frac{A_c\omega}{\cosh\left(k_{\mathrm{n}}h\right)}\frac{2}{a}\left(\frac{1}{k_{\mathrm{n}}}\right)^2(-1)^n \tag{4.27}$$

The free surface $\zeta(x,t)$ as a function of time and at any point x along the tank breadth can then be found using a modified free surface boundary condition:

$$\zeta(x,t) = -\frac{1}{g}\left(\left.\frac{\partial\Phi}{\partial t}\right|_{y=0} + \mu_p\ \Phi|_{y=0}\right) \tag{4.28}$$

The last term takes into account the artificial damping in the linear model. The wave elevation predicted by Eq. 4.28 is compared with results from the CIP simulations. Figures 4.11 and 4.12 shows the free surface elevation for $T = 0.8$ s and $T = 2.4$ s, respectively. For the linear theory, 7% of critical damping is used for the former excitation period, while 1% of critical damping is used for the latter. This gave the best match with CIP simulations for the two cases. The agreement is best for the longest excitation period. For both periods, the linear theory and CIP simulations agree best at the beginning of the simulations. Both observations may indicate that the discrepancy is due to the damping models. The CIP method has, as discussed in Sec. 4.3, some numerical dissipation. However, the potential theory models the damping in a simplified manner. The agreement should thus be better when the free surface elevation is small and the damping is of little importance, i.e. for the longest period.

4.5 Added mass and damping of a circular cylinder

The hydrodynamic forces on a circular cylinder undergoing forced oscillations in heave are computed. A body is thus introduced in the numerical model. The use

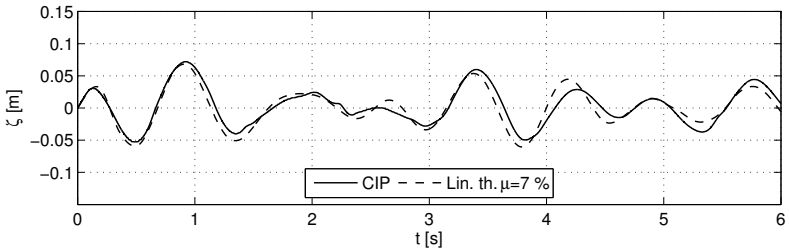

Figure 4.11: CIP vs. potential theory: Free surface elevation at $x = -0.9a$ for $T = 0.8$ s.

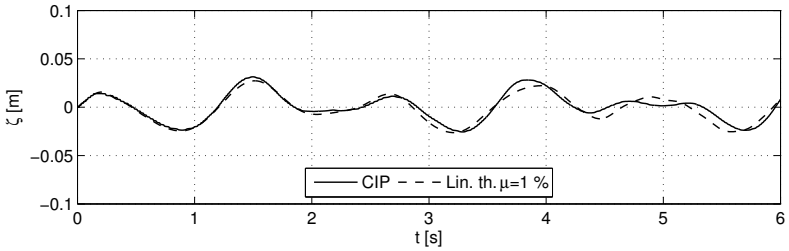

Figure 4.12: CIP vs. potential theory: Free surface elevation at $x = -0.9a$ for $T = 2.4$ s.

of ϕ_3 to impose the body boundary condition and the force computation described in Ch. 3 is implemented in the code. Two cases are tested. A circular cylinder fully submerged in a square tank, and a circular cylinder with its axis at the mean free surface. The former test includes no free surface and serves as a verification of the implementation of the body boundary condition and the force computations. Forces can be compared with an analytical solution. This test is presented in App. B.4. The discrepancy between the computed added mass and the analytical value for the fully submerged cylinder is found to be 4% for the base case grid. The discrepancy in the static buoyancy force is 0.5%.

The test with the cylinder at the free surface is presented below. Several parameter studies are performed. The added mass and damping coefficient of the cylinder is derived from the computed forces and compared with results from a linear BEM code (Baarholm, 2001, Ch. 5).

4.5.1 Case set-up

A circular cylinder of radius $r_c = 0.5$ m is placed with its axis at the free surface and is subjected to forced harmonic heave motion η_3, see Eq. 4.29.

$$\eta_3 = \eta_A \cos(\omega t) \tag{4.29}$$

The heave amplitude is η_A and the excitation frequency is ω. The vertical force on the cylinder is computed for different oscillation periods. The cylinder is placed in the middle of the tank. The tank length varies between 18 m and 52 m depending on the oscillation period of the cylinder. For long periods, a long tank is needed to provide sufficient damping of the produced waves at the tank ends. Damping zones (see Sec 5.2.2) are included at the right and left hand walls of the tank. Figure 4.13 shows the test set-up. Table 4.4 lists which excitation periods T are run, together with information about the tank set-up and base case grid configuration.

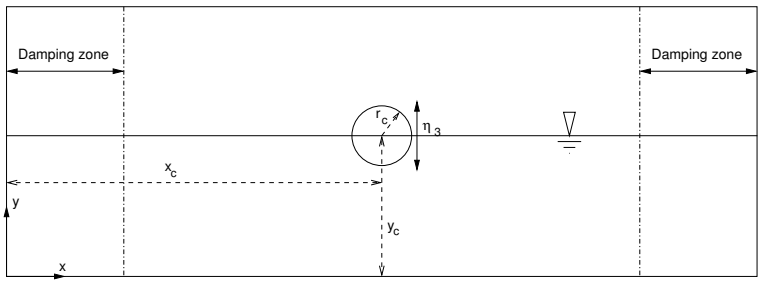

Figure 4.13: Case set-up for circular cylinder with forced heave oscillations.

At the start-up of the CIP simulations, the artificial pressure field inside the body oscillates somewhat. This leads to transients in the computed force. The effect is also observed for hydrostatic simulations where the cylinder is fixed. To avoid disturbance from these transients, the computed force history is bandpass-filtered with cut-off periods at $0.5\ T$ and $1.5\ T$ before computing added mass and damping coefficients, see Sec. 4.5.6.

4.5.2 Sensitivity to grid variations

It is the flow in the vicinity of the body that is of interest in this case. Grid refinement around the cylinder is used to increase the efficiency of the computations. The minimum cell size is kept constant in an area on each side of the cylinder. Outside this area, the horizontal cell size is increased toward the tank ends. Linear stretching is used. There are no abrupt changes in the cell size throughout the domain. The minimum cell size is $\Delta x = 0.01$ m. In the vertical direction, the cells are kept constant at the minimum size for the entire domain height, so $r_c/\Delta x = r_c/\Delta y = 50$. The length of the refined area in the horizontal direction is varied to study the sensitivity to grid stretching. Three cases are run, with refinement length $L_{\mathrm{R}} = 2.4$, 4.0 and 6.0 times the cylinder radius. Two excitation

Table 4.4: Excitation period, tank length and base case grid size.

Excitation period T [s]	Domain size [m × m]	Grid size
1.00	18.0×3.0	320×400
1.06	18.0×3.0	320×400
1.12	18.0×3.0	320×400
1.20	18.0×3.0	400×400
1.27	18.0×3.0	320×400
1.42	18.0×3.0	320×400
1.50	18.0×3.0	320×400
1.64	30.0×3.0	400×400
1.83	30.0×3.0	400×400
2.00	30.0×3.0	400×400
2.24	52.0×3.0	510×400
2.84	52.0×3.0	510×400

periods are tested, $T = 1.5$ s and $T = 2.0$ s. This means that two different tank lengths are tested as well. Details of the grid configurations are shown in Tab. 4.5. Figure 4.14 shows the computed force for the three different grid configurations. The force is normalized by the static buoyancy force $F_b = \frac{1}{2}\rho g \pi r_c^2$. The results do not show dependence on the size of the refined area outside the cylinder. The shortest refinement length is therefore used in the further simulations.

Table 4.5: Grid configuration details for refinement area test.

Grid no.	Period T [s]	Refined length L_{R}/r_c [-]	Domain size [m × m]	Grid size
1	1.50	2.4	18.0×3.0	320×400
2	1.50	4.0	18.0×3.0	420×400
3	1.50	6.0	18.0×3.0	500×400
4	2.00	2.4	30.0×3.0	400×400
5	2.00	4.0	30.0×3.0	420×400
6	2.00	6.0	30.0×3.0	480×400

Figure 4.14 also shows the initial oscillations of the force mentioned in Sec. 4.5.1. The oscillations are more pronounced for longer periods than for short periods.

A more traditional grid dependency test is also performed. The grid cell size is varied in the refinement area. Cell sizes of $r_c/\Delta x = r_c/\Delta y = 100$, 50 and 25 are tested for $T = 1.5$ s. Figure 4.15 shows the computed vertical force for the three grids. For the finer grid, transient oscillations are much more pronounced, so that the steady state takes longer to develop. But the steady state force seems to be

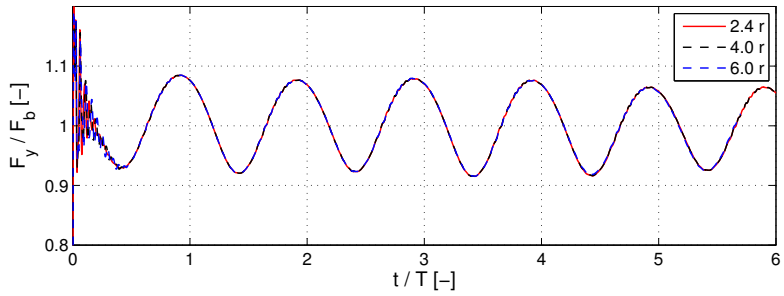

(a) $T = 1.5$ s

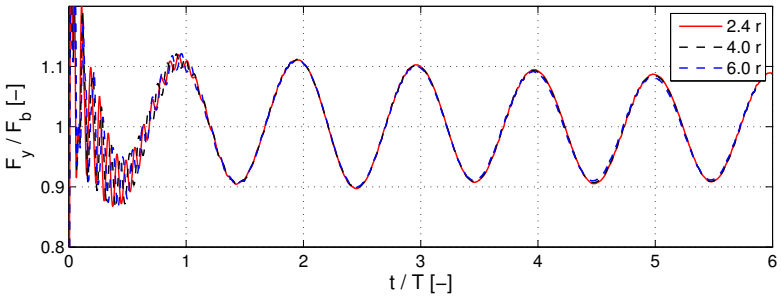

(b) $T = 2.0$ s

Figure 4.14: Grid refinement test: Force history for three grid configurations with different refinement length around the cylinder.

converged for the two finest grids.

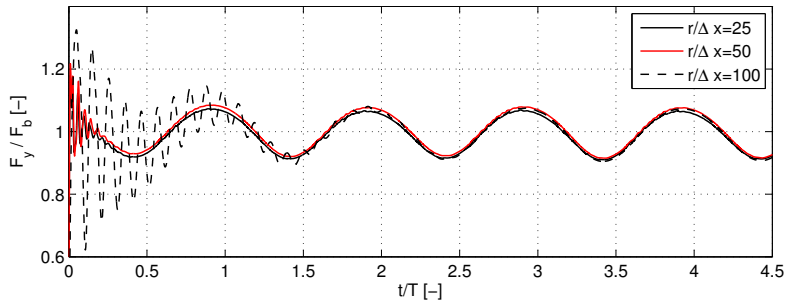

Figure 4.15: Cell size dependency test.

4.5.3 Sensitivity to water depth

The BEM results presented in Sec. 4.5.6 are obtained assuming infinite water depth. They are in good agreement with experiments performed by Vugts (1968), where the ratio between the water depth and the radius d/r_c was reported to be 12-15. In the CIP simulations, a finite domain must also be used. It is however beneficial to minimize the water depth to avoid large grids. The effect of the water depth is therefore studied. Simulations with water depths of $d = 2.0$ m, 3.0 m and 4.0 m, corresponding to $d/r_c = 4$, 6 and 8 are performed. The oscillation period is 2.0 s. The waves generated by the oscillating cylinder has the same period. Thus, the effect of the water depth on the waves can be examined. Deep water waves can be considered when $kh > \pi$ (Dean and Dalrymple, 1984). For the present oscillation period, $kh = 2, 3$ and 4 for the three water depths. Table 4.6 shows some details of the simulations.

Figure 4.16 shows the computed force for the three cases. In 2 m water depth, there is a discrepancy in the steady force, and also more oscillations in the transient phase. There is not much difference between the cases with 3 m and 4 m. It can be assumed that the bottom no longer influences the steady state force at $d = 3$ m. This corresponds well with the deep water condition discussed above. Most of the other oscillation periods tested in this case are shorter than 2.0 s (see Tab. 4.4), so it can be assumed that these results are not affected by the water depth. For the two longest periods however, some effect may be present.

Table 4.6: Grid details for water depth sensitivity tests

d/r_c	Osc. period	kh	Domain size	Grid size	Min. cell size
4.0	2.00 s	2.0	18×3 m	520×400	0.01 m
6.0	2.00 s	3.0	18×2 m	520×300	0.01 m
8.0	2.00 s	4.0	18×4 m	520×500	0.01 m

4.5.4 Sensitivity to heave amplitude

Simulations for all excitation periods are run with a heave amplitude $\eta_A = 0.05$ m, i.e. 10% of the cylinder radius. To check for nonlinearity, simulations are also run with $\eta_A = 0.1$ m for some periods. The differences in the force history when normalizing with the amplitude is insignificant. Figure 4.17 shows the normalized force history for $T = 1.12$ s and $T = 1.83$ s. The force history is filtered with a bandpass filter with cut-off frequencies $0.5T$ and $1.5T$, and normalized with η_A.

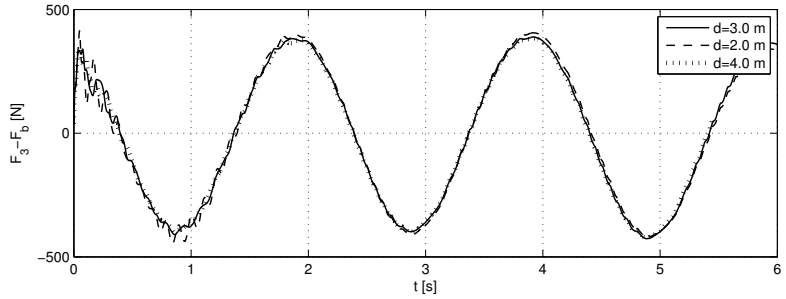

Figure 4.16: Water depth sensitivity: Vertical force computed for the cylinder in 2, 3 and 4 m water depth.

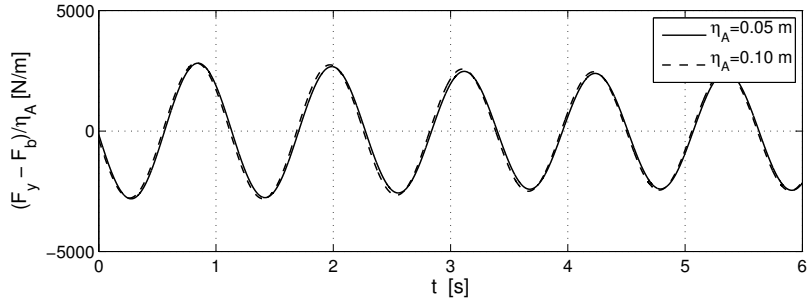

(a) $T = 1.12$ s

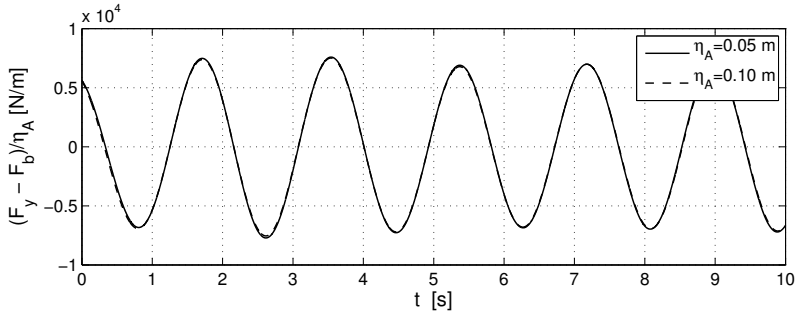

(b) $T = 1.83$ s

Figure 4.17: Nonlinearity of hydrodynamic forces: Normalized force history for two heave amplitudes. Transient oscillations are filtered out

4.5.5 Alternative body density scheme

In the simulations above, the body density function is used to update the material properties and the body boundary condition as described in Secs. 3.5 and 3.6. To

mitigate the transient oscillations in the force, an alternative approach following Mohd-Yusof (1997); Fadlun et al. (2000) is tested. The body density function is then only used to update the body boundary condition. The material properties are computed using ϕ_1 and ϕ_2 as if the body is not there. Thus, ϕ_3 overlap with the two other density functions. The artificial pressure inside the body is thus decided only by the body velocity. This gives a more benign behavior at the start of the simulations, as hydrostatic equilibrium is automatically achieved. Figure 4.18 shows the force history for $T = 1.5$ s for the two approaches. The alternative method is successful in reducing the transient oscillations. The difference in the steady state force is negligible. The alternative approach is further tested for impact forces in Sec. 4.6.3. The resulting added mass and damping coefficients presented below are obtained using the original scheme.

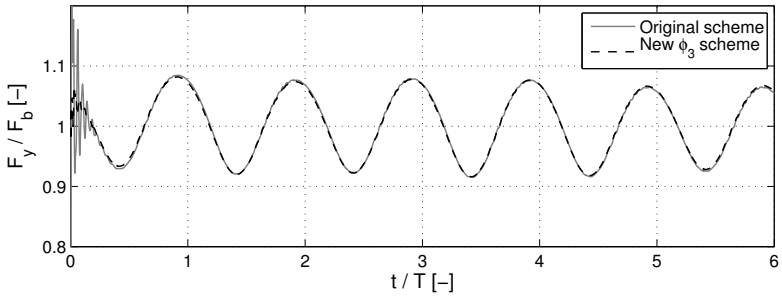

Figure 4.18: Vertical force computed using both original density function scheme and alternative approach.

4.5.6 CIP versus linear potential theory for different oscillation frequencies

The vertical force F_3 on the cylinder can be computed as in Eq. 4.30.

$$F_3(t) = -A_{33}\ddot{\eta}_3(t) - B_{33}\dot{\eta}_3(t) - C_{33}\eta_3(t) + F_\mathrm{b} \tag{4.30}$$

where A_{33} is the added mass coefficient in heave, B_{33} is the damping coefficient in heave and C_{33} is the stiffness coefficient. The derivative and double derivative of the heave motion, i.e. the heave velocity and acceleration is denoted $\dot{\eta}_3$ and $\ddot{\eta}_3(t)$, respectively. F_b is the static buoyancy force.

In the submerged case, an analytical frequency independent expression can be derived for the added mass A_{33} using potential theory, see App. B.4. The potential damping is zero. This is not the case for a cylinder with its axis in the free surface. Both added mass and damping must be found experimentally or computed using

e.g. a Boundary Element Method (BEM). Steady-state values of 2–D added mass and damping in heave for infinite water depth is given in e.g. Faltinsen (1990) and Baarholm (2001). The buoyancy force will also vary. In linear theory this is expressed as a varying stiffness force $-C_{33}\eta_3$ and a constant buoyancy force $F_\mathrm{b} = 1/2\rho g\pi r_c^2$. The stiffness coefficient is $C_{33} = 2\rho g r_c$.

Figures 4.19 and 4.20 show the added mass and damping coefficients estimated from the CIP simulations compared with BEM results presented in Baarholm (2001). The computed force history is run through a bandpass filter with cut-off at $0.5T$ and $1.5T$ to filter out the transient oscillations of the force. Other cut-off periods were tested also, to ensure that this did not affect the resulting steady state force. The added mass and damping is then computed from the filtered force history using Eq. 4.30. The damping coefficients agree well with the BEM computations, while the added mass is somewhat overestimated for many frequencies.

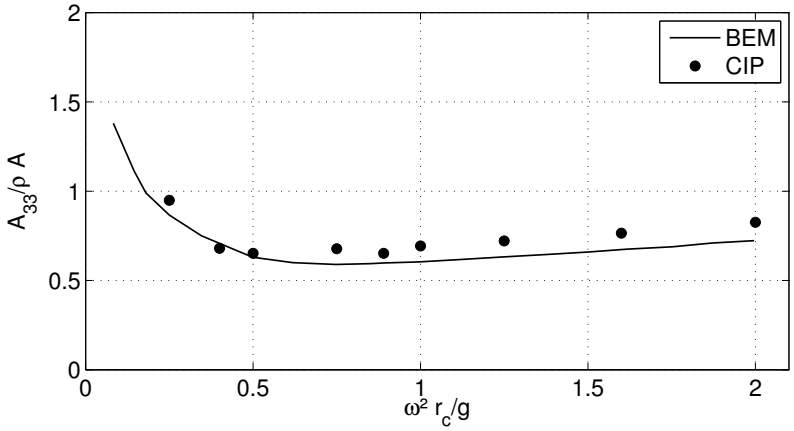

Figure 4.19: Added mass for different frequencies estimated using CIP and BEM.

One reason for the discrepancy of the added mass coefficient may be due to nonlinearities or inaccuracies of C_{33}. When estimating A_{33} from the CIP time series, $C_{33} = 2\rho g r_c$ is assumed. The oscillation amplitude used for the results in Figs. 4.19 and 4.20 is $\eta_A = 0.05$ m, i.e. 5 % of the cylinder diameter. It is thus assumed that a linear assumption is appropriate. This is confirmed by the simulations using $\eta_A = 0.1$ m. Simulations with the cylinder at rest is run to check the hydrostatic force, which is accurate within 1% of F_b for the base case grid.

The body boundary condition specified using Eq. 3.31 gives an uncertainty of one grid cell, as discussed in Sec. 3.6. But if this was the cause of the discrepancy between CIP and BEM results, the grid refinement test should show differences in the results.

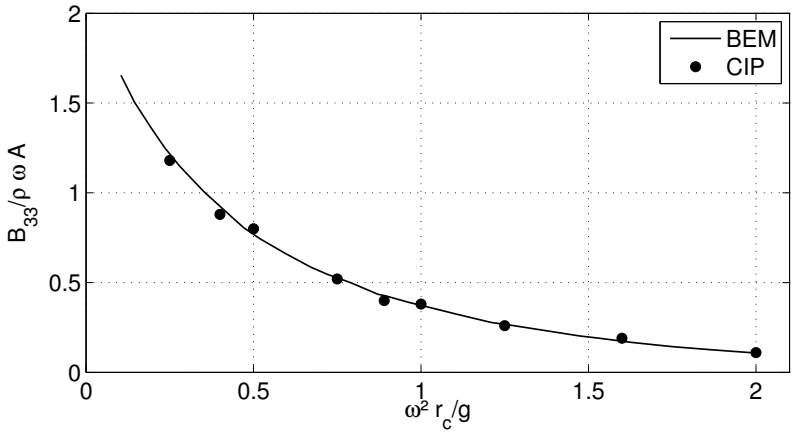

Figure 4.20: Damping coefficient for different frequencies estimated using CIP and BEM.

The discrepancy between the BEM and CIP may be due to the presence of a boundary layer in the CIP simulations, giving somewhat different flow around the cylinder than for the BEM computations. The two force computation methods in Sec. 3.7 did not give any significant differences for the CIP simulations. However, the modeling of viscous flow and air flow may give a difference in the pressure field compared to potential theory (Schlichting and Gersten, 2000).

The reason why the added mass is somewhat overestimated is thus unclear. Possible numerical inaccuracies in the CIP code are tested through the parameter studies, see Secs. 4.5.2– 4.5.5:

- Grid configurations and different grid refinement
- Hydrostatic checks
- Water depth dependency
- Sensitivity to amplitude of oscillation
- Alternative treatment of the ϕ_3/ϕ_1 interface
- Different filters and cut-off frequencies
- Different force computation methods

4.6 Water entry of a circular cylinder

4.6.1 Case set-up

A circular cylinder with radius $R = 0.0625$ m is forced into still water at constant speed. Different speeds are tested. The water depth is $d = 1.0$ m. In the CIP computations, a 25 m long tank is used. A sketch of the case is shown in Fig 4.21.

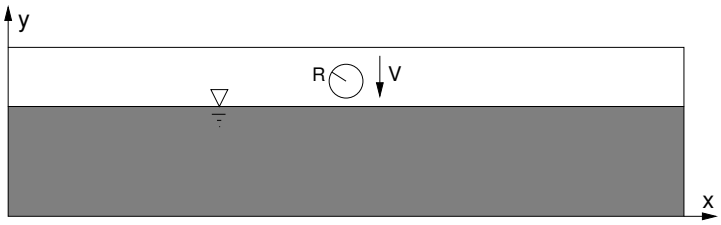

Figure 4.21: Case set-up for the water entry of a cylinder with constant velocity.

The slamming coefficient C_S on the cylinder is computed as:

$$C_S = \frac{F_y}{\frac{1}{2}\rho V^2 2R} \tag{4.31}$$

where F_y is the vertical force on the cylinder, V is the velocity and ρ is the mass density of water.

4.6.2 Temporal and spatial grid dependency

The effect of the time step size on C_S at the very early stages of the impact was also investigated in Zhu (2006). For the early stage of the impact, no convergence was achieved. This behavior is not found in the present computations, see Fig 4.22. Although the simulations are not completely converged, a value of 4.4-4.6 is found for C_S at the time of impact. In Zhu (2006), C_S varied between 5 and 20 at initial impact, while a value of approximately 4.5 was found when time averaging for Vt/R =0.0–0.02. Wagner's analytical solution (Wagner, 1932) gives $C_S = 2\pi$ at $t = 0$ s. Three different constant time steps are run, $\Delta t = T_c/1000$, $T_c/2000$ and $T_c/4000$, where $T_c = R/V$. The minimum grid sizes are used at the cylinder, with $\Delta x/R = \Delta y/R = 0.01$. The total number of cells is 582×765.

Grid dependency is tested for the current case by comparing the results using the grid above with two coarser grids, see Tab. 4.7. Adaptive time stepping is applied to optimize the time steps during these runs. Figure 4.23 shows the computed slamming coefficient for the three grids. As in Zhu (2006), the computed time trace of the slamming coefficient shows oscillations that are probably not physical but

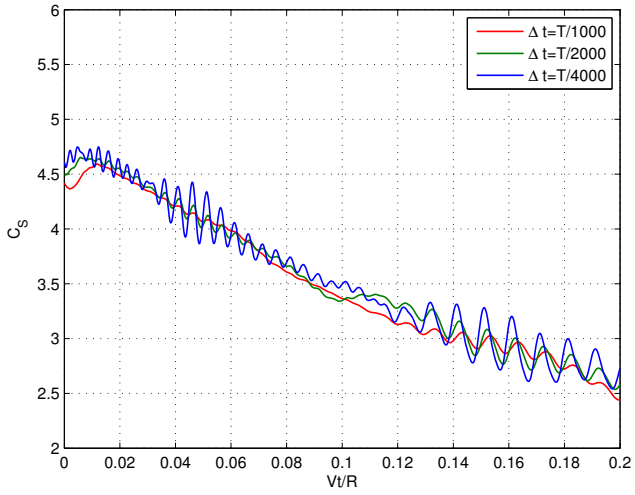

Figure 4.22: Effect of the time step size for the water entry case. Slamming coefficient C_S versus dimensionless submergence Vt/R.

related to numerical pressure oscillations. Smaller grid sizes or small time steps seem to increase the oscillations, as is also evident from Fig. 4.22. Due to the pronounced pressure oscillations and long computation time using Grid no. 1, the further simulations are performed with Grid no. 2.

Pressure oscillations is a known problem for projection methods. While the velocity field is computed with higher-order accuracy, the pressure field is only computed to first order, see also Sec. 3.4.1.

Table 4.7: Grid details for the grid dependency test.

Grid no.	Grid size	Min. $\Delta x/R$	Min. $\Delta y/R$
1	582×765	0.001	0.001
2	450×412	0.002	0.002
3	366×286	0.004	0.004

4.6.3 Alternative body density scheme

As discussed in Sec. 4.5.5, an alternative method for including the body is to let ϕ_3 govern the body velocity only. For the added mass computations, the transient oscillations in the force is reduced using this method. Pressure oscillations occur also in the present case. Therefore, the method is tested for the water entry case

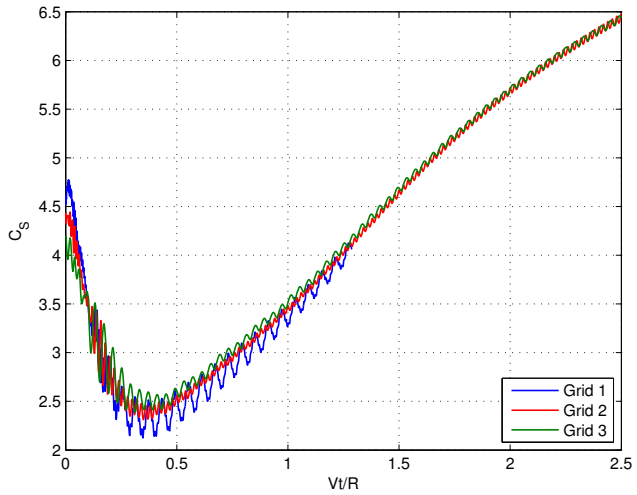

Figure 4.23: Spatial convergence test for the water entry case. Slamming coefficient versus non-dimensional submergence. Grid details for Grid 1-3 are given in Tab. 4.7.

with $V = 0.876$ m/s. Figure 4.24 shows C_S for the original and new scheme. The oscillations are reduced as expected. However, the C_S value at the initial impact phase is largely reduced. The method does not seem to capture the initial impact very well. Figure 4.25 shows the pressure field at $Vt/R = 0.2$. The pressure field is quite different for the two cases, as should be expected. The pressure field is less smooth for the original scheme compared to the alternative scheme due to the oscillations. Figure 4.26 shows snapshots of ϕ_1 for different time instances for the two methods at the early stages of the impact. The alternative method does not give any spray during impact, which seems unphysical. It can be concluded that the alternative scheme may be suited for cases with slow loading processes, and may reduce pressure oscillations as shown in Sec. 4.5.5, but is not suited for impact processes. The method is therefore not considered suitable for the wave impact simulations.

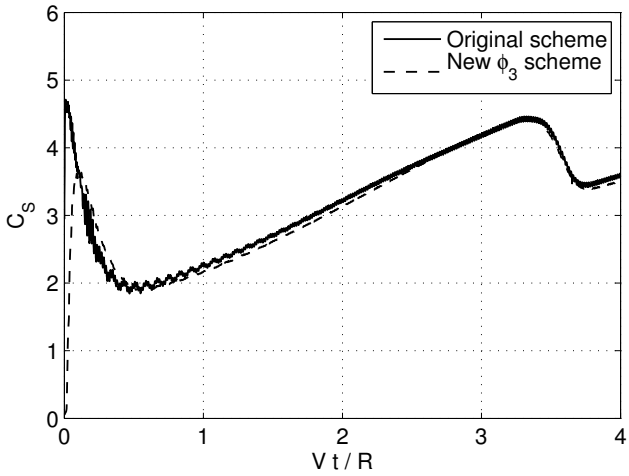

Figure 4.24: Computed slamming coefficient using different schemes for the body boundary and material properties.

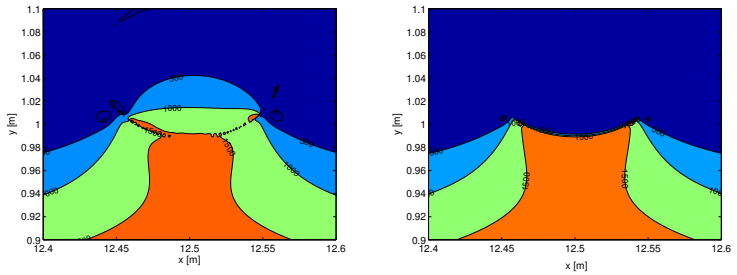

(a) Original scheme (b) Alternative scheme

Figure 4.25: Pressure field at $Vt/R = 0.20$ for the two body density function schemes.

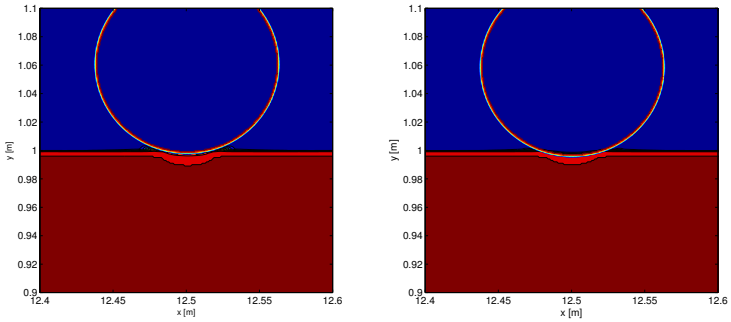

(a) Original, $Vt/R = 0.04$ (b) Alternative, $Vt/R = 0.07$

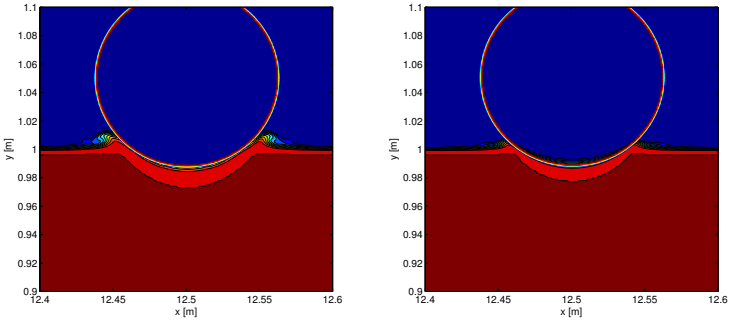

(c) Original, $Vt/R = 0.20$ (d) Alternative, $Vt/R = 0.20$

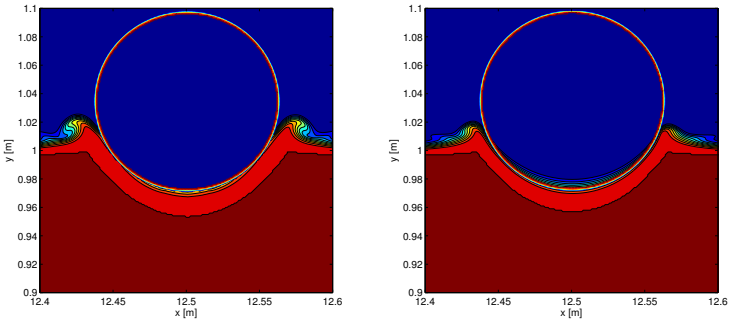

(e) Original, $Vt/R = 0.45$ (f) Alternative, $Vt/R = 0.45$

Figure 4.26: Water density function contours for the two body density function schemes.

4.6.4 Comparison with previous CIP simulations and model tests

Figure 4.27 shows a comparison of the slamming coefficient computed using the present CIP method with the CIP method of Zhu (2006) and experiments by Miao (1989) for $V = 0.638$ m/s.

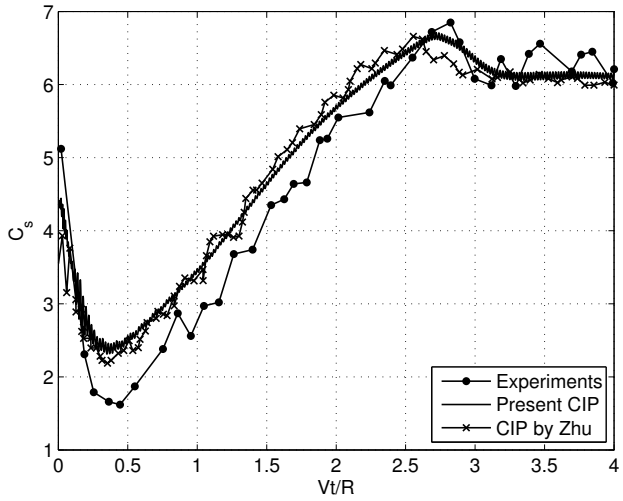

Figure 4.27: Comparison of computed slamming coefficient with other CIP computation and experiments

The present CIP method is compared with experimental results for more impact velocities in Fig. 4.28. The reference data are taken from Zhu (2006, Figs. 4.5–4.9). The two CIP methods seem to agree as expected, and are also in fair agreement with the experiments. However, the CIP methods do not model the minimum force well. Some of the discrepancy may be due to experimental error sources, as discussed in Zhu (2006). The possible error sources are natural frequencies of the test rig, hydroelastic effects, air cavity oscillations, buoyancy force of the stiffened end plates, 3D flow effects and cross flow and necklace vortices at the edges of the end plates.

4.7 Summary of findings and results from the benchmark tests

In this chapter, several benchmark tests are presented where the present CIP code is compared with other results. Parameter studies are performed for different parts of the code. The following results are found:

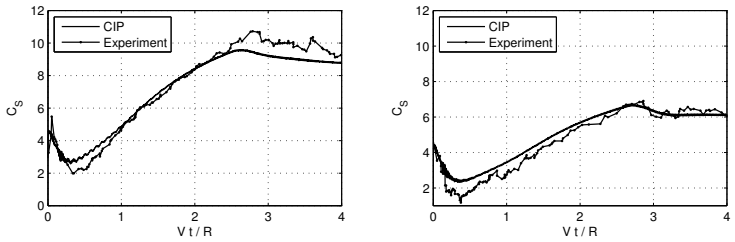

(a) $V = 0.5124$ m/s

(b) $V = 0.639$ m/s

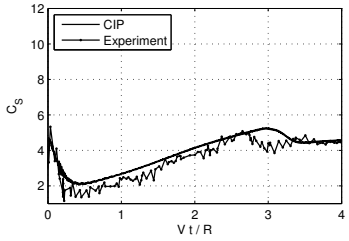

(c) $V = 0.760$ m/s

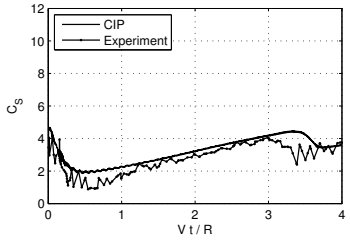

(d) $V = 0.876$ m/s

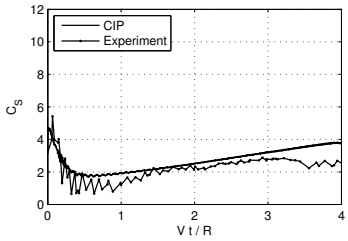

(e) $V = 1.024$ m/s

Figure 4.28: Comparison of computed slamming coefficient with experiments.

- The mass and energy conservation is sufficient for the intended application.
- A relatively fine grid is necessary to ensure energy conservation.
- The adaptive time stepping scheme gives a more effective and more robust code.
- Grid refinement using variable cell sizes at different parts of the domain gives a more effective code. Care must however be taken so that the grid stretching

does not give undesirable effects such as increased surface layer growth.

- Given that the grid cells are sufficiently small and the grid size changes are continuous, the simulation results are generally not very sensitive to different grid configurations.
- The tangent surface enhancement is far more successful in reducing surface layer growth than the linear surface enhancement. The tangent surface enhancement is computationally more costly.
- The added mass force is somewhat overpredicted by the CIP code compared to BEM results for a circular cylinder in the free surface, while the damping seems to agree well.
- First-order pressure computations may give small oscillations in the force history. The oscillations increase with decreasing cell size.
- Pressure oscillations may be mitigated by an alternative density function approach, but this approach is not suited for impact simulations.
- Impact force is computed with similar accuracy as a previous CIP code.

The improvements and experience gained by studying the presented benchmark tests are used in the further work with the numerical wave tank and wave impact simulations. New challenges with the code are also found for these applications and are thus discussed in the next chapters.

Chapter 5

The numerical wave tank

5.1 Introduction

Being able to generate propagating waves with the correct kinematics is an important part of the wave impact model. Since only the top of the wave crest hits the deck box, it is expected that even small differences in the properties of the incoming wave may have significant effects on the impact force. It is therefore important to compare the simulated wave elevation and kinematics with physical water waves.

Codes dealing with wave structure interaction often model the wave by specifying the wave kinematics directly. This reduces domain size and simulation time. In this work, an approach using a numerical wave tank (NWT) is chosen. The computational domain models a wave tank with wavemaker and beach. This is computationally more costly, but enables more direct comparison with experiments performed in physical wave tanks. The waves are generated in a similar way, which may give more correct wave kinematics as well. Irregular waves can also be modeled using this approach. A general description of the present NWT model is given in Sec. 5.2.

Three tanks are considered in the present work. One is set up to simulate the narrow wave flume at the Coastal- and Harbor Laboratory at NTNU. Simulations compared with wave calibration runs in this flume are presented in Sec. 5.3. The present work on this tank is not extensive, but is included since the experience and findings are used in the further work. The wavemaker stroke was measured in these experiments. Direct comparison of the physical and numerical wavemaker is thus performed. The second wave tank is set up to model the glass wave flume at the Department of Marine Hydrodynamics, NTNU. The 2-D wave impact experiments discussed in Sec. 6.2 are performed in this flume. In this chapter, the undisturbed

waves from the same experiment are studied. The set-up details and simulations performed for the glass flume are presented in Sec. 5.4. The wave elevation and the velocity field underneath the wave crest is compared with fifth order Stokes theory. Surface layer growth is discussed, comparing the THINC surface capturing method with the tangent surface enhancement algorithm. The third wave tank is set up to model the small towing tank at MARINTEK. In this tank, 3D and 2D wave impact experiments were performed, see Sec. 6.5. The measured undisturbed waves are compared with simulated waves in Sec. 5.5. The dimensions of the three wave tanks are given in Tab. 5.1

Table 5.1: Dimensions of the three wave tanks modeled in the present work: Coastal- and Harbor Laboratory (CHL), Flume at Dept. of of Marine Hydrodynamics (DMH) and Small towing tank at MARINTEK (STM)

Tank	Tank length L [m]	Tank breadth B [m]	Water depth d [m]
CHL	26.5	0.60	0.543
DMH	13.5	0.60	1.000
STM	25.0	2.80	1.000

5.2 General description of the numerical tank model

A numerical wave tank consists of a computational domain that is very long compared to its height. This gives some challenges for the grid configuration. A variable grid is needed to obtain a grid with reasonable size. In one end of the domain, a wave generating device is modeled, and in the other end a damping zone, often referred to as a numerical beach, is implemented. Figure 5.1 shows a sketch of a numerical wave tank.

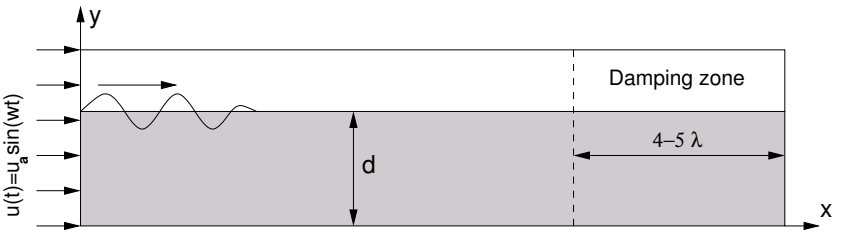

Figure 5.1: Sketch of a numerical wave tank.

5.2.1 Wave generation

There are different ways of generating waves in a numerical wave tank. In the early phases of this work, a solid body was used, mimicking a real piston, flap or wedge. This causes undesirable initial surface layer growth. It also gives increased CPU-time. Another method is to start the simulation with a prescribed velocity field corresponding to some theoretical wave kinematics, using either linear wave theory or some higher order wave theory, much in the same way as is done for the benchmark test described in Sec. 4.3. This method has not been attempted here. Instead, a simplified wavemaker is modeled by prescribing a fluid velocity in the cells at the left wall. The fluid velocity corresponds to the motion of a physical wavemaker. The waves are thus generated from initially calm water.

Linear steady-state wavemaker theory, as described in e.g. Dean and Dalrymple (1984) is used as a basis. The necessary wavemaker stroke S_0 for a desired wave height H is given as Eqs. 5.1 and 5.2 for piston and flap type wavemakers, respectively.

$$\frac{H}{S_0} = \frac{2\left(\cosh 2kd - 1\right)}{\sinh 2kd + 2kd} \tag{5.1}$$

$$\frac{H}{S_0} = 4\left(\frac{\sinh kd}{kd}\right)\frac{kd\sinh kd - \cosh kd + 1}{\sinh 2kd + 2kd} \tag{5.2}$$

where k is the wave number of the progressing wave and d is the water depth. When solving the boundary value problem for the wavemaker, the total velocity potential Φ is written as:

$$\Phi = A_p \cosh k(d+y)\sin\left(kx - \omega t\right) + \sum_{n=1}^{\infty} C_{\mathrm{n}} e^{-k_s(n)x}\cos\left[k_s(n)\left(d+y\right)\right] \tag{5.3}$$

where A_p and C_{n} are determined from the boundary conditions. The first term represents the progressive wave, while the second series of terms are evanescent modes that decay exponentially away from the wavemaker. $k_s(\mathrm{n})$, $\mathrm{n} = 1, 2, 3\ldots$ are the wave numbers for the standing waves. The dispersion relation between the wave number k and the circular wave frequency ω for the progressive waves are given in Eq. 5.4, while Eq. 5.5 relate the wave numbers for the evanescent modes to the frequency of the wavemaker. Both are found by substituting the assumed solution above into the combined linear free surface condition $\partial\Phi/\partial y - \omega^2\Phi/g = 0$ for $z = 0$.

$$\omega^2 = gk\tanh kd \tag{5.4}$$

$$\omega^2 = -gk_s \tan k_s d \tag{5.5}$$

When a structure is to be tested in steady state waves, the presence of the evanescent modes affects the position of the model in the tank. The structure needs to be placed far enough away from the wavemaker to ensure that the disturbance from the wavemaker does not affect the results. In experiments, it is common to place the structure in the middle of the tank, well away from the wavemaker. In the numerical simulations, it is however beneficial to place the structure as close to the wavemaker as possible to minimize computational time. An estimate of the minimum distance can be computed by considering the first term in the series in Eq. 5.3, which has the slowest decay. The wave amplitude decays with $e^{-k_s(1)x}$. For the wave conditions discussed below, the amplitude of the standing wave is reduced with a factor of $10^{-4} - 10^{-6}$ at $x = 2\lambda$, depending on water depth and wave period. This is considered sufficient to neglect any evanescent effects from the wavemaker.

A linear or parabolic ramp-up of the wavemaker stroke is performed in the present simulations. The ramp-up of the wavemaker motion in physical wave tanks is often linear. A further discussion on the ramp-up of the wavemaker motion is given in Secs. 5.3 and 5.5.

5.2.2 The numerical beach

To avoid disturbance from waves reaching the end of the tank and reflecting back, a damping zone is included in the numerical model. A simple damping force is added to the first non–advection step, see Eq. 3.7 (Hu and Kashiwagi, 2004). The damping force, which is only used for the y–direction, is given in the following form:

$$f_d = \alpha \left(\frac{x - x^s}{x^s - x^e} \right)^m \left(1 - \left| \frac{y - y^f}{y^t - y^b} \right| \right)^n v \tag{5.6}$$

where x^s and x^e denotes the start and end of the damping zone in the horizontal direction, y^t and y^b is the top and bottom of the damping zone. y^f is the average free–surface position. The constants used are $\alpha = 0.5/\Delta t$, $m = 4$ and $n = 1$.

Experience from earlier studies show that the damping zone should have a length of four wave lengths or more to be effective. Also, it is important that the horizontal dimension of the grid cells are relatively large, and increasing, in this region. The grid stretching works as a damping devise in the horizontal direction. In the vertical direction, the entire height of the wave tank is included in the damping zone.

When a body is present in the numerical wave tank, waves are also reflected by the body back toward the wavemaker. Numerical one-way damping devises are a possible solution to this problem, but is not attempted in this work. The wave impact simulations are not run long enough after the first impact for this effect to pose a major problem, see Sec. 6.3.5.

5.3 Modeling of the flume at the Coastal- and Harbor Laboratory

Wave-body interaction experiments in the Coastal- and Harbor Laboratory at NTNU was reported in Kristiansen and Faltinsen (2008). The wave tank is 26.5 m long and the water depth d was 0.543 m during the experiment. Regular waves were generated using a piston wavemaker. In this section, the wave calibration tests from these experiments are compared with CIP simulations.

5.3.1 Case set-up

The numerical wave tank is set up with the same dimensions as the physical flume. The CIP simulations are performed with adaptive time stepping, a variable grid and the tangent surface enhancement algorithm for the density function ϕ_1. The grid has 450×364 cells, where the minimum cell sizes are $\Delta x = 0.005$ m and $\Delta y = 0.0005$ m. The smallest cell size is used close to the wavemaker ($x < 0.1$ m) in the x-direction and in the vertical refinement zone (0.527 m $< y <$ 0.559 m) in the y-direction. The tank length L is shortened to 18 m to reduce the total number of cells and thus CPU time. This is not assumed to have any effect on the generated waves. The tested wave length is relatively short; $L/\lambda = 12$. A damping zone is implemented at the end of the tank. The length of the zone is 5 λ. In this zone, a damping force is added in the y-direction as described in Sec. 5.2.2. To ensure damping in the horizontal direction, the horizontal cell size is gradually increased to a maximum of 0.9 λ at the end of the tank. An overview of the grid configuration is given in Fig. 5.2 and Tab. 5.2.

The wavemaker used in the experiments is of the piston type. In the numerical wave tank, a prescribed horizontal velocity is input in the boundary cells at the left hand wall. The wavemaker stroke estimated using linear wavemaker theory does not yield high enough wave amplitudes for neither the physical nor the numerical wave tank. The amplitude of the horizontal velocity input to the numerical model is therefore estimated from the measured stroke of the physical wavemaker. Two procedures are used. In the first method, the velocity amplitude is estimated using the mean measured stroke of the piston motion from the experiments. A linear

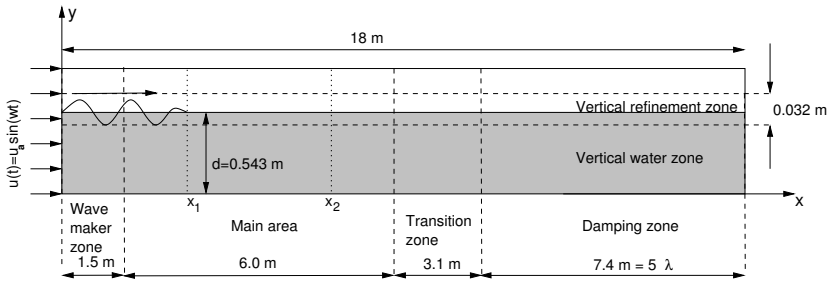

Figure 5.2: Schematic overview of the Coastal- and Harbor NWT.

Table 5.2: Specification of the grid configuration used for the Coastal- and Harbor NWT.

	Zone length [m]	Cell size [m]
Wavemaker zone	1.500	0.0050-0.0150
Main area	6.000	0.0150-0.0350
Transition zone	3.100	0.0350-0.1225
Damping zone	7.400	0.1225-1.3475
Vertical refinement zone	0.032	0.0005
Vertical water zone	0.527	0.0020

up-ramping of the velocity is then used from $t = 0 - 5$ s. The velocity u_b at the left hand boundary cells is thus described as:

$$u_b = \begin{cases} \frac{1}{2}\frac{t}{5} S_0 \omega \sin(\omega t) & \text{for } t \leq 5.0\text{s} \\ \\ \frac{1}{2} S_0 \omega \sin(\omega t) & \text{for } t > 5.0\text{s} \end{cases} \tag{5.7}$$

This method is denoted "Constant input" hereafter. For the other method, the measured piston motion is used directly. The measured motion is first filtered to remove spikes in the time series and then differentiated numerically to obtain the velocity of the wavemaker piston. This time series is then input as the horizontal velocity at the left hand boundary cells. The method is denoted "Signal input" below.

5.3.2 Wave cases

Two calibration runs from the experiments are simulated, both with a wave period of $T = 0.981$ s. The experimentally obtained wave heights for the two tests were $H_1 = 0.029$ m and $H_2 = 0.048$ m, respectively. Table 5.3 lists the wave conditions and the corresponding wavemaker stroke.

Table 5.3: Wave cases and wavemaker details for the wave calibration runs at the Coastal- and Harbor Laboratory narrow wave flume

			Case 1	Case 2
Wave period	T	[s]	0.9811	0.9811
Target wave height	H	[m]	0.0290	0.0480
Wave steepness	$\zeta_A k$	[-]	0.0626	0.1019
Measured mean stroke	S_0	[m]	0.0173	0.0302
Linear theory stroke	S_0^{lin}	[m]	0.0161	0.0267
Wave probe position	x_2	[m]	6.4800	6.4800

The simulated and measured wave elevation can be compared at $x_2 = 6.48$ m ($= 4.4\lambda$) where the first wave probe was placed during experiments. Figure 5.3 shows the measured wave together with the two CIP simulations for H_1. There is a phase difference between the measured and simulated waves. This is probably due the modeling of the wavemaker in the CIP code as an oscillating velocity at a constant x-position, whereas the real piston oscillates physically in the tank. The Constant input gives more stable amplitudes than the Signal input, as can be expected. The discrepancy is however small. The greatest difference between the Signal input and the Constant input is seen in the up-ramping of the waves. The up-ramping is faster and agrees better with the measured wave elevation for the Signal input method than for the Constant input. This does not seem to have any effect on the steady state waves after the ramp-up is completed. The wave height of the simulated wave is somewhat less than the measured wave. The crest height is close to the measured crest height, but the trough is about 0.85 of the measured trough. For the test case with greater steepness, the same effects apply.

When comparing simulated wave elevation at x_2 with simulations at a position closer to the wavemaker ($x_1 = 1.47$ m, see Fig. 5.2), it is clear that the simulated wave height decreases as the wave propagates (Vestbøstad and Faltinsen, 2007a). It is assumed that the amplitude decay is partly due to grid stretching used in the main area of the numerical wave tank. The horizontal grid size is increased from $\lambda/100$ to $\lambda/42$ for $1.5 < x < 7.5$ m.

5.3.3 Discussion on the surface layer

The water volume change and surface layer growth is monitored during the simulations. The volume change is small; after 30 s the largest volume change for the simulations above is 0.4 %.

Figure 5.4 shows the surface layer width δy_L defined as $0.05 < \phi_1 < 0.95$ as a function of time at x_1 and x_2 for the lowest wave height. The surface layer

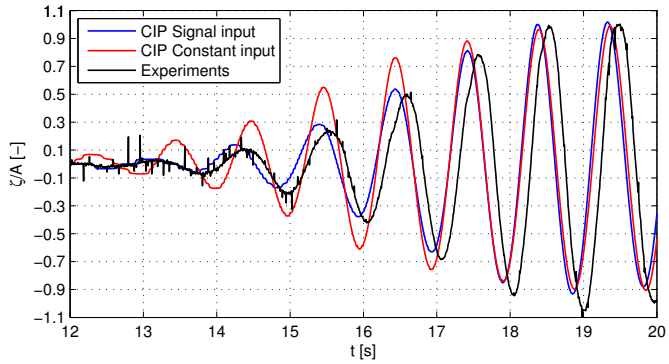

(a) , $t = 12 - 20$ s.

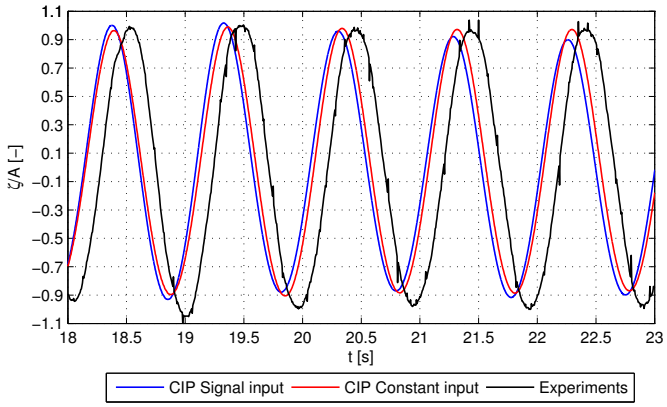

(b) $t = 18 - 23$ s

Figure 5.3: Simulated and measured waves in the Coastal and Harbor Laboratory; H_1 at $x_2 = 4.4\lambda$.

increases in time. At x_1, the wave amplitudes are stable at least 13 wave length after the up-ramping is completed. At this time, the surface layer width has become $0.3H - 0.4H$. At x_2, the surface layer starts to increase when the waves reach the position at $t = 10 - 12$ s. When examining the surface layer growth in time, it is seen that when the layer comes into the vertical transition zone where grid stretching occur, the surface layer growth increases more rapidly than in the vertical refinement zone. For the present NWT, this happens in wave troughs, i.e.

the vertical refinement zone turns out to be too narrow in this case (see Fig. 5.2). Increasing the zone with minimum Δy may mitigate this effect.

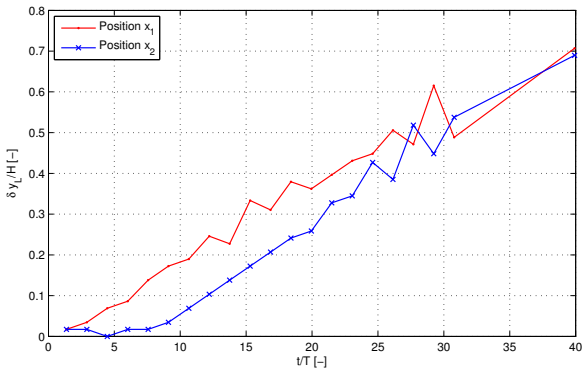

Figure 5.4: Surface layer height δy_L at positions $x_1 = 1.47$ m and $x_2 = 6.48$ m as a function of time.

5.3.4 Lessons learned

Further work could obviously have been performed to improve the model presented above. However, the lessons learned are rather transferred to the work on the glass wave flume at Department of Marine Hydrodynamics, presented below. The findings can be summarized as:

- Constant wavemaker amplitude gives the most stable wave amplitudes. Linear wavemaker theory underestimates the necessary stroke for obtaining the target wave height. The numerical and physical wavemaker seem to be fair in agreement. The numerical wavemaker stroke can thus be calibrated from experiments to obtain the target wave height.

- The up-ramping of the waves in the numerical wave tank is in fair agreement with the up-ramping of the waves for the physical wave tank when Signal input is used, except for the small phase difference.

- Care must be taken when setting up the grid configuration. The refinement in the free surface zone must be sufficiently wide. Stretching of the grid in the x-direction may cause amplitude decay. From the wavemaker to the area of interest, the grid should be constant.

- The surface layer growth becomes large for waves propagating many wave lengths down the tank, even when using the tangent surface enhancement algorithm. The area of interest should be kept as close to the wavemaker as possible, and a more efficient surface capturing method should be considered.

5.4 Modeling of the flume at the Department of Marine Hydrodynamics

Deck impact experiments were performed in the glass flume at the Department of Marine Hydrodynamics by Baarholm (2001). The wave flume is 13.5 m long, 0.6 m wide and 1.3 m high. The water depth was 1.0 m during the experiments. The wavemaker is of the flap type, hinged 0.1 m above the tank bottom. A parabolic arc profile beach is fitted at the opposite end of the tank. The experimental set-up is further described in Sec. 6.2.

In this section, the numerical model of the wave flume is described, and simulated waves are compared with both 5th order Stokes waves and measured wave elevation from wave calibration runs.

5.4.1 Case set-up

The simulations are set up to 'model the model', using the same dimensions as in the experiments described above. The wavemaker is modeled by prescribing a sinusoidal horizontal velocity at the boundary cells at the left end of the tank. At the start of the simulations, the signal from the wavemaker is ramped up as for the Constant input described in Sec. 5.3. The wavemaker stroke in the experiments was not measured, so the measured stroke from the Coastal- and Harbor Laboratory is used to estimate the required stroke for the present tank. Some calibration is necessary for some of the wave cases.

A flap wavemaker is installed in the flume. A flap wavemaker can be modeled in the NWT by adjusting the velocity field in the boundary cells. In physical wave tanks, a piston wavemaker is often used for shallow water waves, while a flap is more commonly used for generating deep water waves. A piston wavemaker may cause parasitic waves in deep water (Hughes, 1993). In addition, it is more power consuming to use a piston than a flap for deep water waves. The wave conditions considered in the present and previous case are in an intermediate water depth range where both flap and piston wavemaker can be used. In the physical tanks, it is then a question of power consumption (Dean and Dalrymple, 1984). This is of course not a problem in the numerical wave tank. Since the measured stroke is

available from the piston wavemaker of the Coastal- and Harbor Laboratory, the glass wave flume is also modeled using a piston wavemaker. At the right end of the tank, a damping zone is used to damp out the waves and thus avoid reflections.

The wave cases run in the numerical wave tank are given in Tab. 5.4 together with the wavemaker stroke used in the NWT. The wave steepness $k\zeta_A$ for the 10 wave cases is given in Tab. 5.5.

Table 5.4: Wavemaker stroke S_0 [m] used in the Dept. of Marine Hydrodynamics NWT for all wave cases

Wave amplitude	Wave period T [s]		
ζ_A [m]	1.00	1.11	1.25
0.05	0.0321	0.0298	0.0298
0.06	0.0398	0.0371	0.0371
0.07	0.0504	0.0432	0.0432
0.08	-	0.0494	-

Table 5.5: Wave steepness $k\zeta_A$ [-] for all wave cases run in the Dept. of Marine Hydrodynamics flume.

Wave amplitude	Wave period T [s]		
ζ_A [m]	1.00	1.11	1.25
0.05	0.194	0.150	0.128
0.06	0.229	0.190	0.153
0.07	0.263	0.218	0.177
0.08	-	0.246	-

5.4.2 Grid configuration and grid dependency

The cell sizes of the present numerical wave tank is governed by the lowest wave amplitude and the deck size used in the impact experiments (see Sec. 6.2). Two different grids are tested, where the deck length is divided into 45 and 90 cells, respectively. For the shortest wavelength, this corresponds to a discretization of 116 and 231 cells per wave length. Both grids are thus more refined than for the previous NWT. The vertical cell size is set to 25 cells per wave amplitude for the lowest wave. The total number of cells are 460×434 and 595×434. It is thus only the horizontal cell size that is varied for the two grids. Details of the grid configuration are shown in Tab. 5.6 and Fig. 5.5.

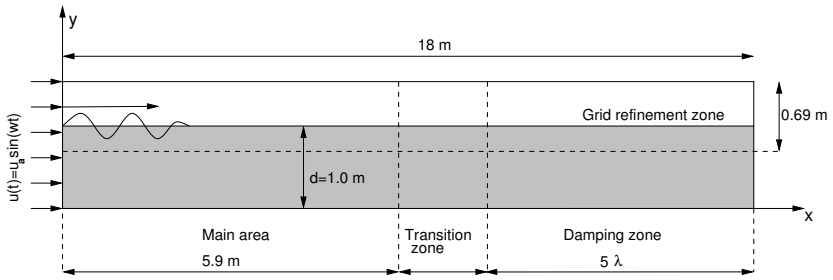

Figure 5.5: Schematic overview of the numerical wave tank modeling the glass flume at the Department of Marine Hydrodynamics.

Table 5.6: Specification of the grid in the different wave tank zones. In the zones where the grid size varies, the end size is given. The start size is shown in the previous zone

	Grid 1		Grid 2	
	Zone length [m]	Cell size [m]	Zone length [m]	Cell size [m]
Wavemaker zone	2.80	0.014	2.80	0.014
Main area	3.08	0.014	3.08	0.007
Transition zone	2.00	0.186	2.56	0.186
Damping zone	10.12	0.826	10.12	0.826
Vertical refinement zone	0.69	0.002	0.69	0.002
Vertical water zone	0.69	0.010	0.69	0.010

The numerical tank is somewhat longer than the physical tank, this is to make sure that the numerical beach provides enough damping. The seiching frequency will thus be different for the physical and the numerical tank. In the numerical tank, the damping zone seems to eliminate seiching. Very little seiching was reported for the experiments (Baarholm, 2001). The vertical refinement zone stretches from twice the amplitude below the mean waterline to the tank roof. The vertical refinement zone is extended to the tank roof to prepare for impact simulations.

The grid dependency tests are performed for a wave with wave period $T = 1.11$ s, and wave amplitudes $\zeta_A = 0.05$ m and 0.06 m. Negligible difference is found in the wave elevation for the two grids. The effect of grid refinement at the wavemaker is also tested, but did not have any effect on the simulated waves either. The velocity profiles for $\zeta_A = 0.06$ m are studied for the two grids. Steady state waves are reached at $x = 2\lambda = 3.9$ m for $t = 9T$. The velocities at the wave crest, wave trough, zero up-crossing and down-crossing are plotted in Fig. 5.6.

Surface layer growth for the same wave at $t = 5T$ and $10T$ are shown in

Fig. 5.7. The differences between the two grids are small. The coarsest grid without grid refinement at the wavemaker (denoted Grid 1 in Tab. 5.6) is thus used in the further work on wave generation. The two grid configurations are further discussed in Sec. 6.3.1.

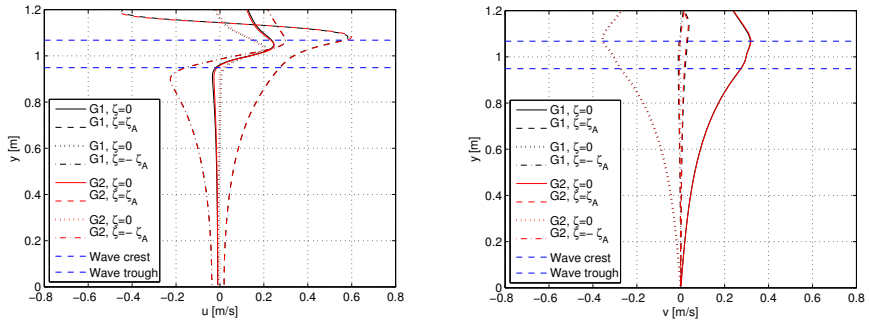

(a) Horizontal velocity (b) Vertical velocity

Figure 5.6: Grid dependency test: Velocity profiles at $x = 2\lambda$ m, $T = 1.11$s. G1 and G2 denoted the two grids in Tab. 5.6. $\zeta = \zeta_A$, $\zeta = -\zeta_A$ and $\zeta = 0$, denotes that the velocity profiles are plotted at the wave crest, wave trough and mean water line, respectively.

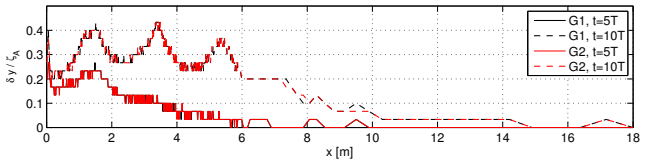

Figure 5.7: Grid configuration test: Surface layer growth at $t = 5T$ and $t = 10T$. The surface layer thickness δy is made non-dimensional using the wave amplitude ζ_A. G1 and G2 denotes the two grids in Tab. 5.6.

The surface layer thickness can also be compared with the findings in the previous section. The present NWT has finer grid and wider grid refinement zone than the previous. Still, the surface layer growth is quite comparable for the two tanks, see Fig. 5.4. Another surface capturing method is therefore considered. A comparison between the present tangent surface enhancement and the THINC method is presented in the next section.

5.4.3 Sensitivity to the surface capturing method

Simulations using both the tangent surface enhancement and THINC surface capturing method (see Sec. 3.5.3) are performed for waves with wave period $T = 1.11$ s. Figure 5.8 shows the wave elevation at $x = 2\lambda$ for three wave steepnesses. The wave elevation is practically identical for the two methods. The surface layer thickness is plotted in Fig. 5.9. In the main NWT area, the surface layer increases with time when using the tangent enhancement method, as discussed above. After $t = 10T$, the surface layer thickness has increased to $0.4\zeta_A$. For the THINC method, δy remains within 1-2 cells in the main wave tank area.

Figure 5.10 shows the velocity profiles at $x = 2\lambda$. The maximum velocities are plotted for $t = 9T$. Note that the velocity profiles includes both air and water flow. Also note that the maximum vertical velocity occurs as the wave passes the mean water level. The difference in the surface layer thickness clearly affects the velocity profiles in the wave zone. The wave kinematics is further discussed in the next section. It should be noted that the THINC method is computationally more costly than the tangent enhancement method.

5.4.4 Comparison with Stokes 5th order wave theory

The simulated wave elevation can be compared with measured wave elevation time series from the wave flume tests as done in Sec. 5.3, but measured wave kinematics from experiments are less available. The computed wave elevation and kinematics are therefore first compared with 5th order Stokes theory as described by Fenton (2001). According to Gudmestad (1993), the kinematics in the wave crest predicted by 5th order Stokes theory fit well with measured wave crest kinematics for regular waves.

Figures 5.11–5.13 show the simulated wave elevation at $x = 2\lambda$ compared with Stokes 5th order theory. The wave cases given in Tab. 5.4 are used. For all the cases, the wave period and asymmetric crest-to-trough ratio agree well. The CIP wave is slightly fuller than the Stokes wave, as it is not completely symmetric about a vertical axis through the crest, such as the Stokes wave is. As the wave steepness increases, the CIP code underestimates the troughs somewhat.

Figure 5.14 shows the computed horizontal and vertical velocity profiles two wave lengths from the wavemaker using 5th order Stokes' theory and the CIP method. Results using both tangent enhancement and the THINC surface capturing method is shown. For the tangent enhancement method, the magnitude of the computed horizontal velocity is greater than the theoretical prediction in the wave crest. However, since the surface layer has a finite thickness in the simulations, the mass density of the water is somewhat reduced in the crest. It is therefore

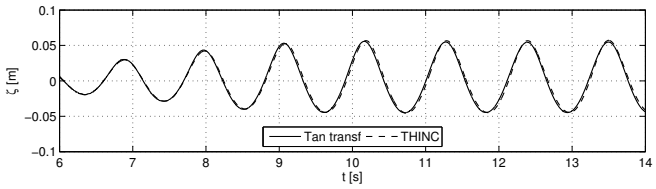

(a) $\zeta_a = 0.05$ m

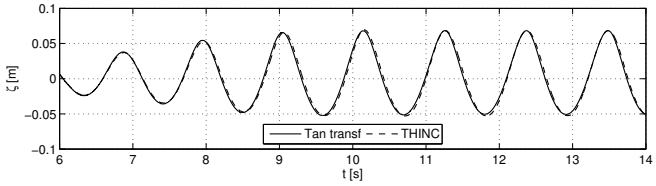

(b) $\zeta_a = 0.06$ m

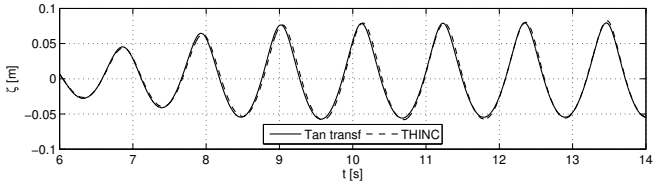

(c) $\zeta_a = 0.07$ m

Figure 5.8: Tangent enhancement versus THINC surface capturing method: Wave elevation for $T = 1.11$ s at $x = 2\lambda$, wave steepness $k\zeta_A$ is 0.15, 0.19 and 0.22, respectively.

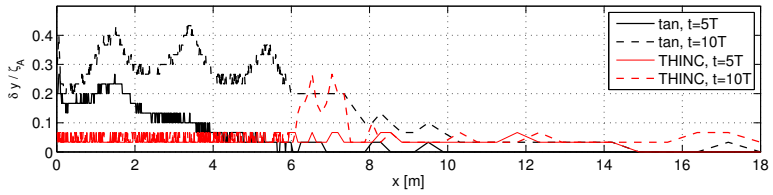

Figure 5.9: Tangent enhancement versus THINC surface capturing method: Surface layer growth at $t = 5T$ and $t = 10T$.

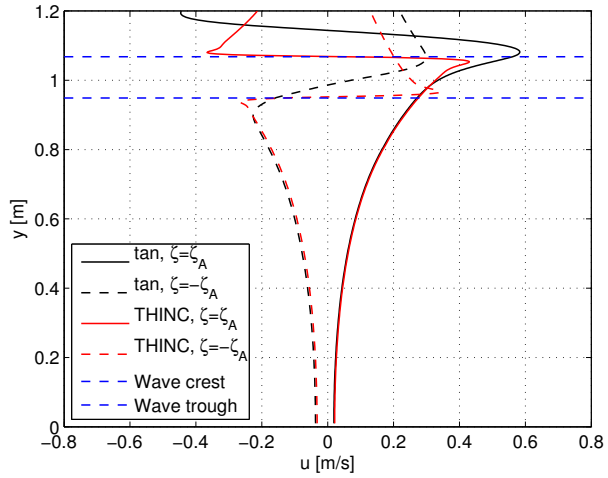

(a) Horizontal velocity

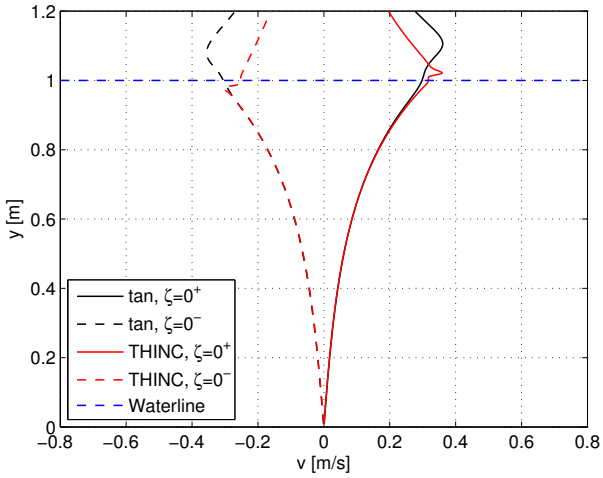

(b) Vertical velocity

Figure 5.10: Tangent enhancement versus THINC surface capturing method: Velocity profiles at $x = 2\lambda$, $T = 1.11$s. $\zeta = \zeta_A$, $\zeta = -\zeta_A$, $\zeta = 0^+$ and $\zeta = 0^-$ denotes that the velocity profiles are plotted at the wave crest, wave trough, zero up-crossing and zero down-crossing, respectively.

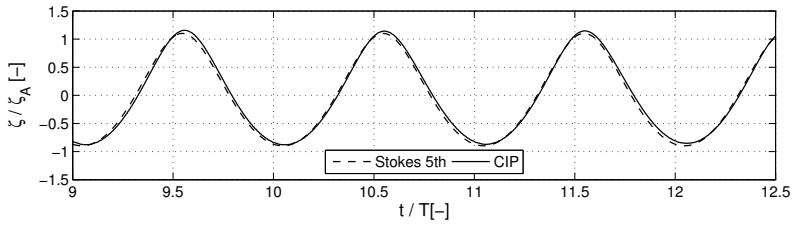

(a) $\zeta_a = 0.05$ m

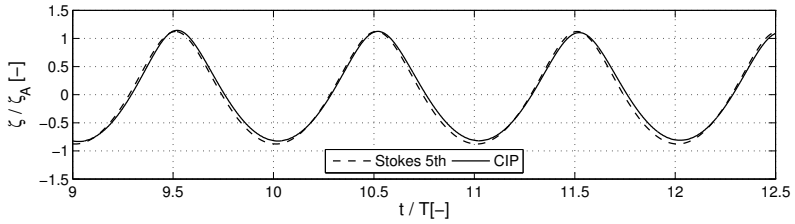

(b) $\zeta_a = 0.06$ m

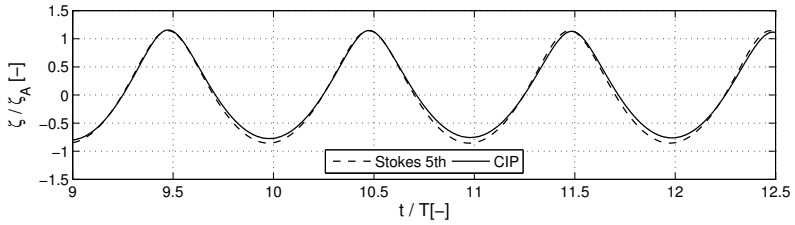

(c) $\zeta_a = 0.07$ m

Figure 5.11: CIP compared with 5th order Stokes' theory: Wave elevation for $T = 1.00$ s at $x = 2\lambda$. Wave steepness $k\zeta_A$ is 0.19, 0.23 and 0.26, respectively.

difficult to predict a priori what the total effect on computed forces will be. For the THINC surface capturing method, the velocity profiles seem to agree well with 5th order Stokes' theory. Note that at the free surface, a discontinuity is observed for the velocity profiles when using THINC. This is to be expected due to the sharp interface, but such steep gradients may cause numerical problems in the flow solver. This did however not occur for the present wave simulations. The performance of the surface capturing methods is further discussed in Sec. 6.3.2.

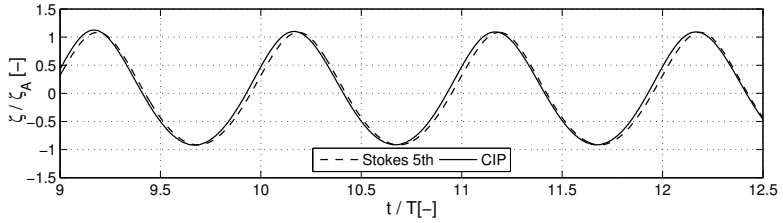

(a) $\zeta_a = 0.05$ m

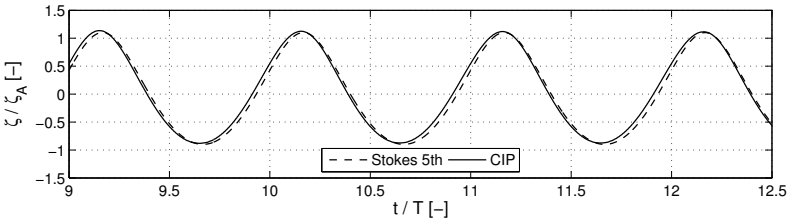

(b) $\zeta_a = 0.06$ m

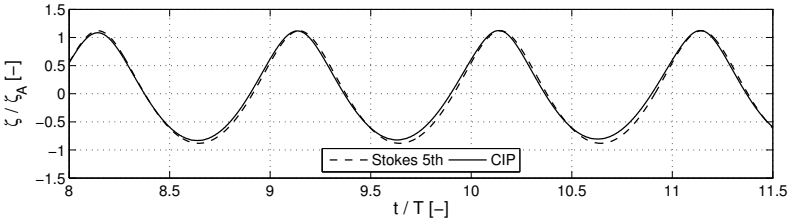

(c) $\zeta_a = 0.07$ m

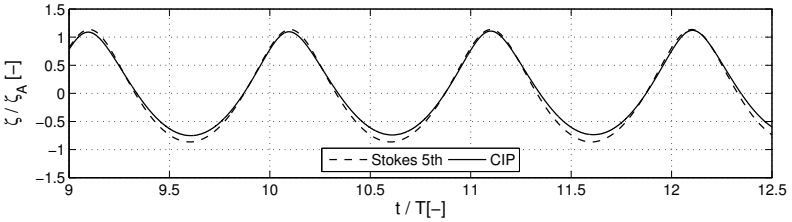

(d) $\zeta_a = 0.08$ m

Figure 5.12: CIP compared with 5th order Stokes' theory: Wave elevation for $T = 1.11$ s at $x = 2\lambda$. Wave steepness $k\zeta_A$ is 0.15, 0.19, 0.22 and 0.25, respectively.

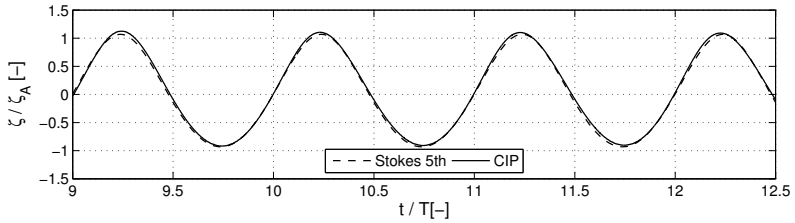

(a) $\zeta_a = 0.05$ m

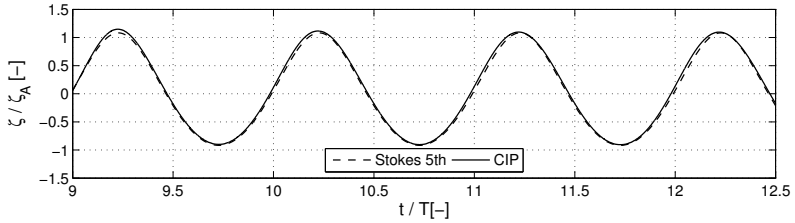

(b) $\zeta_a = 0.06$ m

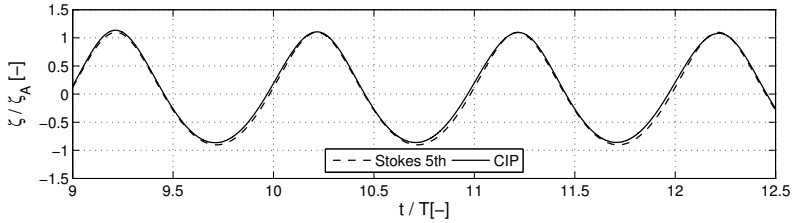

(c) $\zeta_a = 0.07$ m

Figure 5.13: CIP compared with 5th order Stokes' theory: Wave elevation for $T = 1.25$ s at $x = 2\lambda$. Wave steepness $k\zeta_A$ is 0.13, 0.15 and 0.18, respectively.

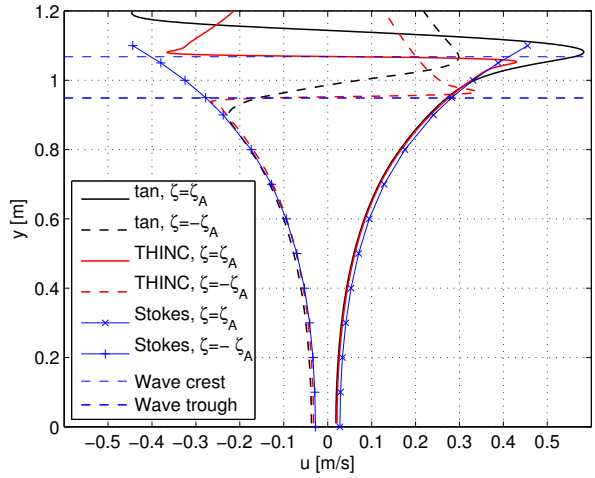

(a) Horizontal velocity profile

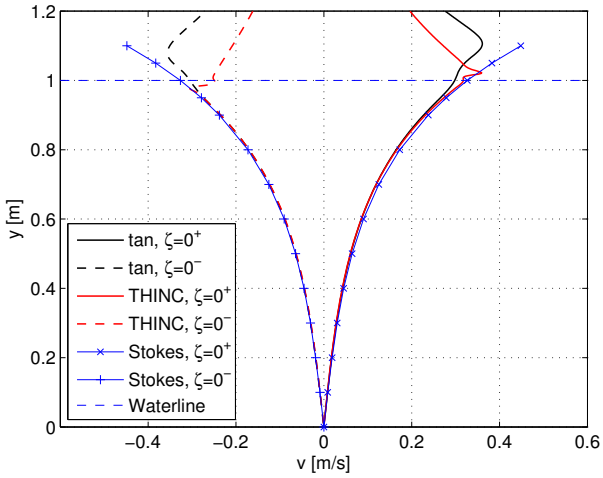

(b) Vertical velocity profile

Figure 5.14: CIP compared with 5th order Stokes' theory: Velocity profiles for u and v underneath the wave for $\zeta_A = 0.06$ m, $T = 1.11$ s, $k\zeta_A = 0.19$.

5.4.5 Comparison with measured waves in the glass flume

In this section, the computed wave elevation is compared with the undisturbed measured wave elevation from the glass flume experiments (see Sec. 6.2). The wave probe position in the tank does not correspond with the position where the simulated free surface is computed. The simulated and measured time series are therefore adjusted so that they are as closely in phase with each other as possible. For the undisturbed waves, the exact tank position is not important since the waves are steady-state regular waves. Note that during experiments, the recording of the wave elevation was started 4 s after the wavemaker was started, so the entire up-ramping of the waves was not recorded.

Figures 5.15– 5.17 show the measured and simulated wave elevation for the wave cases in Tab. 5.4. The measured and simulated wave crests for the three first stable waves are given in Tab. 5.7. The crest height obtained from 5th order Stokes theory is also given. The difference between simulated and measured wave crest is included, given in percent of the measured value. The agreement between measured and simulated wave elevation is generally acceptable. The simulated troughs are somewhat too shallow in some of the cases. This effect increases with wave steepness, and is also seen when comparing with 5th order Stokes waves. In the experiments, a wave with somewhat larger wave crest occurs before steady state is achieved for some cases. This overshoot does not occur in the numerical simulations. The discrepancy will of course affect the force history for the first wave impacts.

It should be noted that the target wave height for the simulated waves were the same as the target value for the measured waves. The simulated waves were thus not calibrated to match the actual measured waves. This sometimes causes a discrepancy since the measured wave deviates somewhat from the target value (see Tab. 5.7). This is the case e.g. for the waves with wave period of 1.0 s. A parameter study of the influence of the wave crest height on the wave-in-deck force is presented in Sec. 6.3.3.

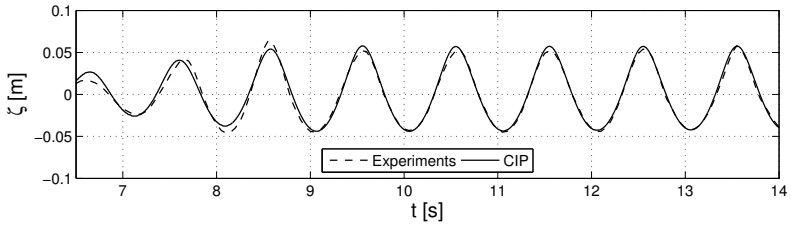

(a) $\zeta_a = 0.05$ m

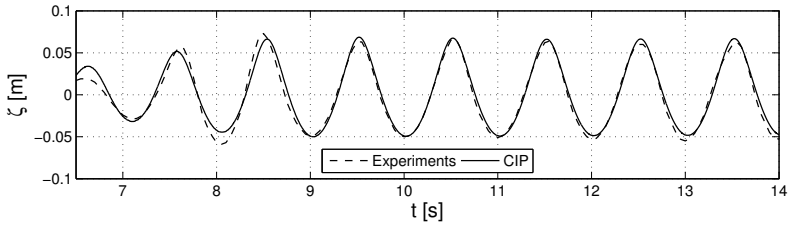

(b) $\zeta_a = 0.06$ m

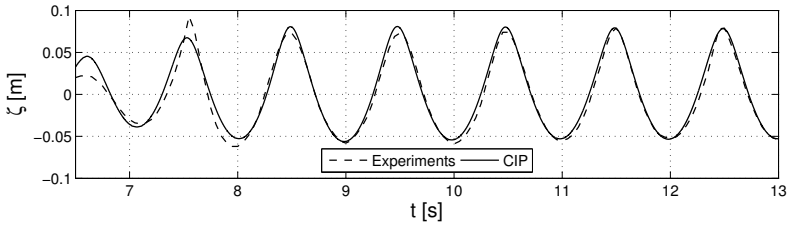

(c) $\zeta_a = 0.07$ m

Figure 5.15: Measured and simulated wave elevation for $T = 1.00$ s. Wave steepness $k\zeta_A$ is 0.19, 0.23 and 0.26, respectively.

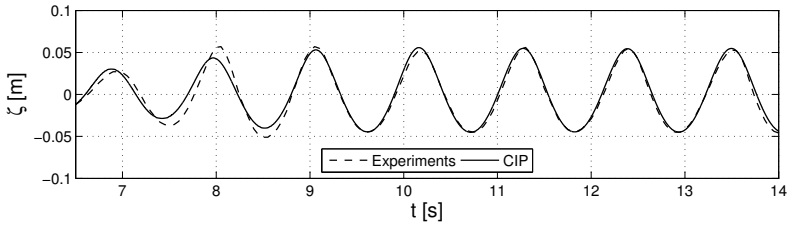

(a) $\zeta_a = 0.05$ m

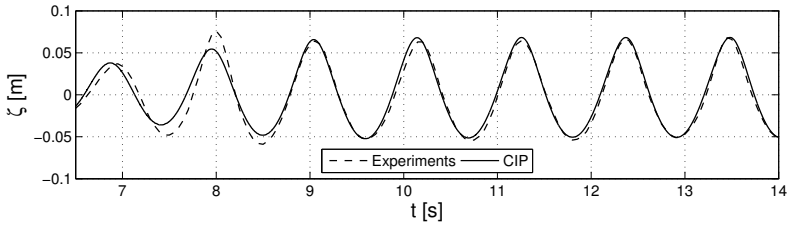

(b) $\zeta_a = 0.06$ m

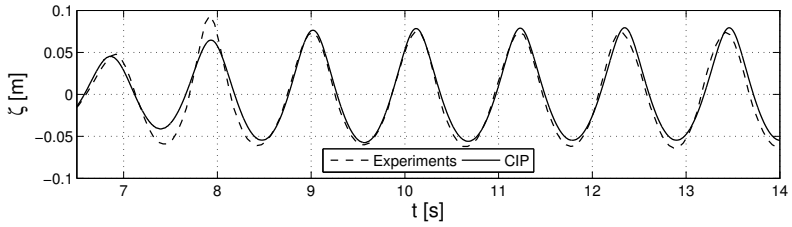

(c) $\zeta_a = 0.07$ m

Figure 5.16: Measured and simulated undisturbed wave elevation for $T = 1.11$ s. Wave steepness $k\zeta_A$ is 0.15, 0.19 and 0.22, respectively.

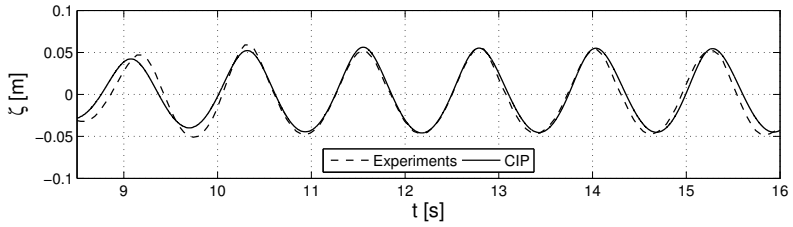

(a) $\zeta_a = 0.05$ m

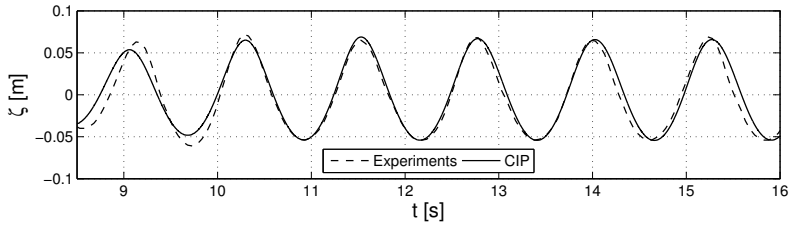

(b) $\zeta_a = 0.06$ m

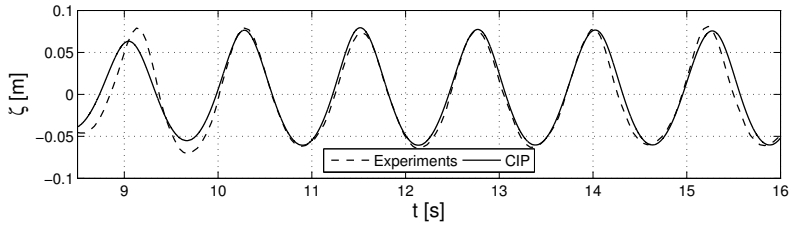

(c) $\zeta_a = 0.07$ m

Figure 5.17: Measured and simulated undisturbed wave elevation for $T = 1.25$ s. Wave steepness $k\zeta_A$ is 0.13, 0.15 and 0.18, respectively.

Table 5.7: Measured and simulated wave crest height for the first three stable waves. The target wave height and Stokes 5th order crest height are also given. Exp. denotes experimental values, CIP denotes simulated values and Diff. denotes the difference between the two, given in % of the measured value.

Period	Target height.	Stokes crest	Crest no.	Crest height		Diff. (CIP/Exp.)
T [s]	H [m]	ζ_C [m]		Exp.	CIP	%
1.00	0.10	0.0551	1	0.0520	0.0578	11
			2	0.0530	0.0578	9
			3	0.0520	0.0573	10
1.00	0.12	0.0675	1	0.0630	0.0685	9
			2	0.0670	0.0675	1
			3	0.0640	0.0662	3
1.00	0.14	0.0800	1	0.0730	0.0807	11
			2	0.0730	0.0809	11
			3	0.074	0.0802	8
1.11	0.10	0.0542	1	0.0570	0.0531	7
			2	0.0520	0.0556	7
			3	0.0560	0.0549	2
1.11	0.12	0.0661	1	0.0640	0.0657	3
			2	0.0630	0.0680	8
			3	0.0640	0.0682	7
1.11	0.14	0.0783	1	0.0740	0.0764	3
			2	0.0760	0.0784	3
			3	0.0740	0.0789	7
1.25	0.10	0.0535	1	0.0520	0.0562	8
			2	0.0560	0.0552	1
			3	0.0540	0.0551	2
1.25	0.12	0.0650	1	0.0650	0.0688	6
			2	0.0680	0.0669	2
			3	0.0650	0.0658	1
1.25	0.14	0.0767	1	0.0740	0.0756	2
			2	0.0760	0.0781	3
			3	0.0740	0.0785	6

5.5 Modeling of the small towing tank

Deck impact experiments were performed in the small towing tank at MARINTEK, (Baarholm, 2008). The experiments and results are further described in Sec. 6.5. In this section, the numerical model of the wave tank is described and the simulated undisturbed waves are compared with the measured waves from the calibration tests.

5.5.1 Case set-up

As for the two previous wave tanks, the NWT is set up with the same dimensions as the physical tank, see Tab. 5.1. The water depth is 1.0 m. In the small towing tank, a flap wavemaker is installed. The wavemaker motion was not measured during experiments. In the NWT, a piston wavemaker is used, as before.

In the two previous NWT's (Secs. 5.3 and 5.4), only linear up-ramping of the wavemaker motion is used. To improve the simulation of the up-ramping compared to measurements, two types of up-ramping schemes are tested in the simulations: one is linear as before (see Eq. 5.7), while the other is parabolic. Both up-ramping schemes are performed over a time period of 5 seconds.

Table 5.8 shows the wave conditions run in the tank. It should be noted that the waves in the experiments were calibrated to obtain a target wave crest rather than a wave height.

Table 5.8: Wave cases for the experiments in the small towing tank. Wave crest height was specified as target value.

Wave period T [s]	Wave crest ζ_C [m]	Wave steepness $k\zeta_C$ [-]
1.3	0.110	0.253
1.3	0.120	0.274
1.3	0.160	0.349
1.6	0.100	0.164
1.6	0.105	0.172
1.6	0.110	0.180
1.6	0.120	0.197
1.6	0.160	0.254

5.5.2 Grid configuration and grid dependency

As for the glass flume case described above, the grid is governed by the size and placement of the deck box used in the wave-in-deck experiments. The experimental set-up is further described in Sec. 6.5.1. Since the longest waves in this experiment is longer than for the experiment in the glass flume, the deck box must be placed further away from the wavemaker, giving a somewhat longer main area than for the glass flume case. The total length of the tank is also greater, and equals the length of the physical towing tank. The tank elongation ensures sufficient damping of the long waves. Two different grid configurations with different refinement in the main wave zone is tested. Figure 5.18 shows a schematic overview of the grid for the present NWT, and Tab. 5.9 shows the refinement zone lengths and corresponding grid sizes.

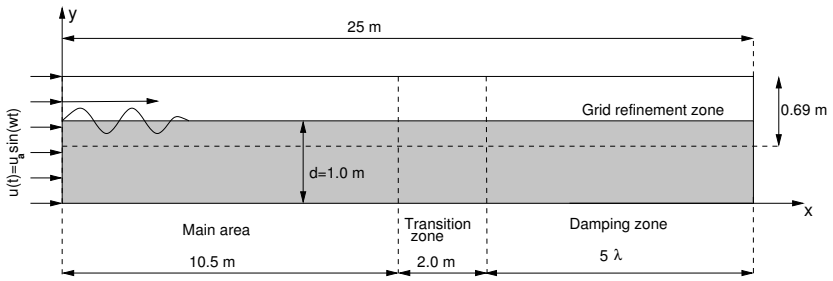

Figure 5.18: Schematic overview of the numerical wave tank modeling the small towing tank at MARINTEK.

Table 5.9: Specification of the grid in the different wave tank zones. In the zones where the grid size varies, the end size is given. The start size is shown in the previous zone.

	Grid 1		Grid 2	
	Zone length [m]	Cell size [m]	Zone length [m]	Cell size [m]
Main area	10.50	0.020	10.50	0.014
Transition zone	2.00	0.180	2.00	0.186
Damping zone	12.50	1.880	12.50	1.986
Vertical refinement zone	0.69	0.002	0.69	0.002
Vertical water zone	0.69	0.010	0.69	0.010

The total number of grid cells for the two grids are 786×434 and 560×434, respectively. The largest grid with nearly 800 cells in the horizontal direction is

resulted in long simulation time. Only one wave case is run. Examining wave elevation and velocity fields, little difference is seen for the two grids. The grid dependency is discussed further for the corresponding impact simulations in Sec. 6.5.

5.5.3 Comparison of simulated and measured waves

In this section, the simulated undisturbed wave elevations are compared with the wave calibration tests run in the small towing tank. Four of the wave cases given in Tab. 5.8 are simulated. It should be noted that in the glass flume experiments, the simulated waves were calibrated against the target wave height. In the present case, the simulated waves are calibrated against the target wave crest. Since the waves are generated for wave impact purposes, the focus is on the crest above a certain height. For all the waves discussed below, a crest height of 0.1 m will cause impact.

Figures 5.19 - 5.20 show the measured and simulated waves for different wave conditions. Both up-ramping schemes are included for the simulated waves. The parabolic up-ramping scheme is used to try to match the first wave that causes impact, see further discussion in Sec. 6.5. Several simulations with different strokes in addition to those shown here are attempted for both up-ramping schemes. This is the reason for the discrepancy in the wave crest height that is sometimes observed between the two simulated waves after the up-ramping is finished (see e.g. Fig 5.19(a)). The simulated waves with the best match either for the first crest height or the stable crest heights are shown in the figures.

Table 5.10 shows the measured and simulated crest heights for the waves given in Figs. 5.19 - 5.20. The target crest height is given together with the value for the 5 first crests exceeding a height of 0.1 m. The mean of the four last crests are also given, as these crest are meant to be stable regular waves. The corresponding discrepancies in percent between the measured wave crest and the wave crests for the two simulations are included. Note that the resulting experimental waves in some cases deviate from the target wave crest.

Studying the discrepancies for the two first crests in each case, the difficulty of modeling the up-ramping without having the actual measured wavemaker motion time series is illustrated. For the first crest, the parabolic up-ramping scheme is generally the best fit, while for the next crest, the discrepancy is large. For the linear up-ramping scheme, the discrepancy is large for the first crest, while the next is generally in good agreement with the measured crest. Note that the measured crest varies as much as 5% within the same wave train. The measured wave is thus not as stable as the waves generated in the glass wave flume. However, amplitude modulation is seen for the simulated waves as well. Wave steepness may be one reason for this. The waves are steeper than for the glass flume experiments for

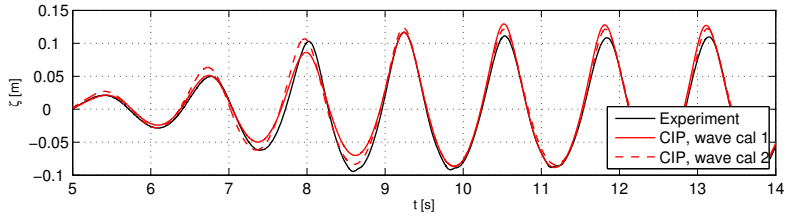

(a) $\zeta_C = 0.12$ m

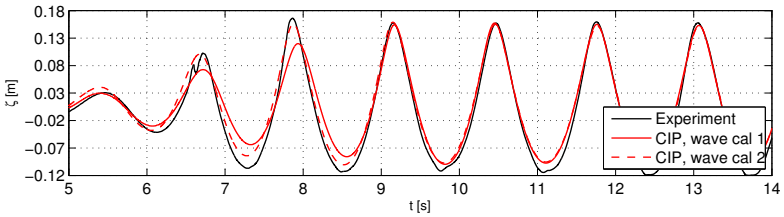

(b) $\zeta_C = 0.16$ m

Figure 5.19: Measured and simulated undisturbed wave elevation for $T = 1.3$ s

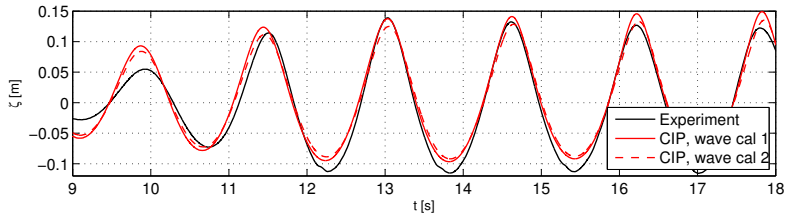

(a) $\zeta_C = 0.12$ m

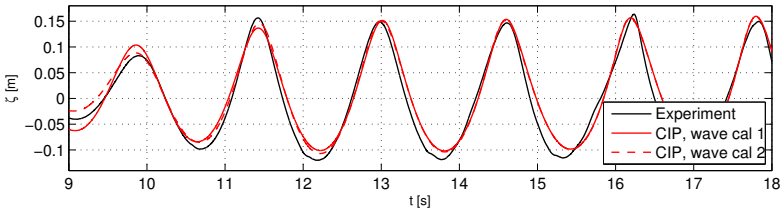

(b) $\zeta_C = 0.16$ m

Figure 5.20: Measured and simulated undisturbed wave elevation for $T = 1.6$ s

many of the cases, see Tabs. 5.5 and 5.8. The agreement between measured and simulated wave is generally better for the glass flume experiments than in the small towing tank (compare Tabs. 5.7 and 5.10).

It should be noted that the small towing tank is 2.80 m wide, while the two previous cases are narrow wave flumes. There may thus be a greater chance for the waves in the small towing tank to be contaminated by cross flow than for the waves in the flumes. The tank is 2.80 m wide, and the shortest wave has a wave length of 2.75 m, which is close to the breadth of the tank. This means that the 2D conditions in the towing tank may be weakened faster than in the flumes. Error sources for the small towing tank experiments are further discussed in Sec. 6.5.3.

Table 5.10: Measured and simulated wave crest for the first five waves exceeding a crest height of 0.1 m. The mean crest heights σ of the last 4 crests are also included. The difference in percent between the measured wave crest (Exp.) and the two CIP simulations are given. Lin. denotes linear up-ramping scheme, and Parab. denotes parabolic up-ramping scheme.

Crest no.	Period	Target	Wave crest height			Diff (%)	
	T [s]	ζ_C [m]	Exp.	CIP Lin.	CIP Parab.	Lin./Exp.	Parab./Exp.
1	1.3	0.12	0.103	0.086	0.107	16.5	3.9
2			0.117	0.116	0.123	0.9	5.1
3			0.111	0.130	0.121	17.1	9.0
4			0.108	0.128	0.126	18.5	16.7
5			0.110	0.128	0.122	16.4	10.9
σ (2-5)			0.112	0.125	0.123	11.6	9.8
1	1.3	0.16	0.166	0.120	0.156	27.7	6.0
2			0.158	0.154	0.159	2.5	0.6
3			0.157	0.158	0.155	0.6	1.3
4			0.160	0.155	0.152	3.1	5.0
5			0.158	0.153	0.153	3.2	3.2
σ (2-5)			0.158	0.155	0.155	1.9	1.9
1	1.6	0.12	0.114	0.124	0.112	8.8	1.8
2			0.139	0.138	0.125	0.7	10.1
3			0.132	0.141	0.128	6.8	3.0
4			0.127	0.147	0.133	15.7	4.7
5			0.122	0.149	0.135	22.1	10.7
σ (2-5)			0.130	0.143	0.130	10.0	0.0
1	1.6	0.16	0.156	0.137	0.146	12.2	6.4
2			0.149	0.152	0.151	2.0	1.3
3			0.147	0.154	0.151	4.8	2.7
4			0.164	0.157	0.156	4.3	4.9
5			0.149	0.160	0.159	7.4	6.7
σ (2-5)			0.152	0.156	0.154	2.6	1.3

Chapter 6

Wave impact on a deck box

6.1 Introduction

In this chapter, CIP simulations of wave impacts on a deck box are presented and compared with experimental results.

A fixed solid box with no substructure is placed in a wave tank with an initial clearance to the mean water level. This simplified set-up models an offshore platform with a small-volume substructure, e.g. a jacket. For this type of structures, the disturbance from the substructure on the incoming waves is small and can be neglected. Wave conditions and airgap are varied to obtain wave impacts on the deck box with varying severity. Two experiments with such a set-up were performed by Rolf Baarholm, one in 1998 and one in 2008 (Baarholm, 2001, 2008). The first experiment was performed in the glass flume at the Department of Marine Hydrodynamics, while the latter was performed in the small towing tank at MARINTEK. The first experiment was performed with 2D conditions, and only the vertical force on the deck box was considered. Both 2D and 3D conditions were tested in the experiment performed in 2008. Forces in all three directions were measured. The wave impact experiments are described in Secs. 6.2 and 6.5, respectively. CIP simulations are set up to model the two experiments, and are presented in Secs. 6.3 and 6.6. The comparison between numerical and experimental results are presented in Secs. 6.4 and 6.7, respectively.

6.2 Description of the experiments in the glass wave flume

Two variants of this experiment were performed. For the first type, the deck box was lowered down into the flume between two wave crests after steady state regular waves had been obtained. The focus was on the first impact. Results from these

tests were published in Baarholm (2001), and is not considered in this work. For the other type of experiments, the deck box was fixed in the wave flume during the entire test run. The impacts on the deck box then include events during the up-ramping of the waves, and multiple impacts after steady state waves are obtained. Results from these tests are discussed in the present work. The force history differs for the first impact compared to the consecutive impacts because the incoming waves are disturbed by previous impacts (see Sec. 6.2.2). Multiple impact events are realistic in extreme seas. In irregular waves, extreme waves can appear in a wave group, where several large crests succeed each other. Such an event may be severe for a platform, as the first wave can cause some initial damage, which may escalate as the next impact occurs.

6.2.1 Experimental set-up

Details of the experimental set-up can be found in Baarholm (2001). It is however convenient to repeat some of the information here. The model test was performed in the narrow wave flume at the Department of Marine Hydrodynamics, NTNU (see Sec. 5.4). The deck box model with height $H_b = 0.3$ m and length $L = 0.65$ m was placed in the middle of the tank. Two-dimensional flow was sought. The breadth of the box was 0.58 m, i.e. nearly the same as the breadth of the flume. A 10 mm gap was left on each side to protect the flume walls. These gaps were filled with soft rubber foam. The deck plate, with a total length $L_D = 0.63$ m, was made stiff enough for hydro-elastic effects to be negligible. The vertical force on the deck plate was the primary parameter to be measured, but also the wetted area underneath the deck and the free surface elevation at different positions were measured. Figure 6.1 shows a sketch of the model and the primary instrumentation. The instrumentation consisted of the following:

- One surface piercing wave probe.
- Three force transducers with measuring range of ± 1000 N.
- Three wetted deck measuring devices fastened underneath the deck.

The position of the wave probe in the tank varied for different runs. The wave probe was placed 1 m in front of the deck box for some tests, and 0.15 m in front of the deck box for other runs. Also, wave calibration runs were performed without the deck box present. The wave probe was then placed at the center of the deck box to record the undisturbed waves.

The three force transducers were set up such that the total force on the deck box is found by summing up the force measured by each transducer. Only the

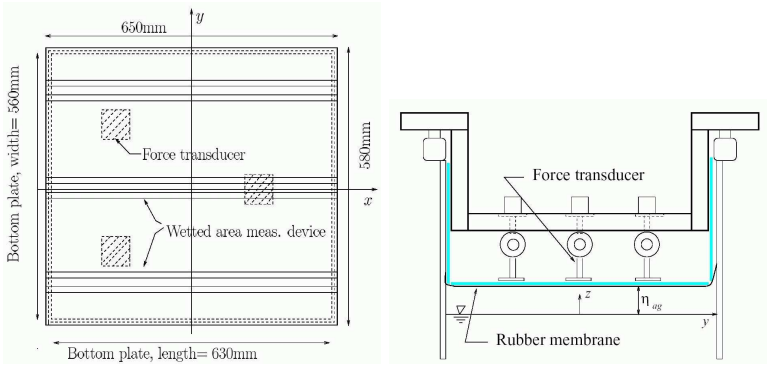

(a) Fish-eye view. (b) Front view

Figure 6.1: Deck box model and instrumentation: Fish-eye and front view of the model.

vertical force was measured. The sampling frequency was 100 Hz. Since the force measurements are to be compared with 2D simulations, all results presented in the further work are normalized with the breadth of the deck box ($B = 0.58$ m), i.e. all values are given in N/m.

The wetted deck measuring devices were made up of two parallel copper tapes fastened underneath the deck in the direction of the wave propagation. One such device was placed along the middle of the box and the other two on each side. The run-up at the front of the deck box was not measured.

Different wave heights, wave periods and deck clearances were tested, giving a total of 21 test cases, see Tab. 6.1.

Table 6.1: Model test cases for the glass flume experiments.

Wave period T [s]			Wave amplitude ζ_A [m]	Deck clearance η_D [m] 0.04	0.06	0.08
1.00	1.11	1.25	0.05	×		
1.00	1.11	1.25	0.06	×	×	
1.00	1.11	1.25	0.07	×	×	
1.00	1.11	1.25	0.08		×	×

6.2.2 Experimental results and physical observations

The impact process as the wave hits the deck was studied in detail during the experiments and reported in Baarholm (2001). As mentioned, only the vertical force was considered. For the first impact, where the wave is not disturbed from previous impacts, the force history is characterized by a positive upward directed force peak during water entry, followed by a negative force peak during water exit. The positive force peak generally has a smaller magnitude than the negative force peak for the first impact. The duration of the water entry phase is also shorter than the water exit phase.

In Baarholm (2001), a simplified Wagner-based method was developed for computing the vertical force on the deck during impact. It is useful to review the basis for this method, to understand the physics of the impact process. The impact force can be found by imposing the conservation of fluid momentum (see Faltinsen, 1990, Ch. 9). The vertical impact force can be expressed as:

$$F_3 = \frac{d(A_{33}^{\infty} V)}{dt} = V\frac{dA_{33}^{\infty}}{dt} + A_{33}^{\infty}\frac{dV}{\partial t} \tag{6.1}$$

where A_{33}^{∞} is the 2-D added mass in heave for infinite frequency and V is the impact velocity. The derivation of Eq. 6.1 is based on potential theory with a free-surface condition $\Phi = 0$. The effect of gravity is neglected. The impact force is thus the sum of a slamming term (dA_{33}^{∞}/dt) and an added mass term ($A_{33}^{\infty}dV/dt$). The total force on the deck box also includes the incident wave force, consisting of a hydrostatic force and a Froude-Kriloff force. Fig. 6.2 shows an example of the total impact force and its contributions from the slamming term, added mass term and incident wave term using the Wagner based method (Baarholm, 2001, Fig. 3.8 a)).

The positive water entry force is dominated by the slamming force caused by the rapid increase of added mass as the body is rapidly wetted. The incident wave force also contributes with a positive force, while the added mass force is negative during the entire impact due to the negative acceleration underneath the wave crest. During the water exit phase, the total force is thus dominated by this negative added mass force. In the Wagner-base method, the slamming force is set to zero when the increase in the wetted deck length is zero, i.e. when the maximum wetted deck length is reached. The initial assumption of the free-surface condition and neglecting gravity is then no longer a good approximation. This approach is also followed by Kaplan (1992).

Only the first impact is well modeled using the simplified method described above. For the consecutive wave impacts, where the incoming wave has been disturbed by previous impacts, the force history is somewhat different. The magni-

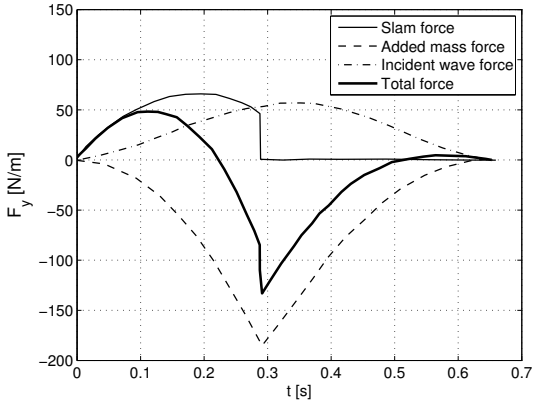

Figure 6.2: Total vertical impact force and its contributions from the slamming term, the added mass term and the incident wave term, estimated from a Wagner based method (Baarholm, 2001, Fig. 3.8 a). $T = 1.11$ s, $\zeta_A = 0.06$ m and $\eta_D = 0.04$ m.

tude of the positive peak is generally greater for the consecutive impacts. During experiments, a second impact was sometimes observed at the end of the water entry phase. The water then impacts underneath the deck in the vicinity of the final detachment point of the preceding wave. Figure 6.3 shows the force history for the two first impacts recorded for $T = 1.11$ s, $\zeta_A = 0.06$ m and deck height $\eta_D = 0.04$ m.

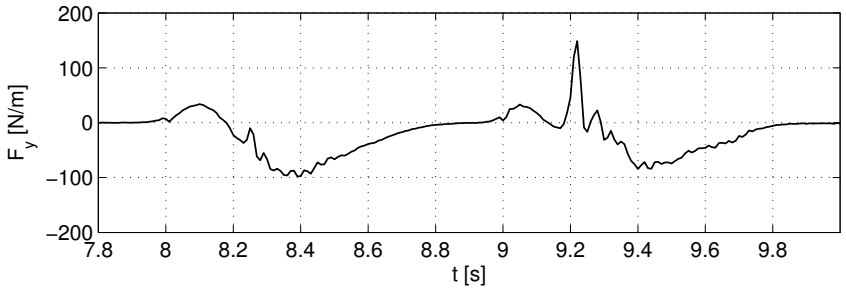

Figure 6.3: Time history of measured vertical force for first and second impact in deck.

In the following work with the glass flume experiments, emphasis is laid on the consecutive impacts rather than the first impact. The nonlinear BEM model developed in Baarholm (2001) obtained good results for the first impact, but could not

handle the final detachment of the water from the deck, and could therefore not run beyond the first impact. One reason for using a CFD method for this application, is that it is robust enough to handle multiple impacts. It is thus interesting to see if the consecutive impacts can be modeled accurately.

6.2.3 Experimental error sources

When trying to validate a new numerical code with the use of experimental results, it is important to remember that the experiments are not the absolute truth either. Common error sources such as reflections from the beach and wavemaker, seiching in the wave flume, transverse waves and wave probe errors were evaluated in Baarholm (2001) and found to be insignificant.

An error source that was not discussed, is the possibility of 3-D instability in the waves after the first impact. As mentioned, it was the first impact that was in focus in the previous work. In the present work, it is important that also the consecutive impacts are dominated by 2-D flow. Since the wetted deck length was measured in three positions underneath the deck, comparing these measurements can give some idea of any 3-D development of the flow underneath the deck. As an example of the measurements, Fig. 6.4 shows the measured wetted length for $T = 1.11$ s and $\eta_D = 0.04$ m for two wave amplitudes. The three sensors (see Fig. 6.1) show some deviation from each other after the first impact, but 2-D flow can be said to be dominating.

Repeatability of measured values is often used for evaluating the quality of experiments. All test cases were run two times, and many cases were run four times. It should however be noted that all the repetitions were not performed consecutively for each case. Pairs of repetitions were performed after one another, but the next pair was run several days later. Sometimes this is seen in the data, as two and two of the force histories compare quite well, while the two pairs deviate from each other, see Fig. 6.5. The difference may be due to a small change in the water depth causing a small difference in the airgap. Also, a somewhat different initial wavemaker position may give a small difference in the incoming wave. The position of the wave probe is different for the two pairs of runs, see Tab. 6.2. It is therefore difficult to compare the incoming waves directly. In the present work, all available repetitions are presented when comparing with simulations.

Note that for some repetitions, there is also a phase difference in the measured forces. This is often the case between two pairs of repetition runs as described above, but it may also occur for two consecutive runs, see e.g. Fig 6.7(a). This is probably due to a small difference in the start time of the data logging, or a small difference in the initial position of the wavemaker. This is not considered important when comparing the force history of the different repetitions, and is

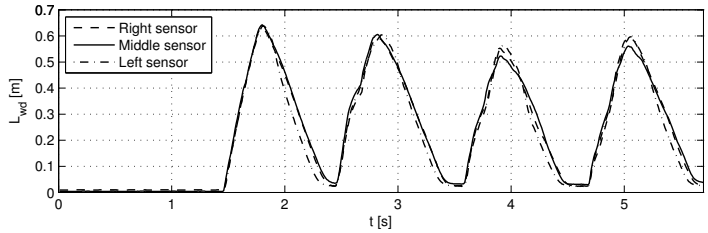

(a) $\zeta_A = 0.06$ m

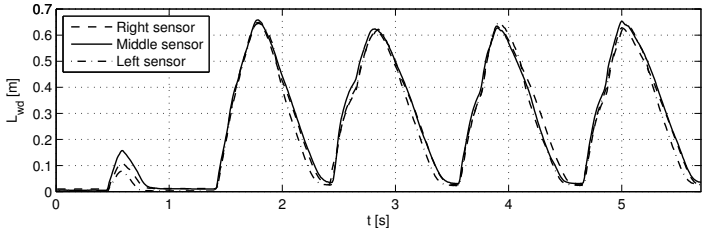

(b) $\zeta_A = 0.07$ m

Figure 6.4: Measurements of wetted deck length for $T = 1.11$ s and $\eta_D = 0.04$ m.

simply corrected by shifting the time series accordingly.

Generally, the repeatability of the force history is better when the airgap exceedance is large, than when the wave barely touches the deck. This can be expected, since a small impact force will be more sensitive to small differences in the inflow conditions. The repeatability of the negative force is reasonably good for all runs. The positive maximum force often varies from test to test even for large airgap exceedances. Some variation can be expected, as the water entry phase includes a violent impact of short duration. But a part of the variation may be due to oscillations in the model rig. In Baarholm (2001), it was stated that during the most violent impacts, some oscillations were observed in the measured force

Table 6.2: Position of wave probe relative to deck box for the four repetitions of each case.

Repetition pair	Run no.	Wave probe pos.
1	1	0.15 m
	2	-1.00 m
2	3	1.00 m
	4	1.00 m

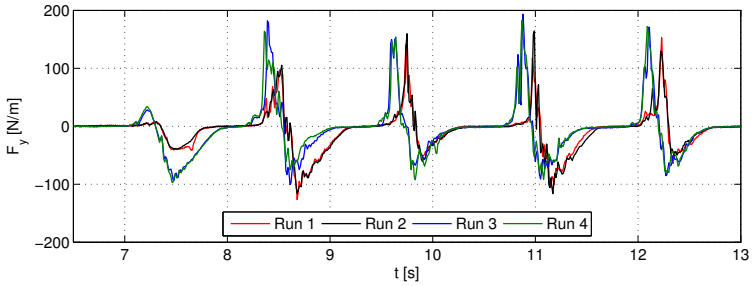

Figure 6.5: Four repetitions of the measured force history for $T = 1.25$ s, $\zeta_A = 0.05$ m and $\eta_D = 0.04$ m. Two and two runs are consecutive in time, and show better repeatability.

history that may originate from structural oscillations of the model. Studying the measured force history in e.g. Fig. 6.5, oscillations are observed.

6.2.4 Filtering of the measured force

Since the measured forces are to be compared with deterministic simulations, some choices must be made regarding how to handle the variability in the data. If structural oscillations of the model are included in the force history, it is natural to filter out these oscillations. The eigenfrequency of the model rig is however not known (Baarholm, 2008, priv. comm.). This makes it difficult to decide what the cut-off frequency should be. Spectral analyses of the force histories are therefore performed to try to identify natural periods. Fast Fourier transformations are performed on each time series, and a power spectrum is computed. Figure 6.6 shows a typical spectrum.

The main part of the energy is located at the excitation frequency as expected, and also on multiples of the excitation frequency. An increase in the energy is observed at 5-10 Hz and 20-25 Hz. This was found for all the excitation periods. Note that the spectrum analysis can only give meaningful data up to the Nyquist frequency $f_{\mathrm{N}} = f_{\mathrm{s}}/2$, where f_s is the sampling frequency of 100 Hz. Oscillations with higher frequencies than the Nyquist frequency (i.e. 50 Hz) will not be identified by the spectral analysis. Very little energy is however present above 25-30 Hz.

The natural frequency of the model rig was measured for the experiments performed in the small towing tank, (see Sec. 6.5). In air, the natural frequency was 25 Hz in the vertical direction. Oscillations of the rig during impact events were observed also in these experiments, see Sec. 6.5.2. The model test rig in the towing tank is assumed to be stiffer than the rig in the glass flume was. The spectrum

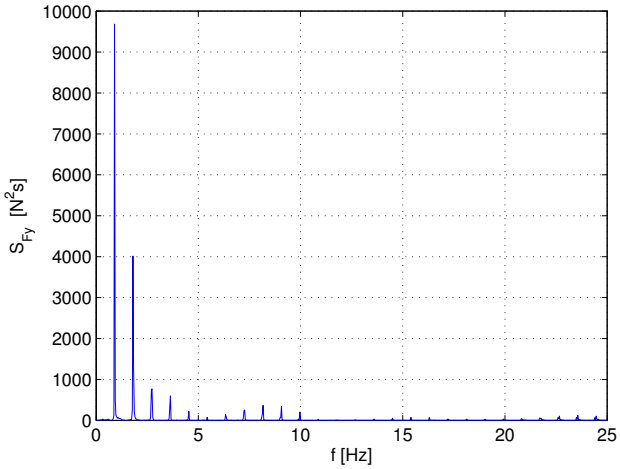

Figure 6.6: Power spectrum of the measured vertical force history for $T = 1.11$ s, $\zeta_A = 0.06$ m and $\eta_D = 0.04$ m.

peaks observed at 5-10 Hz may indicate the presence of wet eigenfrequencies of the glass flume model in this frequency range.

To investigate the effect of filtering further, two impact events are studied. Figure 6.7 shows the unfiltered force history for $T = 1.11$ s (a) and $T = 1.25$ s (b). The wave amplitude is $\zeta_A = 0.06$ m and the airgap is $\eta_D = 0.04$ m for both tests. All available repetitions of the same test are included.

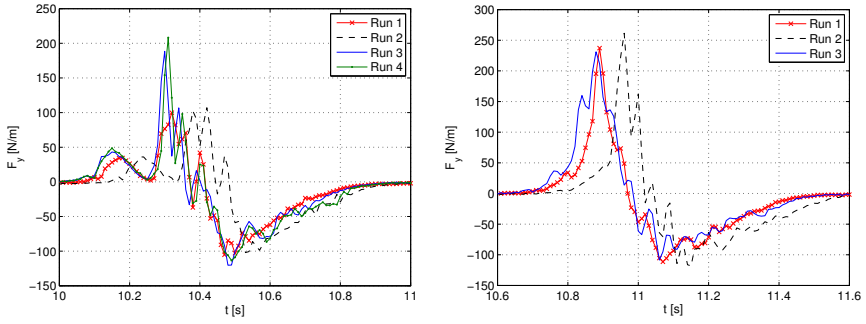

(a) $T = 1.11$ s (b) $T = 1.25$ s

Figure 6.7: All repetitions of the measured force history for two impact events with $\zeta_A = 0.06$ m and $\eta_D = 0.04$ m.

Figures 6.8 and 6.9 show the same measured force histories filtered with a cut-off frequency f_c of 5, 7.5, 10 and 15 Hz. An eighth-order low-pass Butterworth filter is used. Note that the force history obtained after filtering with $f_c = 5$ Hz differs somewhat from the results using higher cut-off frequencies. This is especially evident for $T = 1.11$ s, where two positive force peaks are present. Figure 6.10 and 6.11 shows the same impact events as in Figs. 6.7(a) and 6.7(b) after filtering with 5 and 10 Hz. The repeatability is improved after filtering the force histories. There is however still a discrepancy between repetitions run on separate days (see Sec. 6.2.3).

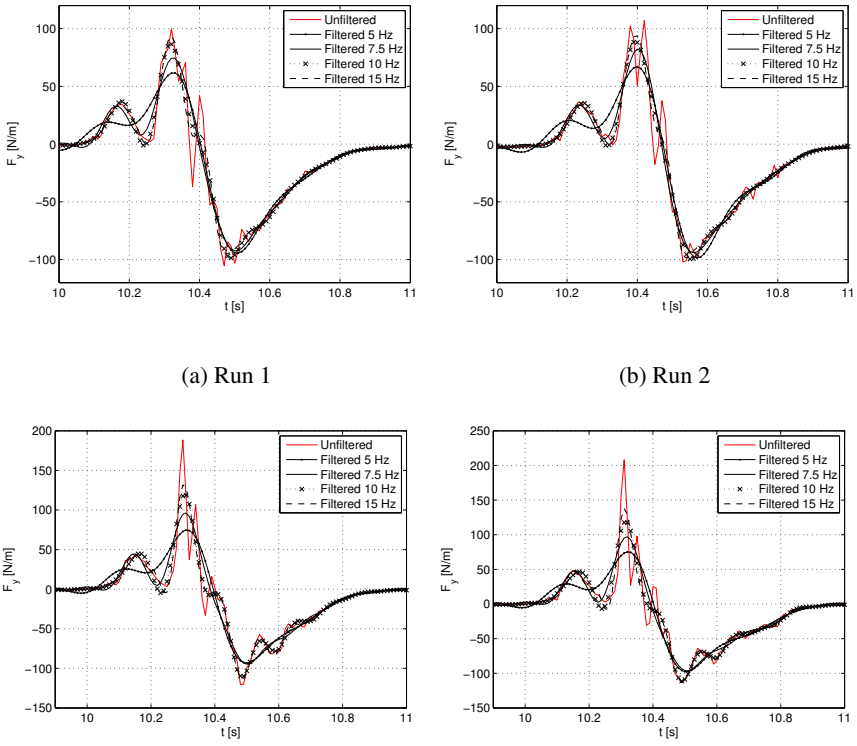

(a) Run 1

(b) Run 2

(c) Run 3

(d) Run 4

Figure 6.8: Four repetitions of the measured vertical force history filtered at 5, 7.5, 10 and 15 Hz. $T = 1.11$ s, $\zeta_A = 0.06$ m and $\eta_D = 0.04$ m.

Table 6.3 shows the maximum and minimum forces, together with the mean and standard deviation for the same case as in Fig. 6.7(a). Four repetitions of 4 consecutive impacts (i.e. not the very first impact) are included. Values for the

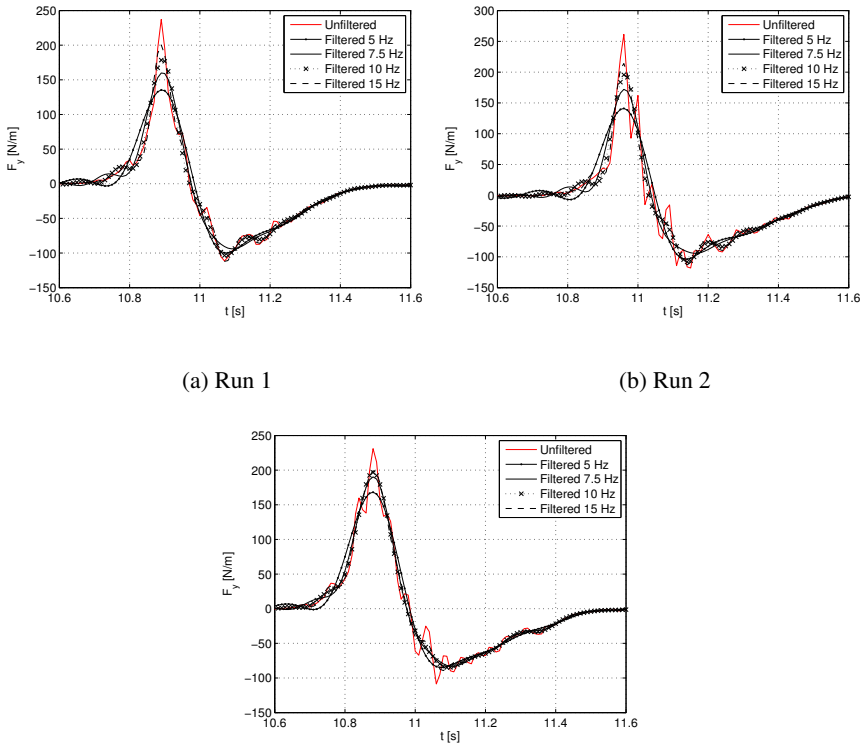

(a) Run 1

(b) Run 2

(c) Run 3

Figure 6.9: Three repetitions of the measured vertical force history filtered at 5, 7.5, 10 and 15 Hz. $T = 1.25$ s, $\zeta_A = 0.06$ m and $\eta_D = 0.04$ m.

unfiltered force history is given together with values filtered at 10 and 5 Hz. Since the magnitude of one impact may be influenced by the previous impacts, it does not seem reasonable to average the maximum and minimum values along the time axis. The variance of the maximum peak is large for the unfiltered measurements. The variability of the minimum force is considerably lower. The filtering improves the repeatability, and reduces the magnitude of the measured positive force significantly.

It seems clear that the cut-off frequency should lie between 5 and 15 Hz. It is however not easy to see what is the correct choice in this range. If f_c is too low, the filtering may remove physical effects of the loading process. To avoid this, $f_c = 10$ Hz is chosen as a basis when comparing with simulations, see Sec. 6.4. In some cases, comparison using $f_c = 5$ Hz is also performed. Some uncertainties of

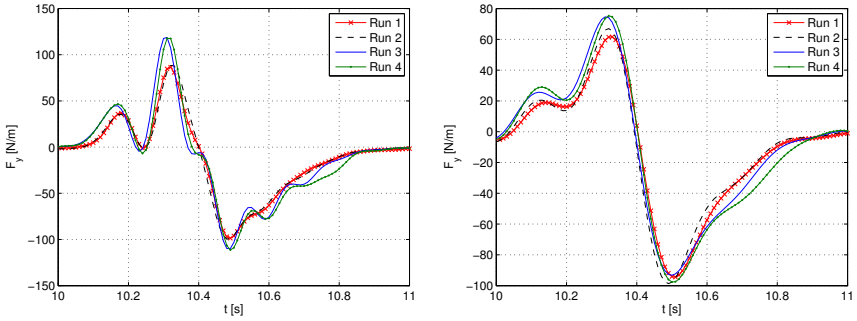

(a) Cut-off frq. $f_c = 10$ Hz (b) Cut-off frq. $f_c = 5$ Hz

Figure 6.10: Four repetitions of the filtered force history for $T = 1.11$ s, $\zeta_A = 0.06$ m and $\eta_D = 0.04$ m.

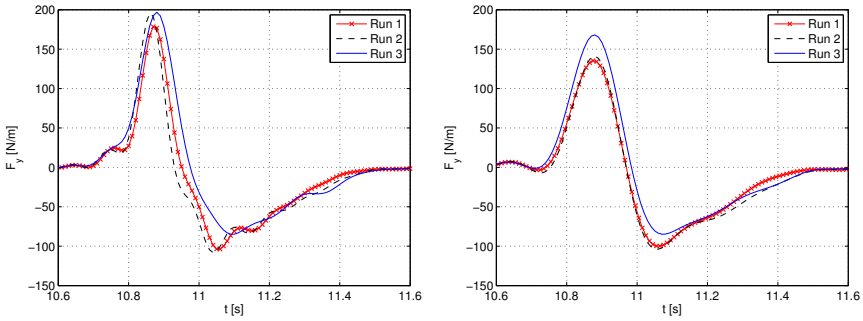

(a) Cut-off frq. $f_c = 10$ Hz (b) Cut-off frq. $f_c = 5$ Hz

Figure 6.11: Three repetitions of the filtered force history for $T = 1.25$ s, $\zeta_A = 0.06$ m and $\eta_D = 0.04$ m.

the measured impacts are thus unresolved. A further discussion on the choice of filtering is given in Sec. 6.4.4.

Table 6.3: Measured maximum and minimum vertical force F_y [N/m]. Values for 4 consecutive impacts for $T = 1.11$ s, $\zeta_A = 0.06$ m and $\eta_D = 0.04$ m. Mean value μ and standard deviation σ is included for each impact.

Unfiltered

Impact no.	Run no.	1	2	3	4	μ	σ
2	Max	143.5	154.0	160.3	161.7	154.9	7.2
	Min	-94.8	-89.95	-104.1	-96.1	-96.2	5.1
3	Max	99.9	107.0	188.5	208.2	150.9	48.0
	Min	-105.3	-102.1	-120.4	-113.5	-110.3	7.2
4	Max	135.4	105.9	116.8	135.9	123.5	12.8
	Min	-121.4	-131.3	-133.7	-130.5	-129.2	4.7
5	Max	225.4	164.2	180.5	166.8	184.2	24.6
	Min	-142.9	-129.5	-138.0	-138.1	-137.1	4.83

Cut-off frequency $f_c = 10$ Hz

Impact no.	Run no.	1	2	3	4	μ.	σ
2	Max	81.3	87.2	89.5	82.4	85.1	3.4
	Min	-92.7	-88.1	-91.9	-89.4	-90.5	1.9
3	Max	86.5	88.3	118.6	117.7	102.8	15.4
	Min	-98.7	-99.5	-109.9	-111.3	-104.8	5.8
4	Max	88.2	79.6	91.6	97.5	89.2	6.5
	Min	-115.7	-113.6	-127.4	-126.0	-120.7	6.1
5	Max	122.2	117.4	120.3	113.1	118.3	3.4
	Min	-122.1	-118.9	-128.9	-125.9	-124.0	3.8

Cut-off frequency $f_c = 5$ Hz

Impact no.	Run no.	1	2	3	4	μ.	σ
2	Max	45.3	44.6	53.0	53.5	49.1	4.1
	Min	-86.0	-89.8	-89.9	-88.8	-88.6	1.6
3	Max	61.6	67.0	74.6	75.3	69.6	5.6
	Min	-94.4	-97.8	-93.2	-97.6	-95.8	2.0
4	Max	61.8	61.1	70.9	73.1	66.7	5.3
	Min	-106.5	-107.0	-110.5	-108.2	-108.1	1.5
5	Max	72.1	73.2	77.9	75.8	74.8	2.3
	Min	-101.1	-104.1	-103.9	-103.2	-103.1	1.2

6.3 The numerical model for the glass flume experiments

The CIP simulations are set up to 'model the model', using the same dimensions as in the model test. The numerical wave tank used in the simulations is presented in Sec. 5.4.

The fixed deck-box, with same height and length as in the model test, is placed approximately two wave lengths from the wavemaker. This differs from the experiments, where the box was placed at the middle of the tank. The position of the box in the numerical wave tank is closer to the wavemaker to avoid long simulations. It is verified that the waves at this position are no longer affected by the wavemaker, as discussed in Sec. 5.2. However, reflections after wave impacts will reach the wave maker faster than in the experiments. After the first impact in the deck box occurs, reflected waves will travel back toward the wavemaker and eventually return as disturbances on the incoming wave. Assuming that the reflected wave front travels with the same group velocity as the prescribed wave, 3-4 more impacts can be simulated before the disturbances reach the wavemaker, which is sufficient for our purposes. Figure 6.12 shows a schematic drawing of the numerical wave tank and deck box. Not all test cases from the experiments are simulated. Table 6.4 shows the selected cases where simulations are performed.

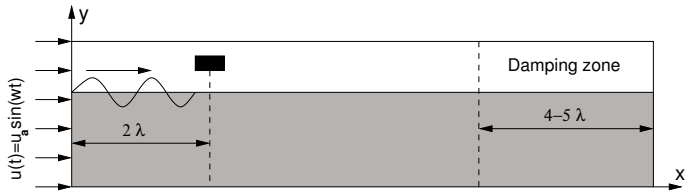

Figure 6.12: Sketch of the numerical wave tank set-up for the glass flume experiment.

6.3.1 Grid configuration and grid dependency

The two grids described in Sec. 5.4.2 are used in the simulations. For Grid 1, the deck box is divided into 45 cells, while for Grid 2, the box is divided into 90 cells. As discussed in Sec. 5.4.2, the refinement does not have any significant effect on the wave elevation, crest velocity or surface layer growth. There is however a difference in the force history for the two grids. Figure 6.13 shows the simulated horizontal and vertical force for Case 5. The magnitudes of both the horizontal and vertical force peaks are somewhat greater for Grid 2 after the first impact. The discrepancy is about 10% for the positive and negative vertical force peaks, and

Table 6.4: Glass flume model test cases where CIP simulations are performed.

Case no.	Wave period T [s]	Wave amplitude ζ_A [m]	Deck clearance η_D [m]
1	1.00	0.05	0.04
2	1.00	0.06	0.04
3	1.00	0.07	0.04
4	1.11	0.05	0.04
5	1.11	0.06	0.04
6	1.11	0.07	0.04
7	1.25	0.05	0.04
8	1.25	0.06	0.04
9	1.25	0.07	0.04
10	1.11	0.06	0.06
11	1.11	0.07	0.06
12	1.11	0.08	0.06

somewhat less for the horizontal force peaks. The duration of the exit phase is also somewhat longer. It can be assumed that the finer grid is more accurate, this is further discussed in Sec. 6.4. Simulations using Grid 2 are however quite slow due to a large number of cells. To be able to run different cases within a reasonable amount of time, Grid 1 is used for most of the simulations.

6.3.2 Effect of surface capturing method

Simulations using both the tangent surface enhancement and THINC surface capturing methods are performed, as discussed in Sec. 5.4.3. For the undisturbed waves, no difference is seen in the computed wave elevation (see Fig. 5.8). However, the surface layer growth is greater for the tangent enhancement method than for the THINC method. Because of this, there are also differences in the velocity profile beneath the wave crest, see Fig. 5.10. The sharp interface obtained by the THINC method is expected to yield more accurate results. However, the discontinuity in the velocity field at the free surface causes numerical problems during impact simulations. Figure 6.14 shows the vertical force for Cases 4-6.

For all simulations performed using the THINC method, violent oscillations are seen after one or two impact events. It is assumed that pressure oscillations occur due to the discontinuity of the velocity field. Several alternatives for the numerical model are tested to mitigate this problem:

- Smoothing procedure for the mass density, as recommended by Hu (priv. comm.).

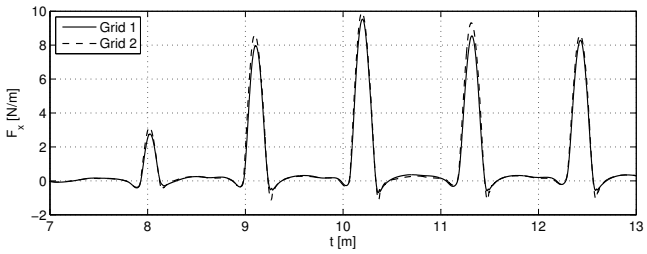

(a) Horizontal force F_x

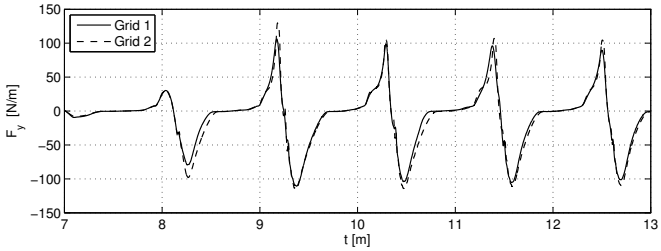

(b) Vertical force F_y

Figure 6.13: Simulated force history for Case 5, two grid configurations with different refinement at deck box.

- Regulating the steepness of the surface layer by changing the value of the THINC parameter β (see Sec. 3.5.3)
- Using the alternative body definition described in Sec. 4.5.5
- Defining the deck box using boundary cells

None of these approaches resulted in significant improvements in the performance of the force computations using the THINC method, and will not be described in detail here. It is rather concluded that although the THINC method seems promising with respect to accuracy, more work must be done to obtain a robust algorithm when a body is included in the simulations. The tangent transformation method is thus used in the further simulations.

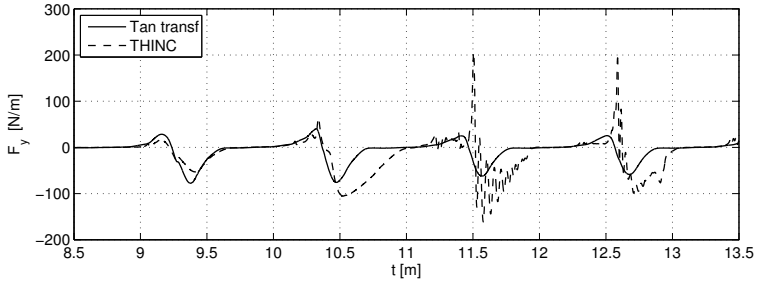

(a) Case 4, $\zeta_A = 0.05$ m

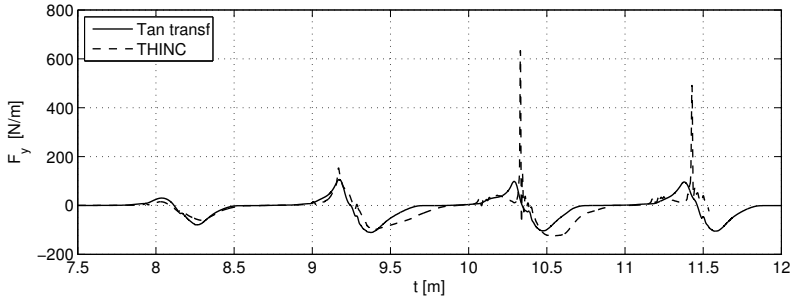

(b) Case 5, $\zeta_A = 0.06$ m

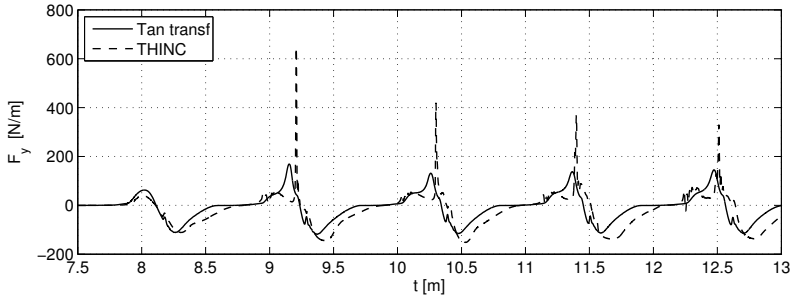

(c) Case 6, $\zeta_A = 0.07$ m

Figure 6.14: Sensitivity to surface capturing method: Simulated force history for Cases 4-6 ($T = 1.11$ s), tangent transfer enhancement versus THINC surface capturing method

6.3.3 Sensitivity to variation in the wave crest

It may be difficult to make the simulated waves match the experimentally obtained incoming wave exactly. The agreement is generally good for the undisturbed waves for most of the cases (see Sec. 5.4.5), the largest discrepancy for the stable waves is however about 10%. Also, the overshoot in the experimental waves cause discrepancies between simulations and experiments for the disturbed waves. The up-ramping is also different, which sometimes causes different timing of the first impact. It is therefore interesting to investigate how sensitive the forces are to variations in the wave crest height.

The wave crest height is varied with about 10% for Cases 2 and 3 (see Tab. 6.4). "Crest 1" denotes the target value, and "Crest 2" denotes a wave with 10% lower crest height. Figures 6.15 and 6.16 show the incoming wave when the deck box is present, and the corresponding simulated force history for the two crest heights.

For the vertical force, the magnitudes of both the positive and negative peak force is decreased for Crest 2 compared to Crest 1, as can be expected. The decrease is greatest for the positive peak. For the first impact, the difference in the positive peak is almost 50%, while for the consecutive impacts, the difference is 30-35%. For the negative peaks, the difference for the first impact is large (30-40%). For the consecutive impacts, the reduction in the force peaks are more in the order of the wave crest reduction, i.e. 10% or less. The negative force is thus generally not as sensitive to the crest height variation. For the horizontal force, the magnitude of the peak is also reduced with 30-40% for most of the impact events.

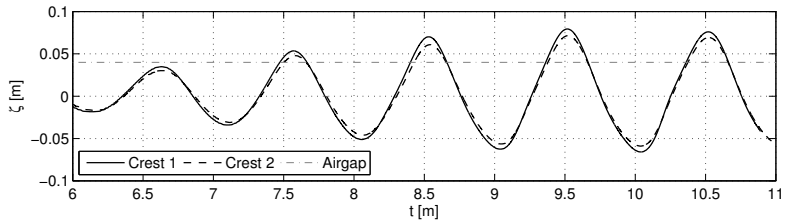

(a) Incoming wave when deck box is present, measured 15 cm in front of the box.

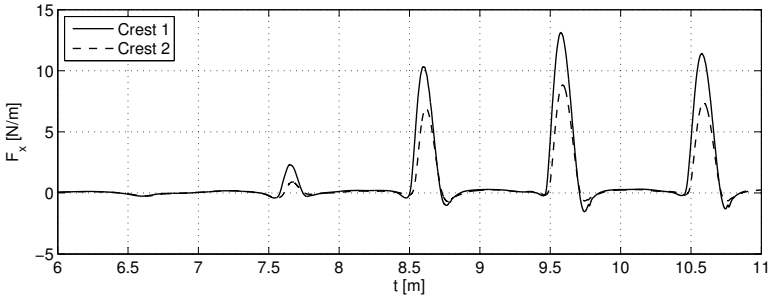

(b) Horizontal force F_x

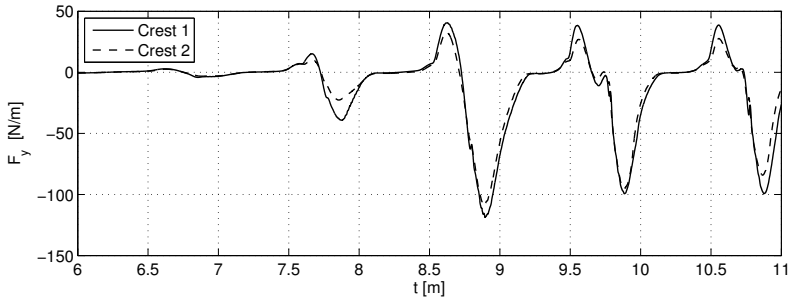

(c) Vertical force F_y

Figure 6.15: Wave crest height variation: Simulated incoming wave and corresponding vertical force history for Case 2 (denoted Crest 1) together with simulated results for 10% less crest height (denoted Crest 2). The dash-dot line in the top figure indicates the deck height.

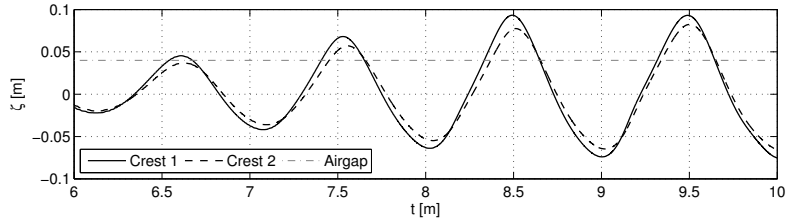

(a) Incoming wave when deck box is present, measured 15 cm in front of the box.

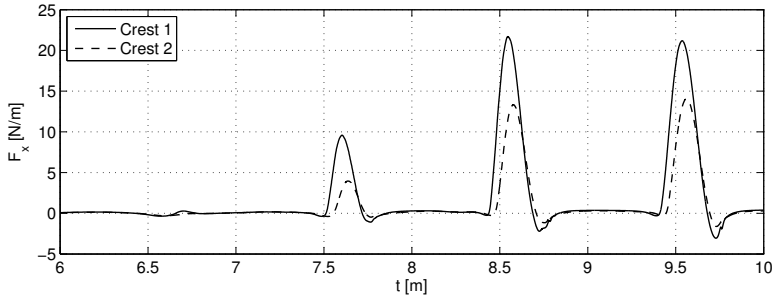

(b) Horizontal force F_x

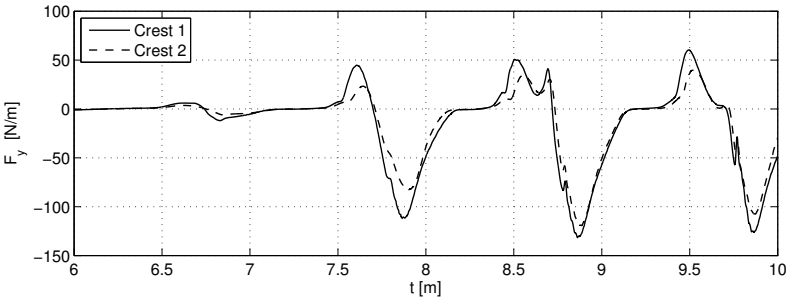

(c) Vertical force F_y

Figure 6.16: Wave crest height variation: Simulated incoming wave and corresponding horizontal and vertical force history for Case 3 (denoted Crest 1) together with simulated results for 10% less crest height (denoted Crest 2). The dash-dot line in the top figure indicates the deck height.

6.3.4 Sensitivity to variation of the airgap

In the previous section, the wave crest height is varied. Another way to change the impact force is to change the airgap. It should be noted that increasing the airgap is not equivalent to decreasing the wave height. A different part of the wave crest with another velocity profile hits the deck. This difference is investigated by comparing Case 4 with Case 11 and Case 5 with Case 12 in Tab. 6.4. The airgap exceedance and wave period is the same, but the wave height is different. Figure 6.17 shows the computed incoming wave together with the horizontal and vertical force for the two cases with airgap exceedance of 0.01 m. Figure 6.18 shows the same for the cases with airgap exceedance of 0.02 m.

For the horizontal force, the steepest wave gives the greatest force peak, since the horizontal velocity in the top of the wave crest increases with the wave height. For the vertical force, the opposite effect apply. The vertical velocity is zero as the wave crest passes. When a smaller part of the wave crest hits the deck, the positive force peak, governed by the vertical velocity, is reduced. The negative force is however governed by the vertical acceleration (see Eq. 6.1), which has a higher magnitude for a higher wave. Thus, the higher wave gives a larger negative force peak. The trends of the computed forces are thus in agreement with what is expected from the wave theory and the Wagner based theory discussed in Sec. 6.2.2. The disturbances due to previous impacts does not seem to change this trend. A phase shift is also seen in the force histories, because the steeper wave hits the deck somewhat earlier. To study the effect of airgap increase for a given wave, Case 6 and 11 is compared. The force is greatly reduced, as expected, see Fig. 6.19.

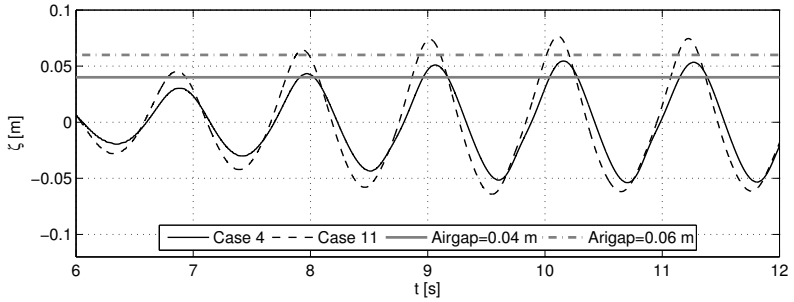

(a) Incoming wave when deck box is present, measured 15 cm in front of the box.

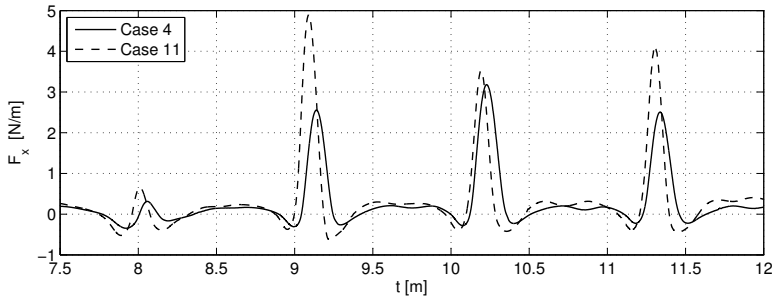

(b) Horizontal force F_x

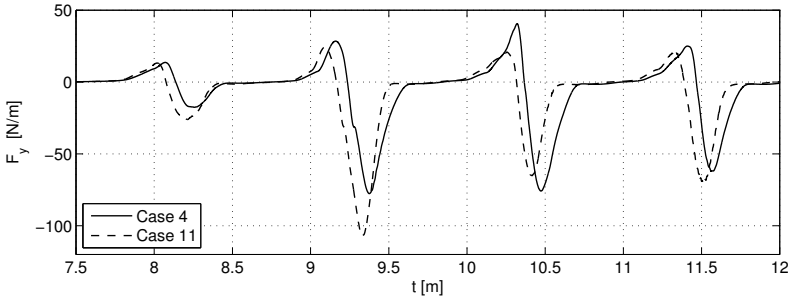

(c) Vertical force F_y

Figure 6.17: Effect of airgap increase: Simulated force history for Case 4 ($T = 1.11$ s, $\zeta_A = 0.05$ m and $\eta_D = 0.04$ m) and 11 ($T = 1.11$ s, $\zeta_A = 0.07$ m and $\eta_D = 0.06$ m), i.e. two cases with same airgap exceedance of 0.01 m.

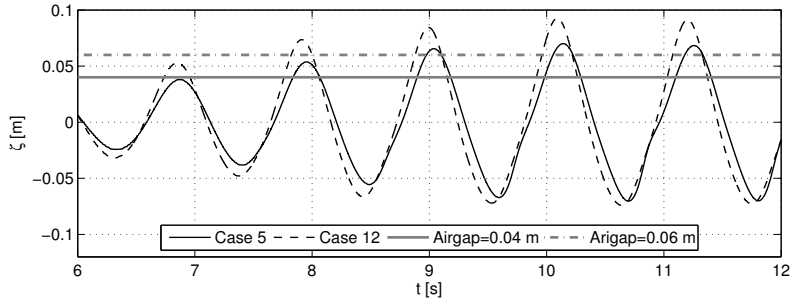

(a) Incoming wave when deck box is present, measured 15 cm in front of the box.

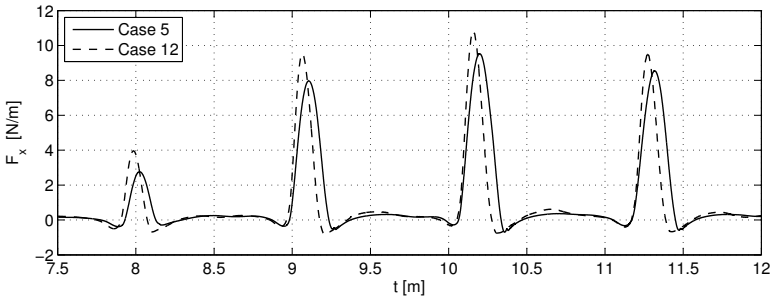

(b) Horizontal force F_x

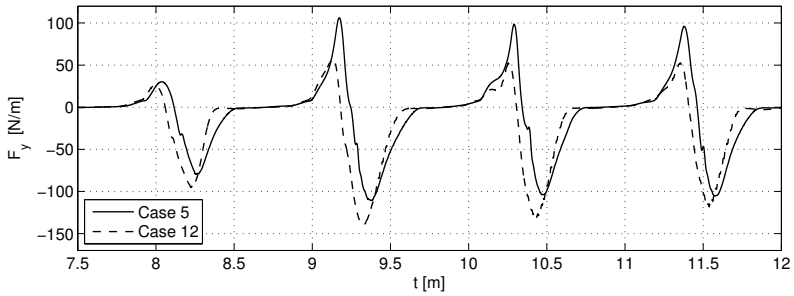

(c) Vertical force F_y

Figure 6.18: Effect of airgap increase: Simulated force history for Cases 5 ($T = 1.11$ s, $\zeta_A = 0.06$ m and $\eta_D = 0.04$ m) and 12 ($T = 1.11$ s, $\zeta_A = 0.08$ m, and $\eta_D = 0.06$ m), i.e. two cases with same airgap exceedance of 0.02 m.

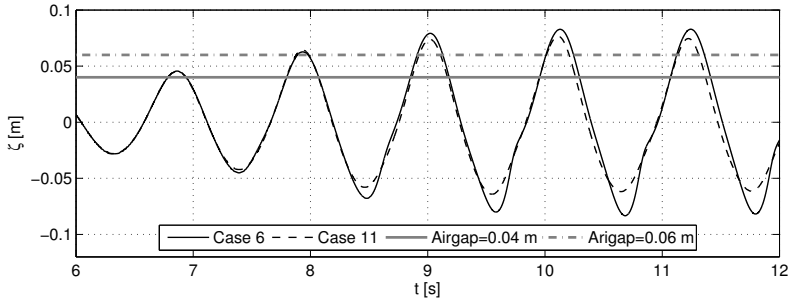

(a) Incoming wave when deck box is present, measured 15 cm in front of the box.

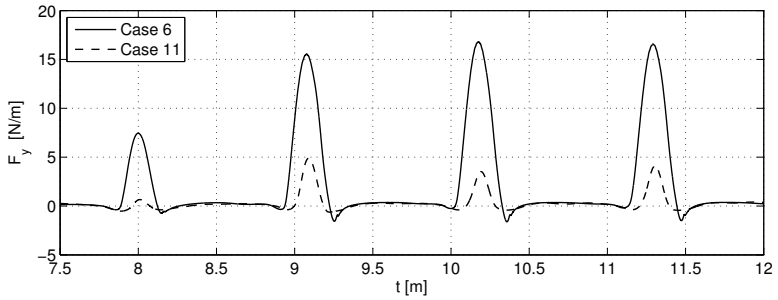

(b) Horizontal force F_x

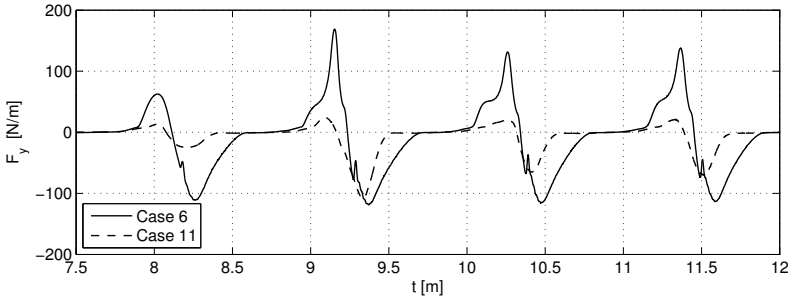

(c) Vertical force F_y

Figure 6.19: Effect of airgap increase: Simulated force history for Cases 6 ($T = 1.11$ s, $\zeta_A = 0.07$ m, $\eta_D = 0.04$ m) and 11 ($T = 1.11$ s, $\zeta_A = 0.07$ m, $\eta_D = 0.06$ m), i.e. the same wave for two different deck heights.

6.3.5 Numerical error sources

The experimental error sources are discussed in Sec. 6.2.3. Although some are discussed before, the errors in the numerical model that is assumed to affect the wave impact simulations are summed up here:

Finite surface layer thickness As mentioned earlier, the surface layer has a finite thickness that increase during simulations. In Sec. 5.4.4, it is shown that the velocities in the crest are affected by this. Also, the mass density of the water is reduced in the surface layer. It is difficult to predict what the combination of these two effects has on the computed forces.

Body boundary condition The body is modeled using the body density function, and the body boundary condition is enforced using Eq. 3.31. This inherently gives an uncertainty of one cell for the velocity at the body boundary, which is thus not an exact no-slip condition. However, since the deck box is fixed and has a simple geometry, the grid is set up along the body boundaries to reduce this uncertainty in the present case.

Reflections from wavemaker and damping zone Since the computational domain is set up as a numerical wave tank, reflections from the beach and wavemaker must be considered. The numerical beach is assumed to be quite effective. Moreover, the length of the tank enables relatively long simulations before reflections come back to the deck box. The fact that the deck box is placed only two wave lengths from the wavemaker is a greater challenge. The simulations are usually not run for more than 3 or 4 impact events, and reflections from the wavemaker are thus avoided.

Length of deck box In the experiments, the total length of the deck box is $L = 0.65$ m, while the deck plate where the force is measured is $L_B = 0.63$ m. In the simulations, $L_B = 0.63$ m is chosen. This means that there may be a discrepancy in the computed flow compared to experiments during the impact events. Relative to other uncertainties, this is however assumed to have minor effect on results.

6.4 Comparison of results for the glass flume experiments

In this section, the numerical results are compared with the experimental results from the glass flume experiments. In addition to measured data, observations of the impact process documented in Baarholm (2001) is used. Also, some high-speed videos of wave impacts in deck are available. These videos were taken at a later time than the actual experiments, and the wave conditions and airgap were not registered for the videos. However, the pictures illustrates the flow during the impacts quite well, and a qualitative comparison with the simulations is therefore presented. Note that when comparing the measured and computed force histories, only the 3-4 first impacts are used. In the numerical model, inaccuracies increase during simulation both due to surface layer growth and disturbances due to reflections from the wave maker, see Sec. 6.3.5. It is also assumed that the 2D conditions in the experiments are weakened with time.

6.4.1 Details of the impact process

Details of the simulated impact process are discussed and compared with experimental observations and snapshots from the high-speed video recordings. Fig. 6.20 shows the computed force history for the second impact of Case 5 (see Tab. 6.4). Figure 6.21 shows the corresponding computed free surface (defined as $\phi_1 = 0.5$) at the deck box. Figures 6.22 and 6.23 show still pictures from the high-speed video at selected situations during an impact.

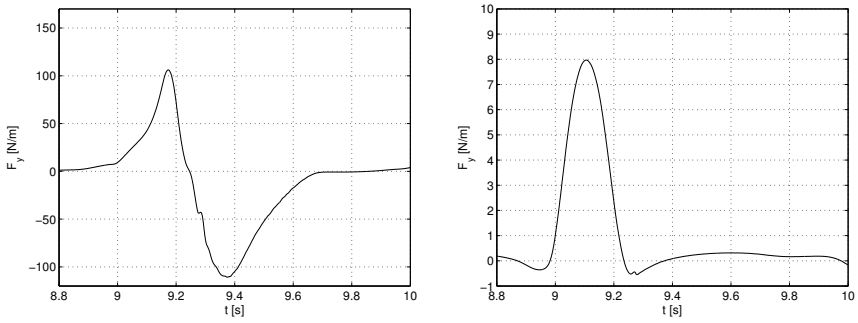

(a) Vertical force F_y (b) Horizontal force F_x

Figure 6.20: Simulated force history for Case 5, second impact.

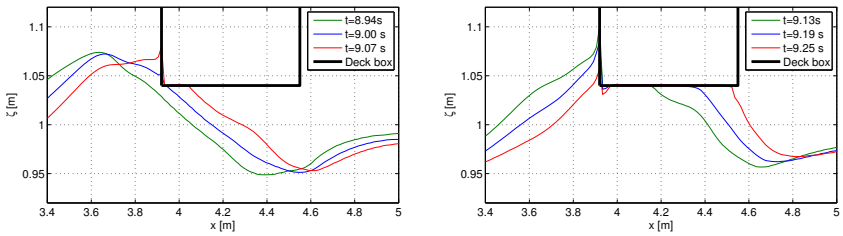

(a) $t = 8.94 - 9.07$ s

(b) $t = 9.13 - 9.25$ s

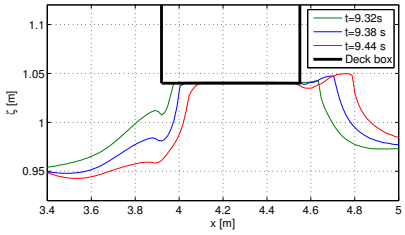

(c) $t = 9.32 - 9.44$ s

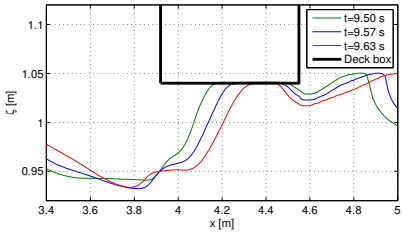

(d) $t = 9.50 - 9.63$ s

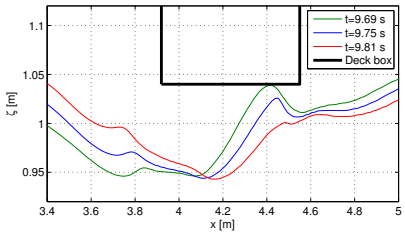

(e) $t = 9.69 - 9.81$ s

Figure 6.21: Computed free surface during impact. Maximum and minimum vertical force occurs at $t = 9.17$ s and $t = 9.37$ s, respectively. Maximum horizontal force occurs at $t = 9.11$ The small discontinuity in the vertical force (see Fig. 6.20) occurs at $t \approx 9.25$ s, i.e. when the water separates from the front end of the deck.

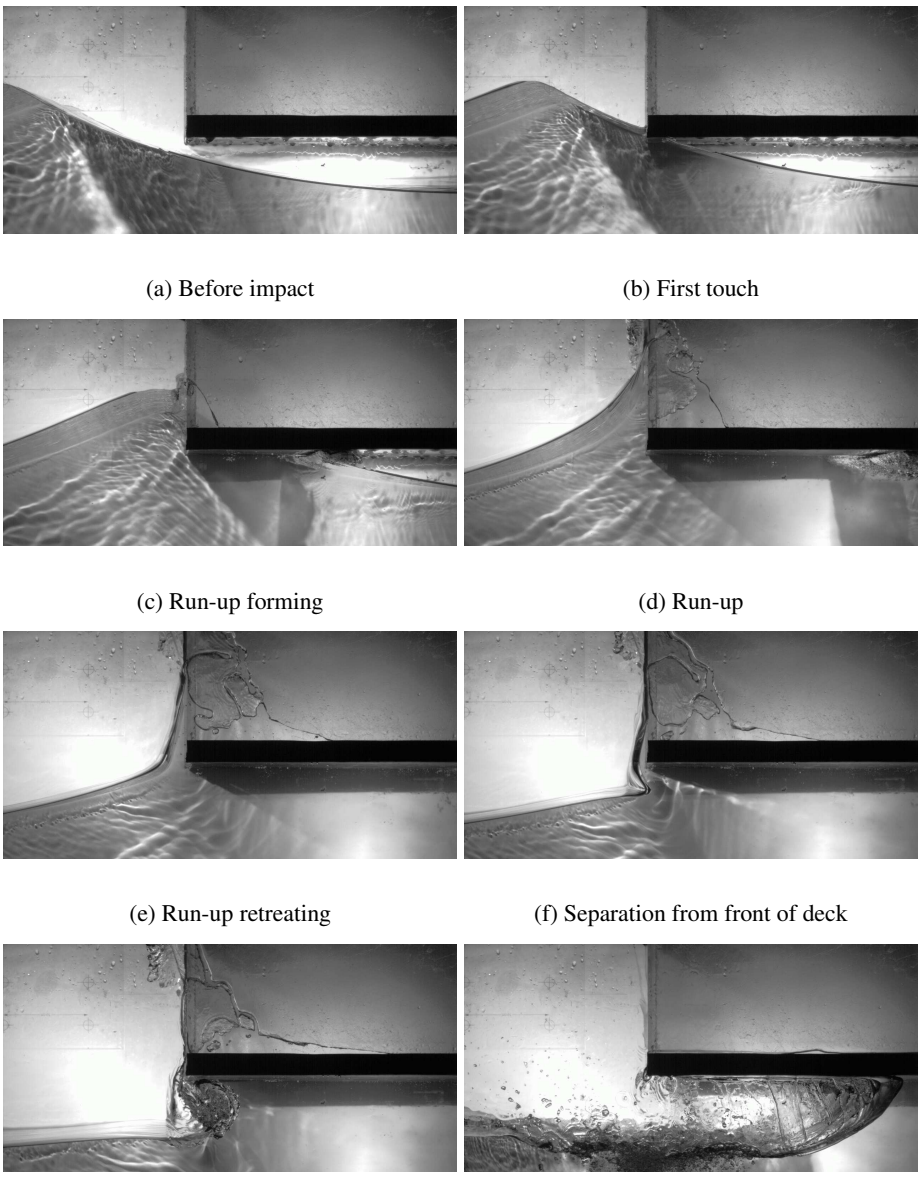

(a) Before impact

(b) First touch

(c) Run-up forming

(d) Run-up

(e) Run-up retreating

(f) Separation from front of deck

(g) Vortex forming during separation

(h) Front detachment finished

Figure 6.22: Still pictures from high-speed video for different situations during entry phase of impact. The pictures show the front end of the deck box. Photo: Rolf Baarholm and Trygve Kristiansen.

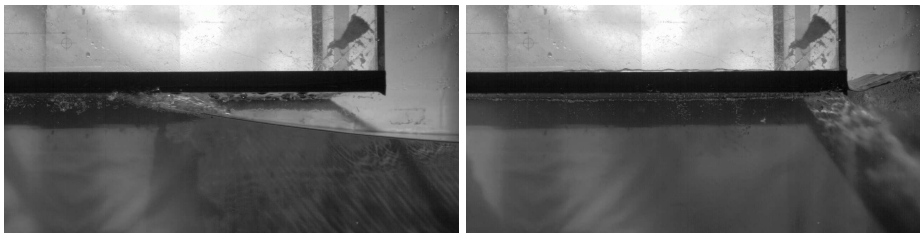

(a) Jet flow underneath deck

(b) Tangential flow from deck end

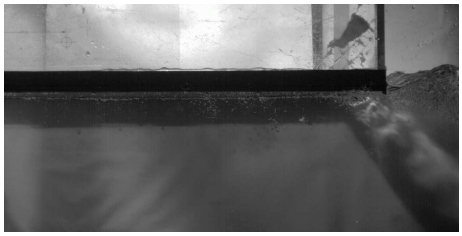

(c) Upwelling behind the deck

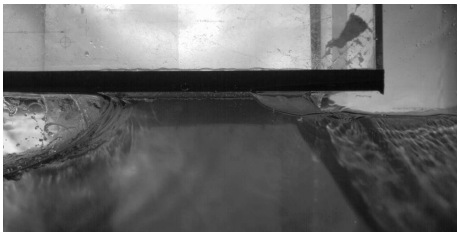

(d) Separation from aft end of deck

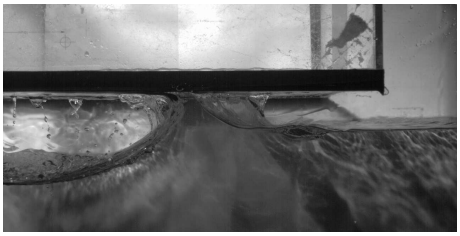

(e) Exit phase

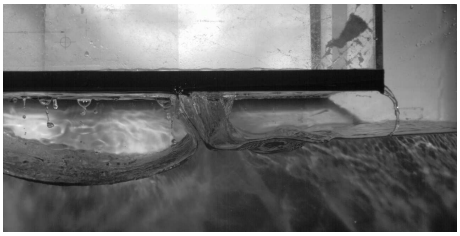

(f) Final detachment

Figure 6.23: Still pictures from high-speed video for different situations during exit phase of impact. The pictures show the aft end of the deck box. Photo: Rolf Baarholm and Trygve Kristiansen, NTNU.

Observations from the simulations and experiment can be summarized as follows:

- There is a small force build-up before the computed free surface reaches the deck box at $t = 9.0$ s. This effect is due to the finite surface layer thickness, and is not a physical effect.
- The duration and development of the horizontal force corresponds as expected with the computed duration of the run-up.
- Large surface curvatures are computed as the wave separates from the front end of the deck, see Figs. 6.21(b) and 6.21(c). This was also observed in the model tests, where a vortex was formed at the front corner, see Figs. 6.22(f) and 6.22(g). The event is seen as a small discontinuity in the vertical force history at $t \approx 9.25$ s.
- In the model test, a jet was observed as the wave propagates underneath the deck, see Fig. 6.23(a). This is not observed for the computed free surface, at least not along the $\phi_1 = 0.5$ contour, see Fig. 6.21(b).
- No distinct second impact is observed in the simulations for this case.
- When the wave reaches the aft end of the deck, the water leaves the deck tangentially. After some time, an upwelling in the free surface is seen behind the deck, see Fig. 6.21(c) and 6.21(d). This behavior was also observed in the experiments, see Figs. 6.23(b) and 6.23(c).
- The position of the final detachment point is at approximately $3/4L$ from the front of the deck, see Fig. 6.21(e). This was also observed during model tests. However, the computations show less surface curvature and a somewhat faster detachment than the experiments, see Figs. 6.23(d)-6.23(f).

6.4.2 Comparison of simulated and measured vertical forces

In this section, the simulated and measured vertical force histories are compared. The two cases used in the discussions in Sec. 6.2.4 (i.e. Cases 5 and 8) are also used here to illustrate some main trends. Comparisons for all the 12 cases in Tab. 6.4 are given in App. C. Unless otherwise noted, the measured force history is low-pass filtered with a cut-off frequency of 10 Hz (see discussion in Sec. 6.2.4).

Figure 6.24(b) shows the simulated vertical force compared with the measured force history for Case 5. Figure 6.24(a) shows the corresponding wave elevation 15 cm in front of the deck. Figure 6.25 shows close-ups of the first four impact

events for the same case. For the first impact, the simulated wave is significantly lower than the measured wave. This is due to the overshoot in the wave flume and a slower up-ramping in the numerical wave tank, as discussed in Sec. 5.4.5. For the first impact, the magnitude of the simulated maximum and minimum force peaks is thus significantly lower than the corresponding measured peaks. For the next three peaks, the wave crest heights are more comparable, and so are the force peak magnitudes.

For both simulations and experiments, there is clearly a difference in the force history between the first impact and the consecutive impacts. In the experimental results, the force history has two distinct peaks. This behavior is not well captured in the CIP simulations. For the second impact, the first positive peak is only barely present in the CIP simulations. This may be explained by the relatively mild first impact giving less disturbance of the wave. For the third and fourth impact (at $t = 10$ s and $t = 11$ s), the magnitude of the first peak is better captured by the simulations , but two separate peaks are not present. It should however be recalled that the structural oscillations of the model also render some uncertainties of the measured force history for this case. The negative force peak seem to be captured for impacts nos. 2-4. The small discontinuity in the force history at the time when the wave detaches from the front end of the deck seem to be a physical effect as discussed in Sec. 6.4.1. The duration of the exit phase is however generally somewhat underestimated by the CIP simulations. The grid dependency test indicates that this may parlty be due to too low grid resolution, see discussion in Sec. 6.4.3. Another reason may be discrepancies in the incoming wave. The measured wave is somewhat fuller than the simulated wave.

Figure 6.26(b) shows the simulated vertical force compared with the measured force history for Case 8. Figure 6.26(a) shows the corresponding wave elevation 15 cm in front of the deck. Figure 6.27 shows close-ups of the first four impact events. The wave period is longer for this case than for the previous case. For a given crest height and airgap, the maximum vertical force increases with increasing period due to more rapid wetting of the deck (Baarholm, 2008). This is confirmed both by simulations and experiments.

Comparing the force history for the consecutive impact events for Case 8 and Case 5, the positive force no longer has two peaks for Case 8. The magnitude of the peak is far greater for the consecutive impacts than for the first impact for Case 8. Comparing the simulations with the experimental results, the agreement is generally better for this case than for Case 5. The computed wave crest of the first impact event is somewhat disturbed in the simulations due to the previous wave (at $t = 8$ s). This may explain why the first positive force peak is relatively high compared to experiments. The negative peak value for the first wave is less for the simulations than for the experiments, as expected. For the next three impacts,

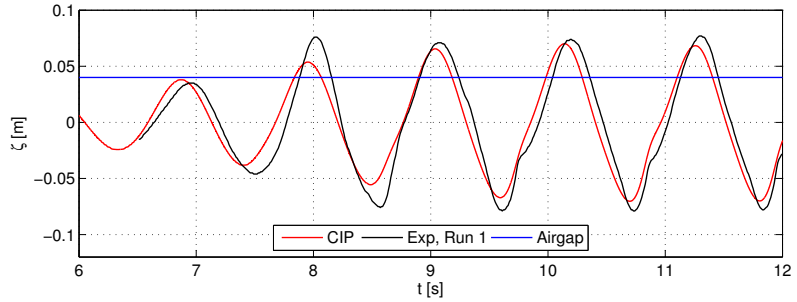

(a) Wave elevation 15 cm in front of deck box.

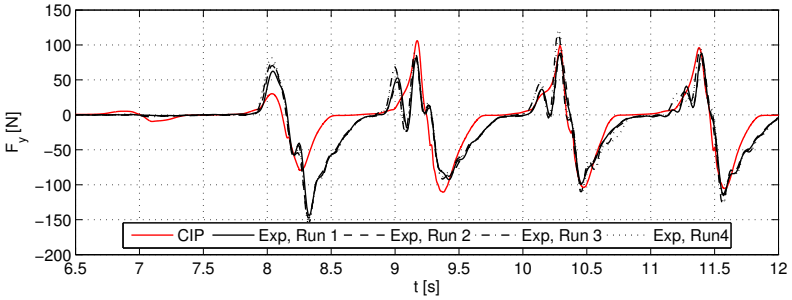

(b) Vertical force history F_y

Figure 6.24: Measured and simulated wave elevation and force history for Case 5 ($\zeta_A = 0.06$ m, $T = 1.11$ s and $\eta_A = 0.04$ m).

the simulated and measured incoming waves correspond better, and the agreement between the simulated force history and the experimental results is relatively good.

Tab. 6.5 shows the measured and simulated maximum and minimum vertical forces for the Cases 2, 5 and 8. For the experimental values, the average of the available repetitions are used. For Case 2, experimental results filtered with cut-off frequency of both 5 and 10 Hz are shown. For all the cases with wave period of $T = 1.00$, measured and simulated maximum peak force agrees better with $f_c = 5$ Hz, see also Figs. C.1–C.7.

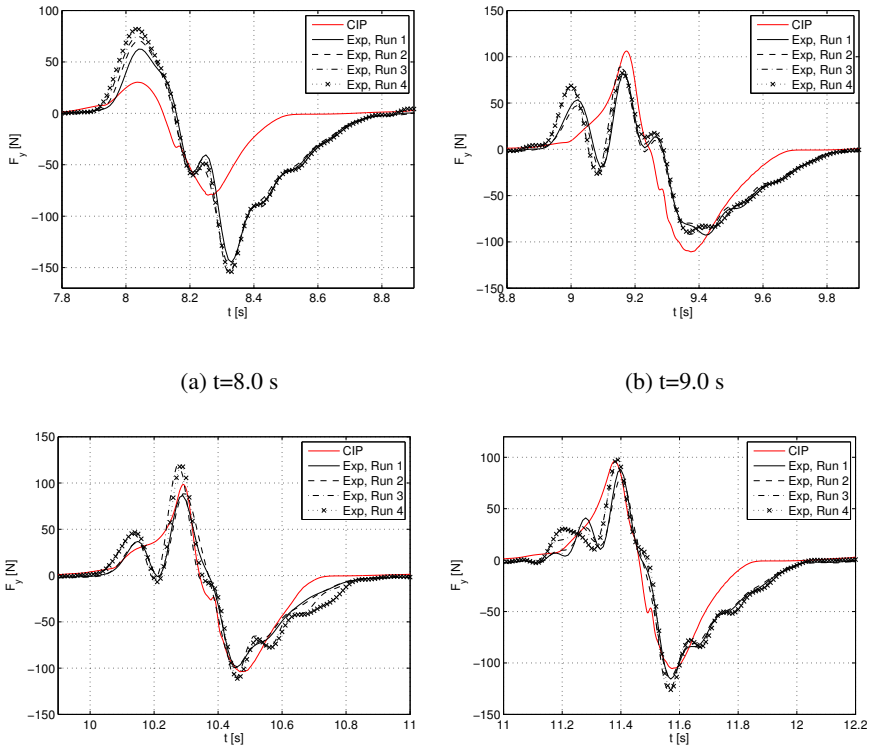

(a) t=8.0 s

(b) t=9.0 s

(c) t=10.0 s

(d) t=11.0 s

Figure 6.25: Measured and simulated vertical force for the first four impact events for Case 5 ($\zeta_A = 0.06$ m, $T = 1.11$ s and $\eta_A = 0.04$ m).

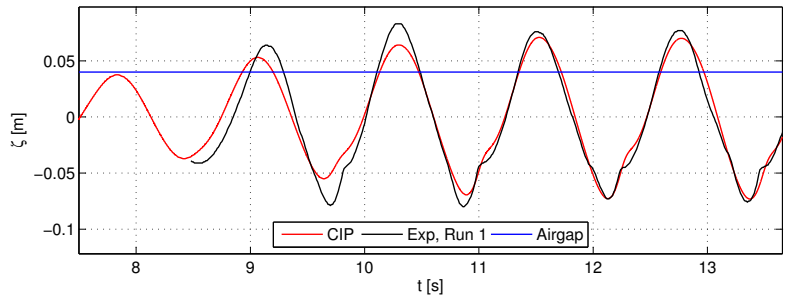

(a) Wave elevation 15 cm in front of deck box.

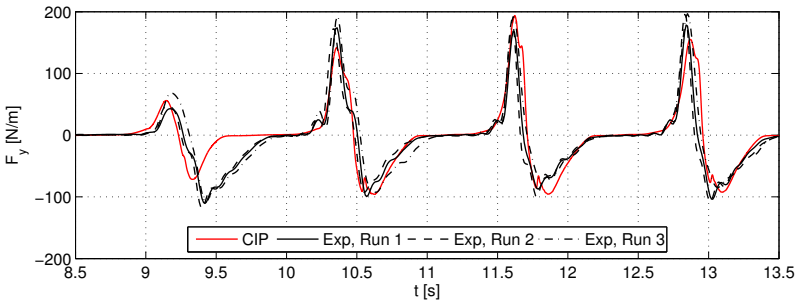

(b) Vertical force history F_y

Figure 6.26: Measured and computed wave elevation and force history for Case 8 ($\zeta_A = 0.06$ m, $T = 1.25$ s and $\eta_A = 0.04$ m).

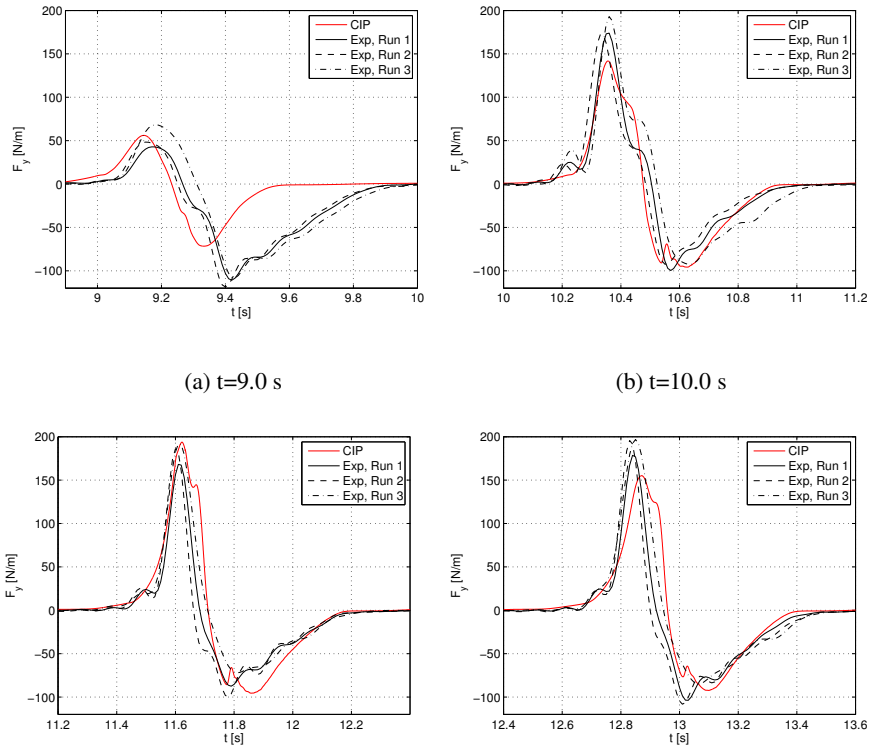

(a) t=9.0 s

(b) t=10.0 s

(c) t=11.0 s

(d) t=12.0 s

Figure 6.27: Measured and simulated vertical force for the first four impact events for Case 8 ($\zeta_A = 0.06$ m, $T = 1.25$ s and $\eta_A = 0.04$ m).

Table 6.5: Comparison of measured and simulated maximum and minimum vertical forces for three impact events. The first event is not included. For the experimental values, the average of all available repetitions is used. The difference between the experimental and simulated values are given as the ratio between the two. Case numbers correspond to Tab. 6.4. For Case 2, experimental values are given for $f_c = 5$ Hz and 10 Hz, for the rest of the Cases, $f_c = 10$ Hz.

		Max. F_y [N/m]		
Case	Impact no.	Exp.	CIP	CIP/Exp. ratio
2	2	78.2	40.6	0.52
	3	56.5	38.4	0.68
	4	60.7	38.7	0.64
2	2	73.9	40.6	0.55
(5 Hz)	3	42.5	38.4	0.90
	4	49.2	38.7	0.79
5	2	85.1	106.2	1.25
	3	102.8	98.48	0.96
	4	89.2	96.06	1.08
8	2	179.7	141.8	0.79
	3	182.1	193.7	1.06
	4	190.3	155.1	0.82

		Min. F_y [N/m]		
Case	Impact no.	Exp.	CIP	CIP/Exp. ratio
2	2	105.6	118.5	1.12
	3	89.3	99.4	1.11
	4	98.0	99.4	1.01
2	2	102.1	118.5	1.16
(5 Hz)	3	89.6	99.4	1.11
	4	102.1	99.4	0.97
5	2	90.5	110.2	1.22
	3	104.8	103.8	0.99
	4	120.7	105.7	0.87
8	2	94.8	95.7	1.01
	3	86.5	95.6	1.11
	4	98.9	92.3	0.93

The comparison of the vertical force using CIP simulations and experimental results can be summarized as follows:

- There is clearly a difference between the first impact after airgap exceedance and the consecutive impacts. The disturbed wave leads to greater positive peak forces for the consecutive impacts. This effect is seen both in the numerical and in the experimental results.
- The presence of a double positive peak force is dependent on the wave period, see Fig. 6.24(a) and 6.26(a). The CIP simulations does not capture the first peak well. There are however some uncertainties in the measured data related to the filtering for the cases with double peaks.
- The agreement between simulations and experiments is poorest for the impact cases with the smallest airgap exceedance, see Figs. C.1, C.9, C.16 and C.23. This is to be expected, since uncertainties and inaccuracies in both the numerical and experimental results are greater relative to the force magnitude.
- The first impact is often underestimated by the CIP method due to differences in the first wave.
- The simulation of the consecutive peaks are challenging since the force is dependent on the previous impact. An example is seen in Tab. 6.5. The agreement between measured and simulated force of the second positive peak is often poor, because of large discrepancies in the incoming wave for the first impact event.
- The overall agreement between simulations and experimental results is best for $T = 1.25$ s. For this excitation period, the structural oscillations of the model seems to be less than for the other excitation periods. This minimizes the uncertainty due to filtering for the measured forces.
- For the cases with $T = 1.00$ s, the agreement between simulations and experiments are better when the measured force histories are filtered with $f_c = 5$ Hz, see Figs. C.1–C.7
- The CIP method captures the small discontinuity in the force occurring when the wave detaches from the front end of the deck.
- Comparing both computed incoming wave and vertical force, it is seen that when the computed incoming wave agrees with the measured incoming wave, the agreement is generally good also for the vertical force history.

- The discrepancy between the measured and simulated positive force peak is large in some cases, but is mostly in the order of 20% or less (see Tab. 6.5). Taking the discussed uncertainties into consideration, such an uncertainty can be expected. For the negative force peak, the discrepancy is usually about 10%.

- The duration of the exit phase is however often underestimated by the simulations.

6.4.3 Discussion on grid refinement

As mentioned in Sec 6.3.1, some simulations are run with a finer grid at the deck box. This gave somewhat higher force peak values and longer duration of the exit phase. Fig. 6.28 shows the computed force history for both grids compared with experimental results for an impact event of Case 5. The differences between the two grids are small compared to other uncertainties in the comparisons. The increased accuracy due to the refinement may thus not be worth the increased CPU time.

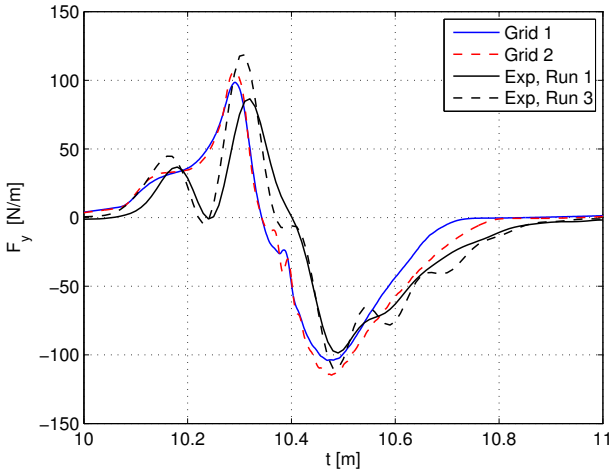

Figure 6.28: Grid dependency: Measured and simulated vertical force history for Case 5 ($T = 1.11$ s, $\zeta_A = 0.06$ m and $\eta_D = 0.04$ m).

6.4.4 Discussion on the filtering

The above comparison between simulations and experimental results has not given any more clarity on the uncertainties regarding filtering of the measured force time series because of assumed structural oscillations. To investigate the issue further, filtering of both the measured and the simulated time series is performed. First, a spectral analysis of the simulated force histories is performed. Figure 6.29 shows the spectrum for the measured and simulated vertical force for Case 5. To compare directly, only a part of the time series is used in the spectral analysis. Four consecutive impacts are included, i,e, about 4.5 s of the time series is used. Thus, for the spectrum of the measured force, the total energy content is less than in Fig. 6.6, where the entire measured time series is used. For the simulated case, there is no energy increase at 5-15 Hz as is seen for the measured force history, but there is some energy present in this frequency band also for the simulations. Note that the energy content at the excitation frequency and the double frequency is nearly equal for the simulations. For the measurements, the energy content at the double frequency is closer to half that of the excitation frequency, which is more as expected.

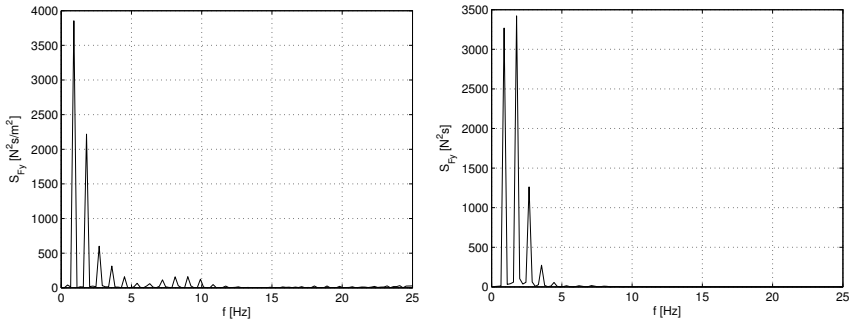

(a) Experiment (b) CIP simulations

Figure 6.29: Power spectrum of the measured and simulated vertical force history for 4 impacts of Case 5: $T = 1.11$ s, $\zeta_A = 0.06$ m and $\eta_D = 0.04$ m..

To investigate this further, the time series of both the computed and measured vertical force are low-pass filtered. Cut-off frequencies of 5 and 10 Hz are used. Also, the time series are band-pass filtered using a Gaussian window with limits of 5 and 15 Hz to examine the oscillations in this frequency range. Figures 6.30 and 6.31 show the unfiltered time series together with the filtered time series for $T = 1.11$ s and $T = 1.25$ s, respectively. The wave amplitude is $\zeta_A = 0.06$ m and

the airgap is $\eta_D = 0.04$ m for all cases. The first impact event and a later event are shown.

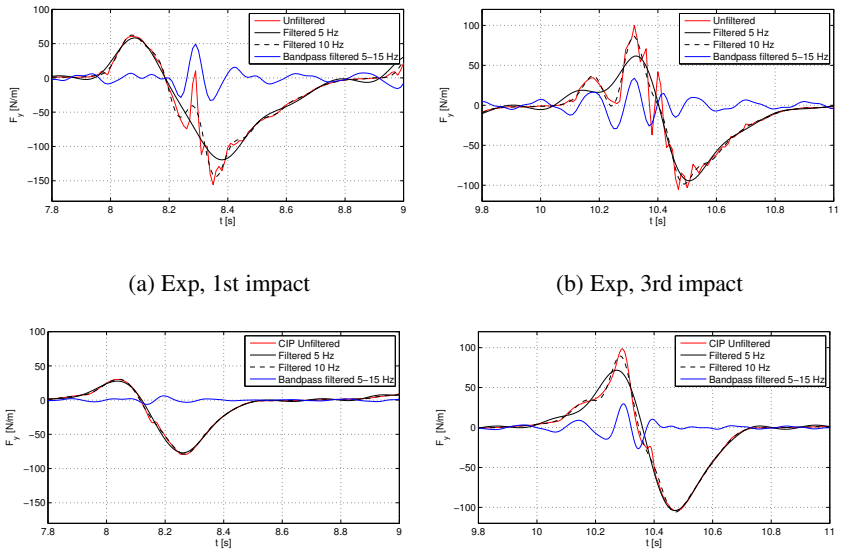

(a) Exp, 1st impact

(b) Exp, 3rd impact

(c) CIP, 1st impact

(d) CIP, 3rd impact

Figure 6.30: The measured and simulated vertical force history filtered at 5 and 10 Hz, and bandpass filtered with range 5-15 Hz. $T = 1.11$ s, $\zeta_A = 0.06$ m and $\eta_D = 0.04$ m.

The bandpass filtered time series show that during an impact event, oscillations at the frequency band of 5-15 Hz occur both in the experiments and in the simulations. Looking at the first impact, the oscillations seems to be triggered after the positive force peak, at the time when water detaches from the deck front. Large surface curvatures and a vortex forming at the front corner were observed for the separation (see Sec. 6.4 for a description of the flow). For the consecutive impacts, the oscillations seem to be triggered earlier. This may have connection with the second slam observed in the experiments. The oscillations are less for the simulations than for the experiments. This may indicate that the simulations do not capture all the physics of the impact event. It may also indicate that some of the oscillation observed for the experimental results are indeed due to structural oscillations at this frequency band, but also that some is part of the impact process.

The available information does thus not seem to be sufficient for resolving the nature of the measured force components in the range from 5-15 Hz.

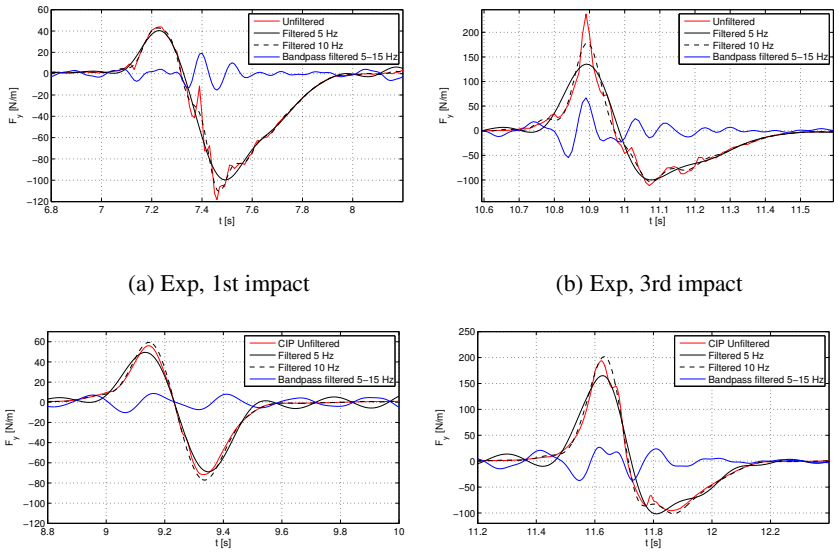

(a) Exp, 1st impact

(b) Exp, 3rd impact

(c) CIP, 1st impact

(d) CIP, 3rd impact

Figure 6.31: The measured and simulated vertical force history filtered at 5 and 10 Hz, and bandpass filtered with range 5-15 Hz. $T = 1.25$ s, $\zeta_A = 0.06$ m and $\eta_D = 0.04$ m.

6.5 Description of the experiment in the small towing tank

In August 2008, a new wave-in-deck experiment was performed in the small towing tank at MARINTEK (Baarholm, 2008, 2009). The experiment is part of the research work carried out within the Wave Impact Loads Joint Industry Project (JIP) lead by MARINTEK. The JIP has 9 industry participants including Statoil-Hydro. The global forces on the deck box were the main interest of the experiment. Both 2D and 3D conditions were tested. For the 3D tests, the effect of girders underneath the deck was studied, where position, number and size of the girders were varied. The 2D tests were performed for a smooth deck only. The author participated in parts of the experiment. The use of the results from the 2D tests in the present work has been allowed by the JIP steering committee. In this section, the experimental set-up and results are presented. The comparison between experimental results and simulations are presented in Sec. 6.7. The NWT used for the simulations and the comparison of undisturbed measured and simulated waves are presented in Sec. 5.5.

6.5.1 Experimental set-up

The small towing tank at MARINTEK is 25.0 m long, 2.8 m wide, and had a water depth of 1.0 m during the present experiment. A flap wavemaker is installed at one end of the tank, and a parabolic beach is used as a wave damping device in the other end. A prismatic box with a length and breadth of 0.70 m and a height of 0.35 m was installed in the middle of the tank. No substructure was installed. The assumption of negligible effects from the substructure is thus used for the present experiment as well. The model scale is taken to be 1:100, but in the present work, the model dimensions are used. All discussions of results and comparisons with CIP simulations are thus performed using model scale. Table 6.6 gives a summary of the model dimensions.

Table 6.6: Details of the experimental set-up in the small towing tank.

Wave tank length		25.00	m
Wave tank breadth		2.80	m
Water depth	d	1.00	m
Deck box length	L	0.70	m
Deck box breadth	B	0.70	m
Deck box height	H_{b}	0.35	m

A stiff frame of steal bars kept the deck box in place. The inside of the box is fitted with frames and stiffeners to ensure a stiff structure. Hydroelastic effects is considered negligible. Dynamometers consisting of six one-degree force gauges measured the force on the deck box in six degrees of freedom. The sampling frequency was 1200 Hz. The deck height relative to the mean water level was adjustable, such that tests with different airgaps could be performed. Two wave probes were installed. One was placed along the centerline of the tank, 0.43 m in front of the box. The other was placed 0.17 m from the side of the box, along its centerline. A copper tape at the middle of the front wall of the box measured the run-up on the box. Two copper tapes underneath the box measured the wetted deck length. The tapes were placed approximately 0.05 m on either side of the middle of the box. One measured the entire wetted length in the same way as for the glass flume experiment, while the other was divided into four segments, each covering one fourth of the deck. For the 2D tests, dummy elements were placed on either side of the deck box. A small gap was provided between the deck box and the dummy elements to avoid any load transfer between them. The gaps were covered with tape to ensure 2D conditions of the flow. The wave probe at the side of the deck box had to be removed for the 2D tests. Figure 6.32 shows sketches of the 2D experimental set-up. Figure 6.33 shows the arrangement of the force gauges

inside the deck box, and Fig. 6.34 shows pictures of the model rig including the steel frame and the dummy elements.

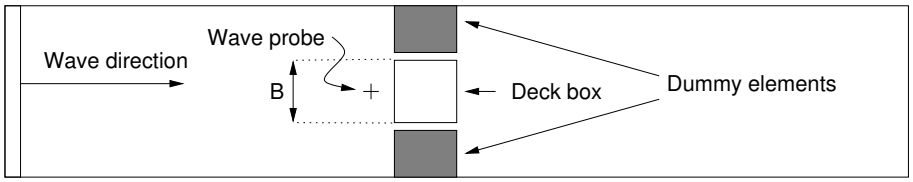

(a) Top view

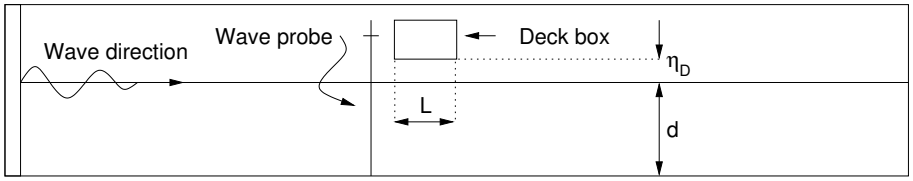

(b) Side view

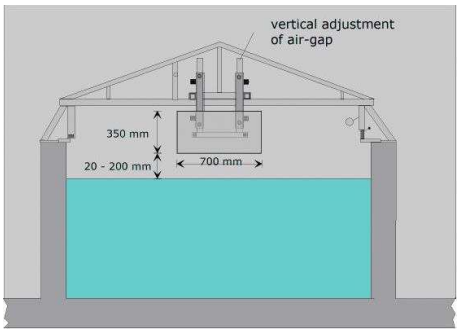

(c) Cross section view (Courtesy of MARINTEK)

Figure 6.32: Schematic overview of the 2D wave-in-deck experiment in the small towing tank.

For the 2D tests, two wave periods and two airgap heights were tested. As mentioned in Sec. 5.5, the wave crest ζ_C rather than the wave amplitude ζ_A was used as a target value when calibrating the waves. Wave crests from 0.10 m up to 0.16 m was used. A total of 13 different combinations were run, see Tab. 6.7. Repetitions were run for some of the cases.

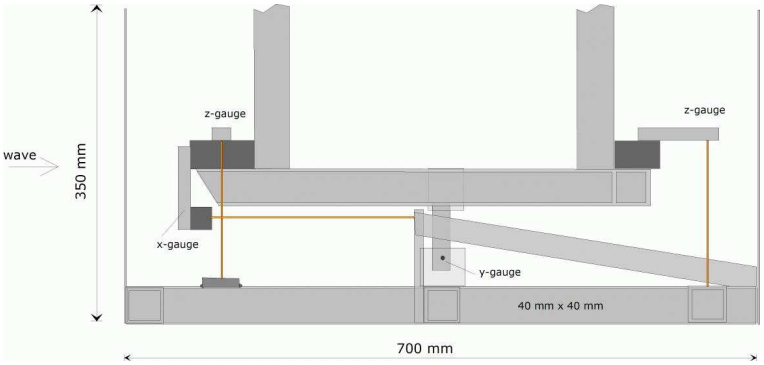

Figure 6.33: The arrangement of the force gauges inside the deck box (Courtesy of MARINTEK).

Table 6.7: Test cases for the experiments in the small towing tank. Only the target wave crest height was specified.

Case no.	Wave period T [s]	Wave crest ζ_C [m]	Airgap η_D [m]
1	1.3	0.110	0.08
2	1.3	0.120	0.08
3	1.6	0.100	0.08
4	1.6	0.110	0.08
5	1.6	0.120	0.08
6	1.3	0.110	0.10
7	1.3	0.120	0.10
8	1.3	0.160	0.10
9	1.6	0.100	0.10
10	1.6	0.105	0.10
11	1.6	0.110	0.10
12	1.6	0.120	0.10
13	1.6	0.160	0.10

6.5.2 Experimental results and filtering

During the experiment, structural oscillations of the rig were observed. The natural frequencies of the rig in air was measured. The lowest frequencies were 14.7 Hz and 25 Hz in the horizontal and vertical direction, respectively. Figure 6.35 shows typical spectra for the measured horizontal and vertical forces. Case 7 from Tab. 6.7 is chosen. Since the sampling frequency f_s is 1200 Hz, the resolution of the spectrum is far better than for the glass flume experiments. For the vertical force, there

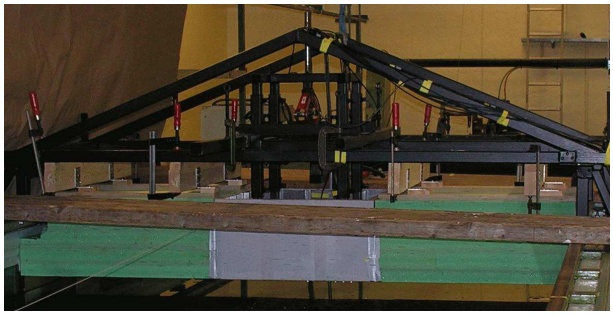

(a) Overview of rig set-up

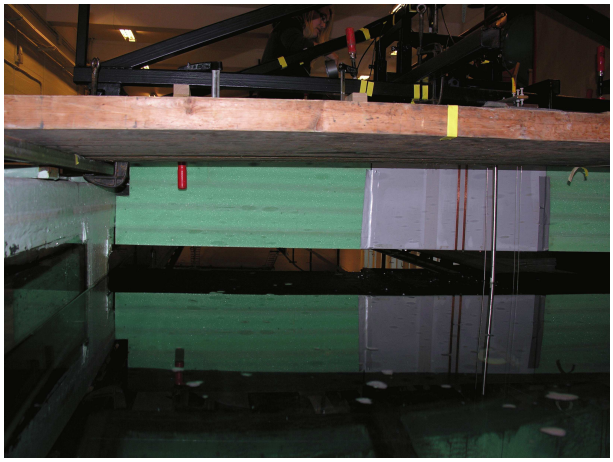

(b) Close-up of deck box

Figure 6.34: Pictures of rig set-up and instrumentation for the 2D experiment in the small towing tank. Photo: MARINTEK.

is an increase in energy at 5-15 Hz, especially for the with cases $T = 1.3$ s. For the horizontal force, there is some amplification at 5-10 Hz, but not as much as for the vertical force. Figure 6.36 shows the vertical and horizontal force history during an impact event for Case 8. The unfiltered time series are shown together with low-pass filtered force histories with cut-off frequencies of 8, 10 and 15 Hz. The first and second impacts are shown. As for the glass flume case, vertical oscillations are triggered during the water exit phase for the first impact, while they seem to be triggered earlier for the consecutive impacts. As before, it seems that for the frequency range of 5-15 Hz, a mixture of load components and response of the structure are present in the time series for the vertical forces. The horizontal forces

are generally not as sensitive to the cut-off frequency. A 8th order Butterworth low-pass filter with a cut-off frequency of 10 Hz is used in the further work.

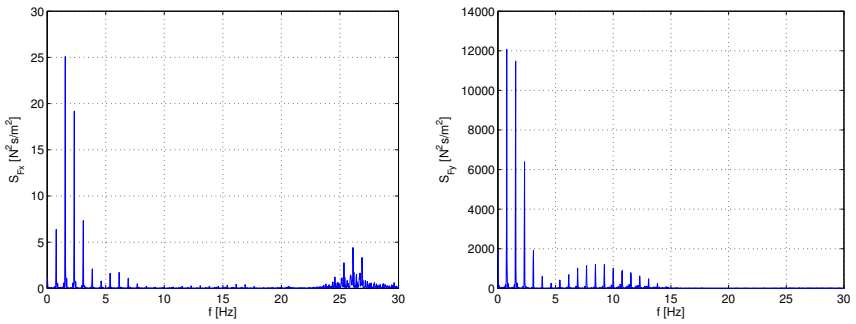

(a) Horizontal force F_x (b) Vertical force F_y

Figure 6.35: Spectra for the measured force history of Case 7. Sampling frequency is 1200 Hz.

The repeatability of the measured data is checked for two cases were two consecutive runs were performed. Figure 6.37 shows the measured incoming wave 0.43 m in front of the deck box, run-up at the front of the deck box, and horizontal and vertical forces for Case 7. There is a phase difference between the two runs, which is simply caused by different start time of the data logging. The phase difference will thus be ignored in the further work. As before, the time series are shifted to get the results in phase with each other. The incoming waves show good repeatability. The run-up varies somewhat more. For the horizontal force, the repeatability seems to be good, and not as sensitive to the run-up as might be expected. The positive peak of the vertical force varies somewhat more when taking into account the magnitude of the vertical force versus the horizontal force.

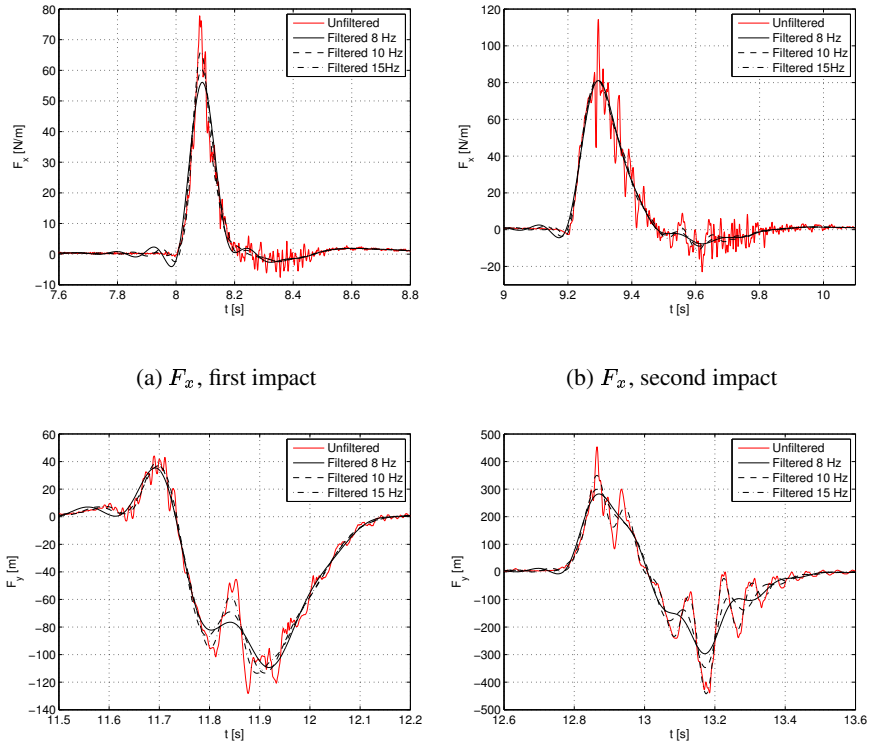

(a) F_x, first impact

(b) F_x, second impact

(c) F_y, first impact

(d) F_y, second impact

Figure 6.36: Filtering of the measured force histories using different cut-off frequencies for Case 8. Sampling frequency is 1200 Hz.

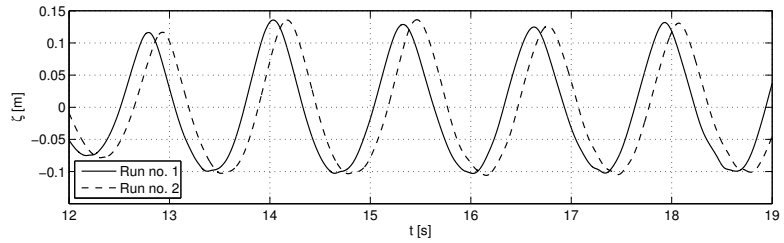

(a) Incoming wave ζ

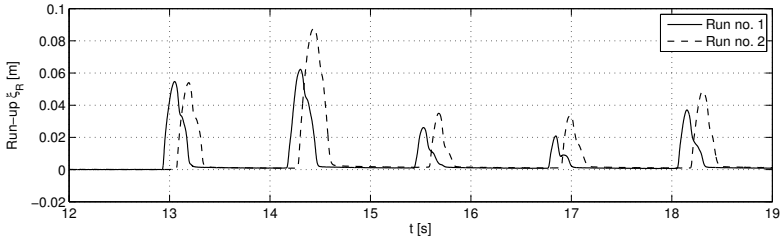

(b) Run-up at front end ξ_R

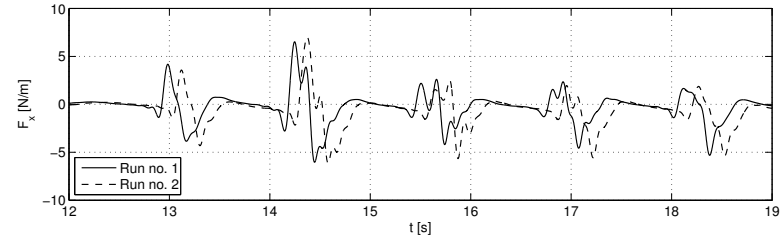

(c) Horizontal force F_x

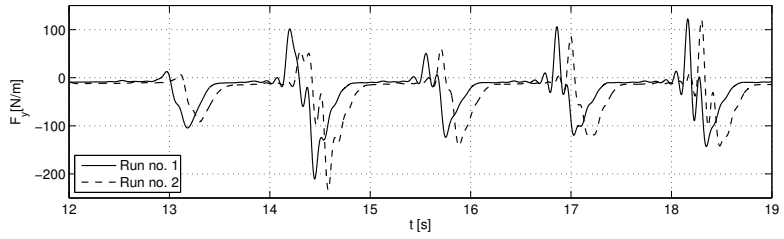

(d) Vertical force F_y

Figure 6.37: Repeatability of measured data: Incoming wave, run-up, horizontal and vertical force for Case no 7.

6.5.3 Error sources for the small towing tank wave impact experiments

As mentioned above, oscillations of the test rig were observed. From the spectral analysis of the force time series, it seems that the frequency of the structural oscillations overlap the frequency range where load components also are present. This was also the case for the glass flume experiment. In the present work, a simple low-pass filter is used. Alternative methods are to use system analysis tools to estimate the load on the force transducers or perform wavelet analysis.

Another error source touched upon earlier, is that 3D effects may be more important in the present experiment than in the glass flume case. Possible cross flow for the undisturbed waves are discussed in Sec. 5.5.3. The breadth of the tank corresponds approximately to the length of the shortest wave. Lateral waves were observed in the tank after some few impacts for all cases. For the glass flume experiments, three wetted deck devices were installed underneath the deck. The measurements were used to assess the flow conditions, see Sec. 6.2.3. In the present case, there are two such devices. One is however split into four segments, to obtain more accurate information of the position of the wave underneath the deck during impact. To compare the two measurements, the sum of the four segments can be used for the split wetted deck measuring device. However, this makes the comparison between the two somewhat more uncertain. Figure 6.38 shows the measured wetted length for the two sensors for Case 13. Taking the mentioned uncertainty into account, the agreement between the two sensors is satisfactory for the first four impacts. It is thus believed that 2D conditions are dominating, at least for the first few impacts. A discussion of the 3D versus 2D experimental results is given in Baarholm (2009).

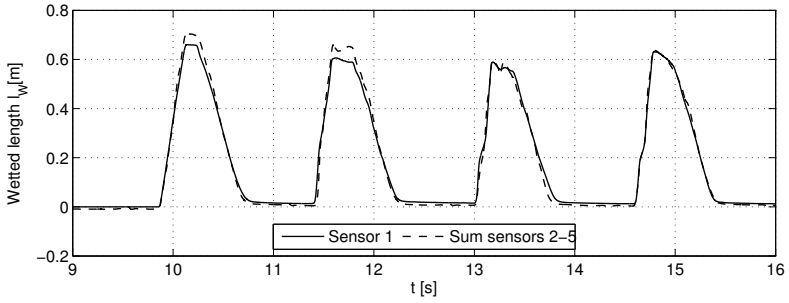

Figure 6.38: Measured wetted deck length for Case no 13.

The force gauges inside the box are set up to measure the forces in each direction independently. However, a coupling between the vertical and horizontal

force was detected during the tests. This has an effect on the measured negative horizontal force occurring during the exit phase of the impacts. The magnitude is somewhat too large due to the coupling, see e.g. Fig. 6.37(c).

Also, the horizontal forces measured in the 2D experiments are generally somewhat smaller (up to 10%) than those measured in the 3D experiments (Baarholm, 2008, priv. comm.). This is not as expected, as 3D conditions would probably reduce the force somewhat. The difference in horizontal forces for 2D and 3D is however assumed to be small. The effect seen in the measurements may be due to some load transfer to the dummy elements. The measured horizontal forces are compared with simulated forces in Sec. 6.7. It is seen that the simulated forces are somewhat larger than the measured, see Fig. 6.54.

6.6 The numerical model for the small towing tank experiments

In this section, the numerical model of the small towing tank experiment is presented. The work on this model is not as extensive as for the glass flume experiments. Fewer cases are simulated. The grid dependency test is limited. The main interest for the present simulations, is the possibility to compare the simulated and measured horizontal loads in addition to the vertical loads that were studied for the glass flume case. The run-up at the front of the deck box is also of interest in this connection.

The NWT is built up in the same way as for the glass flume case. There is however a difference in the up-ramping scheme and wave calibration strategy, as discussed in Sec. 5.5. In the present model, two up-ramping schemes are used. The first is the linear up-ramping used in the previous case. The second is a parabolic up-ramping that better matches the up-ramping of the waves in the tank. An attempt is thus made to model the first wave causing impact more accurately than in the glass flume case.

Another issue that is notable compared to the glass flume experiments, is that the wave steepness for some of the waves is significantly higher for the present case than for the glass flume case. It is interesting to study how the CIP method performs for steeper waves (see Tabs. 5.5 and 5.8). This issue is partly discussed in Sec. 5.5. The main conclusions are that the wave amplitudes are not as regular for the steep waves, not only in the simulations but also for the measured waves. Together with discrepancies between target and measured wave crest, this means that the match between the measured and simulated undisturbed waves are not as good for the present experiment as for the glass flume experiments. The consequences of these issues on the wave impact analysis are discussed in Sec. 6.7.

6.6.1 Grid configuration and grid dependency

Two grid configurations are used in the analysis. The base case grid divides the length of the deck box into 35 cells, while a finer grid uses 50 cells. The vertical refinement is the same as for the previous grids. The details of the two grids are given in Fig. 5.18 and Tab. 5.9. The purpose of the grid dependency test is to check that the somewhat reduced discretization of the deck box gives sufficient accuracy. The deck box was placed approximately two wave lengths from the wavemaker using the longest wave with wave length ($\lambda = 3.85$ m). The front of the deck box is thus placed 7.7 m from the wavemaker. The wave elevation is computed 0.43 m in front of the box, corresponding to the position of the wave probe in the wave tank.

A grid dependency test is performed for test case no. 9, i.e. $T = 1.6$ s, $\zeta_C = 0.1$ m and $\eta_D = 0.10$ m. The simulated incoming wave elevation (i.e. with deck box present) and horizontal and vertical force on the deck box for the two grids are shown in Fig 6.39. For this case, the wave barely touches the deck, making it a somewhat awkward example for the horizontal force. It is however seen that the differences between the two grids are small. As discussed in Sec. 5.5, using the fine grid gives a large model and thus slow simulations. The coarsest grid is therefore used in the rest of the simulations. The present grid dependency test shows that this grid give similar accuracy as the somewhat finer grids used for the previous NWT's.

6.7 Comparison of results for the small towing tank experiment

In this section, the CIP simulations are compared with the experimental results. The main focus is the horizontal and vertical loads on the deck box. The incoming wave elevation and the run-up at the front end of the box are also compared. Cases 7, 8, 12 and 13 in Tab. 6.7 are used for the comparison.

Figures 6.40–6.42 show the incoming wave, run-up, horizontal force and vertical force for Case 7. For this case, the agreement between the measured and simulated incoming wave is poor for both up-ramping schemes. The first simulated wave is too low compared to the measured waves, and the run-up and forces are thus underestimated too. It should also be noted that the resulting run-up and forces are quite small for this case. As seen in Sec. 6.4, the moderate impacts are more difficult to model correctly.

Figures 6.43–6.45 show the incoming wave, run-up, horizontal force and vertical force for Case 8. For this case, the wave crest height of the first wave is

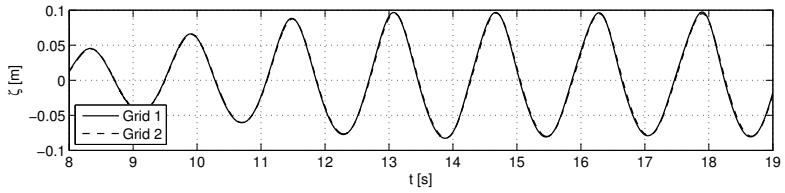

(a) Incoming wave

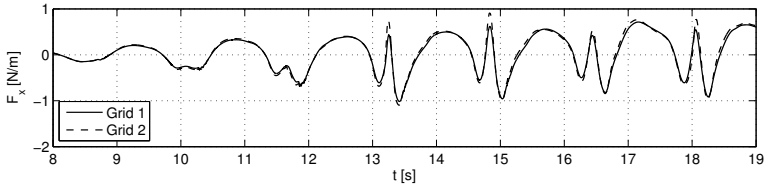

(b) Vertical force F_y

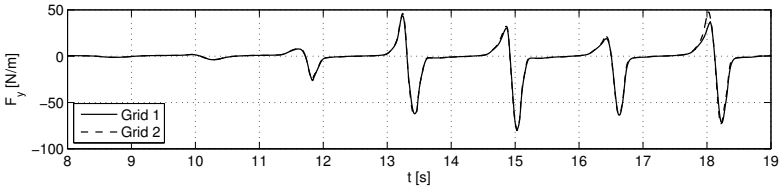

(c) Horizontal force F_x

Figure 6.39: Grid dependency test: Simulation results for case no. 9. Grid 1 (base case) and Grid 2 (refined) denotes the two grids specified in Tab. 5.9.

somewhat too high for the parabolic up-ramping scheme, and too low for the linear scheme. Also, the shape of the measured wave is somewhat distorted and quite steep compared to the simulated wave. The run-up is thus as expected too high for the parabolic scheme, and too low for the linear scheme, but for the horizontal force, both simulations underestimates the force. This may be due to the steepness of the measured wave, causing a large impact. For the second wave (at t=9 s), the linear up-ramping scheme provides a wave that is in fair agreement with the measured wave. Figure 6.46 shows close-ups of the measured and simulated incoming wave, run-up and forces for this impact. The run-up and horizontal force is underestimated by the CIP model, while the vertical force is overestimated. Differences in the previous impact may be a reason for the discrepancy.

Figures 6.47–6.49 show the incoming wave, run-up, horizontal force and ver-

tical force for Case 12. For the first wave, the linear up-ramping scheme matches the crest height, although the shape of the wave is somewhat different. Figure 6.50 shows close-ups of the measured and simulated incoming wave, run-up and forces for this impact. The simulated run-up and horizontal force is in fair agreement with the measurements, while the vertical force is overestimated.

Finally, Figures 6.51–6.53 show the incoming wave, run-up, horizontal force and vertical force for Case 13. For the first wave, the parabolic up-ramping scheme matches the measured crest height and the shape of the wave quite closely. Figure 6.50 shows close-ups of the measured and simulated incoming wave, run-up and forces for this impact. The simulated run-up and horizontal force is in fair agreement with the measurements. As mentioned earlier, there is a coupling between the measured horizontal and vertical force causing the measured negative horizontal force to be overestimated. The positive vertical force peak is somewhat overestimated, but less than for the previous case.

Since the match between the simulated and measured incoming wave often is poor, scatter plots of forces and run-up versus wave elevation are presented in Figs. 6.55 and 6.56 for $T = 1.3$ s and $T = 1.6$ s, respectively. Also, scatter plots of the maximum horizontal and vertical force versus run-up is shown in Figs. 6.57 and 6.58. It should be noted that the impacts are influenced by the previous impact, so the scatter plots must be examined with this in mind.

The comparison between experiments and simulations can be summarized as follows:

- Trying to match the incoming waves during up-ramping is challenging when the wavemaker motion is unavaiable.
- As seen before, the previous impact affects the upward force peak of the vertical force. This effect is also seen for the positive horizontal force, which also increases for consecutive impacts. The CIP method seems to capture this effect also for the horizontal forces, see e.g. Fig. 6.48(b).
- The positive vertical peak force seems more sensitive to small changes in the flow than the horizontal peak force. This may however be due to the structural oscillations, which are more pronounced for the vertical loads than for the horizontal loads.
- For the case with a good match for the first incoming wave (Case 13), the simulated run-up, horizontal and vertical force are in fair agreement with measurements, see Fig. 6.54.
- The scatter plots show a reasonable match between the measured and simulated run-up, maximum F_x and maximum and minimum F_y as a function

of the crest height of the incoming wave. The simulated horizontal force is somewhat greater than the measured force (see Fig 6.56(b)). This may be due to some load transfer to the dummy elements, see discussion in Sec. 6.5.3.

- Measured and simulated maximum horizontal force compare well when plotted against run-up, see Figs. 6.57(a) and 6.58(a).
- The simulated minimum vertical force has a greater magnitude than the measured values for the larger wave crests, see Figs. 6.55(d) and 6.56(d). This is probably due to structural oscillations in the model rig, see e.g. Fig. 6.53.

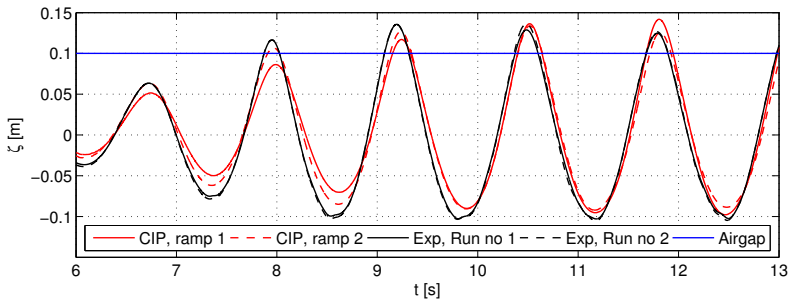

Figure 6.40: Comparison between experiments and simulations: Incoming wave ζ 0.43 m in front of the deck box for Case no 7.

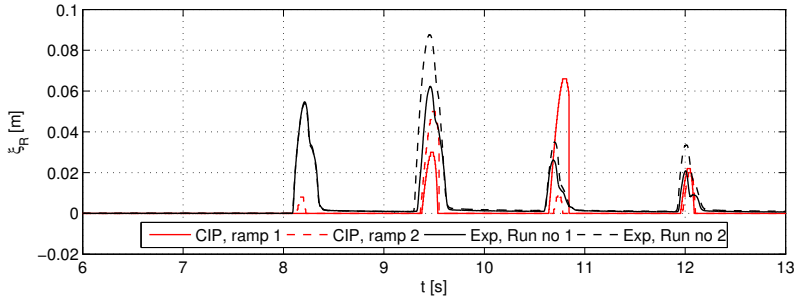

(a) Run-up at front end ξ_R

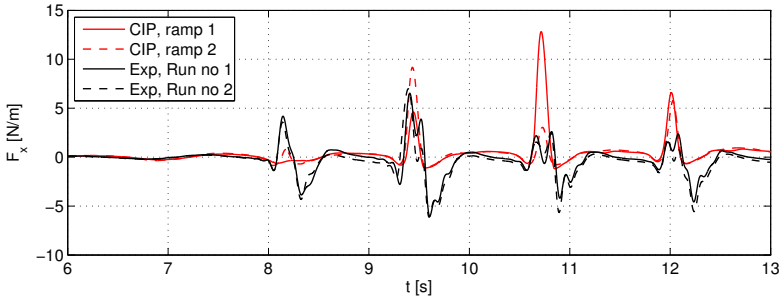

(b) Horizontal force F_x

Figure 6.41: Comparison between experiments and simulations: Run-up ξ_R and horizontal force F_x for Case no 7.

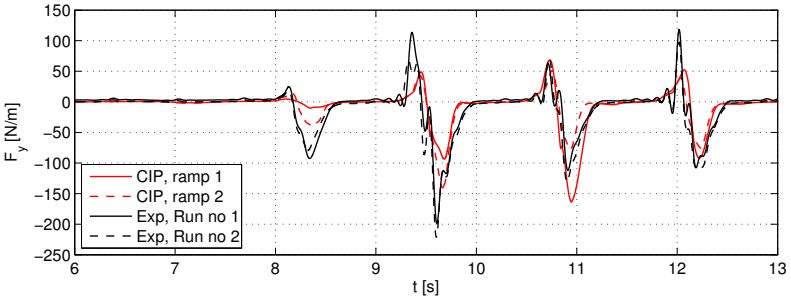

Figure 6.42: Comparison between experiments and simulations: Vertical force F_y for Case no 7.

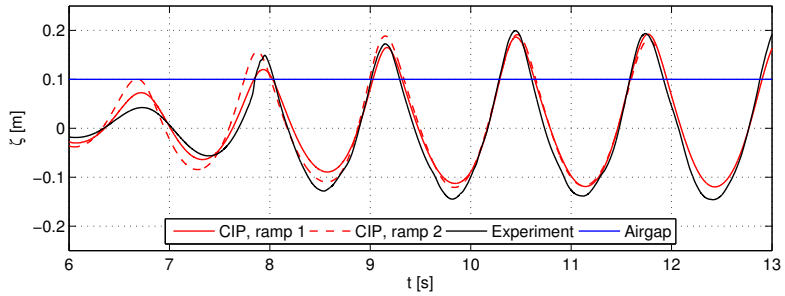

Figure 6.43: Comparison between experiments and simulations: Incoming wave ζ 0.43 m in front of the deck box for Case no 8.

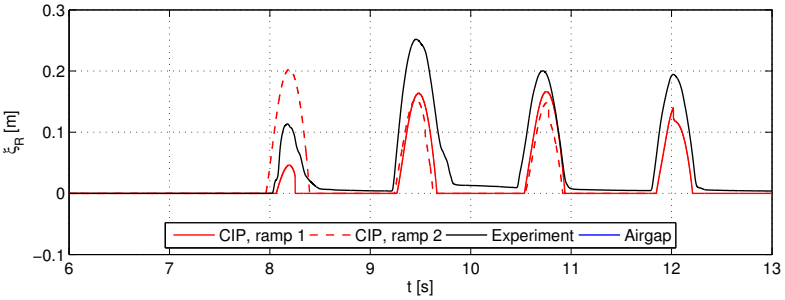

(a) Run-up at front end ξ_R

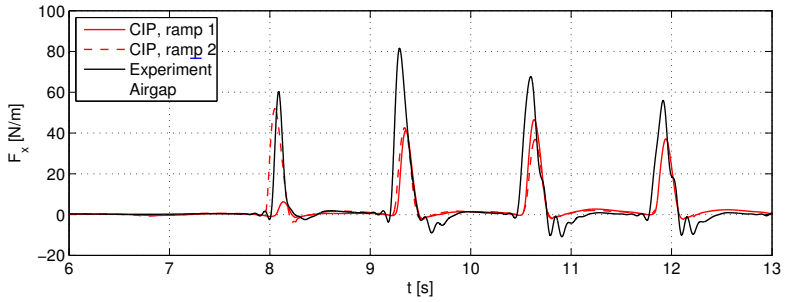

(b) Horizontal force F_x

Figure 6.44: Comparison between experiments and simulations: Run-up ξ_R and horizontal force F_x for Case no 8.

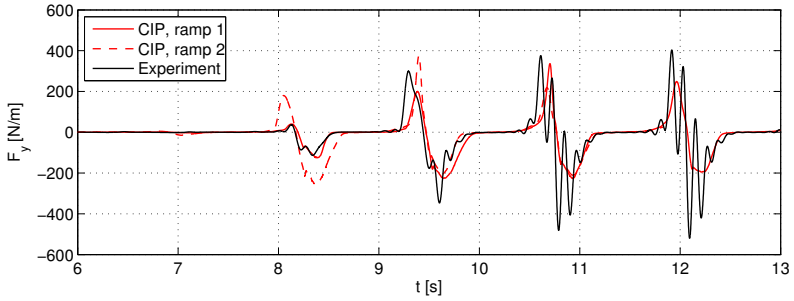

Figure 6.45: Comparison between experiments and simulations: Vertical force F_y for Case no 8.

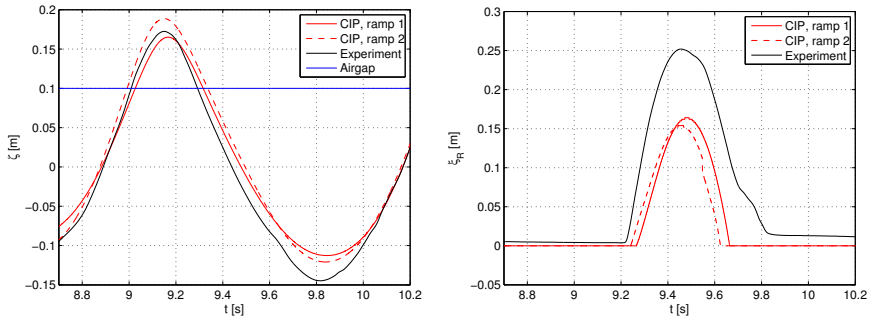

(a) Incoming wave ζ

(b) Run-up at front end ξ_R

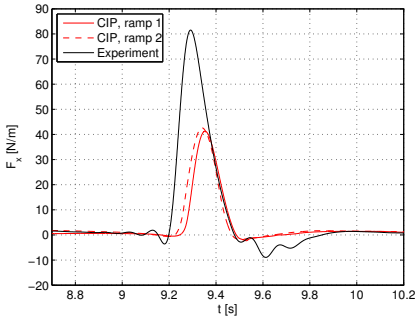

(c) Horizontal force F_x

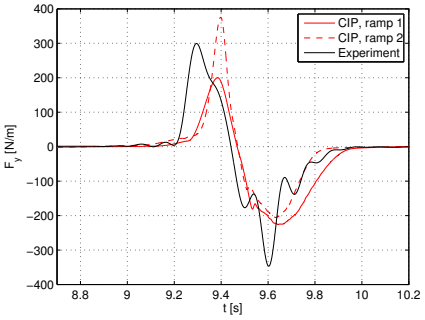

(d) Vertical force F_y

Figure 6.46: Comparison between experiments and simulations: Close-up of the second impact for for Case no 8.

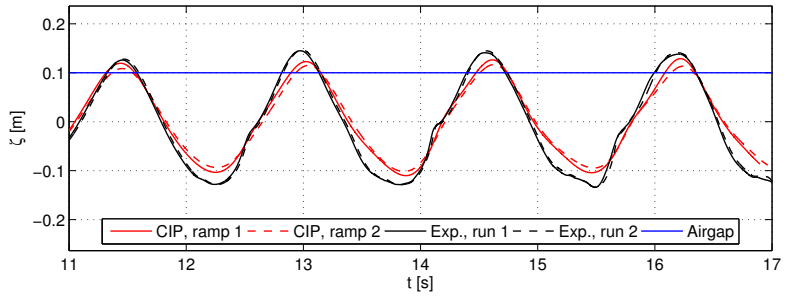

Figure 6.47: Comparison between experiments and simulations: Incoming wave ζ 0.43 m in front of the deck box for Case no 12.

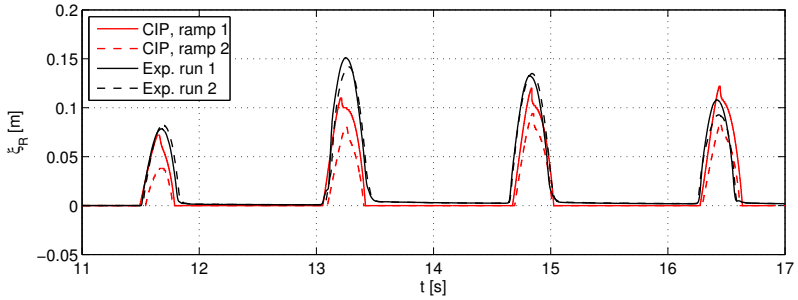

(a) Run-up at front end ξ_R

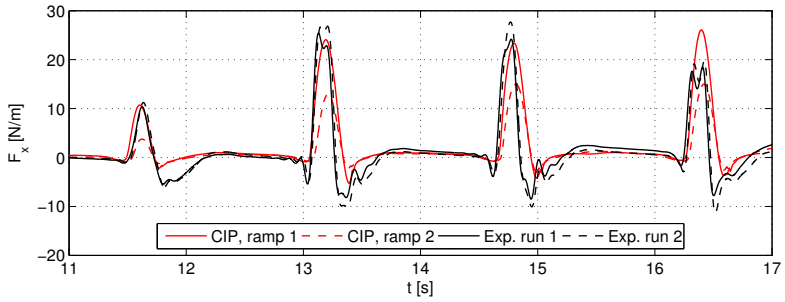

(b) Horizontal force F_x

Figure 6.48: Comparison between experiments and simulations: Run-up ξ_R and horizontal force F_x for Case no 12.

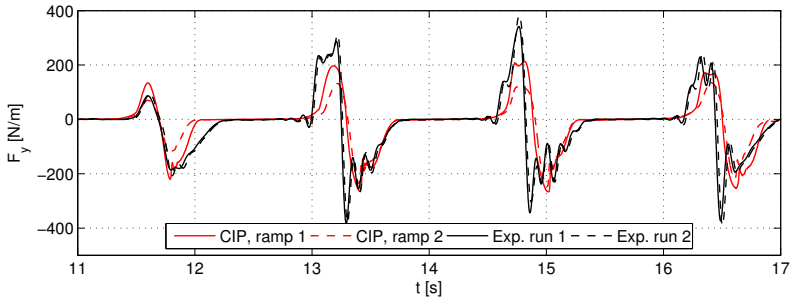

Figure 6.49: Comparison between experiments and simulations: Vertical force F_y for Case no 12.

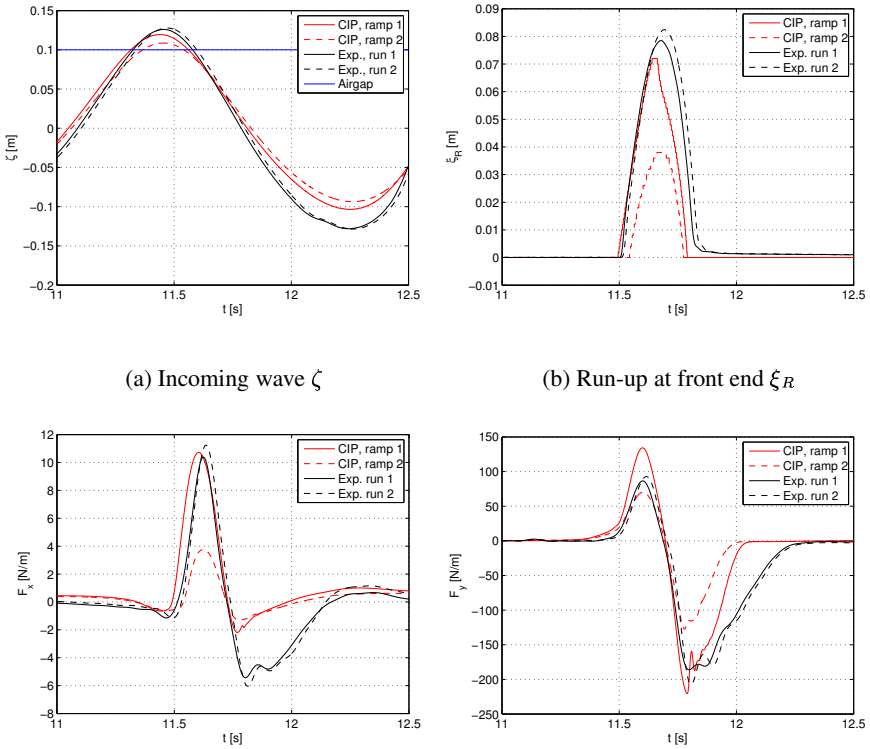

(a) Incoming wave ζ

(b) Run-up at front end ξ_R

(c) Horizontal force F_x

(d) Vertical force F_y

Figure 6.50: Comparison between experiments and simulations: Close-up of the first impact for for Case no 12.

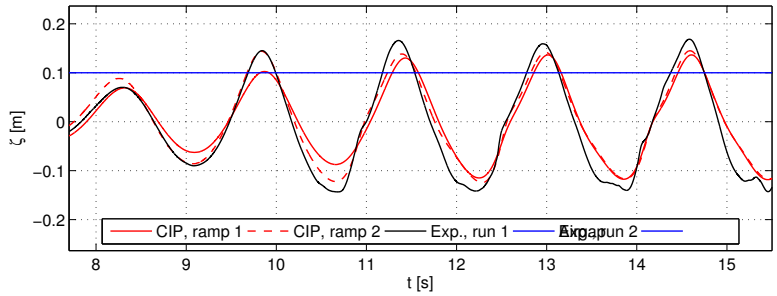

Figure 6.51: Comparison between experiments and simulations: Incoming wave ζ 0.43 m in front of the deck box for Case no 13.

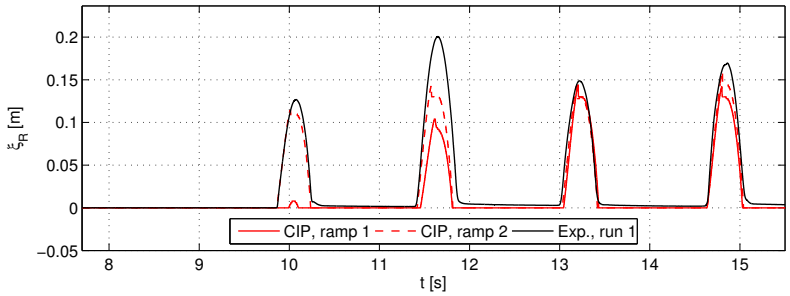

(a) Run-up at front end ξ_R

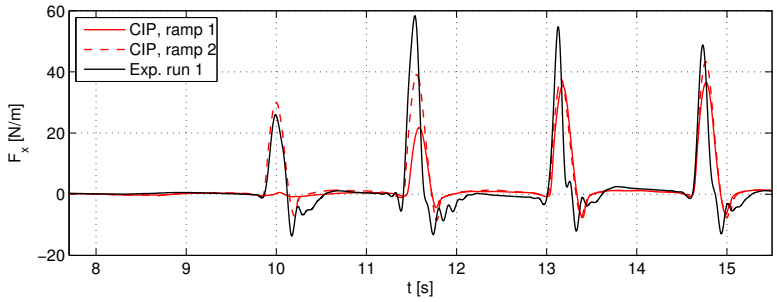

(b) Horizontal force F_x

Figure 6.52: Comparison between experiments and simulations: Run-up ξ_R and horizontal force F_x for Case no 13.

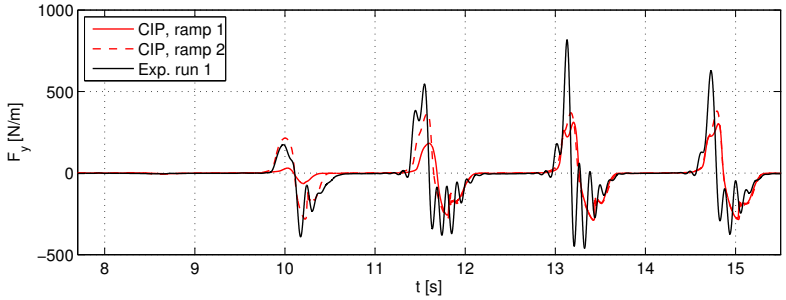

Figure 6.53: Comparison between experiments and simulations: Vertical force F_y for Case no 13. Structural oscillations are observed for the negative force peak.

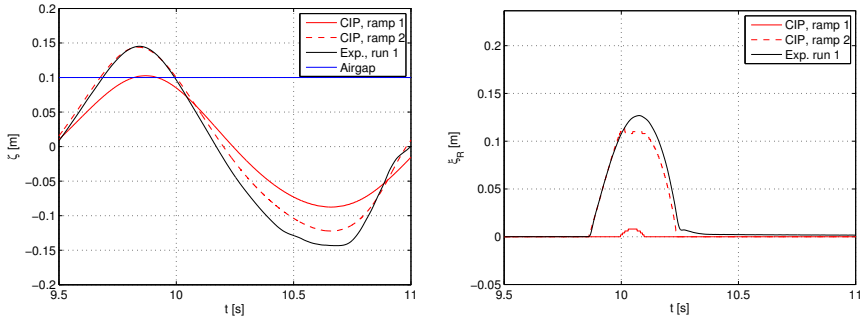

(a) Incoming wave ζ

(b) Run-up at front end ξ_R

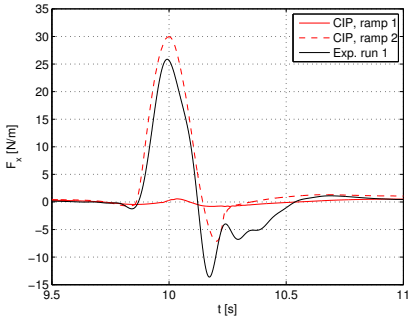

(c) Horizontal force F_x

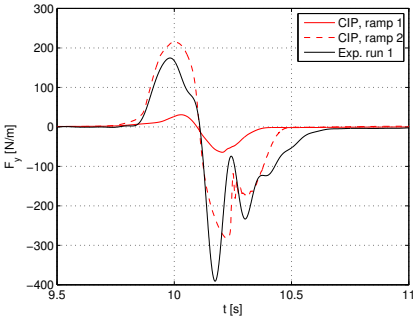

(d) Vertical force F_y

Figure 6.54: Comparison between experiments and simulations: Close-up of the first impact for for Case no 13.

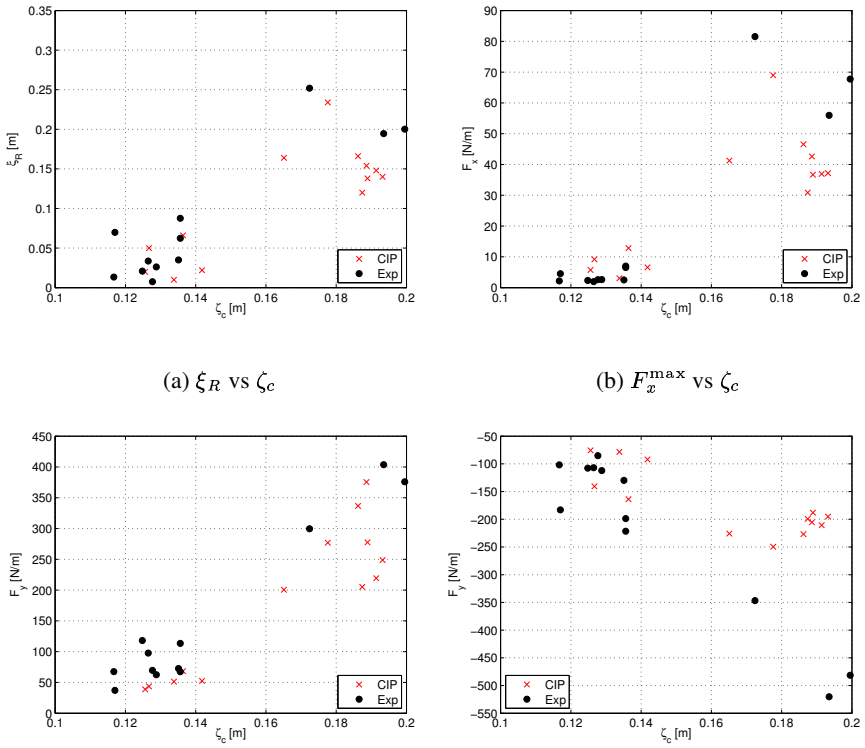

(a) ξ_R vs ζ_c

(b) $F_x^{\max}$ vs ζ_c

(c) $F_y^{\max}$ vs ζ_c

(d) $F_y^{\min}$ vs ζ_c

Figure 6.55: Maximum run-up and forces versus wave crest before impact for $T = 1.3$ s. Only consecutive peaks are included, i.e. results from first impacts are excluded.

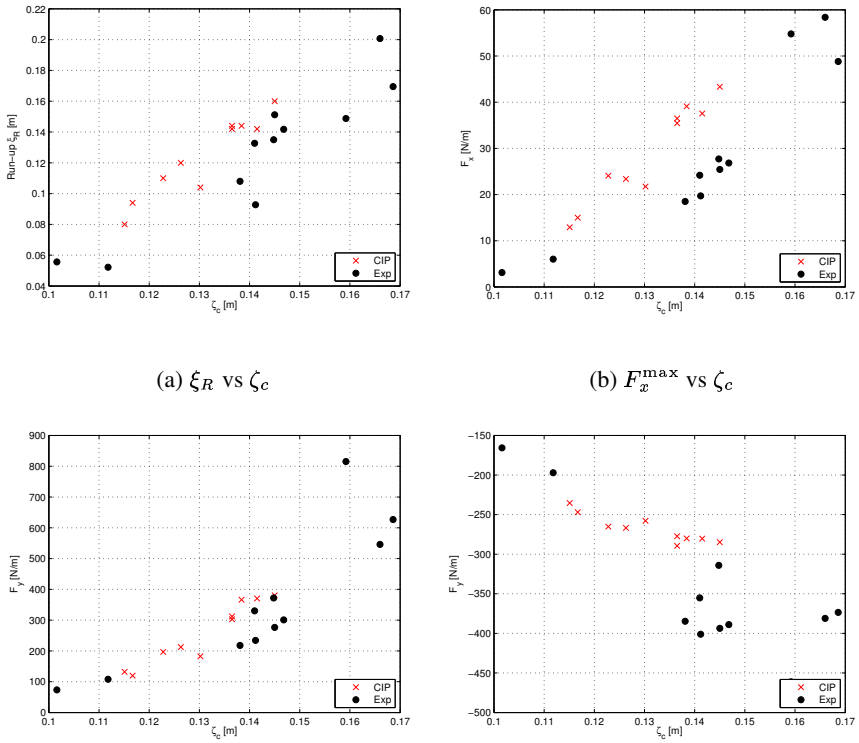

(a) ξ_R vs ζ_c

(b) $F_x^{\max}$ vs ζ_c

(c) $F_y^{\max}$ vs ζ_c

(d) $F_y^{\min}$ vs ζ_c

Figure 6.56: Maximum run-up and forces versus wave crest before impact for $T = 1.6$ s. Only consecutive peaks are included, i.e. results from first impacts are excluded.

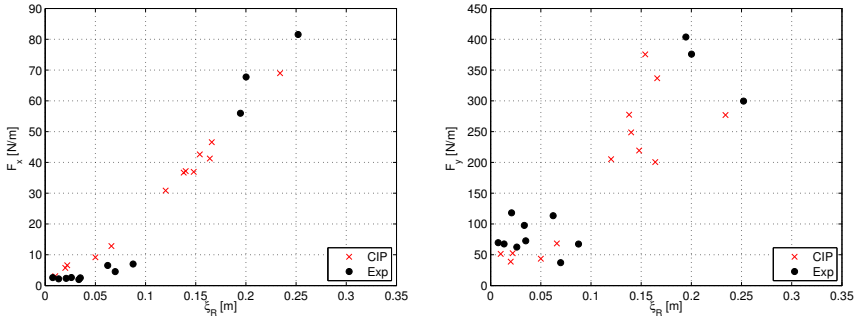

(a) $F_x^{\max}$ vs ξ_R (b) $F_y^{\max}$ vs ξ_R

Figure 6.57: Maximum horizontal and vertical force versus run-up for $T = 1.3$ s.

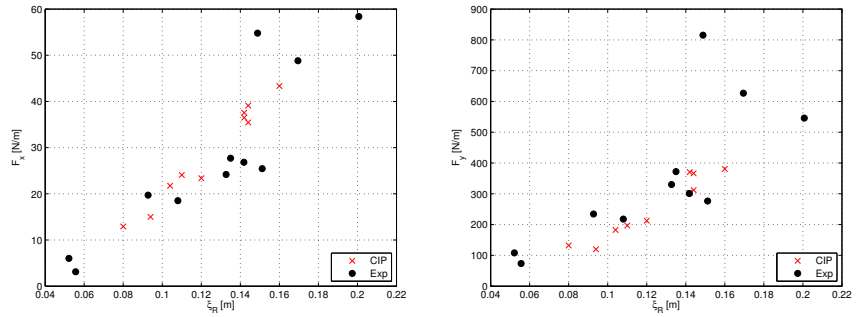

(a) $F_x^{\max}$ vs ξ_R (b) $F_y^{\max}$ vs ξ_R

Figure 6.58: Maximum horizontal and vertical force versus run-up for $T = 1.6$ s.

Chapter 7

Summary and future perspectives

7.1 Summary

A Constrained Interpolation Profile method following Hu and Kashiwagi (2004) is developed for wave impact applications. Two-dimensional, unsteady, viscous and incompressible flow is assumed. No turbulence model is included. Several benchmark tests focusing on marine applications are used to demonstrate the capabilities and limitations of the method. A numerical wave tank using the CIP code is developed and validated. Wave impact simulations are run on a simplified deck structure and compared with experimental results.

- The application of a CIP code for computing global loads on a structure subjected to multiple wave impacts is demonstrated.
- A variable grid is used for many of the benchmark tests and for the application of the code. Grid dependency tests are performed for all cases. When the cell size is sufficiently small, the results are not very sensitive to changes in the grid configuration. Simulations are generally stable. Grid stretching must however be used with caution for wave generation applications. A steady increase in the horizontal cell size cause wave amplitude decay.
- Using an adaptive time stepping scheme ensures a more stable and effective code.
- Mass and energy conservation is shown to be satisfactory for the intended application.
- Added mass and damping in heave for a circular cylinder is computed. The computed damping is in fair agreement with values from the BEM method, while some discrepancy is found for the added mass.

- The performance of several surface capturing methods are tested. All perform well in terms of modeling the free surface at $\phi_1 = 0.5$. The original CIP method and the linear transformation enhancement method show large increase in the surface layer thickness (defined by $0.05 < \phi_1 < 0.95$) for long simulations. The surface layer shows less growth using the tangent transformation surface enhancement method for long simulations. Some stepwise behavior of the free surface may however occur at the beginning of simulations. The THINC surface capturing method is more complicated to implement and is computationally more costly than the other methods. Using this method, the surface layer stays within one or two cells even for long simulations. The use of the THINC method may however lead to numerical problems during simulations. Undisturbed waves were simulated obtaining good agreement with theoretical wave kinematics using the THINC method. Successful wave impact simulations were however not obtained due to numerical instabilities. The tangent transformation surface enhancement method is easy to implement and robust during simulations. The tangent transformation surface enhancement algorithm is therefore used for the wave impact simulations.

- A numerical wave tank capable of generating regular progressive waves is developed. The generated waves are compared with 5th order Stokes theory and experimental results and show good agreement with theoretical and measured wave elevations and kinematics.

- The wave impact process is studied using both numerical and experimental results. The numerical model is able to capture the main phenomena of the flow during impact.

- Both experiments and simulations show that the maximum loads increase when the wave is disturbed from previous impacts. This may be important in realistic cases, where wave groups may cause multiple impacts on the deck of an offshore structure in extreme seas.

- Comparison between simulations and experiments show that when the simulated incoming wave agrees with the measured incoming wave, a fair agreement between the computed and measured horizontal and vertical force histories are obtained.

- There is some uncertainty connected to the vertical positive peak force. The positive peak force is sensitive to small variations in crest height and air-gap. Variability in the measured data is present. Some of the variability is

assumed to be due to small differences in the water level for different repetitions of the same experimental run, and some is assumed to be due to structural oscillations of the model rig. The frequencies of the structural oscillations seem to coincide with some of the load components, making it difficult to eliminate all of the assumed structural oscillations with low-pass filtering.

7.2 Future perspectives

For further research on wave-in-deck impact using the CIP code, it would be natural to run simulations with impacts from breaking or near-breaking waves, employing the ability of the code to model violent flow in a robust way. For comparison, dedicated experiments should probably be conducted.

Many improvements can obviously be made on the present 2D code. A more efficient matrix solver can be implemented, together with a second order pressure computation scheme. The possibility of a more accurate time-marching scheme should then also be explored. If the pressure is computed to second order, the numerical problems seen when using the THINC surface capturing scheme might be avoided. In combination, this would probably increase the accuracy for wave impact modeling. The possibility of handling floating bodies is relatively easy to implement in the code. For realistic cases, 3D effects are however important for floating offshore structures such as semi-submersibles.

To be able to model realistic structures, a 3D code must thus be developed. With a 3D code, the effect of the platform substructure can be included. The CIP method seems to capture the disturbance of the waves due to the previous impacts, and this is promising with respect to capturing diffraction from the substructure. However, for the implementation and use of a 3D code to be realistic, the efficiency of the code must be greatly improved. A more efficient body geometry representation that can handle complex geometry must be implemented. A more effective wave generation can maybe be obtained by using domain decomposition techniques. A BEM model can then be used to generate the incoming wave, while the CIP method can be used as a local solver for the impact events.

Bibliography

Baarholm, R. (2001). *Theoretical and Experimental Studies of Wave Impact underneath Decks of Offshore Structures*. PhD thesis, Norwegian University of Science and Technology, Trondheim, Norway.

Baarholm, R. (2005). A simple numerical method for evalutation of water impact loads on decks of large-volume offshore platforms. In *Proc. of 24th Intl. Conf. on Offshore Mechanics and Arctic Engineering*, Halkidiki, Greece.

Baarholm, R. (2008). MARINTEK wave impact loads JIP: Task 2- small scale wave impact tests. Technical report, MARINTEK.

Baarholm, R. (2009). Experimental and theoretical study of three-dimensional effects on vertical wave-in-deck forces. In *Proc. of 28th Intl. Conf. on Offshore Mechanics and Arctic Engineering*, Hawaii, USA.

Berthelsen, P. A. and Faltinsen, O. M. (2008). A local directional ghost cell approach for incompressible viscous flow problems with irregular boundaries. *Journal of Computational Physics*, 227:4354–4397.

Brown, D. L., Cortez, R., and Minion, M. L. (2001). Accurate projection methods for the incompressible Navier-Stokes equations. *Journal of Computational Physics*, 168:464–499.

Bruaset, A. M. (1995). *A Survey of Preconditioned Iterative Methods*, volume 328 of *Pitman Research Notes in Matematics Series*. Longman Scientific & Technical.

Buchner, B. and Bunnik, T. (2007). Extreme wave effects on deepwater floating structures. In *Proc. of 2007 Offshore Technology Conference*, OTC 18493, Houston, Texas.

Canuto, C., Hussaini, M., Quarteroni, A., and Zang, T. A. (2006). *Spectral Methods. Fundamentals in Single Domains*. Springer.

Chorin, A. (1968). Numerical solution of the Navier-Stokes equations. *Mathm. Comput.*, 22:745–762.

Colicchio, G., Greco, M., and Faltinsen, O. (2006). A BEM-Level Set domain-decomposition strategy for non-linear and fragmented interfacial flows. *International Journal for Numerical Methods in Engineering*, 67:1385–1419.

Dalton, C. and Nash, J. M. (1976). Wave slam on horizontal members of an offshore platform. In *Proc. of 8th Offshore Technology Conference*, number OTC 2500, pages 769–780, Dallas, USA.

Dean, R. G. and Dalrymple, R. A. (1984). *Water Wave Mechanics for Engineers and Scientists*. Prentice–Hall, Inc.

Enright, D., Fedkiw, R., Ferziger, J., and Mitchell, I. (2002). A hybrid particle Level Set method for improved interface capturing. *Journal of Computational Physics*, 183:83–116.

Ersdal, G. (2008). Aging and life extension of offshore structures. In *Proc. of 27th Intl. Conf. on Offshore Mechanics and Arctic Engineering*, Estoril, Portugal.

Fadlun, E. A., Verzicco, R., P. Orlandi, P., and Mohd-Yusof, J. (2000). Combined immersed-boundary finite-difference methods for three-dimensional complex flow simulations. *Journal of Computational Physics*, 161:35–60.

Faltinsen, O. M. (1978). A numerical nonlinear method of sloshing in tanks with two–dimensional flow. *Journal of Ship Research*, 22(3):193–202.

Faltinsen, O. M. (1990). *Sea Loads on Ships and Offshore Structures*. Cambridge University Press.

Faltinsen, O. M., Kjærland, O., and Nøttveit, A. (1977). Wave impact loads and dynamic response of horizontal circular cylinders in offshore structures. In *Proc. of 9th Offshore Technology Conference*, number OTC 2741, pages 119–126, Houston, Texas.

Faltinsen, O. M. and Timokha, A. (2009). *Sloshing*. Cambridge University Press.

Faltinsen, O. M., Zhu, X., and Hu, C. (2005). Strongly nonlinear flows in seakeeping. In *Proc. of ICMRT*. Keynote lecture.

Fenton, J. (2001). A 5th order Stokes theory for steady waves. *Journal of Waterway, Port, Coastal and Ocean Engineering*, 3(2).

Ferziger, J. H. and Perić, M. (2002). *Computational Methods for Fluid Dynamics*. Springer-Verlag.

Ghia, U., Ghia, K., and Shin, C. T. (1982). High–Re solutions for incompressible flow using the Navier–Stokes equations and a Multi–Grid Method. *Journal of Computational Physics*, 48:387–411.

Greco, M. (2001). *A Two-Dimensional Study of Green-Water Loading*. PhD thesis, Norwegian University of Science and Technology, Trondheim, Norway.

Gudmestad, O. T. (1993). Measured and predicted deep water wave kinematics in regular and irregular seas. *Marine Structures*, 6:1–73.

Herfjord, K. (1995a). Computational methods in viscous fluid flow. Lecture Notes.

Herfjord, K. (1995b). *A Study of Two-Dimensional Separated Flow by a Combination of the Finite Element Method and Navier-Stokes Equations*. PhD thesis, The Norwegian Institute of Technology, Trondheim, Norway.

Hirsch, C. (1988). *Numerical Computation of Internal and External Flows*, volume 1 of *Wiley Series in Numerical Methods in Engineering*. John Wiley & Sons.

Hirt, C. W. and Nichols, B. D. (1981). Volume of fluid (VOF) method for the dynamics of free boundaries. *Journal of Computational Physics*, 39:201–225.

Hu, C. (2005). CIP method. Lecture Note for MR8300 Hydrodynamic Analysis of Marine Structures.

Hu, C. and Kashiwagi, M. (2003). A CIP-based numerical simulation method for extreme wave-body interactions. In *Proc. of 18th International Workshop on Water Waves and Floating Bodies*, pages 81–84, Le Croisic, France.

Hu, C. and Kashiwagi, M. (2004). A CIP-based method for numerical simulations of violent free-surface flows. *Journal of Marine Science and Technology*, 9:143–157.

Hu, C. and Kashiwagi, M. (2007). Numerical and experimental studies on three-dimensional water on deck with a modified Wigley model. In *9th International Conference of Numerical Ship Hydrodynamics*, Ann Arbour, Michigan.

Hughes, S. A. (1993). *Physical Models and Laboratory Techniques in Coastal Engineering*, volume 7 of *Advanced Series on Ocean Engineering*. World Scientific.

ITTC (1990). Report of the panel on validation procedures. In *Proceedings of the 19th ITTC*, pages 577–604, Madrid, Spain.

ITTC (2002). Verfication and validation methodology and procedures. In *ITTC Recommended Procedures and Guidelines*.

Kaplan, P. (1992). Wave impact forces on offshore structures: Re–examination and new interpretations. In *Proc. of the 24th Offshore Technology Conference*, number OTC 6814, pages 79–86, Houston, Texas.

Kaplan, P., J., M. J., and Yu, W. C. (1995). Theoretical analysis of wave impact forces on platform structures. In *Proc. of 14th Offshore Mechanics and Arctic Engineering Conference*, pages 189–198, Copenhagen, Denmark.

Kaplan, P. and Siblert, N. (1976). Impact forces on platform horizontal members in the splash zone. In *Proc. of 8th Offshore Technology Conference*, number OTC 2498, pages 749–758, Dallas, USA.

Kishev, Z. R., Hu, C., and Kashiwagi, M. (2005). Numerical simulation of violent sloshing by CIP method with experimental validation. In *Proc. of 15th International Offshore and Polar Engineering Conference*, pages 274–281, Seoul, Korea.

Kishev, Z. R., Hu, C., and Kashiwagi, M. (2006). Numerical simulation of violent sloshing by a CIP-based method. *Journal of Marine Science and Technology*, 11:111–122.

Kleefsman, K. M. T., Fekken, G., Veldman, A. E. P., Iwanowski, B., and Buchner, B. (2005). A Volume-of-Fluid based simulation method for wave impact problems. *Journal of Computational Physics*, 206:363–393.

Kota, R. S. and Moan, T. (2008). Stochastic analysis of vertical wave loads on deck. In *Proc. of the 27th Intl. Conf. on Offshore Mechanics and Arctic Engineering*, Estoril, Portugal.

Kristiansen, D. and Faltinsen, O. M. (2008). Wave loads on floaters of aquaculture plants. In *Proc. of the 27th Intl. Conf. on Offshore Mechanics and Arctic Engineering*, Estoril, Portugal.

Löhner, R., Yang, C., and Oñate, E. (2005). Large-scale simulations of flows with violent free surface motion. In Bergan, P., García, J., Oñate, E., and T., K., editors, *First International Conference on Computational Methods in Marine Engineering*, pages 55–81. CIMNE, International Center for Numerical Methods in Engineering.

Mathiesen, E. (2004). A working museum. *Norwegian Continental Shelf*, 2:22–25.

Meling, T. S. (1998). *A Numerical Study of Flow about Fixed and Flexibly Mounted Circular Cylinders*. PhD thesis, Norwegian University of Science and Technology, Trondheim, Norway.

Miao, G. (1989). *Hydrodynamics Forces and Dynamic Responses of Circular Cylinders in Wave Zones*. PhD thesis, Norwegian University of Science and Technology, Trondheim, Norway.

Mohd-Yusof, J. (1997). Combined immersed boundaries/B-splines methods for simulations of flows in complex geometries. Technical report, CTR Annual Research Briefs, NASA Ames/Stanford University.

Monaghan, J. J. (1992). Smoothed particle hydrodynamics. *Annual Review of Astrophysics*, 30:534–574.

Monaghan, J. J., Kos, A., and Issa, N. (2003). Fluid motion generated by impact. *Journal of Waterway, Port, Coastal and Ocean Engineering*, 125:145–154.

Mutsuda, H. and Faltinsen, O. M. (2007). A coupled Eulerian-Lagrangian method for free surface problems. In *Proc. of International Conference on Violent Flows*, Fukuoka, Japan.

Nakamura, T., Tanaka, R., Yabe, T., and Takizawa, K. (2001). Exactly conservative semi-Lagrangian scheme for multi-dimensional hyperbolic equations with directional splitting technique. *Journal of Computational Physics*, 174:171–207.

Osher, S. J. and Fedkiw, R. P. (2002). *Level Set Methods and Dynamic Implicit Surfaces*. Springer.

Pàkozdi, C. (2008). *A Smoothed Particle Hydrodynamics Study of Two-dimensional Nonlinear Sloshing in Rectangular Tanks*. PhD thesis, Norwegian University of Science and Technology, Norway.

PSA (2001). Regulations relating to design and outfitting of fascilities etc. in the petroleum avtivities. Petroleum Safety Autority.

Roache, P. J. (1998). *Verification and Validation in Computer Science*. Hermosa publishers.

Rognebakke, O. F. (2002). *Sloshing in Rectangular Tanks and Interaction with Ship Motions*. PhD thesis, Norwegian University of Science and Technology, Norway.

Schlichting, H. and Gersten, K. (2000). *Boundary Layer Theory*. Springer.

Sleijpen, G. L. G. and Fokkema, D. R. (1993). BICGSTAB(L) for linear equations involving unsymmetric matrices with complex spectrum. *Electronic Transactions on Numerical Analysis*, 1:11–32.

Smith, E. (2006). Gulf of Mexico hurricanes in 2005 - damages, lessons learned and strategies for the way forward. In *Presentations at Petroleumstilsynets Konstruksjonsseminar*, Stavanger, Norway.

Solaas, F. (1995). *Analytical and Numerical Studies of Sloshing in Tanks*. PhD thesis, Norwegian University of Science and Technology, Trondheim, Norway.

Stansberg, C. T., Baarholm, R., Fokk, T., Gudmestad, O. T., and Haver, S. (2004). Wave amplification and possible deck impact on gravity based structure in 10^{-4} probability extreme crest heights. In *Proc. of 23rd Intl. Conf. on Offshore Mechanics and Arctic Engineering*, Vancouver, Canada.

Stansberg, C. T., Baarholm, R., Hansen, E. W. M., and Rortveit, G. (2005). Extreme wave amplification and impact loads on offshore structures. In *Proc. of 2005 Offshore Technology Conference*, number OTC 17487, Houston, Texas.

Strikwerda, J. C. (2004). *Finite Difference Schemes and Partial Differential Equations*. Siam.

Succi, S. (2001). *The Lattice Boltzmann Equation for Fluid Dynamics and Beyond*. Oxford University Press.

Sun, H. and Faltinsen, O. M. (2006). Water impact of horizontal circular cylinders and cylindrical shells. *Applied Ocean Research*, 28:299–311.

Takewaki, H., Nishiguchi, A., and Yabe, T. (1985). Cubic interpolated pseudo-particle method (CIP) for solving hyperbolic-type equations. *Journal of Computational Physics*, 61:261–268.

Takizawa, K., Tanizawa, K., Yabe, T., and Tezduyar, T. E. (2007). Ship hydrodynamics computations with the CIP method based on adaptive Soroban grids. *International Journal for Numerical Methods in Fluids*, 54:1011–1019.

Tanaka, R., Nakamura, T., and Yabe, T. (2000). Constructing exactly conservative scheme in a non-conservative form. *Computer Physics Communications*, 126:232–243.

Tønnesen, R. (1999). *A Finite Element Method Applied to Unsteady Viscous Flow around 2D Blunt Bodies with Sharp Corners*. PhD thesis, Norwegian University of Science and Technology, Trondheim, Norway.

Utsumi, T., Kunugi, T., and Aoki, T. (1997). Stability and accuracy of the cubic interpolation propagation scheme. *Computer Physics Communications*, 101:9–20.

van Raaij, K. (2005). *The Dynamic Behaviour of Jackets exposed to Wave-in-Deck Forces*. PhD thesis, University of Stavanger, Norway.

Veldman, A. E. P. (2006). The simulation of violent free-surface dynamics at sea and in space. In *Proc. of European Conference on Computational Fluid Dynamics*.

Veldman, A. E. P. and Rinzema, K. (1992). Playing with nonuniform grids. *Journal of Engineering Mathematics*, 26:119–130.

Vestbøstad, T. M., Baarholm, R. J., and Faltinsen, O. M. (2008). A study of wave impact using a 2-D CIP method. In *Proc. of 8th International Conference on Hydrodynamics*, Nantes, France.

Vestbøstad, T. M. and Faltinsen, O. M. (2007a). Validation methods and benchmark tests for a 2-D CIP method applied to marine hydrodynamics. In *Proc. of 17th International Offshore and Polar Engineering Conference*, Lisboa, Portugal.

Vestbøstad, T. M. and Faltinsen, O. M. (2007b). Wave impact on a deck box using a 2-D CIP method. In *Proc. of International Conference on Violent Flows*, Fukuoka, Japan.

Vugts, J. H. (1968). The hydrodynamic coefficients for swaying, heaving and rolling of cylinders in a free surface. Technical report, Shipbuilding Laboratory, Technological University of Delft.

Wagner, H. (1932). Über stoss– und gleitvorgänge an der oberfläche von flüssigkeiten. *Zeitschr. f. Angewandte Mathematik und Mechanik*, 12:193–235.

Xiao, F., Honma, Y., and T., K. (2005). A simple algebraic interface capturing scheme using hyperbolic tangent function. *International Journal for Numerical Methods in Fluids*, 48:1023–1040.

Xiao, F. and Yabe, T. (2001). Completely conservative and oscillationless semi-Lagrangian schemes for advection transportation. *Journal of Computational Physics*, 170:498–522.

Yabe, T., Takizawa, K., Tezduyar, T. E., and Im, H.-N. (2007). Computation of fluid-solid and fluid-fluid interfaces with the CIP method based on adaptive Soroban grids — An overview. *International Journal for Numerical Methods in Fluids*, 54:841–853.

Yabe, T., Tanaka, R., T., N., and Xiao, F. (2001). An exactly conservative semi-Lagrangian scheme (CIP–CSL) in one dimension. *Monthly Weather Review*, 129:332–344.

Yabe, T., Xiao, F., and Utsumi, T. (2000). The constrained interpolation profile method for multiphase analysis. *Journal of Computational Physics*, 169:556–593.

Yokoi, K. (2007). Efficient implementation of THINC scheme: A simple and practical smoothed VOF algorithm. *Journal of Computational Physics*, 226:1985–2002.

Zhu, X. (2006). *Application of the CIP Method to Strongly Nonlinear Wave-Body Interaction Problems*. PhD thesis, Norwegian University of Science and Technology, Trondheim, Norway.

Zhu, X., Faltinsen, O. M., and Hu, C. (2005). Water entry and exit of a horizontal circular cylinder. In *Proc. of 24th International Conference on Offshore Mechanics and Arctic Engineering*.

Appendix A

Details of the Numerical Model

A.1 Overview

In this appendix, details of the implementation of the numerical model is given. The coefficients for the 2D CIP method is given in Sec. A.2. The discretized equations for the flow solver is given in Sec. A.3. It is especially the staggered grid and the nonuniform cell sizes that complicates the formulations. Care must be taken so that the variables are evaluated at the correct positions. The numerical procedure of the THINC surface capturing method is given in Sec. A.4.

A.2 Coefficients for 2D CIP

The coefficients of Eq. 2.29 are computed in the following manner:

$$
\begin{aligned}
C_{30} &= \frac{k_s\left[f_x(kw,l)+f_x(k,l)\right]\Delta x - 2\left[f(k,l)-f(kw,l)\right]}{k_s\Delta x^3} \\
C_{03} &= \frac{l_s\left[f_y(k,lw)+f_y(k,l)\right]\Delta y - 2\left[f(k,l)-f(k,lw)\right]}{l_s\Delta y^3} \\
C_{21} &= \frac{f(k,l)-f(k,lw)-f(kw,l)+f(kw,lw)-i_s\left[f_x(k,lw)-f_x(k,l)\right]\Delta x}{k_s\Delta x^2\Delta y} \\
C_{12} &= \frac{f(k,l)-f(k,lw)-f(kw,l)+f(kw,lw)-l_s\left[f_y(kw,l)-f_y(k,l)\right]\Delta y}{k_s\Delta x\Delta y^2} \\
C_{20} &= \frac{3\left[f(kw,l)-f(k,l)\right]+k_s\left[f_x(kw,l)+2f_x(k,l)\right]\Delta x}{\Delta x^2} \\
C_{02} &= \frac{3\left[f(k,lw)-f(k,l)\right]+l_s\left[f_y(k,lw)+2f_y(k,l)\right]\Delta y}{\Delta y^2} \\
C_{11} &= \frac{f_y(kw,l)-f_y(k,l)+C_{21}\Delta x^2}{k_s\Delta x} \\
C_{10} &= f_x(k,l) \\
C_{01} &= f_y(k,l) \\
C_{00} &= f(k,l)
\end{aligned}
\tag{A.1}
$$

where $k_s = \text{sign}(u)$ and $l_s = \text{sign}(v)$. The upwind indices kw and lw are defined in Eq. A.2.

$$
kw = k - \text{sign}(u_{k,l}) \quad \text{and} \quad lw = l - \text{sign}(v_{k,l}) \tag{A.2}
$$

The advected variable f is approximated by a 2-D cubic polynomial F:

$$
\begin{aligned}
F(k,l) &= C_{30}X^3 + C_{21}X^2Y + C_{12}XY^2 + C_{03}Y^3 \\
&\quad + C_{20}X^2 + C_{11}XY + C_{02}Y^2 + C_{10}X + C_{01}Y + C_{00}
\end{aligned}
\tag{A.3}
$$

where X and Y have somewhat different definitions for the different variables due to the use of a staggered grid, see Tab. A.1.

The subscripts up, vp and mp denotes that the velocity is evaluated at the grid point of the horizontal velocity, vertical velocity and midpoint, respectively:

$$
\begin{aligned}
v^n_{up} &= \frac{1}{4}\left[v^n(k,l) + v^n(k,l-1)\right. \\
&\quad \left. + v^n(k+1,l) + v^n(k+1,l-1)\right]
\end{aligned}
\tag{A.4}
$$

Table A.1: Definitions of X and Y for the advection variables.

Variable f	X	Y
u	$-u^n(k,l)\Delta t$	$-v^n_{up}(k,l)\Delta t$
v	$-u^n_{vp}(k,l)\Delta t$	$-v^n(k,l)\Delta t$
ϕ_1	$-u^n_{mp}(k,l)\Delta t$	$-v^n_{mp}(k,l)\Delta t$

$$\begin{aligned} u^n_{vp} &= \frac{1}{4}\left[u^n(k,l) + u^n(k-1,l)\right. \\ &\quad \left. + u^n(k,l+1) + u^n(k-1,l+1)\right] \end{aligned} \tag{A.5}$$

$$u^n_{mp} = \frac{1}{2}\left[u^n(k,l) + u^n(k-1,l)\right] \tag{A.6}$$

$$v^n_{mp} = \frac{1}{2}\left[v^n(k,l) + v^n(k,l-1)\right] \tag{A.7}$$

For a variable grid such as in the present code, the variation in Δx and Δy must also be accounted for when computing v^n_{up} and u^n_{vp}:

$$\begin{aligned} v^n_{up} &= \frac{1}{4\Delta x_C(k)}\left[\left(v^n(k,l) + v^n(k,l-1)\right)\Delta x(k+1)\right. \\ &\quad \left. + \left(v^n(k+1,l) + v^n(k+1,l-1)\right)\Delta x(k)\right] \end{aligned} \tag{A.8}$$

$$\begin{aligned} u^n_{vp} &= \frac{1}{4\Delta y_C(l)}\left[\left(u^n(k,l) + u^n(k-1,l)\right)\Delta y(l+1)\right. \\ &\quad \left. + \left(u^n(k,l+1) + u^n(k-1,l+1)\right)\Delta y(l)\right] \end{aligned} \tag{A.9}$$

where $\Delta x(k)$, $\Delta y(l)$, $\Delta x_C(k)$ and $\Delta y_C(l)$ are defined as:

$$\Delta x(k) = x(k) - x(k-1) \tag{A.10}$$

$$\Delta y(l) = y(l) - y(l-1) \tag{A.11}$$

$$\Delta x_C(k) = x_C(k+1) - x_C(k) \tag{A.12}$$

$$\Delta y_C(l) = y_C(l+1) - y_C(l) \tag{A.13}$$

where $x_C(k) = \frac{1}{2}(x(k) + x(k-1))$, i.e. $\Delta x_C(k) = \frac{1}{2}(x(k+1) - x(k-1))$ and $y_C(l) = \frac{1}{2}(y(l) + y(l-1))$, i.e. $\Delta y_C(l) = \frac{1}{2}(y(l+1) - y(l-1))$.

The spatial derivatives of f, f_x and f_y, must also be updated using the CIP method. As shown in Eq. 2.2, there are residual source terms for the spatial derivatives. These terms are computed using a central difference scheme. Equation A.14–A.15 gives the advection part of the spatial derivatives, while Eqs. A.16–A.17 shows the updated spatial derivatives including the source term computations.

$$f_x^*(k,l)_{\mathrm{Adv}} = 3C_{30}X^2 + 2C_{21}XY + C_{12}Y^2 + 2C_{20}X + C_{11}Y + C_{10} \quad \text{(A.14)}$$

$$f_y^*(i,j)_{\mathrm{Adv}} = 3C_{03}Y^2 + C_{21}X^2 + 2C_{12}XY + 2C_{02}Y + C_{11}X + C_{01} \quad \text{(A.15)}$$

$$\begin{aligned} f_x^*(k,l) = \quad & f_x^*(k,l)_{\mathrm{Adv}} - \\ & \tfrac{\Delta t}{\Delta x(k)+\Delta x(k+1)} \left[f_x^*(k,l)_{\mathrm{Adv}} \left(u_C(k+1,l) - u_C(k-1,l) \right) \right. \\ & \left. + \; f_y^*(k,l)_{\mathrm{Adv}} \left(v_C(k+1,l) - v_C(k-1,l) \right) \right] \end{aligned} \quad \text{(A.16)}$$

$$\begin{aligned} f_y^*(k,l) = \quad & f_y^*(k,l)_{\mathrm{Adv}} - \\ & \tfrac{\Delta t}{\Delta y(l)+\Delta y(l+1)} \left[f_x^*(k,l)_{\mathrm{Adv}} \left(u_C(k,l+1) - u_C(k,l-1) \right) \right. \\ & \left. + \; f_y^*(k,l)_{\mathrm{Adv}} \left(v_C(k,l+1) - v_C(k,l+1) \right) \right] \end{aligned} \quad \text{(A.17)}$$

The velocities u_C and v_C are defined as:

$$u_C(k,l) = \begin{cases} u(k,l) & \text{for } f = u \\ u_{vp}(k,l) & \text{for } f = v \\ u_{mp}(k,l) & \text{for } f = \phi_1 \end{cases} \quad \text{(A.18)}$$

$$v_C(k,l) = \begin{cases} v_{up}(k,l) & \text{for } f = u \\ v(k,l) & \text{for } f = v \\ v_{mp}(k,l) & \text{for } f = \phi_1 \end{cases} \quad \text{(A.19)}$$

A.3 The flow solver

A.3.1 The diffusion step - discretized equations

Equation 3.7 is a simplified version of what is done in the numerical code. The double derivatives are in principle computed using a simple central difference scheme,

but due to the staggered (and variable) grid, the values of the viscosity μ and density ρ must be treated with some care. The values of these variables are first updated using the new values from the surface capturing method (see Sec.3.5).

$$\rho^*(k,l) = \rho_1\phi_1(k,l) + \rho_3\phi_3(k,l) + \rho_2\left(1 - \phi_1(k,l) - \phi_3(k,l)\right) \tag{A.20}$$

$$\mu^*(k,l) = \mu_1\phi_1(k,l) + \mu_3\phi_3(k,l) + \mu_2\left(1 - \phi_1(k,l) - \phi_3(k,l)\right) \tag{A.21}$$

Here ρ_1, ρ_2 and ρ_3 are the densities for fluid, gas and solid, respectively. Likewise, μ_1, μ_2 and μ_3 are the viscosity coefficients for fluid, gas and solid, respectively.

First, the viscous terms of the momentum equation in x–direction is computed. The density is averaged over the staggered grid (see Fig. 3.1) in the following manner:

$$\tilde{\rho_x}(k,l) = \frac{\rho^*(k,l)\Delta x(k+1) + \rho^*(k+1,l)\Delta x(k)}{2\Delta x_C(k)} \tag{A.22}$$

Four values of the viscosity coefficient is computed:

$$\mu_e = \mu^*(k+1,l) \tag{A.23}$$

$$\mu_w = \mu^*(k,l) \tag{A.24}$$

$$\begin{aligned}\mu_t = \quad + \quad & \tfrac{1}{4}\left[\left(\mu^*(k,l)\Delta y(l+1) + \mu^*(k,l+1)\Delta y(l)\right)\Delta x(k+1)\right. \\ & \left.\left(\mu^*(k+1,l)\Delta y(l+1) + \mu^*(k+1,l+1)\Delta y(l)\right)\Delta x(k)\right] \\ & / \left(\Delta x_C(k)\Delta y_C(l)\right)\end{aligned} \tag{A.25}$$

$$\begin{aligned}\mu_b = \quad + \quad & \tfrac{1}{4}\left[\left(\mu^*(k,l)\Delta y(l-1) + \mu^*(k,l-1)\Delta y(l)\right)\Delta x(k+1)\right. \\ & \left.\left(\mu^*(k+1,l)\Delta y(l-1) + \mu^*(k+1,l)\Delta y(l)\right)\Delta x(k)\right] \\ & / \left(\Delta x_C(k)\Delta y_C(l)\right)\end{aligned} \tag{A.26}$$

The double derivatives of the viscous terms in Eq. 3.7 can now be computed as:

$$\begin{aligned}\widetilde{\partial^2 u} &= \mu\left(\frac{\partial^2 u}{\partial x^2}+\frac{\partial^2 u}{\partial y^2}\right) \\ &\approx \begin{cases} & \mu_e\left(u^*(k+1,l)-u^*(k,l)\right)/\left(\Delta x(k+1)\Delta x_C(k)\right) \\ - & \mu_w\left(u^*(k,l)-u^*(k-1,l)\right)/\left(\Delta x(k)\Delta x_C(k)\right) \\ + & \mu_t\left(u^*(k,l+1)-u^*(k,l)\right)/\left(\Delta y(l)\Delta y_C(l)\right) \\ - & \mu_b\left(u^*(k,l)-u^*(k,l-1)\right)/\left(\Delta y(l)\Delta y_C(l-1)\right) \end{cases}\end{aligned} \tag{A.27}$$

The new intermediate horizontal velocity is then given by Eq. A.28.

$$u^{**}(k,l) = u^*(k,l) + \tilde{\rho}_x(k,l)\widetilde{\partial^2 u}\Delta t \tag{A.28}$$

Similarly, the viscous terms of the momentum equation in y–direction can be computed. The averaged density then becomes:

$$\tilde{\rho}_y(k,l) = \frac{\rho^*(k,l)\Delta y(l+1)+\rho^*(k,l+1)\Delta y(l)}{2\Delta y_C(l)} \tag{A.29}$$

The four values of the viscosity coefficient becomes:

$$\begin{aligned}\mu_e = \; + \;& \tfrac{1}{4}\left[\left(\mu^*(k,l)\Delta x(k+1)+\mu^*(k+1,l)\Delta x(k)\right)\Delta y(l+1)\right. \\ & \left.\left(\mu^*(k,l+1)\Delta x(k+1)+\mu^*(k+1,l+1)\Delta x(k)\right)\Delta y(l)\right] \\ & /\left(\Delta x_C(k)\Delta y_C(l)\right)\end{aligned} \tag{A.30}$$

$$\begin{aligned}\mu_w = \; + \;& \tfrac{1}{4}\left[\left(\mu^*(k,l)\Delta x(k-1)+\mu^*(k-1,l)\Delta x(k)\right)\Delta y(l+1)\right. \\ & \left.\left(\mu^*(k,l+1)\Delta x(k-1)+\mu^*(k-1,l+1)\Delta x(k)\right)\Delta y(l)\right] \\ & /\left(\Delta x_C(k)\Delta y_C(l)\right)\end{aligned} \tag{A.31}$$

$$\mu_t = \mu^*(k,l+1) \tag{A.32}$$

$$\mu_b = \mu^*(k,l) \tag{A.33}$$

The double derivatives of the viscous terms in the vertical direction can now be computed as:

$$\begin{aligned}\widetilde{\partial^2 v} &= \mu\left(\frac{\partial^2 v}{\partial x^2}+\frac{\partial^2 v}{\partial y^2}\right) \\ &\approx \begin{cases} & \mu_e\left(v^*(k+1,l)-v^*(k,l)\right)/\left(\Delta x(k)\Delta x_C(k)\right) \\ - & \mu_w\left(v^*(k,l)-v^*(k-1,l)\right)/\left(\Delta x(k)\Delta x_C(k-1)\right) \\ + & \mu_t\left(v^*(k,l+1)-v^*(k,l)\right)/\left(\Delta y(l+1)\Delta y_C(l)\right) \\ - & \mu_b\left(v^*(k,l)-v^*(k,l-1)\right)/\left(\Delta y(l)\Delta y_C(l)\right) \end{cases}\end{aligned} \tag{A.34}$$

The new intermediate vertical velocity is then given by Eq. A.35.

$$v^{**}(k,l) = v^{*}(k,l) + \tilde{\rho}_y(k,l)\widetilde{\partial^2 v}\Delta t - g\Delta t \tag{A.35}$$

New intermediate values for the fluid velocities, u^{**} and v^{**} are thus obtained.

A.3.2 Discretization of the pressure Poisson equation

Equation 3.9 can be written in a finite difference form as:

$$\begin{aligned} & \tfrac{1}{\Delta x(k)}\left[\tfrac{p^{n+1}(k+1,l)-p^{n+1}(k,l)}{\rho(k,l)\Delta x_C(k)} - \tfrac{p^{n+1}(k,l)-p^{n+1}(k-1,l)}{\rho(k-1,l)\Delta x_C(k-1)}\right] \\ + \quad & \tfrac{1}{\Delta y(l)}\left[\tfrac{p^{n+1}(k,l+1)-p^{n+1}(k,l)}{\rho(k,l)\Delta y_C(l)} - \tfrac{p^{n+1}(k,l)-p^{n+1}(k,l-1)}{\rho(k,l-1)\Delta y_C(l-1)}\right] \\ = \quad & \tfrac{1}{\Delta t}\left[\tfrac{u^{**}(k,l)-u^{**}(k-1,l)}{\Delta x(k)} + \tfrac{v^{**}(k,l)-v^{**}(k,l-1)}{\Delta y(l)}\right] \end{aligned} \tag{A.36}$$

Equation A.36 represents a sparse linear system for p^{n+1} that can be rewritten as $A\mathbf{p^{n+1}} = \mathbf{b}$. A is then an M $\times$ M matrix where M $= N_x \times N_y$, i.e. the number of grid cells in x–direction times the number of grid cells in y–direction. $\mathbf{p^{n+1}}$ and $\mathbf{b}$ are vectors with M elements.

A.3.3 Second non-advection step

When the pressure for the next time step, p^{n+1} has been found, the computation of the new fluid velocities are fairly straight-forward. Equation 3.8 is used. As for the diffusion step, (see Sec. A.3.1, the density of the fluid must be averaged over the staggered grid, see Eq. A.22 and A.29. The fluid velocities can then be obtained by:

$$u^{n+1}(k,l) = u^{**}(k,l) - \frac{\Delta t}{\tilde{\rho}_x(k,l)\Delta x_C(k)}\left(p^{n+1}(k+1,l) - p^{n+1}(k,l)\right) \tag{A.37}$$

$$v^{n+1}(k,l) = v^{**}(k,l) - \frac{\Delta t}{\tilde{\rho}_y(k,l)\Delta y_C(l)}\left(p^{n+1}(k,l+1) - p^{n+1}(k,l)\right) \tag{A.38}$$

A.3.4 Non-advection computations for the spatial derivatives

As the CIP method requires solving the governing equations also for the spatial derivatives, not only the advection part but also the non-advection part must be computed. The spatial derivatives can be updated using Eq. 3.7. Let the right-hand side of the equations be denoted as κ_x and κ_y:

$$\frac{u^{**} - u^*}{\Delta t} = \kappa_x^* \quad \Rightarrow u^{**} = u^* + \kappa_x^* \Delta t \tag{A.39}$$

$$\frac{v^{**} - v^*}{\Delta t} = \kappa_y^* \quad \Rightarrow v^{**} = v^* + \kappa_y^* \Delta t \tag{A.40}$$

The spatial derivatives of u and v, $\frac{\partial u}{\partial x}$, $\frac{\partial u}{\partial y}$, $\frac{\partial v}{\partial x}$,$\frac{\partial v}{\partial y}$ can then be written as:

$$\frac{\partial u^{**}}{\partial x} = \frac{\partial u^*}{\partial x} + \frac{\partial \kappa_x^*}{\partial x} \Delta t \tag{A.41}$$

$$\frac{\partial u^{**}}{\partial y} = \frac{\partial u^*}{\partial y} + \frac{\partial \kappa_x^*}{\partial y} \Delta t \tag{A.42}$$

$$\frac{\partial v^{**}}{\partial x} = \frac{\partial v^*}{\partial x} + \frac{\partial \kappa_y^*}{\partial x} \Delta t \tag{A.43}$$

$$\frac{\partial v^{**}}{\partial y} = \frac{\partial v^*}{\partial y} + \frac{\partial \kappa_y^*}{\partial y} \Delta t \tag{A.44}$$

κ^* can be expressed using a central difference form. For $\frac{\partial u}{\partial x}$ this gives the following:

$$\frac{\partial u^{**}}{\partial x} = \frac{\partial u^*}{\partial x} + \frac{\kappa_x^*(k+1,l) - \kappa_x^*(k-1,l)}{2\Delta x} \Delta t \tag{A.45}$$

From Eq. A.39, κ_x can be written as:

$$\kappa_x^*(k+1,l) = \frac{1}{\Delta t} \left(u^{**}(k+1,l) - u^*(k+1,l) \right) \tag{A.46}$$

$$\kappa_x^*(k-1,l) = \frac{1}{\Delta t} \left(u^{**}(k-1,l) - u^*(k-1,l) \right) \tag{A.47}$$

The same goes for κ_y, and thus the spatial derivatives can be updated as given in Eq. A.48–A.51.

$$\frac{\partial u^{**}}{\partial x}(k,l) = \frac{\partial u^{*}}{\partial x}(k,l) + \frac{1}{2\Delta x(k)}\left[u^{**}(i+1,j) - u^{*}(i+1,j) - u^{**}(i-1,j) + u^{*}(i-1,j)\right] \tag{A.48}$$

$$\frac{\partial u^{**}}{\partial y}(k,l) = \frac{\partial u^{*}}{\partial y}(k,l) + \frac{1}{2\Delta y(l)}\left[u^{**}(k,l+1) - u^{*}(k,l+1) - u^{**}(k,l-1) + u^{*}(k,l-1)\right] \tag{A.49}$$

$$\frac{\partial v^{**}}{\partial x}(k,l) = \frac{\partial v^{*}}{\partial x}(k,l) + \frac{1}{2\Delta x(k)}\left[v^{**}(k+1,l) - v^{*}(k+1,l) - v^{**}(k-1,l) + v^{*}(k-1,l)\right] \tag{A.50}$$

$$\frac{\partial v^{**}}{\partial y}(k,l) = \frac{\partial v^{*}}{\partial y}(k,l) + \frac{1}{2\Delta y(l)}\left[v^{**}(k,l+1) - v^{*}(k,l+1) - v^{**}(k,l-1) + v^{*}(k,l-1)\right] \tag{A.51}$$

A.4 The numerical procedure of the 1-D THINC scheme

We assume that the cell averaged density function $\bar{\phi}_k^n$ is known from the previous time step. The numerical procedure for one time step can then be summarized as follows:

1. Compute α, β, γ and δ for $F_k(x)$ for all cells
2. Estimate the flux g_k for all cell nodes
3. Update $\bar{\phi}_k^{\mathrm{n}+1}$ for all cells

Compute α, β, γ and δ

The hyperbolic tangent function $F_k(x)$ is given as:

$$F_k(x) = \frac{\alpha_k}{2}\left\{1 + \gamma_k \tanh\left[\beta\left(\frac{x - x_{k-1}}{\Delta x_k} - \delta_k\right)\right]\right\} \tag{A.52}$$

where the coefficients α_k and γ_k are given by the following:

$$\alpha_k = \begin{cases} \bar{\phi}^{\mathrm{n}}_{k+1} & \text{for } \bar{\phi}^{\mathrm{n}}_{k+1} >= \bar{\phi}^{\mathrm{n}}_{k-1} \\ \bar{\phi}^{\mathrm{n}}_{k-1} & \text{otherwise} \end{cases} \tag{A.53}$$

$$\gamma_k = \begin{cases} 1 & \text{for } \bar{\phi}^{\mathrm{n}}_{k+1} >= \bar{\phi}^{\mathrm{n}}_{k-1} \\ -1 & \text{otherwise} \end{cases} \tag{A.54}$$

The coefficient β regulates the steepness of the surface layer. β is set to 3.5, which according to Yokoi (2007), corresponds to a smoothing distance of one cell. δ_k is computed using:

$$\frac{1}{\Delta x_k}\int_{x_{k-1}}^{k_i} F_k(x)dx = \bar{\phi}^{\mathrm{n}}_k \tag{A.55}$$

$$\frac{1}{\Delta x_k}\int_{x_{k-1}}^{x_k} \frac{\alpha_k}{2}\left\{1+\gamma_k \tanh\left[\beta\left(\frac{x-x_{k-1}}{\Delta x_k}-\delta_k\right)\right]\right\}dx = \bar{\phi}^{\mathrm{n}}_k \tag{A.56}$$

$$\frac{\alpha_k}{2\Delta x_k}\left[x+\frac{\gamma_k \Delta x_k}{\beta}\ln\left(\cosh\left(\beta\left(\frac{x-x_{k-1}}{\Delta x_k}-\delta_k\right)\right)\right)\right]_{x_{k-1}}^{x_k} = \bar{\phi}^{\mathrm{n}}_k \tag{A.57}$$

$$\frac{\alpha_k}{2\Delta x_k}\left[\Delta x_k+\frac{\gamma_k \Delta x_k}{\beta}\ln\frac{\cosh\left(\beta\left(1-\delta_k\right)\right)}{\cosh\left(\beta\delta_k\right)}\right] = \bar{\phi}^{\mathrm{n}}_k \tag{A.58}$$

$$\frac{\cosh\left(\beta\left(1-\delta_k\right)\right)}{\cosh\left(\beta\delta_k\right)} = \exp\left[\frac{\beta}{\gamma_k}\left(\frac{2}{\alpha_k}\bar{\phi}^{\mathrm{n}}_k-1\right)\right] \tag{A.59}$$

Let κ denote the right-hand side and express δ_k in terms of κ and β:

$$\kappa = \frac{\cosh\left(\beta\left(1-\delta_k\right)\right)}{\cosh\left(\beta\delta_k\right)} = \frac{e^{\beta}e^{-\beta\delta_k}+e^{-\beta}e^{\beta\delta_k}}{e^{\beta\delta_k}+e^{-\beta\delta_k}} \tag{A.60}$$

Rewriting Eq. A.60 gives:

$$\left(e^{\beta\delta_k}\right)^2 = \frac{\left(e^{\beta}\right)^2-\kappa e^{\beta}}{\kappa e^{\beta}-1} \tag{A.61}$$

$$\delta_k = \frac{1}{2\beta}\ln\left|\frac{e^{2\beta}-\kappa e^{\beta}}{\kappa e^{\beta}-1}\right| \tag{A.62}$$

where:

$$\kappa = \exp\left[\frac{\beta}{\gamma_k}\left(\frac{2}{\alpha_k}\bar{\phi}_k^{\mathrm{n}} - 1\right)\right] \tag{A.63}$$

It should be noted that there are some cases where the coefficients of F cannot be determined as described above. An inspection of Eq. A.63 reveals that if $\alpha = 0.0$, the expression for κ is not valid. If $\kappa = exp(\beta)$, the expression for δ_k is not valid. In these cases, the flux g_k can simply be set to $u_k \Delta t \bar{\phi}_k s^{\mathrm{n}}$, since these are cases where $\bar{\phi}_k s^{\mathrm{n}} = \bar{\phi}_{k\pm1}^{\mathrm{n}}$. If κ becomes very large, δ_k tends to zero, and g_k can be computed as described below. This last case may however be necessary to treat as a special case in the computer code.

Estimate the flux g_k

The coefficients of $F_k(x)$ is now determined. To update the cell-averaged function for the next time step $\mathrm{n}+1$, the flux g_k must be estimated for all x_k. A Semi-Lagrangian approach is used, and Eq. 3.23 is rewritten using $dx = udt$. The computation of g_k is dependent on the direction of the flow. For $u_k >= 0.0$, the flux at x_k is given as:

$$\begin{aligned} g_k &= \int_{x_k - u_k\Delta t}^{x_k} F_k(x)dx \\ &= \frac{\alpha}{2}\left[u_k\Delta t + \frac{\gamma_k \Delta x_k}{\beta}\ln\frac{\cosh\left[\beta\left(1-\delta_k\right)\right]}{\cosh\left[\beta\left(1-\frac{u_k\Delta t}{\Delta x_k}-\delta_k\right)\right]}\right] \end{aligned} \tag{A.64}$$

For $u_k < 0.0$, g_k is given as:

$$\begin{aligned} g_k &= -\int_{x_k}^{x_k+|u_k\Delta t|} F_{k+1}(x)dx \\ &= -\frac{\alpha_{k+1}}{2}\left[|u_k\Delta t| + \frac{\gamma_{k+1}\Delta x_{k+1}}{\beta}\ln\frac{\cosh\left[\beta(\frac{|u_k\Delta t|}{\Delta x_{k+1}}-\delta_{k+1})\right]}{\cosh\left[\beta\delta_{k+1}\right]}\right] \end{aligned} \tag{A.65}$$

Update $\bar{\phi}_k^{\mathrm{n}+1}$

The cell averaged density function can now be computed as:

$$\bar{\phi}_k^{\mathrm{n}+1} = \bar{\phi}_k^{\mathrm{n}} - \frac{1}{\Delta x_k}(g_k - g_{k-1}) + \bar{\phi}_k^{\mathrm{n}}(u_k - u_{k-1})\frac{\Delta t}{\Delta x_k} \tag{A.66}$$

The procedure for one time step is now completed.

Appendix B

Verification details

B.1 Introduction

In this appendix, some early validation work and parameter studies are included. The lid driven flow case is used as a verification case by many authors (Ghia et al., 1982; Ferziger and Perić, 2002; Herfjord, 1995b, see e.g.). In this work, it is used to check the performance of the iterative solvers. The results are reported in Sec. B.2. The case with standing waves in a rectangular tank is used to perform basic parameter studies on regular, relatively coarse grids, see Sec. B.3. The experience gained is used in the further work. The added mass of a fully submerged cylinder is studied in Sec. B.4. This work verified the inclusion of a solid body in the code.

B.2 Lid driven flow

B.2.1 Case set-up

The computational domain is set up as a 2-D square tank with a height and breadth of 1.0 m. The tank is totally filled with a homogenous fluid, and the top wall is moving with a horizontal velocity of 1.0 m/s. All walls have no-slip boundary conditions. In Ghia et al. (1982), the Reynolds number (Re) is varied to investigate the flow for different fluid characteristics. In this test case, Re=100 is used. Re=100 is obtained by letting the mass density ρ be that of water ($\rho = 1000\,\mathrm{kg/m}^3$), but increasing the viscosity to $\mu = 10\,\mathrm{kg/ms}$.

A constant grid of 128×128 cells is used. The simulations are run until steady state is obtained, this takes about 25 s. Time step sizes Δt of $1/1000$ and $1/2000$ are run.

Solving the linear equation system that results from discretizing the Poisson

equation is the computationally most costly part of the CIP algorithm. An efficient matrix solver may therefore greatly increase the efficiency of the code. In this test case, two different solvers are compared. One is called the Successive Overrelaxation method (SOR). This is a well-known stationary method, see e.g. Bruaset (1995) The other is a more efficient non-stationary method, the Bi-Conjugate Gradient Stabilized method (Bi–CGStab), described in many textbooks, e.g. Ferziger and Perić (2002). This particular version of the Bi–CGStab method is described in Sleijpen and Fokkema (1993). The simple case of the driven flow in the square tank provides a good case for validating the flow solver and comparing for the SOR solver versus the Bi–CGStab solver.

B.2.2 CIP simulations compared with the multigrid method

The simulations presented in Ghia et al. (1982) are also performed with a grid of 128×128 cells. The results are documented with tabulated values for the velocity profiles in $x-$ and y direction. Detailed plots of the 2-D flow are also presented. The CIP code using SOR is compared first.. After 25 s of simulated flow, the steady state flow seems to be established. A primary vortex is formed with the center at $(x, y) = (0.6172, 07344)$. This is the same position as obtained by Ghia et. al. for $\mathrm{Re} = 100$ (see Ghia et al., 1982, Tab. V). In the computations by Ghia et. al., secondary vortices were obtained in the lower corners of the tank. When plotting the streamlines for the CIP results, the secondary vortices become visible. According to Ghia et al. (1982) the height and breadth of the left vortex are both 0.0781 m (i.e. equal to 10 grid cells), while the right vortex is 0.1328×0.1484. This is the case using the CIP method as well.

Parameters of the simulation is varied to verify the CIP computations for convergence and consistency. The time step is halved to $\Delta t = 1/2000$. This did not have any effect on the results. The simulation with $\Delta t = 1/1000$ is run until $t = 50$ s, confirming that steady state was reached after 25 s. No apparent dissipation of the velocity field occurred.

The same case as described above, with a 128×128 grid and time step size $\Delta t = 1/1000$ is also run using the Bi–CGStab matrix solver instead of SOR. The simulation time was 25 s. Figure B.1 shows the profiles of the $u-$ and v-velocities at the geometric center of the square tank. Results using SOR, Bi–CGStab and the results from Ghia et. al. are compared. It is seen that the runs using Bi–CGStab does not agree with the results using SOR and the results of Ghia et al. (1982). Runs with Bi–CGStab were made with a smaller time step, $\Delta t = 1/2000$. These results are also shown in Fig. B.1, and are closer to the results of Ghia et. al., but does still not agree as well as the SOR results.

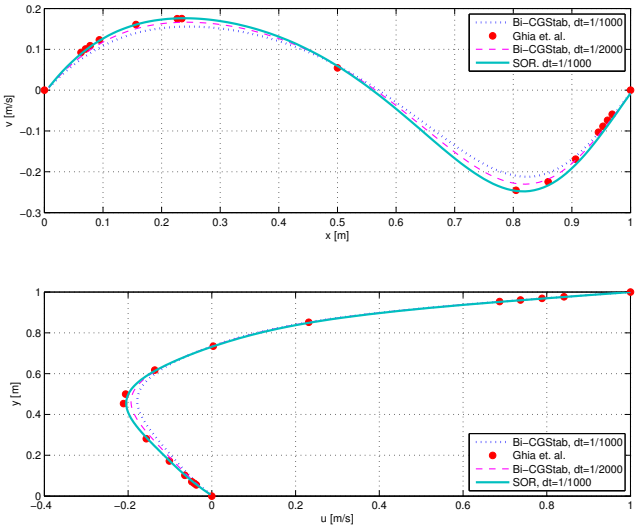

Figure B.1: Velocity profiles in $x-$ and $y-$directions at the geometric center for runs with SOR and Bi–CGStab matrix solvers.

B.2.3 Conclusions for the lid driven flow case

The comparison between the work of Ghia et. al. and the CIP method shows that the CIP method can reproduce the velocity profiles of the fluid flow of this simple case. The secondary vortices seen in the computations using the Multigrid method also appear when using the CIP method.

Two different matrix solvers, SOR and Bi–CGStab was used in the CIP code. It seems that the Bi-CGStab matrix solver has some problems with accuracy, or it needs a finer time step to converge. The simulation results obtained using this solver does not agree as well with the results of Ghia et. al. as the results using the SOR matrix solver does. In its present state, it is not obvious that the Bi–CGStab algorithm is more efficient than SOR. The SOR solver will therefore be preferred in the other benchmark tests.

B.3 Standing waves in a rectangular tank

B.3.1 Introduction

A square tank of dimensions 1.0×1.0 m half-filled with water is given an initial velocity field corresponding to the first natural anti-symmetric eigenmode accord-

ing to linear potential theory, see Sec. 4.3. The velocity potential $\Phi_n(x, y, t)$ is given in Eq. 4.1.

For the first eigen mode, $n = 0$, the wavenumber is $k_0 = \pi$, and the natural period becomes T_0 =1.182 s. For $t = 0$ s, the dynamic pressure is zero for the entire domain, and the free surface is zero for all x. Only the velocity field has non-zero values. This makes the case easy to implement in the numerical model. After the initial condition, no excitation is input to the tank, and the free oscillations of the first mode are studied. In this appendix, some systematic checks of the code are performed using the case to test:

- Grid dependency for regular grids
- Effect of smoothing the spatial derivatives
- Effect of air flow
- Effect of the pressure equation solution
- Effect of the surface capturing scheme

For most checks, the free surface ζ, defined at $\phi_1 = 0.5$, is investigated at $x = -0.45$ m, while the horizontal and vertical velocities u and v is investigated for a horizontal cross-section at $y = -0.1$ m and at a vertical section at $x = 0.0$ m. The coordinate system of the tank is defined in Fig. 4.1, the x-axis lies at the centerline and the y-axis lies at the free surface. The simulations are run for 4 periods.

B.3.2 Grid dependency

Two grids with constant grid size were run, one with $\Delta x = \Delta y = 0.01$ m, i.e. a 100×100 grid. For the other grid, the cell size was halved to give a 200×200 grid using $\Delta x = \Delta y = 0.005$ m. Figure B.2 shows the free surface as a function of time. The two grids are compared with linear theory. The finest grid yields somewhat better results compared to linear theory, as could be expected. The period and total wave height seem to agree, while the crest is somewhat high and the trough too shallow, i.e. the wave is asymmetric in the CIP simulations. The amplitude of the simulated waves is not quite stable, this may be due to the abrupt start of the simulation. Both grids are too coarse to obtain a good fit with linear potential theory.

Figure B.3 shows the velocity profiles in a horizontal cross section at $y = -0.1$ m (Fig. B.3(a)) and in a vertical cross section at $x = 0.0$ m (Fig. B.3(b)). The simulated profiles are compared with linear potential theory for $t = 2.4$ s. In this case, the potential theory is extrapolated up into the air, although the profile is only valid up to the mean free surface at $y = 0.0$ m.

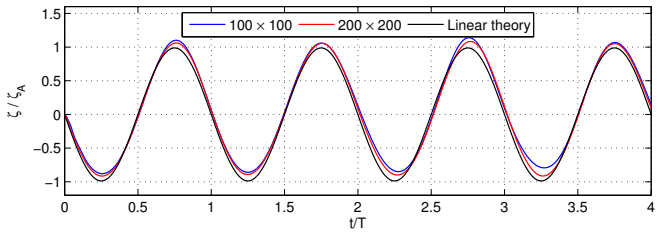

Figure B.2: Free surface for two different grids versus linear potential theory.

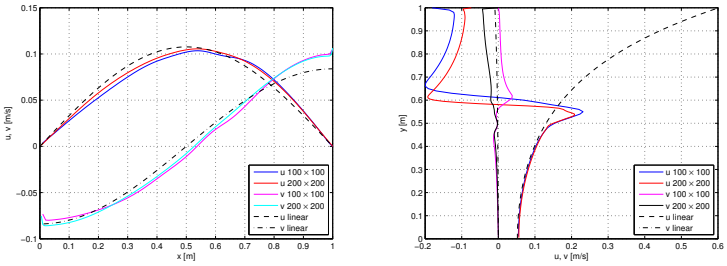

(a) u and v at $y = -0.1$ m

(b) u and v at $x = -0.45$ m

Figure B.3: Horizontal and vertical velocity profiles at $x = -0.45$ and $y = -0.1$ m for two different grids.

B.3.3 Effect of smoothing

In time, the independent computation of the spatial derivatives become inaccurate, as discussed in Sec. 3.4.2. Thus, it may be necessary to update the derivatives by computing them directly from the velocities, i.e. by numerical differentiation. This process is performed at a certain interval and is referred to as smoothing. Figure B.4 shows the free surface for a simulation performed without smoothing and one where smoothing is performed for every 30th time step. The simulations are identical. Figure B.5 shows the same profiles as in Fig. B.3 above for the two simulations, also they are identical. The simulations are probably too short to show any effect of the smoothing.

B.3.4 Effect of air flow

In the simulations above, the initial velocity field given by potential theory is simply extrapolated into the air. A more realistic profile is obtained by mirroring the

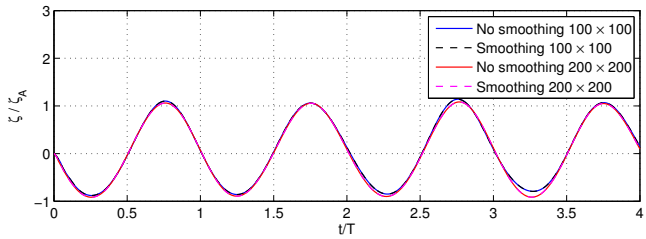

Figure B.4: Simulated free surface with and without smoothing.

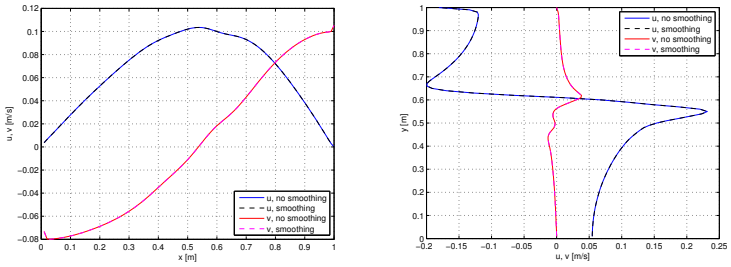

(a) u and v at $y = -0.1$ m

(b) u and v at $y = -0.1$ m

Figure B.5: Horizontal and vertical velocity profiles at $x = -0.45$ and $y = -0.1$ m with and without smoothing.

velocity field about the free surface. The vertical velocity field is thus the same as before, while for the horizontal velocity there is now a discontinuity at the free surface. Figure B.6(a) shows the difference in the initial horizontal velocity at $x = 0.0$ m. Figure B.6(b) shows the simulated free surface for the cases. The difference is small. The amplitude is somewhat more stable for the case with the mirrored initial velocity field. Figure B.7 shows the velocity profiles for the two cases. Surprisingly, the airflow of the extrapolated case seems more benign than that of the mirrored case. The difference in the water is small, but the air flow does have a small influence on the flow in the water.

B.3.5 Effect of pressure computation method

The simulations above are performed using the original CCUP scheme as presented by Hu and Kashiwagi (e.g. 2004). An initial guess of the new pressure field p^* is found using the CIP method. This pressure field is used as a preconditioner

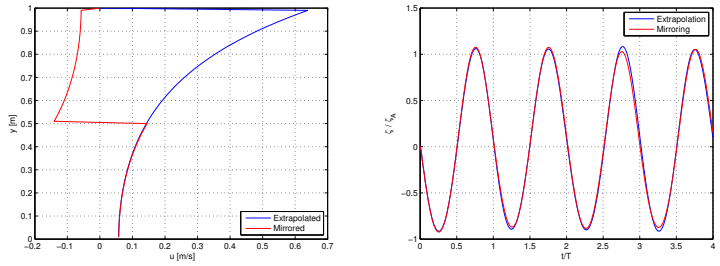

(a) Initial velocity field

(b) Wave elevation

Figure B.6: Difference in initital velocity field

for the iterative solver when solving the Pressure-Poisson equation for the total pressure. The pressure field for the next time step is not affected by the use of the preconditioner, but the solution of the Poisson equation is faster. The velocity field is first advected using CIP, then updated by the diffusion step before used as input to the Pressure-Poisson equation. The final velocity field is then updated after the new pressure p^{n+1} is found. As discussed in Sec. 3.4.1, this is an uncoupled fractional step method.

Another scheme can be devised by assuming that the pressure field changes only a little for each time step. Instead of solving the Poisson equation for the total pressure field, the incremental pressure $dp = p^{n+1} - p^n$ can be solved for. This is called the incremental pressure correction method and is described in Brown et al. (e.g. 2001). The velocity field, already updated by the advection step and the diffusion step is then updated with p^n using Eq. B.1 before solving the Poisson equation.

$$u_i^{*p} = u_i^{**} - \frac{dt}{\rho}\frac{\partial p^n}{\partial x_i} \tag{B.1}$$

After the Poisson equation is solved for dp, the new pressure field is found using Eq. B.2, and the new velocity field is found using Eq. B.3.

$$p^{n+1} = dp + p^n \tag{B.2}$$

$$u_i^{n+1} = u_i^{*p} - \frac{dt}{\rho}\frac{\partial dp}{\partial x_i} \tag{B.3}$$

The two methods for computing the pressure is compared for the 100×100 grid

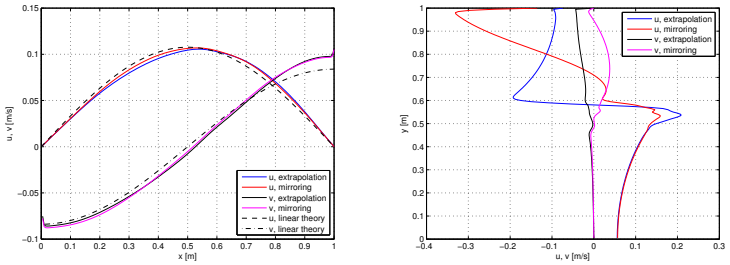

(a) u and v at $y = 0.4$ m (b) u and v at $y = 0.4$ m

Figure B.7: Horizontal and vertical velocity profiles at $x = -0.45$ and $y = -0.1$ m for different initial velocity fields.

case presented above. Figure B.8 shows the free surface, while Fig. B.9 shows the velocity profiles. The differences between the two computation methods are negligible. The incremental pressure method required much longer time before the iterative solver converged, and the simulations became unstable due to convergence failure in some cases. The original scheme is therefore used in the further work.

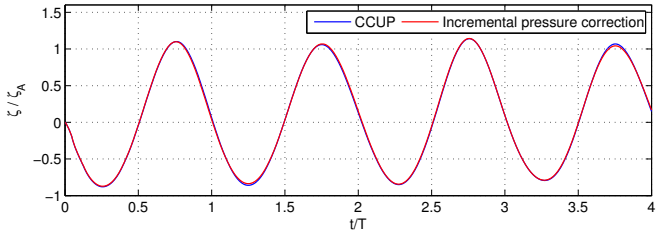

Figure B.8: Simulated free surface for different pressure field solution methods.

B.3.6 Effect of surface capturing method

All the simulations above are performed using the CIP method for advecting the water density function ϕ_1. Before advection, a linear transformation is performed to decrease the smearing of the free surface that occur during simulation, see Eq. 3.18. The tangent transformation is more computational costly, but retains a sharper surface, see Eq. 3.17.

The surface layer thickness δy is defined as the distance between $\phi_1 = 0.05$

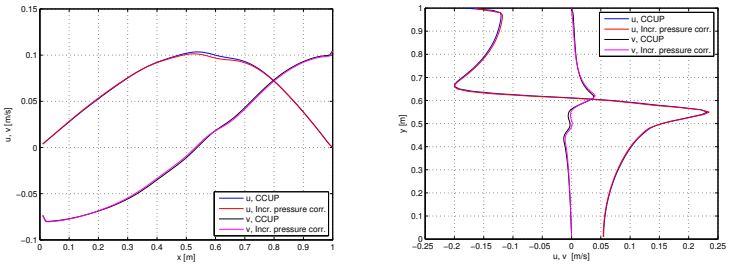

(a) u and v at $y = 0.4$ m

(b) u and v at $y = 0.4$ m

Figure B.9: Horizontal and vertical velocity profiles at $x = -0.45$ and $y = -0.1$ m for different pressure field solution methods.

and $\phi_1 = 0.95$, while the free surface is defined at $\phi_1 = 0.50$. Figures B.10(a) and B.10(b) shows these values of ϕ_1 using linear and tangent transformation, for the 100×100 grid and 200×200 grid, respectively. The increase in surface layer is evident for the linear transformation. The surface layer increase for the tangent transformation is small in comparison, see also Fig. B.11, where $\delta y = y_{\phi_1=0.05} - y_{\phi_1=0.95}$ is plotted against time. A drawback with the tangent transformation is that the surface may not be smooth, but rather obtain a stepwise behavior. This effect is decreased with decreasing cell size. In Fig. B.12, the free surface is plotted using the tangent transformation on three different grid, 100×100, 200×200 and 376×344. For the finest grid, the step-wise behaviour of the surface is no longer observed. For the finest grid, the cells are refined in the y-direction in the free surface zone. This corresponds to the base case grid in Sec. 4.3.

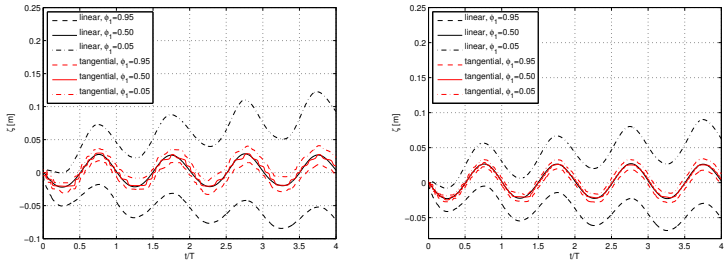

(a) 100 × 100 grid (b) 200 × 200 grid

Figure B.10: Density function contours using linear and tangent transformation.

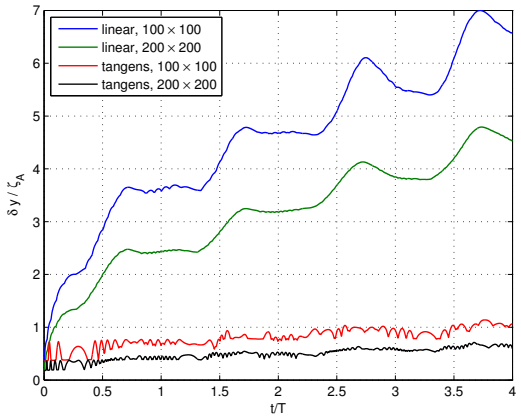

Figure B.11: Surface layer thickness growth using linear and tangent transformation.

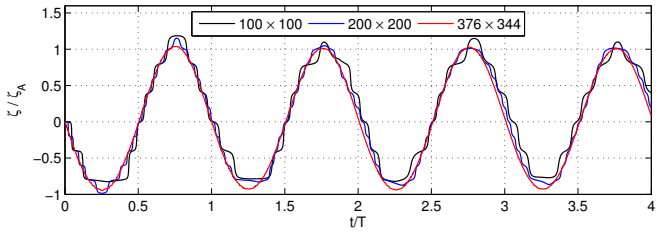

Figure B.12: Free surface using tangent transformation.

B.4 Added mass of a fully submerged cylinder

A fully submerged cylinder is given an oscillatory heave motion η_3:

$$\eta_3 = \eta_A \cos(\omega t) \tag{B.4}$$

Figure B.13 shows the computational domain for the CIP simulations. The tank is $2(x_c \times y_c)$ with the center of the cylinder placed in the middle of the tank. The radius of the cylinder is r_c. The motion of the cylinder leads to a hydrodynamic force on the body, in phase with the acceleration of the cylinder. This force is the added mass force, in this case in heave, i.e. A_{33}. In addition there is a buoyancy force F_{buoy}, which in this case is constant, $F_{\text{buoy}} = \rho g \pi r_c^2$. The total force on the body becomes:

$$F_3(t) = -A_{33}\omega^2 \eta_3(t) + F_{\text{buoy}} \tag{B.5}$$

For a circular cylinder in infinite fluid, potential theory gives a frequency–independent added mass in heave:

$$A_{33} = \rho \pi r_c^2 \tag{B.6}$$

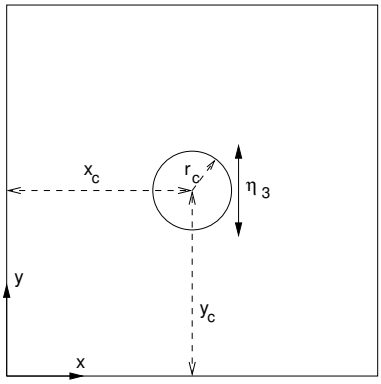

Figure B.13: Square tank with cylinder of radius r_c.

CIP simulations with different sizes of the computational domain and different grid configurations are tested and compared with the analytical solution for infinite water depth. The radius and oscillation amplitude η_{3a} of the cylinder is kept constant, as well as the excitation frequency ω.

Influence of the walls

When using potential theory, it is possible to assume infinite fluid around the cylinder. When using the CIP method, a finite computational domain must be used. Figure B.14 shows the vertical force on the cylinder computed with different domain sizes. Table B.1 shows the different cases run with domain sizes and details of the grid.

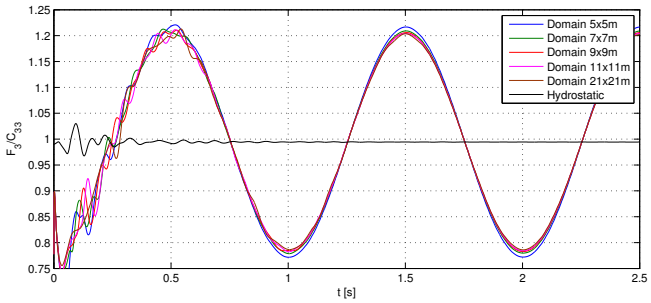

Figure B.14: Vertical force on cylinder computed for different domain sizes.

According to potential theory, the influence of the walls should be negligible if the distance is 5-7 times the diameter of the cylinder. In the CIP simulations, the walls affect the force on the cylinder even for greater distances. From the start of the simulations, the transient oscillations in the vertical force differs for different domain sizes. This is probably due to the elliptic form of the pressure-Poisson equation giving instant changes of the pressure in the entire domain. As steady state is reached, the vertical force decreases for increasing computational domains. The walls contributes to the added mass. Figure B.15 shows CIP results for the largest and the smallest domain together with the analytical force in infinite water. As expected, the larger domain is closer to the analytical solution. There is also a bias in the computed force, the amplitude of the maximum force is smaller than the amplitude of the minimum force. This is at least partly due to the computation of the constant buoyancy force, which is somewhat lower than the analytical value, see Fig. B.14. The discrepancy is 0.5 % and is due to the grid resolution of the cylinder (see Sec. B.4 below). For the 11×11 m computation domain, the discrepancy between the theoretical and computed values are 1.2 % for the minimum value and 0.3 % for the maximum value when the bias is taken into account.

Different grid configurations at the edges of the tank is run to check if this had any effect on the vertical force (Case no. 6010 and 6020, see Tab. B.1). This only had an effect for the transient oscillations in the start-up phase. The steady state solution converges to the same value irrespective of the grid at the edge. It was not

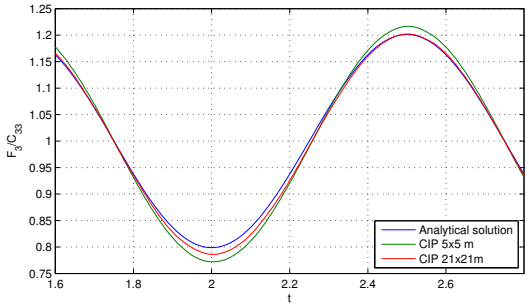

Figure B.15: Vertical force on cylinder. CIP computations with different domain sizes versus potential theory.

attempted to include damping zones at the edges of the tank. It was assumed that the increase in grid size toward the tank walls would give sufficient damping. In the next section, a convergence test for the grid resolution at the cylinder is discussed.

Table B.1: Simulated cases for the submerged cylinder

Case	Domain size	Grid size	Min. cell size
1040	7×7 m	530×530	0.005 m
3010	9×9 m	540×540	0.005 m
5010	5×5 m	520×520	0.005 m
6010	11×11 m	550×550	0.005 m
6020	11×11 m	570×570	0.005 m
6030	11×11 m	350×350	0.010 m
6040	11×11 m	840×840	0.002 m
7010	21×21 m	720×720	0.005 m

Convergence test

A spatial convergence test is performed by changing the grid size at the cylinder area. The base case has a grid size of 0.005 m in both directions, i.e. $r_c/\Delta x = r_c/\Delta y = 100$. A coarser grid, with $r_c/\Delta x = r_c/\Delta y = 50$ and a finer grid, with $r_c/\Delta x = r_c/\Delta y = 250$ is run and the vertical force is computed. Figure B.16 shows the non–dimensional vertical force $(F_3 - F_b)/(\rho g \pi r_c^2)$ for the three different grids. The refinement of the grid leads to a longer period with transient oscillations before steady state is reached.

The hydrostatic force is computed using the CIP method by running the simulations with no motion of the cylinder. After some transient oscillations, the force becomes time-independent as expected. As mentioned above, the accuracy of the hydrostatic force is dependent on the grid resolution at the cylinder, i.e. the finer the grid, the better the accuracy of the hydrostatic force. In Fig. B.16, the computed hydrostatic force is subtracted from the time series to evaluate the accuracy of the added mass force. The added mass force is not as affected by the grid size as the hydrostatic force is. However, transient oscillations of the dynamic force is present. The oscillations decay with time, but are more pronounced for the finer grid. These oscillations are probably due to an inbalance between the initial pressure field inside the body and the pressure field set up by the body motion. When the transients die out, the CIP simulations are in fair agreement with the analytical solution. Using the base case grid, the discrepancy between the added mass computed by the CIP code and the analytical value is 4%.

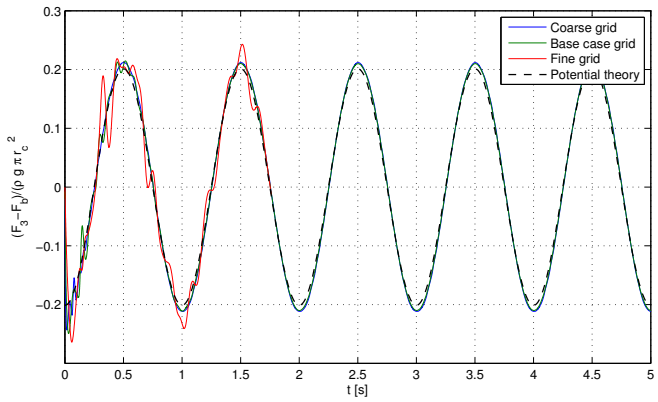

Figure B.16: Added mass force on cylinder. CIP computations with different grid resolutions versus potential theory.

Appendix C

Comparison of vertical forces for the glass flume experiment

C.1 Introduction

In this appendix, figures with comparisons of measured and simulated forces are shown for the 12 cases given in Tab. 6.4. The results are discussed in Sec. 6.4.2.

Case 1	F_y	$T = 1.00$ s	$\zeta_A = 0.05$ m	$\eta_D = 0.04$ m	10 Hz	Fig. C.1
Case 1	F_y	$T = 1.00$ s	$\zeta_A = 0.05$ m	$\eta_D = 0.04$ m	5 Hz	Fig. C.2
Case 1	ζ	$T = 1.00$ s	$\zeta_A = 0.05$ m	$\eta_D = 0.04$ m		Fig. C.3
Case 2	F_y	$T = 1.00$ s	$\zeta_A = 0.06$ m	$\eta_D = 0.04$ m	10 Hz	Fig. C.4
Case 2	F_y	$T = 1.00$ s	$\zeta_A = 0.06$ m	$\eta_D = 0.04$ m	5 Hz	Fig. C.5
Case 2	ζ	$T = 1.00$ s	$\zeta_A = 0.06$ m	$\eta_D = 0.04$ m		Fig. C.6
Case 3	F_y	$T = 1.00$ s	$\zeta_A = 0.07$ m	$\eta_D = 0.04$ m	10 Hz	Fig. C.7
Case 3	F_y	$T = 1.00$ s	$\zeta_A = 0.07$ m	$\eta_D = 0.04$ m	10 Hz	Fig. C.8
Case 4	F_y	$T = 1.11$ s	$\zeta_A = 0.05$ m	$\eta_D = 0.04$ m	10 Hz	Fig. C.9
Case 4	ζ	$T = 1.11$ s	$\zeta_A = 0.05$ m	$\eta_D = 0.04$ m		Fig. C.10
Case 4	F_y	$T = 1.11$ s	$\zeta_A = 0.05$ m	$\eta_D = 0.04$ m	10 Hz	Fig. C.11
Case 5	F_y	$T = 1.11$ s	$\zeta_A = 0.06$ m	$\eta_D = 0.04$ m	10 Hz	Fig. C.12
Case 5	ζ	$T = 1.11$ s	$\zeta_A = 0.06$ m	$\eta_D = 0.04$ m		Fig. C.13
Case 6	F_y	$T = 1.11$ s	$\zeta_A = 0.07$ m	$\eta_D = 0.04$ m	10 Hz	Fig. C.14
Case 6	F_y	$T = 1.11$ s	$\zeta_A = 0.07$ m	$\eta_D = 0.04$ m	10 Hz	Fig. C.15
Case 7	F_y	$T = 1.25$ s	$\zeta_A = 0.05$ m	$\eta_D = 0.04$ m	10 Hz	Fig. C.16

Case 7	ζ	$T = 1.25$ s	$\zeta_A = 0.05$ m	$\eta_D = 0.04$ m		Fig. C.17
Case 7	F_y	$T = 1.25$ s	$\zeta_A = 0.05$ m	$\eta_D = 0.04$ m	10 Hz	Fig. C.18
Case 8	F_y	$T = 1.25$ s	$\zeta_A = 0.06$ m	$\eta_D = 0.04$ m	10 Hz	Fig. C.19
Case 8	ζ	$T = 1.25$ s	$\zeta_A = 0.06$ m	$\eta_D = 0.04$ m		Fig. C.20
Case 9	F_y	$T = 1.25$ s	$\zeta_A = 0.07$ m	$\eta_D = 0.04$ m	10 Hz	Fig. C.21
Case 9	F_y	$T = 1.25$ s	$\zeta_A = 0.07$ m	$\eta_D = 0.04$ m	10 Hz	Fig. C.22
Case 10	F_y	$T = 1.11$ s	$\zeta_A = 0.06$ m	$\eta_D = 0.06$ m	10 Hz	Fig. C.23
Case 11	F_y	$T = 1.11$ s	$\zeta_A = 0.07$ m	$\eta_D = 0.06$ m	10 Hz	Fig. C.24
Case 11	F_y	$T = 1.11$ s	$\zeta_A = 0.07$ m	$\eta_D = 0.06$ m	5 Hz	Fig. C.25
Case 12	F_y	$T = 1.11$ s	$\zeta_A = 0.08$ m	$\eta_D = 0.06$ m	10 Hz	Fig. C.26
Case 12	F_y	$T = 1.11$ s	$\zeta_A = 0.08$ m	$\eta_D = 0.06$ m	5 Hz	Fig. C.27

C.2 Wave period = 1.00 s, airgap = 0.04 m

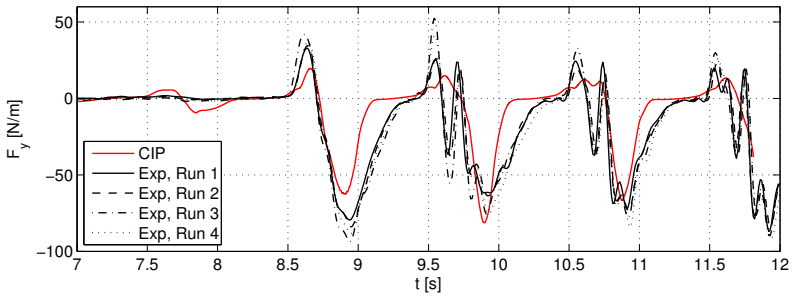

Figure C.1: Force history for $\zeta_A = 0.05$m, $T = 1.00$s and $\eta_D = 0.04$ m.

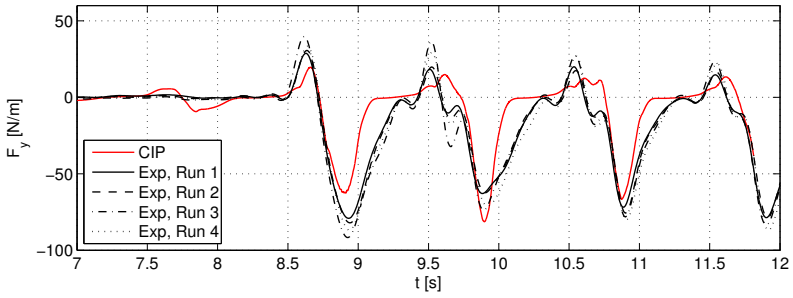

Figure C.2: Force history ($f_c = 5$ Hz) for $\zeta_A = 0.05$m, $T = 1.00$s and $\eta_D = 0.04$ m.

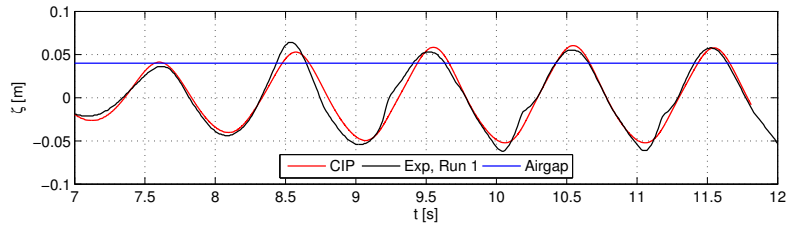

Figure C.3: Wave elevation 15 cm in front of deck box for $\zeta_A = 0.05$m, $T = 1.00$s and $\eta_D = 0.04$ m.

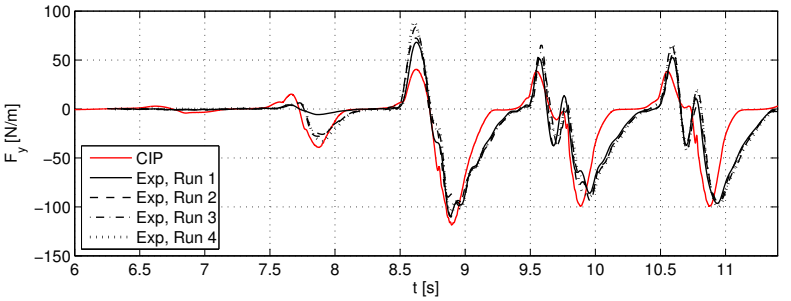

Figure C.4: Force history for $\zeta_A = 0.06$m, $T = 1.00$s and $\eta_D = 0.04$ m.

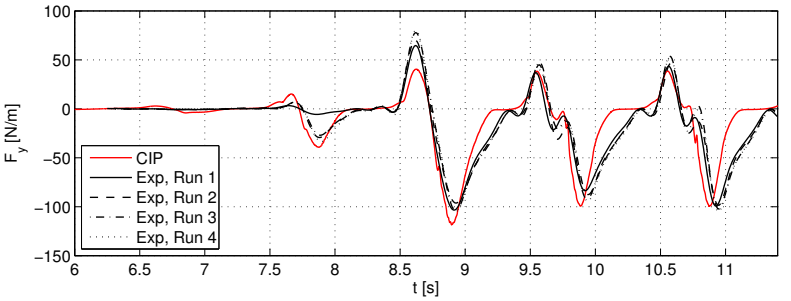

Figure C.5: Force history ($f_c = 5$ Hz) for $\zeta_A = 0.06$m, $T = 1.00$s and $\eta_D = 0.04$ m.

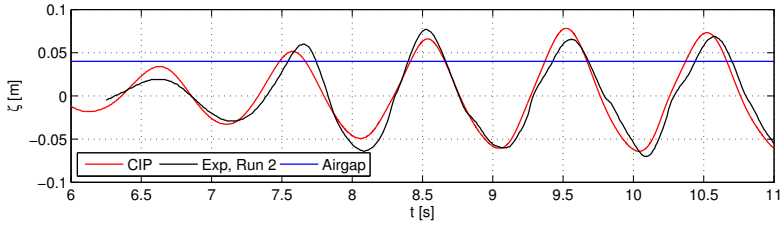

Figure C.6: Wave elevation 15 cm in front of deck box for $\zeta_A = 0.06$m, $T = 1.00$s and $\eta_D = 0.04$ m.

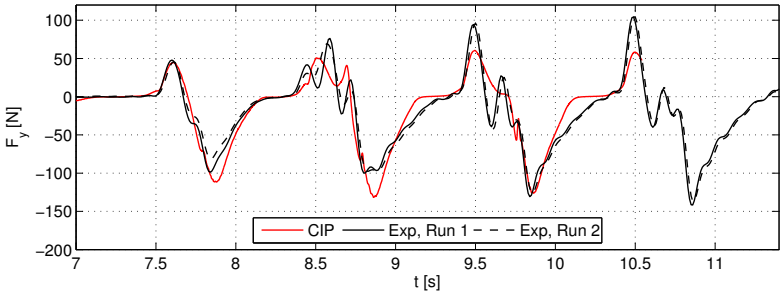

Figure C.7: Force history for $\zeta_A = 0.07$m, $T = 1.00$s and $\eta_D = 0.04$ m.

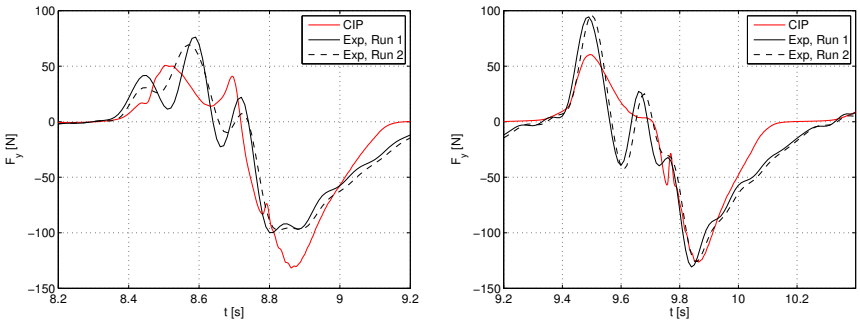

(a) t=8.0 s (b) t=9.0 s

Figure C.8: Impact events for $\zeta_A = 0.07$m, $T = 1.00$s and $\eta_D = 0.04$m

C.3 Wave period = 1.11 s, airgap = 0.04 m

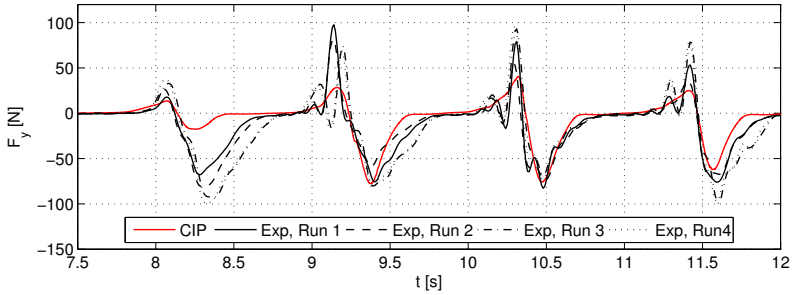

Figure C.9: Force history for $\zeta_A = 0.05$m, $T = 1.11$s and $\eta_D = 0.04$ m.

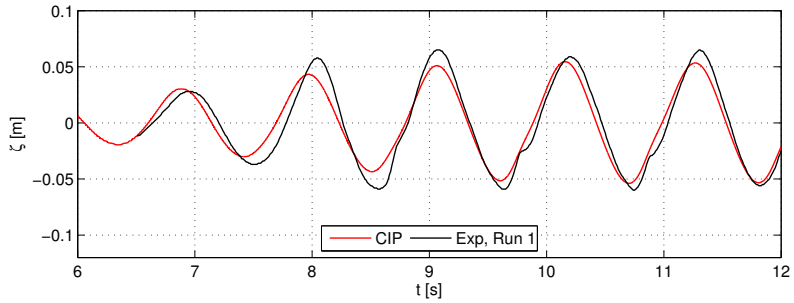

Figure C.10: Wave elevation 15 cm in front of deck box for $\zeta_A = 0.05$m, $T = 1.11$s and $\eta_D = 0.04$ m.

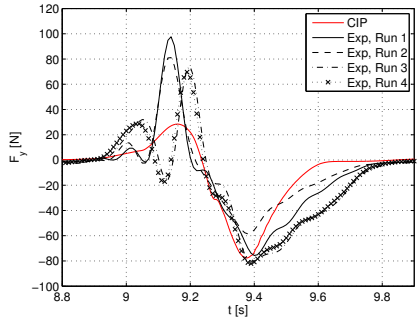

(a) t=9.0 s

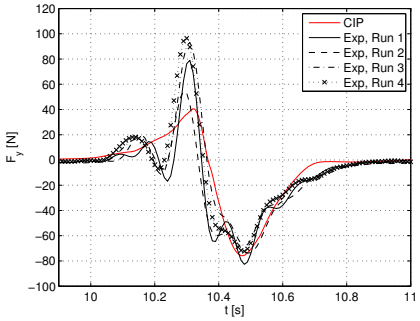

(b) t=10.0 s

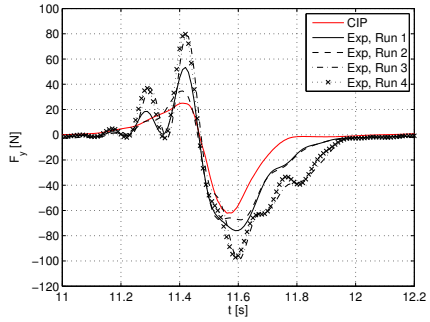

(c) t=11.0 s

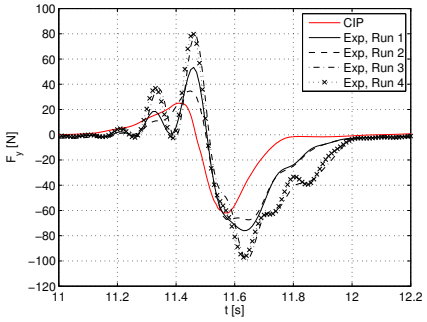

(d) t=12.0 s

Figure C.11: Force history for $\zeta_A = 0.05$m, $T = 1.11$s and $\eta_D = 0.04$m

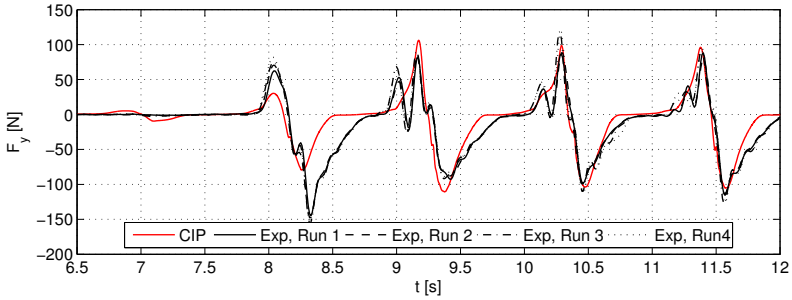

Figure C.12: Force history for $\zeta_A = 0.06$m, $T = 1.11$s and $\eta_D = 0.04$ m.

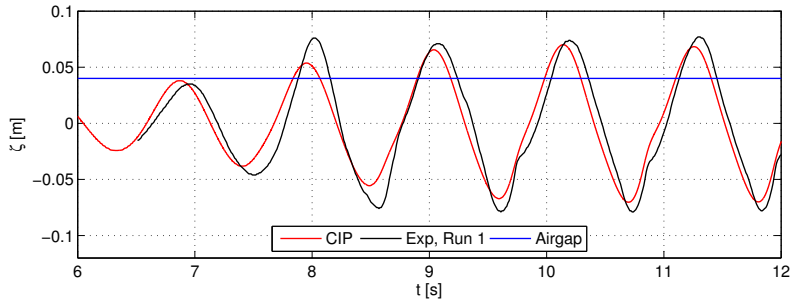

Figure C.13: Wave elevation 15 cm in front of deck box for $\zeta_A = 0.06$m, $T = 1.11$s and $\eta_D = 0.04$ m.

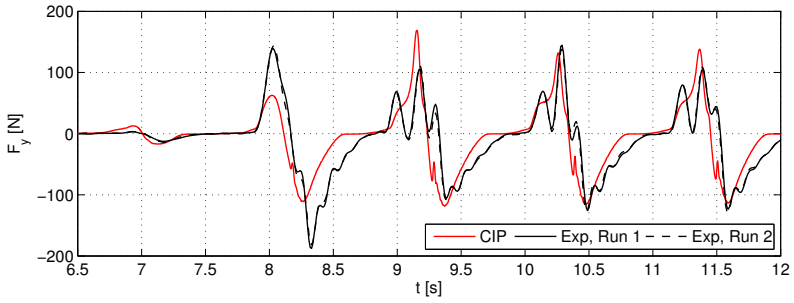

Figure C.14: Force history for $\zeta_A = 0.07$m, $T = 1.11$s and $\eta_D = 0.04$ m.

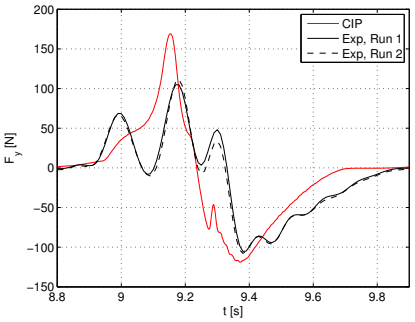

(a) t=9.0 s

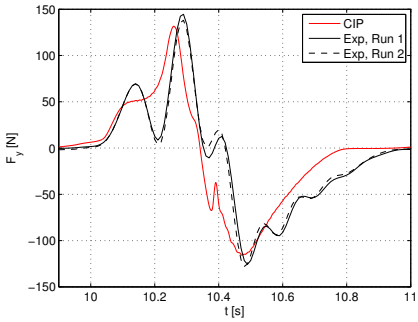

(b) t=10.0 s

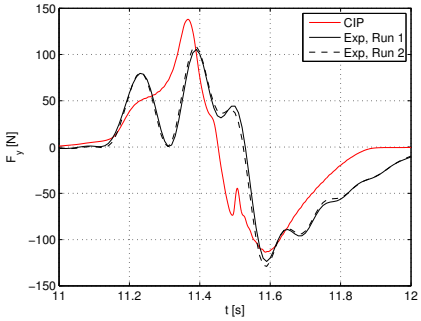

(c) t=11.0 s

Figure C.15: Force history for $\zeta_A = 0.07$m, $T = 1.11$s and $\eta_D = 0.04$m

C.4 Wave period = 1.25 s, airgap = 0.04 m

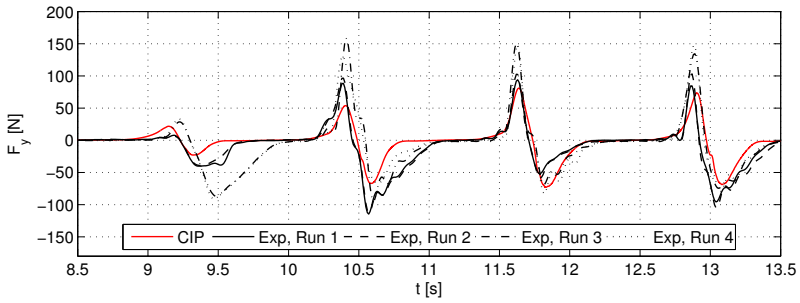

Figure C.16: Force history for $\zeta_A = 0.05$m, $T = 1.25$s and $\eta_D = 0.04$ m.

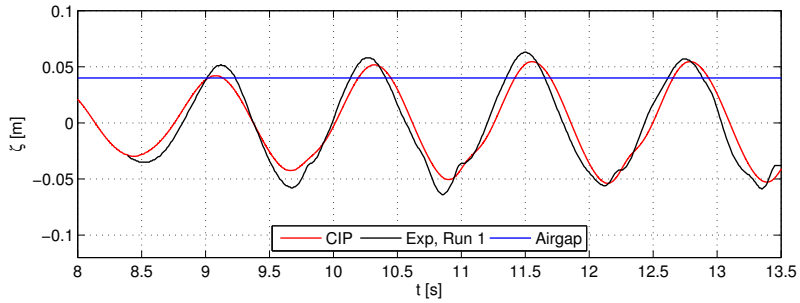

Figure C.17: Wave elevation 15 cm in front of deck box for $\zeta_A = 0.05$m, $T = 1.25$s and $\eta_D = 0.04$ m.

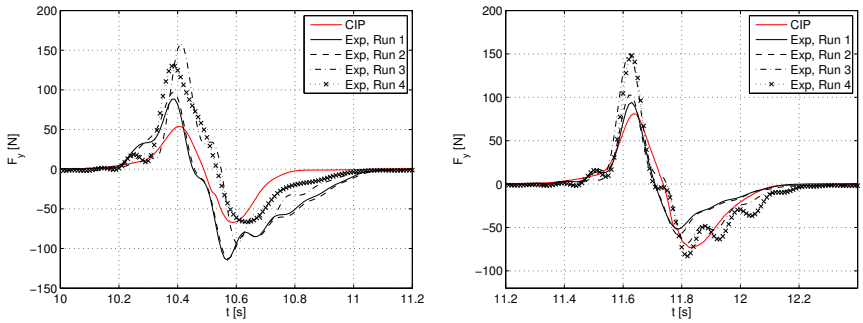

(a) t=10.0 s

(b) t=11.0 s

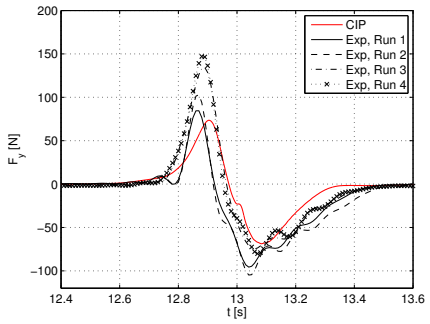

(c) t=12.0 s

Figure C.18: Force history for $\zeta_A = 0.05$m, $T = 1.25$s and $\eta_D = 0.04$m

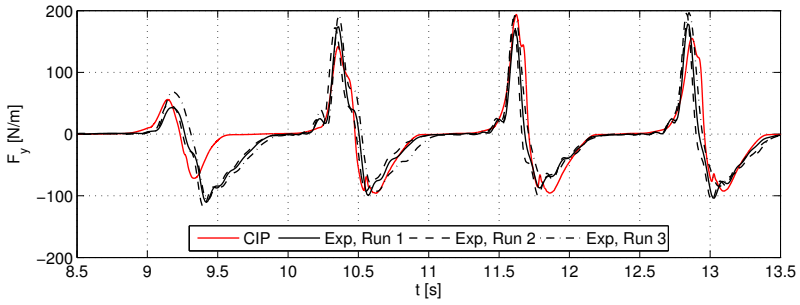

Figure C.19: Force history for $\zeta_A = 0.06$m, $T = 1.25$s and $\eta_D = 0.04$ m.

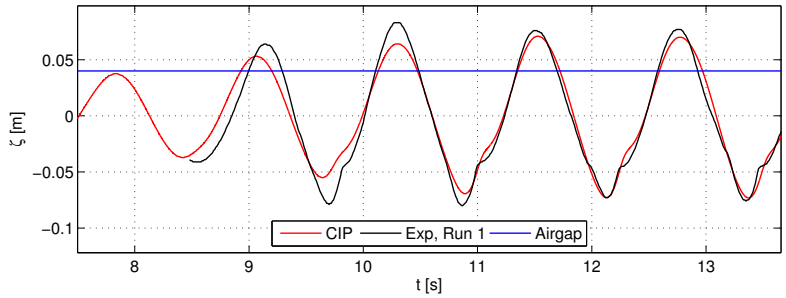

Figure C.20: Wave elevation 15 cm in front of deck box for $\zeta_A = 0.06$m, $T = 1.25$s and $\eta_D = 0.04$ m.

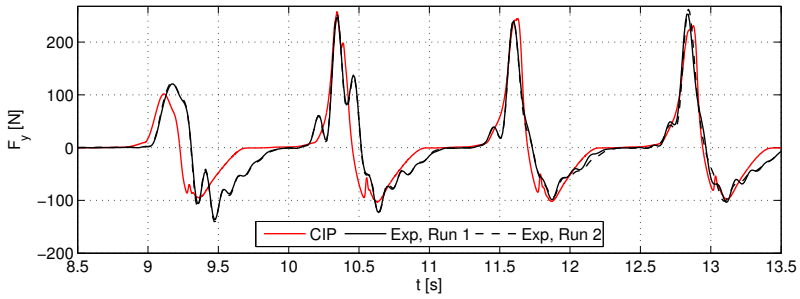

Figure C.21: Force history for $\zeta_A = 0.07$m, $T = 1.25$s and $\eta_D = 0.04$ m.

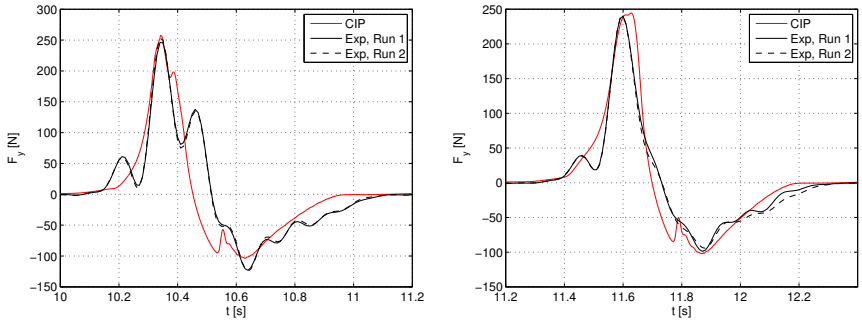

(a) t=10.0 s

(b) t=11.0 s

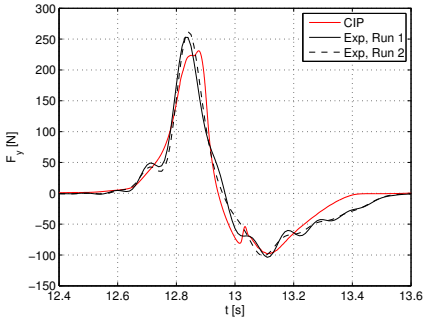

(c) t=12.0 s

Figure C.22: Force history for $\zeta_A = 0.07$m, $T = 1.25$s and $\eta_D = 0.04$m

C.5 Wave period = 1.11 s, airgap = 0.06 m

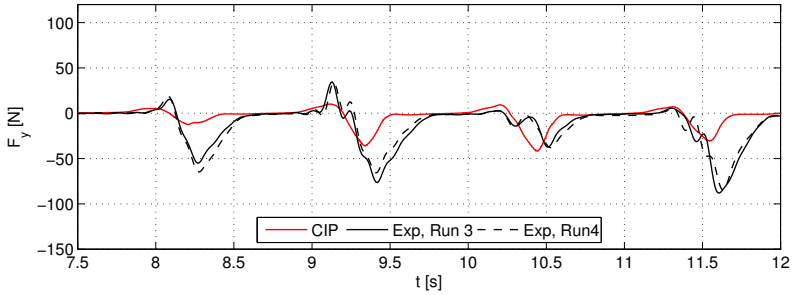

Figure C.23: Force history for $\zeta_A = 0.06$m, $T = 1.11$s and $\eta_D = 0.06$ m.

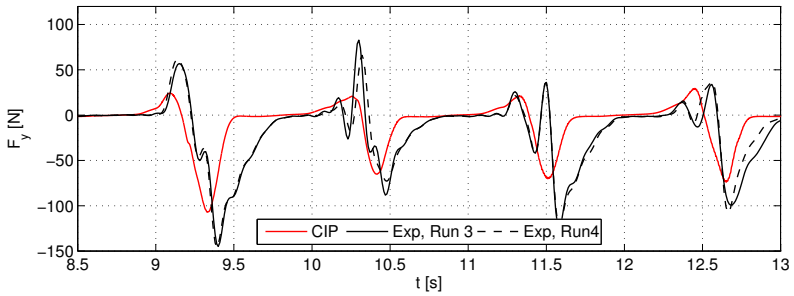

Figure C.24: Force history for $\zeta_A = 0.07$m, $T = 1.11$s and $\eta_D = 0.06$ m.

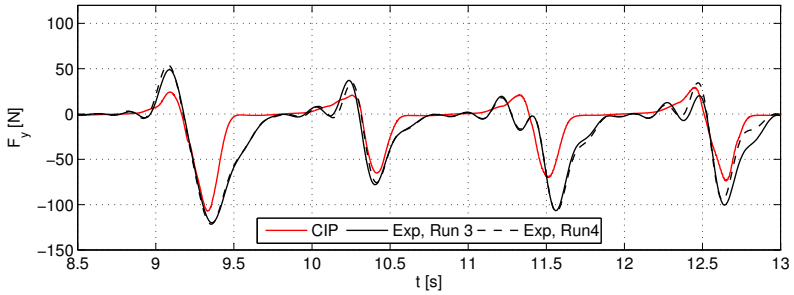

Figure C.25: Force history ($f_c = 5$ Hz) for $\zeta_A = 0.07$m, $T = 1.11$s and $\eta_D = 0.06$ m.

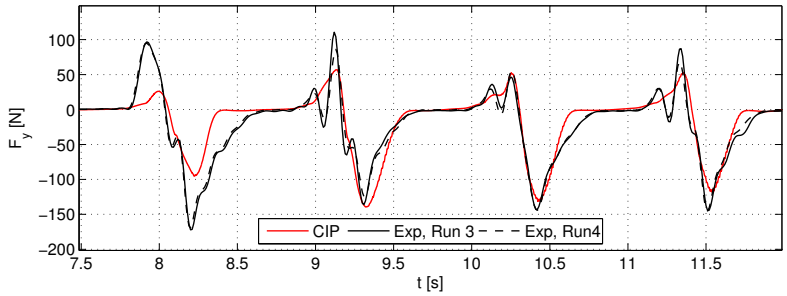

Figure C.26: Force history for $\zeta_A = 0.08$m, $T = 1.11$s and $\eta_D = 0.06$ m.

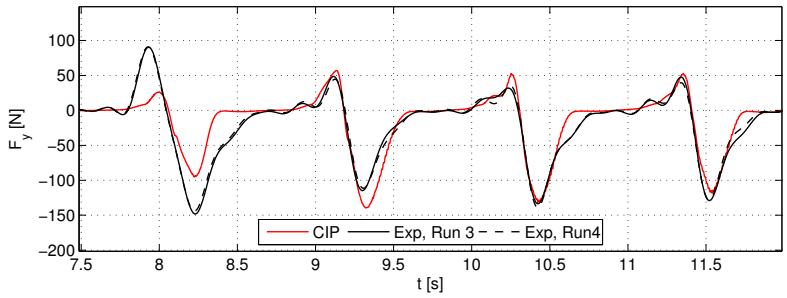

Figure C.27: Force history ($f_c = 5$ Hz) for $\zeta_A = 0.08$m, $T = 1.11$s and $\eta_D = 0.06$ m.

R A P P O R T E R
UTGITT VED
INSTITUTT FOR MARIN TEKNIKK
(tidligere: FAKULTET FOR MARIN TEKNIKK)
NORGES TEKNISK-NATURVITENSKAPELIGE UNIVERSITET

UR-79-01 Brigt Hatlestad, MK:	The finite element method used in a fatigue evaluation of fixed offshore platforms. (Dr.Ing. Thesis)
UR-79-02 Erik Pettersen, MK:	Analysis and design of cellular structures. (Dr.Ing. Thesis)
UR-79-03 Sverre Valsgård, MK:	Finite difference and finite element methods applied to nonlinear analysis of plated structures. (Dr.Ing. Thesis)
UR-79-04 Nils T. Nordsve, MK:	Finite element collapse analysis of structural members considering imperfections and stresses due to fabrication. (Dr.Ing. Thesis)
UR-79-05 Ivar J. Fylling, MK:	Analysis of towline forces in ocean towing systems. (Dr.Ing. Thesis)
UR-80-06 Nils Sandsmark, MM:	Analysis of Stationary and Transient Heat Conduction by the Use of the Finite Element Method. (Dr.Ing. Thesis)
UR-80-09 Sverre Haver, MK:	Analysis of uncertainties related to the stochastic modelling of ocean waves. (Dr.Ing. Thesis)
UR-85-46 Alf G. Engseth, MK:	Finite element collapse analysis of tubular steel offshore structures. (Dr.Ing. Thesis)
UR-86-47 Dengody Sheshappa, MP:	A Computer Design Model for Optimizing Fishing Vessel Designs Based on Techno-Economic Analysis. (Dr.Ing. Thesis)
UR-86-48 Vidar Aanesland, MH:	A Theoretical and Numerical Study of Ship Wave Resistance. (Dr.Ing. Thesis)
UR-86-49 Heinz-Joachim Wessel, MK:	Fracture Mechanics Analysis of Crack Growth in Plate Girders. (Dr.Ing. Thesis)
UR-86-50 Jon Taby, MK:	Ultimate and Post-ultimate Strength of Dented Tubular Members. (Dr.Ing. Thesis)

UR-86-51 Walter Lian, MH:	A Numerical Study of Two-Dimensional Separated Flow Past Bluff Bodies at Moderate KC-Numbers. (Dr.Ing. Thesis)
UR-86-52 Bjørn Sortland, MH:	Force Measurements in Oscillating Flow on Ship Sections and Circular Cylinders in a U-Tube Water Tank. (Dr.Ing. Thesis)
UR-86-53 Kurt Strand, MM:	A System Dynamic Approach to One-dimensional Fluid Flow. (Dr.Ing. Thesis)
UR-86-54 Arne Edvin Løken, MH:	Three Dimensional Second Order Hydrodynamic Effects on Ocean Structures in Waves. (Dr.Ing. Thesis)
UR-86-55 Sigurd Falch, MH:	A Numerical Study of Slamming of Two-Dimensional Bodies. (Dr.Ing. Thesis)
UR-87-56 Arne Braathen, MH:	Application of a Vortex Tracking Method to the Prediction of Roll Damping of a Two-Dimension Floating Body. (Dr.Ing. Thesis)
UR-87-57 Bernt Leira, MR:	Gaussian Vector Processes for Reliability Analysis involving Wave-Induced Load Effects. (Dr.Ing. Thesis)
UR-87-58 Magnus Småvik, MM:	Thermal Load and Process Characteristics in a Two-Stroke Diesel Engine with Thermal Barriers (in Norwegian). (Dr.Ing. Thesis)
MTA-88-59 Bernt Arild Bremdal, MP:	An Investigation of Marine Installation Processes - A Knowledge - Based Planning Approach. (Dr.Ing. Thesis)
MTA-88-60 Xu Jun, MK:	Non-linear Dynamic Analysis of Space-framed Offshore Structures. (Dr.Ing. Thesis)
MTA-89-61 Gang Miao, MH:	Hydrodynamic Forces and Dynamic Responses of Circular Cylinders in Wave Zones. (Dr.Ing. Thesis)
MTA-89-62 Martin Greenhow, MH:	Linear and Non-Linear Studies of Waves and Floating Bodies. Part I and Part II. (Dr.Techn. Thesis)
MTA-89-63 Chang Li, MH:	Force Coefficients of Spheres and Cubes in Oscillatory Flow with and without Current. (Dr.Ing. Thesis)
MTA-89-64 Hu Ying, MP:	A Study of Marketing and Design in

	Development of Marine Transport Systems. (Dr.Ing. Thesis)
MTA-89-65 Arild Jæger, MH:	Seakeeping, Dynamic Stability and Performance of a Wedge Shaped Planing Hull. (Dr.Ing. Thesis)
MTA-89-66 Chan Siu Hung, MM:	The dynamic characteristics of tilting-pad bearings.
MTA-89-67 Kim Wikstrøm, MP:	Analysis av projekteringen for ett offshore projekt. (Licenciat-avhandling)
MTA-89-68 Jiao Guoyang, MR:	Reliability Analysis of Crack Growth under Random Loading, considering Model Updating. (Dr.Ing. Thesis)
MTA-89-69 Arnt Olufsen, MK:	Uncertainty and Reliability Analysis of Fixed Offshore Structures. (Dr.Ing. Thesis)
MTA-89-70 Wu Yu-Lin, MR:	System Reliability Analyses of Offshore Structures using improved Truss and Beam Models. (Dr.Ing. Thesis)
MTA-90-71 Jan Roger Hoff, MH:	Three-dimensional Green function of a vessel with forward speed in waves. (Dr.Ing. Thesis)
MTA-90-72 Rong Zhao, MH:	Slow-Drift Motions of a Moored Two-Dimensional Body in Irregular Waves. (Dr.Ing. Thesis)
MTA-90-73 Atle Minsaas, MP:	Economical Risk Analysis. (Dr.Ing. Thesis)
MTA-90-74 Knut-Aril Farnes, MK:	Long-term Statistics of Response in Non-linear Marine Structures. (Dr.Ing. Thesis)
MTA-90-75 Torbjørn Sotberg, MK:	Application of Reliability Methods for Safety Assessment of Submarine Pipelines. (Dr.Ing. Thesis)
MTA-90-76 Zeuthen, Steffen, MP:	SEAMAID. A computational model of the design process in a constraint-based logic programming environment. An example from the offshore domain. (Dr.Ing. Thesis)
MTA-91-77 Haagensen, Sven, MM:	Fuel Dependant Cyclic Variability in a Spark Ignition Engine - An Optical Approach. (Dr.Ing. Thesis)
MTA-91-78 Løland, Geir, MH:	Current forces on and flow through fish farms.

	(Dr.Ing. Thesis)
MTA-91-79 Hoen, Christopher, MK:	System Identification of Structures Excited by Stochastic Load Processes. (Dr.Ing. Thesis)
MTA-91-80 Haugen, Stein, MK:	Probabilistic Evaluation of Frequency of Collision between Ships and Offshore Platforms. (Dr.Ing. Thesis)
MTA-91-81 Sødahl, Nils, MK:	Methods for Design and Analysis of Flexible Risers. (Dr.Ing. Thesis)
MTA-91-82 Ormberg, Harald, MK:	Non-linear Response Analysis of Floating Fish Farm Systems. (Dr.Ing. Thesis)
MTA-91-83 Marley, Mark J., MK:	Time Variant Reliability under Fatigue Degradation. (Dr.Ing. Thesis)
MTA-91-84 Krokstad, Jørgen R., MH:	Second-order Loads in Multidirectional Seas. (Dr.Ing. Thesis)
MTA-91-85 Molteberg, Gunnar A., MM:	The Application of System Identification Techniques to Performance Monitoring of Four Stroke Turbocharged Diesel Engines. (Dr.Ing. Thesis)
MTA-92-86 Mørch, Hans Jørgen Bjelke, MH:	Aspects of Hydrofoil Design: with Emphasis on Hydrofoil Interaction in Calm Water. (Dr.Ing. Thesis)
MTA-92-87 Chan Siu Hung, MM:	Nonlinear Analysis of Rotordynamic Instabilities in High-speed Turbomachinery. (Dr.Ing. Thesis)
MTA-92-88 Bessason, Bjarni, MK:	Assessment of Earthquake Loading and Response of Seismically Isolated Bridges. (Dr.Ing. Thesis)
MTA-92-89 Langli, Geir, MP:	Improving Operational Safety through exploitation of Design Knowledge - an investigation of offshore platform safety. (Dr.Ing. Thesis)
MTA-92-90 Sævik, Svein, MK:	On Stresses and Fatigue in Flexible Pipes. (Dr.Ing. Thesis)
MTA-92-91 Ask, Tor Ø., MM:	Ignition and Flame Growth in Lean Gas-Air Mixtures. An Experimental Study with a Schlieren System. (Dr.Ing. Thesis)

MTA-86-92 Hessen, Gunnar, MK:	Fracture Mechanics Analysis of Stiffened Tubular Members. (Dr.Ing. Thesis)
MTA-93-93 Steinebach, Christian, MM:	Knowledge Based Systems for Diagnosis of Rotating Machinery. (Dr.Ing. Thesis)
MTA-93-94 Dalane, Jan Inge, MK:	System Reliability in Design and Maintenance of Fixed Offshore Structures. (Dr.Ing. Thesis)
MTA-93-95 Steen, Sverre, MH:	Cobblestone Effect on SES. (Dr.Ing. Thesis)
MTA-93-96 Karunakaran, Daniel, MK:	Nonlinear Dynamic Response and Reliability Analysis of Drag-dominated Offshore Platforms. (Dr.Ing. Thesis)
MTA-93-97 Hagen, Arnulf, MP:	The Framework of a Design Process Language. (Dr.Ing. Thesis)
MTA-93-98 Nordrik, Rune, MM:	Investigation of Spark Ignition and Autoignition in Methane and Air Using Computational Fluid Dynamics and Chemical Reaction Kinetics. A Numerical Study of Ignition Processes in Internal Combustion Engines. (Dr.Ing. Thesis)
MTA-94-99 Passano, Elizabeth, MK:	Efficient Analysis of Nonlinear Slender Marine Structures. (Dr.Ing. Thesis)
MTA-94-100 Kvålsvold, Jan, MH:	Hydroelastic Modelling of Wetdeck Slamming on Multihull Vessels. (Dr.Ing. Thesis)
MTA-94-102 Bech, Sidsel M., MK:	Experimental and Numerical Determination of Stiffness and Strength of GRP/PVC Sandwich Structures. (Dr.Ing. Thesis)
MTA-95-103 Paulsen, Hallvard, MM:	A Study of Transient Jet and Spray using a Schlieren Method and Digital Image Processing. (Dr.Ing. Thesis)
MTA-95-104 Hovde, Geir Olav, MK:	Fatigue and Overload Reliability of Offshore Structural Systems, Considering the Effect of Inspection and Repair. (Dr.Ing. Thesis)
MTA-95-105 Wang, Xiaozhi, MK:	Reliability Analysis of Production Ships with Emphasis on Load Combination and Ultimate Strength. (Dr.Ing. Thesis)
MTA-95-106 Ulstein, Tore, MH:	Nonlinear Effects of a Flexible Stern Seal Bag on Cobblestone Oscillations of an SES. (Dr.Ing. Thesis)

MTA-95-107 Solaas, Frøydis, MH:	Analytical and Numerical Studies of Sloshing in Tanks. (Dr.Ing. Thesis)
MTA-95-108 Hellan, øyvind, MK:	Nonlinear Pushover and Cyclic Analyses in Ultimate Limit State Design and Reassessment of Tubular Steel Offshore Structures. (Dr.Ing. Thesis)
MTA-95-109 Hermundstad, Ole A., MK:	Theoretical and Experimental Hydroelastic Analysis of High Speed Vessels. (Dr.Ing. Thesis)
MTA-96-110 Bratland, Anne K., MH:	Wave-Current Interaction Effects on Large-Volume Bodies in Water of Finite Depth. (Dr.Ing. Thesis)
MTA-96-111 Herfjord, Kjell, MH:	A Study of Two-dimensional Separated Flow by a Combination of the Finite Element Method and Navier-Stokes Equations. (Dr.Ing. Thesis)
MTA-96-112 Æsøy, Vilmar, MM:	Hot Surface Assisted Compression Ignition in a Direct Injection Natural Gas Engine. (Dr.Ing. Thesis)
MTA-96-113 Eknes, Monika L., MK:	Escalation Scenarios Initiated by Gas Explosions on Offshore Installations. (Dr.Ing. Thesis)
MTA-96-114 Erikstad, Stein O., MP:	A Decision Support Model for Preliminary Ship Design. (Dr.Ing. Thesis)
MTA-96-115 Pedersen, Egil, MH:	A Nautical Study of Towed Marine Seismic Streamer Cable Configurations. (Dr.Ing. Thesis)
MTA-97-116 Moksnes, Paul O., MM:	Modelling Two-Phase Thermo-Fluid Systems Using Bond Graphs. (Dr.Ing. Thesis)
MTA-97-117 Halse, Karl H., MK:	On Vortex Shedding and Prediction of Vortex-Induced Vibrations of Circular Cylinders. (Dr.Ing. Thesis)
MTA-97-118 Igland, Ragnar T., MK:	Reliability Analysis of Pipelines during Laying, considering Ultimate Strength under Combined Loads. (Dr.Ing. Thesis)
MTA-97-119 Pedersen, Hans-P., MP:	Levendefiskteknologi for fiskefartøy. (Dr.Ing. Thesis)
MTA-98-120 Vikestad, Kyrre, MK:	Multi-Frequency Response of a Cylinder Subjected to Vortex Shedding and Support

	Motions. (Dr.Ing. Thesis)
MTA-98-121 Azadi, Mohammad R. E., MK:	Analysis of Static and Dynamic Pile-Soil-Jacket Behaviour. (Dr.Ing. Thesis)
MTA-98-122 Ulltang, Terje, MP:	A Communication Model for Product Information. (Dr.Ing. Thesis)
MTA-98-123 Torbergsen, Erik, MM:	Impeller/Diffuser Interaction Forces in Centrifugal Pumps. (Dr.Ing. Thesis)
MTA-98-124 Hansen, Edmond, MH:	A Discrete Element Model to Study Marginal Ice Zone Dynamics and the Behaviour of Vessels Moored in Broken Ice. (Dr.Ing. Thesis)
MTA-98-125 Videiro, Paulo M., MK:	Reliability Based Design of Marine Structures. (Dr.Ing. Thesis)
MTA-99-126 Mainçon, Philippe, MK:	Fatigue Reliability of Long Welds Application to Titanium Risers. (Dr.Ing. Thesis)
MTA-99-127 Haugen, Elin M., MH:	Hydroelastic Analysis of Slamming on Stiffened Plates with Application to Catamaran Wetdecks. (Dr.Ing. Thesis)
MTA-99-128 Langhelle, Nina K., MK:	Experimental Validation and Calibration of Nonlinear Finite Element Models for Use in Design of Aluminium Structures Exposed to Fire. (Dr.Ing. Thesis)
MTA-99-129 Berstad, Are J., MK:	Calculation of Fatigue Damage in Ship Structures. (Dr.Ing. Thesis)
MTA-99-130 Andersen, Trond M., MM:	Short Term Maintenance Planning. (Dr.Ing. Thesis)
MTA-99-131 Tveiten, Bård Wathne, MK:	Fatigue Assessment of Welded Aluminium Ship Details. (Dr.Ing. Thesis)
MTA-99-132 Søreide, Fredrik, MP:	Applications of underwater technology in deep water archaeology. Principles and practice. (Dr.Ing. Thesis)
MTA-99-133 Tønnessen, Rune, MH:	A Finite Element Method Applied to Unsteady Viscous Flow Around 2D Blunt Bodies With Sharp Corners. (Dr.Ing. Thesis)
MTA-99-134 Elvekrok, Dag R., MP:	Engineering Integration in Field Development Projects in the Norwegian Oil and Gas Industry. The Supplier Management of Norne. (Dr.Ing.

	Thesis)
MTA-99-135 Fagerholt, Kjetil, MP:	Optimeringsbaserte Metoder for Ruteplanlegging innen skipsfart. (Dr.Ing. Thesis)
MTA-99-136 Bysveen, Marie, MM:	Visualization in Two Directions on a Dynamic Combustion Rig for Studies of Fuel Quality. (Dr.Ing. Thesis)
MTA-2000-137 Storteig, Eskild, MM:	Dynamic characteristics and leakage performance of liquid annular seals in centrifugal pumps. (Dr.Ing. Thesis)
MTA-2000-138 Sagli, Gro, MK:	Model uncertainty and simplified estimates of long term extremes of hull girder loads in ships. (Dr.Ing. Thesis)
MTA-2000-139 Tronstad, Harald, MK:	Nonlinear analysis and design of cable net structures like fishing gear based on the finite element method. (Dr.Ing. Thesis)
MTA-2000-140 Kroneberg, André, MP:	Innovation in shipping by using scenarios. (Dr.Ing. Thesis)
MTA-2000-141 Haslum, Herbjørn Alf, MH:	Simplified methods applied to nonlinear motion of spar platforms. (Dr.Ing. Thesis)
MTA-2001-142 Samdal, Ole Johan, MM:	Modelling of Degradation Mechanisms and Stressor Interaction on Static Mechanical Equipment Residual Lifetime. (Dr.Ing. Thesis)
MTA-2001-143 Baarholm, Rolf Jarle, MH:	Theoretical and experimental studies of wave impact underneath decks of offshore platforms. (Dr.Ing. Thesis)
MTA-2001-144 Wang, Lihua, MK:	Probabilistic Analysis of Nonlinear Wave-induced Loads on Ships. (Dr.Ing. Thesis)
MTA-2001-145 Kristensen, Odd H. Holt, MK:	Ultimate Capacity of Aluminium Plates under Multiple Loads, Considering HAZ Properties. (Dr.Ing. Thesis)
MTA-2001-146 Greco, Marilena, MH:	A Two-Dimensional Study of Green-Water Loading. (Dr.Ing. Thesis)
MTA-2001-147 Heggelund, Svein E., MK:	Calculation of Global Design Loads and Load Effects in Large High Speed Catamarans. (Dr.Ing. Thesis)

MTA-2001-148 Babalola, Olusegun T., MK:	Fatigue Strength of Titanium Risers - Defect Sensitivity. (Dr.Ing. Thesis)
MTA-2001-149 Mohammed, Abuu K., MK:	Nonlinear Shell Finite Elements for Ultimate Strength and Collapse Analysis of Ship Structures. (Dr.Ing. Thesis)
MTA-2002-150 Holmedal, Lars E., MH:	Wave-current interactions in the vicinity of the sea bed. (Dr.Ing. Thesis)
MTA-2002-151 Rognebakke, Olav F., MH:	Sloshing in rectangular tanks and interaction with ship motions. (Dr.Ing. Thesis)
MTA-2002-152 Lader, Pål Furset, MH:	Geometry and Kinematics of Breaking Waves. (Dr.Ing. Thesis)
MTA-2002-153 Yang, Qinzheng, MH:	Wash and wave resistance of ships in finite water depth. (Dr.Ing. Thesis)
MTA-2002-154 Melhus, Øyvin, MM:	Utilization of VOC in Diesel Engines. Ignition and combustion of VOC released by crude oil tankers. (Dr.Ing. Thesis)
MTA-2002-155 Ronæss, Marit, MH:	Wave Induced Motions of Two Ships Advancing on Parallel Course. (Dr.Ing. Thesis)
MTA-2002-156 Økland, Ole D., MK:	Numerical and experimental investigation of whipping in twin hull vessels exposed to severe wet deck slamming. (Dr.Ing. Thesis)
MTA-2002-157 Ge, Chunhua, MK:	Global Hydroelastic Response of Catamarans due to Wet Deck Slamming. (Dr.Ing. Thesis)
MTA-2002-158 Byklum, Eirik, MK:	Nonlinear Shell Finite Elements for Ultimate Strength and Collapse Analysis of Ship Structures. (Dr.Ing. Thesis)
IMT-2003-1 Chen, Haibo, MK:	Probabilistic Evaluation of FPSO-Tanker Collision in Tandem Offloading Operation. (Dr.Ing. Thesis)
IMT-2003-2 Skaugset, Kjetil Bjørn, MK:	On the Suppression of Vortex Induced Vibrations of Circular Cylinders by Radial Water Jets. (Dr.Ing. Thesis)
IMT-2003-3 Chezhian, Muthu	Three-Dimensional Analysis of Slamming. (Dr.Ing. Thesis)
IMT-2003-4 Buhaug, Øyvind	Deposit Formation on Cylinder Liner Surfaces

	in Medium Speed Engines. (Dr.Ing. Thesis)
IMT-2003-5 Tregde, Vidar	Aspects of Ship Design: Optimization of Aft Hull with Inverse Geometry Design. (Dr.Ing. Thesis)
IMT-2003-6 Wist, Hanne Therese	Statistical Properties of Successive Ocean Wave Parameters. (Dr.Ing. Thesis)
IMT-2004-7 Ransau, Samuel	Numerical Methods for Flows with Evolving Interfaces. (Dr.Ing. Thesis)
IMT-2004-8 Soma, Torkel	Blue-Chip or Sub-Standard. A data interrogation approach of identity safety characteristics of shipping organization. (Dr.Ing. Thesis)
IMT-2004-9 Ersdal, Svein	An experimental study of hydrodynamic forces on cylinders and cables in near axial flow. (Dr.Ing. Thesis)
IMT-2005-10 Brodtkorb, Per Andreas	The Probability of Occurrence of Dangerous Wave Situations at Sea. (Dr.Ing. Thesis)
IMT-2005-11 Yttervik, Rune	Ocean current variability in relation to offshore engineering. (Dr.Ing. Thesis)
IMT-2005-12 Fredheim, Arne	Current Forces on Net-Structures. (Dr.Ing. Thesis)
IMT-2005-13 Heggernes, Kjetil	Flow around marine structures. (Dr.Ing. Thesis)
IMT-2005-14 Fouques, Sebastien	Lagrangian Modelling of Ocean Surface Waves and Synthetic Aperture Radar Wave Measurements. (Dr.Ing. Thesis)
IMT-2006-15 Holm, Håvard	Numerical calculation of viscous free surface flow around marine structures. (Dr.Ing. Thesis)
IMT-2006-16 Bjørheim, Lars G.	Failure Assessment of Long Through Thickness Fatigue Cracks in Ship Hulls. (Dr.Ing. Thesis)
IMT-2006-17 Hansson, Lisbeth	Safety Management for Prevention of Occupational Accidents. (Dr.Ing. Thesis)
IMT-2006-18 Zhu, Xinying	Application of the CIP Method to Strongly Nonlinear Wave-Body Interaction Problems. (Dr.Ing. Thesis)
IMT-2006-19 Reite, Karl Johan	Modelling and Control of Trawl Systems.

	(Dr.Ing. Thesis)
IMT-2006-20 Smogeli, Øyvind Notland	Control of Marine Propellers. From Normal to Extreme Conditions. (Dr.Ing. Thesis)
IMT-2007-21 Storhaug, Gaute	Experimental Investigation of Wave Induced Vibrations and Their Effect on the Fatigue Loading of Ships. (Dr.Ing. Thesis)
IMT-2007-22 Sun, Hui	A Boundary Element Method Applied to Strongly Nonlinear Wave-Body Interaction Problems. (PhD Thesis, CeSOS)
IMT-2007-23 Rustad, Anne Marthine	Modelling and Control of Top Tensioned Risers. (PhD Thesis, CeSOS)
IMT-2007-24 Johansen, Vegar	Modelling flexible slender system for real-time simulations and control applications.
IMT-2007-25 Wroldsen, Anders Sunde	Modelling and control of tensegrity structures. (PhD Thesis, CeSOS)
IMT-2007-26 Aronsen, Kristoffer Høye	An experimental investigation of in-line and combined in-line and cross flow vortex induced vibrations. (Dr.avhandling, IMT)
IMT-2007-27 Zhen, Gao	Stochastic response analysis of mooring systems with emphasis on frequency-domain analysis of fatgue due to wide-band processes. (PhD-thesis CeSOS).
IMT-2007-28 Thorstensen, Tom Anders	Lifetime Profit Modelling of Ageing Systems Utilizing Information about Technical Condition. Dr.ing. thesis, IMT.
IMT-2008-29 Berntsen, Per Ivar B.	Structural Reliability Based Position Mooring. PhD-Thesis, IMT.
IMT-2008-30 Ye, Naiquan	Fatigues Assessment of Aluminium Welded Box stiffener Joints in ships. Dr.ing.-Thesis, IMT.
IMT-2008-31 Radan, Damir	Integrated Control of Marine Electrical Power Systems. PhD-Thesis, IMT.
IMT-2008-32 Norum, Viggo L.	Analysis of Ignituin and Combustion in Otto Lean-Burn Engines with Prechambers. Dr.ing. thesis, IMT.
IMT-2008-33 Pákozdi, Csaba	A Smoothed Particle Hydrodynamics Study of

	Two-dimensional Nonlinear Sloshing in Rectangular Tanks. Dr.ing.thesis, IMT.
IMT-2008-34 Grytøyr, Guttorm	A Higher-Order Boundary Element Method and Applications to Marine Hydrodynamics. Dr.ing. Thesis, IMT.
IMT-2008-35 Drummen, Ingo	Experimental and Numerical Investigation of Nonlinear Wave-Induced Load effects in Containerships Considering Hydroelasticity. PhD-Thesis. CeSOS.
IMT-2008-36 Skejic, Renato	Maneuvering and Seakeeping of a Singel Ship and of Two Ships in Interaction. PhD-Thesis. CeSOS.
IMT-2008-37 Harlem, Alf	An Age-Based Replacement Model for Repairable Systems with Attention to High-Speed Marine Diesel Engines. PhD-Thesis, IMT.
IMT-2008-38 Alsos, Hagbart S.	Ship Grounding. Analysis of Ductile Fracture, Bottom Damage and Hull Girder Response. PhD-thesis, IMT.
IMT-2008-39 Graczyk, Mateusz	Experimental Investigation of Sloshing Loading and Load Effects in Membrane LNG Tanks Subjected to Random Excitation. PhD-thesis, CeSOS.
IMT-2008-40 Taghipour, Reza	Efficient Prediction of Dynamic Response for Flexible amd Multi-body Marine Structures. PhD-thesis, CeSOS.
IMT-2008-41 Ruth, Eivind	Propulsion Control and Thrust Allocation on Marine Vessels. PhD-Thesis, CeSOS.
IMT-2008-42 Nystad, Bent Helge	Technical Condition Indexes and Remaining Useful Life of Aggregated Systems. Ph.d.thesis, IMT.
IMT-2008-43 Soni, Prashant Kumer	Hydrodyynamic Coefficients for Vortex Induced Vibrations of Flexible Beams, Ph.d.thesis, CeSOS.
IMT-2009-43 Amlashi, Hadi K.K.	Ultimate Strength and Reliability-based Design of Ship Hulls with Emphasis on Combined Global and Local Loads. Ph.d-Thesis, IMT.

IMT-2009-44 Pedersen, Tom Arne	Bond Graph Modelling of Marine Power Systems. Phd.Thesis, IMT.
IMT-2009-45 Kristiansen, Trygve	Two-Dimensional Numerical and Experimental Studies of Piston-Mode Resonance. PhD-Thesis CeSOS.
IMT-2009-46 Ong, Muk Chen	Applications of a Standard High Reynolds Number $k-\varepsilon$ Model and a Stochastic Scour Prediction Model for Marine Structures. PhD-thesis, IMT.
IMT-2009-47 Hong, Lin	Simplified Analysis and Design of Ships subjected to Collision and Grounding. PhD-thesis, IMT.
IMT-2009-48 Koushan, Kamarn	Vortex Induced Vibrations of Free Span Pipelines, PhD-thesis, IMT.
IMT-2009-49 Korsvik, Jarl Eirik	Heuristic Methods for Ship Routing and Sceduling. PhD-thesis, IMT.
IMT-2009-50 Lee, Ji Hoon	Experimental Investigation and Numerical Methods in Analyzing the Ocean Current Displacement Phenomena of Longlines. PhD-thesis, IMT.